Physico-Chimie des plasmas de silane pour la formation de nacocristaux de silicium a tempétature ambiante : application à des dispositifs.

Veinardi Suendo

ECOLE POLYTECHNIQUE

Thèse présentée pour obtenir le grade de

DOCTEUR DE L'ECOLE POLYTECHNIQUE

Spécialité : Science des Matériaux

Par

Veinardi Suendo

Sujet

Low temperature plasma synthesis of silicon nanocrystals for photonic applications

Soutenue le 25 novembre 2005 devant le jury composé de:

I. Solomon	Président
L. Boufendi	Rapporteur
A. Halimaoui	Rapporteur
P. Roca i Cabarrocas	Directeur de thèse
A. Gicquel	Examinateur
V. Paillard	Examinateur

Laboratoire de Physique des Interfaces et des Couches Minces
UMR 7647 du CNRS, Ecole Polytechnique

Remerciements

Ce travail de thèse, financé par la direction des relations extérieurs de l'Ecole Polytechnique (DRE) puis par le Laboratoire de Physique des Interface et des Couches Minces (PICM) de l'Ecole Polytechnique a été effectué au PICM de novembre 2001 à novembre 2005. Pendant ces 4 années, j'ai eu la chance de profiter de l'atmosphère chaleureuse et de haut niveau scientifique dans ce laboratoire. Comme tout travail expérimental, cette thèse est bien sur le résultat d'un travail d'équipe. Je tiens donc à remercier collectivement tous les membres du laboratoire.

Je remercie tout particulièrement mon directeur de thèse Monsieur Pere Roca i Cabarrocas, Directeur de Recherches au CNRS, qui a suivi attentivement la progression de ce travail avec beaucoup des discussions constructives et courageuses.

Je dois remercier Monsieur Roland Sénéor et Madame Cynthia Radiman qui ont commencé la collaboration entre l'Ecole Polytechnique et l'Institut Teknologi Bandung en Indonésie où j'ai eu l'occasion de recevoir une bourse pour continuer mes études dans le cadre du programme doctoral à l'Ecole Polytechnique. Je dois remercier également Monsieur Bernard Drévillon directeur du laboratoire PICM qui m'a introduit à mon directeur de thèse et m'a permis de travailler dans ce laboratoire.

J'exprime toute ma gratitude à Monsieur Ionel Solomon, Directeur de Recherches émérite au CNRS du Laboratoire de Physique de la Matière Condensée à l'Ecole Polytechnique de l'honneur qu'il m'a fait de présider le jury de ma thèse. C'etait toujours un grand plaisir de discuter de science avec lui. J'ai appris beaucoup de lui, en particulièr : « comment faire la physique bon marché ».

Je remercie très vivement Monsieur Laifa Boufendi, Professeur à l'Université d'Orléans qui m'a encouragé pendant ma thèse avec beaucoup d'aides expérimentales, des discussions et aussi pour avoir accepté d'être rapporteur de ce travail.

Je remercie Monsieur Aomar Halimaoui de ST Microélectronique qui a bien voulu s'intéresser à ce travail pour avoir accepté d'être rapporteur de ma thèse.

Je remercie Monsieur Vincent Paillard, Professeur à l'Université de Toulouse qui a bien voulu s'intéresser à ce travail pour des mesures Raman et des discussions, et aussi pour avoir accepté d'être une partie de mon jury de thèse.

Je remercie Madame Alix Gicquel, Professeur à l'Université Paris 13 et Directrice Scientifique au INRETS qui a bien voulu faire partie de mon jury de thèse.

Je remercie Monsieur Ganjar Kurnia et toutes les membres de l'ambassade d'Indonésie en France pour leur aide et leurs encouragements.

Mes remerciements vont à Gilles Patriarche, Carlos Barthou, Andriy V. Kharchenko, Jacques Jolly, Gérard Jaskierowicz, Isabelle Sagnes, Georges Adamopoulos, Satyendra Kumar, Andrei Kosarev, Sarah Lebib, Christian Godet, Jean-Eric Bourrée, Pavel Bulkin, Dmitri Daineka, Shunri Oda, et Holger Vach pour leur aide, le partage de leurs connaissances et des discussions pendant la thèse.

Je remercie Debajyoti Das, Kim Geun-Bom, Anna Fontcuberta i Morral, Yves Poissant, Sandesh Jadkar, Tatiana Novikova, Yvan Bonnassieux, Marc Chatelet, Alexei Abramov, Cyril Jadaud, Gary-Kitchner Rose, Dominique Conne, Dominique Clément, Frédéric Liège, Costel Cojocaru, Jean-Luc Moncel, Didier Pribat, Enric Garcia Caurel, Céline Bernon, Razvigor Ossikovski, Chantal Geneste, Josiane Mabred, Marie-Jo Surmont, Laurence Corbel, et Chisato Niikura pour leur aide et leur amitié pendant quatre années au PICM.

Je remercie mes camarades, thésards, postdocs et stagiaires qui ont partagé les joies d'un tel travail: Fatiha Kail, Jérôme Damon-Lacoste, Muriel Matheron, Billel Kalache, Samir Kasouit, Nihed Chaâbane, Svetoslav Tchakarov, Takashi Katsuno, Marie-Estelle Gueunier-Farret, Kim Doh-Hyung, Quentin Brulin, Nguyen Tran-Thuat, Bui Van-Diep, Nguyen Quang, Dao Thien-Hai, Samira Fellah, Yassine Djeridane, Daniel Soujon, Julie Fargin, Matthieu Thomas, Marie Jouanny, Maxime Mikikian, Marjorie Cavarroc, Pae C. Wu, Rao Rui, Razvan Negru, Nihan Kosku, Céline Baron.

Je remercie ma famille et aussi des amis : Wim Effendi K. S., Tjie Soei Lan, Sparisoma Viridi, Missionnaire Amir, Yohanes Handoyo, Oei Ho Tin, Mauw Wen Liang, Hartoto Halim, Nyi Boen, Andy Surya Rikin, Andy Santoso, Ng Suk Fung, Alwen F. Tiu, Bowie Brotosumpeno, Edy Wijaya, Jeffry Christiandy, Alfred Iskandar, Rofikohrokhim, Pascaline Truc, Leandro Jose Raniero, Shinji et Sayoko Kimura, Bungo Kubota, Akihiko Tanioka, Mie Minagawa, Toshihisa Osaki, Ikuyoshi Tomita, Hidetoshi Matsumoto, Eriko Suzuki, Mariko Kinoshita, Damien Farret, Petr Fojtik, Pavla, Fredy, Diene, Javier, Simona et Luo Wei pour leur amitié, leurs prières, et leurs encouragements pendant mon séjour en France.

Table of contents

Chapter 1

Introduction

Information technology has grown rapidly in the last few decades and is becoming one of the basic needs of humankind. As this technology grows, the demand for new materials to develop it also increases. So far, silicon is the main semiconductor material for electronic applications, while III-V semiconductors are the main materials for photonic applications. We readily find silicon integrated circuits (ICs) around us: in our cellular phones, personal computers, cars, home appliances, etc. For the further development of this technology, a material compatible with silicon microelectronics and suitable optoelectronic properties would play an important role. In particular, research should focus on a material which could be used for the next generation of photon emitters and could be integrated directly into an IC. Indeed, it is well-known that due to its indirect band-gap structure, bulk silicon is an extremely inefficient photon emitter. Therefore, scientists have turned their interests to other more complex and expensive semiconductor materials such as GaAs (gallium arsenide), InP (indium phosphide), GaP (gallium phosphide), etc. Even though these materials have allowed the realization of laser diodes, they cannot be easily associated with silicon integrated circuits. They are incompatible because the two materials have different crystal lattice constants, a so-called lattice mismatch. Another type of materials, which also give good luminescent efficiency are organic materials. In this case, one does not encounter the lattice mismatch problem due to their amorphous structure, but their processing into devices is not always compatible with microelectronics industry standards. Moreover, the stability of these materials is quite low compared to their inorganic counterparts. As a short summary, silicon related light emitting materials and their references are listed in Table 1.1.

To simplify these problems and to develop optoelectronic devices, it would be better if silicon itself could emit light. The discovery of luminescence from porous silicon and nanosized silicon structures gave new hope for the development of an all-silicon laser [1, 2]. Hitherto, many approaches have been carried out to produce these nanostructures such as the synthesis of porous silicon, silicon nanocrystals, and silicon nanoclusters using various methods [3-5]. The idea behind these approaches is quantum confinement and the breakdown of the *k*-conservation rule in the silicon nanostructures, which facilitates the radiative recombination in these materials [6]. Moreover, the discovery of luminescence from various

silicon related materials such as porous amorphous silicon [7, 8], amorphous silicon nanoclusters [9,10], siloxenes [11-14], and polysilanes [15-18] has given a strong encouragement to research in this field.

Polymorphous silicon

Another important issue in this research is the synthesis of the material itself, where the growth method is preferably simple, scaleable, and compatible with typical microelectronics industry processes. The formation of silicon particles in the plasma phase using PECVD (plasma enhanced chemical vapor deposition) appears to be an interesting alternative to optimize PL and device fabrication. The discovery of a new material in the field of solar cells and large area electronics, namely hydrogenated polymorphous silicon (*pm-Si:H*), which consists of silicon nanocrystals (formed in the plasma phase) embedded in an amorphous matrix [19], has given a new perspective on the formation of silicon nanostructures using the PECVD technique.

Hydrogenated polymorphous silicon (*pm-Si:H*) has a unique structure (more ordered amorphous matrix, embedded nanocrystals, etc.) [20], good electronic properties (low defect density, stability against light soaking, etc.) and a simple preparation method (standard RF-PECVD at low temperature), which makes it a good alternative to *a-Si:H* for large area electronic devices and optoelectronic applications [21, 22]. *Pm-Si:H* films are deposited from silane (SiH_4) highly diluted in hydrogen (H_2) at high pressure and RF power, close to the regime of powder formation. The deposition regime of polymorphous silicon is indicated by the drastic increase of the deposition rate (α-γ' transition) as a function of the total pressure, due to the contribution of clusters and/or agglomerates to deposition [23].

Hydrogenated polymorphous silicon-carbon alloys (pm-$Si_{1-x}C_x$:H)

Here we introduce hydrogenated polymorphous silicon-carbon alloys (*pm-$Si_{1-x}C_x$:H*) aiming to obtain a material with a higher band-gap than *pm-Si:H* for optoelectronic applications. Their deposition is based on modifying plasma conditions developed for *pm-Si:H*, by adding CH_4 (methane) to the silane-hydrogen mixture at high pressure and RF power. As it is deposited in *pm-Si:H* conditions, the clusters and/or agglomerates should contribute to the deposition. The ideas behind the synthesis of this material are:

i) to deposit thin films with silicon nanocrystals embedded in the amorphous matrix as an inheritance from *pm-Si:H*.

ii) to increase the band-gap of the amorphous matrix so it becomes more transparent in the visible region, thus reducing the absorption of luminescence emitted light.

iii) to confine the nanoclusters with a matrix that can provide a high surface passivation, thus decreasing the probability of non-radiative recombination on the surface of nanocrystals.

iv) to enhance the quantum confinement effect due to the higher band-gap shell.

This approach resembles the idea of growing Si nanocrystals embedded in SiO_2 [4, 24-28] and Si_3N_4 [9, 28] matrices. However, in the case of *pm-*$Si_{1-x}C_x$*:H*, as opposed to SiO_2, amorphous silicon-carbon alloys (*a-*$Si_{1-x}C_x$*:H*) are deposited as a matrix to confine the nanocrystals. For many applications, including electroluminescent (EL) devices, the *a-*$Si_{1-x}C_x$*:H* matrix gives several advantages compared to SiO_2 due to its semiconductor and alloy properties such as the possibility to inject charge carriers into the embedded nanocrystals and the possibility to tune its band-gap by varying the concentration of carbon and hydrogen in the film.

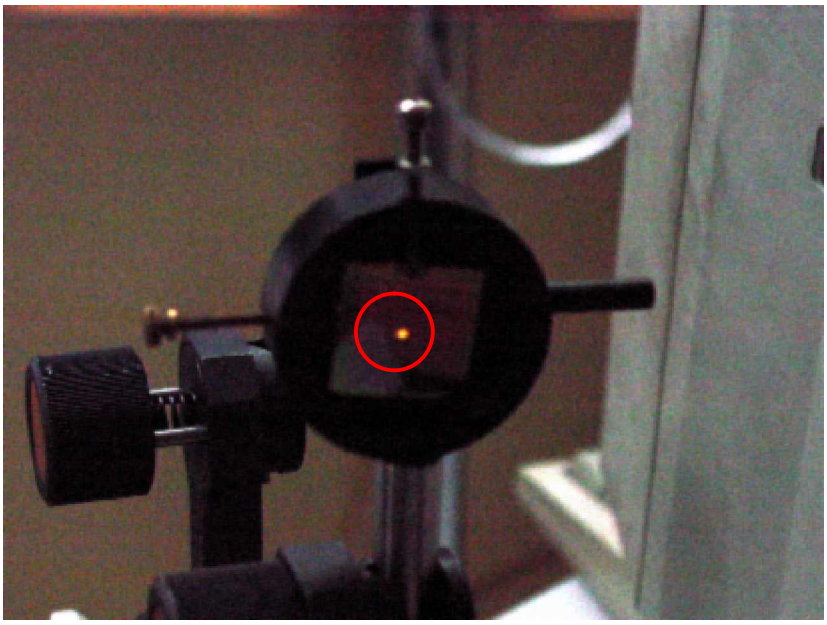

Fig. 1.1. Red light emission of a *pm-*$Si_{1-x}C_x$*:H* film excited by a 4 mW HeCd laser at 325 nm.

pm-*$Si_{1-x}C_x$*:H as a luminescent material

Among amorphous semiconductor materials, hydrogenated silicon-carbon alloys have been widely studied for the development of electroluminescent devices. The challenge of *pm-*$Si_{1-x}C_x$*:H* synthesis is to discover a feasible fabrication route that allows the growth of improved luminescence materials that can be applied in optoelectronic and large area electronic devices. Indeed as shown in Fig. 1.1., *pm-*$Si_{1-x}C_x$*:H* films show quite impressive luminescence properties, where the photoluminescence (PL) signal can be easily observed at

room temperature with the naked eye. Electroluminescent device fabrication is another challenging task to accomplish, considering the carrier injection problem at the *p/i* or *n/i* interfaces and the low conductivity of the amorphous matrix in the intrinsic layer.

To determine the origin of the luminescence in polymorphous silicon carbon is one of the challenges of this thesis. Silicon nanocrystals and silicon nanoclusters are the main candidates for the luminescence source. Besides these sources, molecular luminescence sources such as siloxenes and polysilanes have also to be considered due to the existence of oxygen in the films and the high deposition pressure during fabrication. The contribution of the *a-*$Si_{1-x}C_x$*:H* matrix, which is known to give luminescence [29-34], should also be considered. Moreover, if we recall the existence of defect states in the band tails as usually observed in amorphous materials, the luminescence can still be accepted as the process that might occur in the matrix even if there is an important difference between luminescence energy and optical band-gap energy (~0.5 eV). Furthermore, because the strong luminescent signal is observed at room temperature, the quantum confinement effect also becomes an important factor that should be evaluated as the origin of the luminescence.

Moreover, we have also observed a strong influence on the PL intensity of *pm-*$Si_{1-x}C_x$*:H* by immersing the samples in liquid nitrogen. The difference between PL at 300 K in air and at 77 K in liquid N_2 varies between one and three orders of magnitude. This cannot be explained by the change of temperature or by a change in the dielectric constant of the medium but is probably due to the passivation of defects. This effect describes well the potential of this material to be improved for many applications.

Electroluminescent devices

Electroluminescent devices based on amorphous silicon carbon alloys have been developed for more than 20 years. Towards that purpose, metal-insulator-semiconductor (MIS) structures [35], *p-i-n* structures [36, 37] and *p-i-n* structures with hot-carrier tunneling injection layers [38] have been studied. The realization of electroluminescent devices using *pm-*$Si_{1-x}C_x$*:H* as the active layer is a challenging task to accomplish, especially if we consider the heterogeneous structure of this material, where the luminescence centers are the nanometer size crystallites inside the amorphous matrix. In this case, we have to take into account several problems related to the injection of carriers from the doped layers to the intrinsic layer and into the luminescence centers. The efficiency of the injection might be improved using known methods as described elsewhere [38-40], but the injection of carriers into the nanocrystals embedded in an amorphous matrix is still an open field. The surface

passivation of the nanocrystals, the difference in band-gap energy between the matrix and the nanoclusters, and the electric conductivity of the matrix, are important parameters to take into account to improve electroluminescent devices based on this material.

Table 1.1. Summary of silicon based light emitting materials. The characteristics of III-V and organic materials are also given as a comparison

Material	Synthesis Method	Structure	Characteristics	Year	References
Porous *c-Si*	Electrolysis	Porous thin film on Si wafer	Room temperature, visible emission, slow decay	1990	3
Porous *a-Si*	Electrolysis	Porous thin film on a-Si thin film	Room temperature, visible emission	1996	7, 8
Nanocrystals	Ion implantation + annealing	Embedded inside matrix	Room temperature, visible emission, slow decay	1996	24-27
Nanocrystals	Plasma (+annealing)	Embedded inside matrix or stand alone	Room temperature, visible emission	1990	41, 42
a-Si clusters	Plasma	Embedded inside matrix	Room temperature, visible emission	2001	9, 43
Siloxenes	Chemical synthesis	Thin film	Room temperature, visible emission	1992	11-14
Polysilanes	Chemical synthesis	Thin film	Room temperature, visible emission	1985	15-18
pm-$Si_{1-x}C_x$*:H*	Plasma	Aggregates of Si nanocrystals embedded inside amorphous silicon carbon matrix	Room temperature, visible emission, broad emission range, well encapsulated, slow decay	2004	44
c-Si	Czochralski technique	Stand alone	Low temperature, indirect band gap, very low efficiency, near infra red (NIR) emission	1918	45, 46
a-Si:H	Plasma	Thin film	Low temperature, low efficiency, NIR emission	1978	47-50
pm-Si:H	Plasma	Thin film	Low temperature, low efficiency, red or NIR emission, absorption by matrix	1998	20-23
III-V	Bridgmann method, LPC[a], CVD[b], MBE[c], LPE[d]	Stand alone	Room temperature, direct band gap, high efficiency, wide range UV-visible emission, fast decay	1955	45, 46
Molecular organics	Chemical synthesis with OVPD[e]	Thin film	Room temperature, high efficiency, wide range UV-Visible emission, lower stability than inorganic materials	1960s	51[f] and refs. therein

[a] LPC (Liquid Encapsulated Czochralski)

[b] CVD (Chemical Vapor Deposition).

[c] MBE (Molecular Beam Epitaxy).

[d] LPE (Liquid Phase Epitaxy).

[e] OVPD (Organic Vapor Phase Deposition).

[f] Recent review on the progress of molecular organic materials for electroluminescent applications.

References

[1] L. Canham, *Nature* **408**, 411 (2000).

[2] P. Ball, *Nature* **409**, 974 (2001).

[3] L. T. Canham, *Appl. Phys. Lett.* **57**, 1046 (1990).

[4] Y. Kanemitsu, *J. Lumin.* **70**, 333 (1996).

[5] L. Patrone, D. Nelson, V. I. Safarov, M. Sentis, W. Marine, S. Giorgio, *J. Appl. Phys.* **87**, 3829 (2000).

[6] D. Kovalev, H. Heckler , M. Ben-Chorin, G. Polisski, M. Schwartzkopff, F. Koch, *Phys. Rev. Lett.* **81**, 2803 (1998).

[7] R. B. Wehrspohn, J.-N. Chazalviel, F. Ozanam, I., Solomon, *Phys. Rev. Lett.* **77**, 1885 (1996).

[8] R. B. Wehrspohn, J.-N. Chazalviel, F. Ozanam, I., Solomon, *Thin Solid Films* **297**, 5 (1997).

[9] N. M. Park, C. J. Choi, T. Y. Seong, S. J. Park, *Phys. Rev. Lett.* **86**, 1355 (2001).

[10] K. Nishio, J. Koga, T. Yamaguchi, F. Yonezawa, *Phys. Rev. B* **67**, 195304 (2003).

[11] P. Deak, M. Rosenbauer, M. Stutzmann, J. Weber, M. S. Brandt, *Phys. Rev. Lett.* **69**, 2531 (1992).

[12] H. D. Fuchs, M. Stutzmann, M. S. Brandt, M. Rosenbauer, J. Weber, A. Breitschwerdt, P. Deak, M. Cardona, *Phys. Rev. B* **48**, 8172 (1993).

[13] M. Stutzmann, M. S. Brandt, M. Rosenbauer, J. Weber, H. D. Fuchs, *Phys. Rev. B* **47**, 4806 (1993).

[14] R. F. Pinizzotto, H. Yang, J. M. Perez, J. L. Coffer, *J. Appl. Phys.* **75**, 4486 (1994).

[15] S. Furukawa, N. Matsumoto, *Phys. Rev. B* **31**, 2114 (1985).

[16] R. D. Miller, J. Michl, *Chem. Rev.* **89**, 1359 (1989).

[17] Y. Kanemitsu, K. Suzuki, Y. Nakayoshi, Y. Masumoto, *Phys. Rev. B* **46**, 3916 (1992).

[18] A. Kobayashi, H. Naito, Y. Matsuura, K. Matsukawa, H. Inoue, Y. Kanemitsu, *Jpn. J. Appl. Phys.* **41**, L1467 (2002).

[19] P. Roca i Cabarrocas, *J. Non-Cryst. Solids* **266-269**, 31 (2000).

[20] A. Fontcuberta i Morral, H. Hofmeister, P. Roca i Cabarrocas, *J. Non-Cryst. Solids* **299-302**, 284 (2002).

[21] S. Tchakarov, P. Roca i Cabarrocas, U. Dutta, P. Chatterjee, and B. Equer. *J. Appl. Phys.* **94**, 7317 (2003).

[22] J. P. Kleider, C. Longeaud, M. Gauthier, M. Meaudre, R. Meaudre, R. Butté, S. Vignoli, P. Roca i Cabarrocas, *J. Appl. Phys.* **75**, 3351 (1999).

[23] V. Suendo, A. V. Kharchenko, P. Roca i Cabarrocas, *Thin Solid Films* **451-452**, 259 (2004).

[24] K. S. Min, K. V. Shcheglov, C. M. Yang, H. A. Atwater, M. L. Brongersma, A. Polman, *Appl. Phys. Lett.* **69**, 2033 (1996).

[25] J. Linnros, A. Galeckas, N. Lalic, V. Grivickas, *Thin Solid Fims* **297**, 167 (1997).

[26] M. L. Brongersma, A. Polman, K. S. Min, E. Boer, T. Tambo, H. A. Atwater, *Appl. Phys. Lett.* **72**, 2577 (1998).

[27] M. L. Brongersma, P. G. Kik, A. Polman, K. S. Min, H. A. Atwater, *Appl. Phys. Lett.* **76**, 351 (2000).

[28] L. Torrison, J. Tolle, D. J. Smith, C. Poweleit, J. Menendez, M. M. Mitan, T. L. Alford, J. Kouvetakis, *J. Appl. Phys.* **92**, 7475 (2002).

[29] D. Engemann, R. Fischer, J. Knecht, *Appl. Phys. Lett.* **32**, 567 (1978).

[30] W. Siebert, R. Carius, W. Fuhs, K. Jahn, *Phys. Stat. Sol. (b)* **140**, 311 (1987).

[31] V. A. Vasil'ev, A. S. Volkov, E. Musabekov, E. I. Terukov, V. E. Chelnokov, S. V. Chernyshov, Yu. M. Shernyakov, *Sov. Phys. Semicond.* **24**, 445 (1990).

[32] S. V. Chernyshov, E. I. Terukov, V. A. Vassilyev, A. S. Volkov, *J. Non-Cryst. Solids* **134**, 218 (1991).

[33] C. Palsule, S. Gangopadhyay, D. Cronauer, B. Schröder, *Phys. Rev. B* **48**, 10804 (1993).

[34] L. R. Tessler, I. Solomon, *Phys. Rev. B* **52**, 10962 (1995).

[35] H. Munekata, H. Kukimoto, *Appl. Phys. Lett.* **42**, 432 (1983).

[36] D. Kruangam, T. Endo, G. Wei, H. Okamoto, Y. Hamakawa, *Jpn. J. Appl. Phys.* **24**, L806 (1985).

[37] D. Kruangam, M. Deguchi, T. Toyama, H. Okamoto, Y. Hamakawa, *IEEE Trans. Electron Devices* **35**, 957 (1988).

[38] S. A. Paasche, T. Toyama, H. Okamoto, Y. Hamakawa, *IEEE Trans. Electron Devices* **36**, 2895 (1989).

[39] T. S. Jen, J. W. Pan, N. F. Shin, W. C. Tsay, J. W. Hong, C. Y. Chang, *Jpn. J. Appl. Phys.* **33**, 827 (1994).

[40] J. W. Lee, K. S. Lim, *Jpn. J. Appl. Phys.* **35**, L1111 (1996).

[41] H. Takagi, H. Ogawa, Y. Yamazaki, A. Ishizaki, T. Nakagiri, *Appl. Phys. Lett.* **56**, 2379 (1990).

[42] H. Hofmeister, J. Dutta, H. Hofmann, *Phys. Rev. B* **54**, 2856 (1996).

[43] H.-S. Kwack, Y. Sun, Y.-H. Cho, N.-M. Park, S.-J. Park, *Appl. Phys. Lett.* **83**, 2901 (2003).

[44] V. Suendo, P. Roca i Cabarrocas, G. Patriarche, *Optical Materials* **27**, 953 (2005).

[45] P. P. Yu, M. Cardona, *Fundamentals of Semiconductors: Physics and Materials Properties*, Springer-Verlag, Berlin, 1996.

[46] P. Bhattacharya, *Semiconductor Optoelectronic Devices*, Prentice-Hall, Inc., New Jersey, 1994.

[47] R. A. Street, J. C. Knights, D. K. Biegelsen, *Phys. Rev. B* **18**, 1880 (1978).

[48] K. M. Hong, J. Noolandi, R. A. Street, *Phys. Rev. B* **23**, 2967 (1981).

[49] R. A. Street in J. I. Pankove (Ed.), *Semiconductor and Semimetals* **Vol. 21** : *Hydrogenated Amorphous Silicon* **Part B**, Academic Press, Inc., Orlando, 1984, p197-244.

[50] H. Oheda, *Phys. Rev. B* **52**, 16530 (1995).

[51] L. S. Hung, C. H. Chen, *Materials Science and Engineering R* **39**, 143 (2002).

Chapter 2
Experimental

2.1. Plasma Enhanced Chemical Vapor Deposition (PECVD)

Introduction

Plasma-enhanced (or -assisted) chemical vapor deposition (and etching), also called glow discharge because of the light emitted by the excited species, is an important technique for materials processing. It has been applied to the synthesis of new materials for optoelectronic applications including nanostructured materials, the fabrication of electronic devices, and the modification of surface and interface properties of materials. In recent years, plasma processes have become indispensable for manufacturing large area electronic devices, in addition to their crucial role in the processing of very large scale integrated circuits (ICs) for the microelectronics industry. Moreover, plasma processes are also critical in many other industries such as aerospace, automotive, steel, biomedical and toxic waste management [1]. In the case of hydrogenated amorphous silicon and related materials (a-SiC:H, a-SiGe:H, a-SiN:H,…) the RF glow discharge technique has become widely used because of its flexibility with respect to other deposition techniques [2].

By definition, a plasma is a ionized gas which remains electrically neutral from a macroscopic point of view [1, 3]. The presence of charged particles (electrons and ions) results in long-range Coulomb force interactions which are responsible for its unique properties. Industrial applications of plasma processes are mainly based on weakly ionized plasma discharges, characterized by the following properties: a) they are electrically driven, b) the collisions between charged particles and neutral gas molecules are important, c) there are boundaries at which surface losses are important, d) ionization of neutrals sustains the plasma in the steady state and e) electrons are not in thermal equilibrium with ions [1]. In the case of PECVD, the plasma processes are usually driven by an ac (alternating current) high frequency power supply, typically above 50 kHz and usually in the range of several megahertz or radio frequency (RF) range [1, 4]. The advantage of using high frequency excitation, compared to direct current plasma, is that a steady-state discharge can be sustained even with insulator coated electrodes, i.e., one can deposit insulating layers. This is possible

as the period of an RF half-cycle is shorter than the time needed for charging the insulator surface. This point is very important for applications where the glow discharge is used to deposit thin films on the surface of insulating materials (glasses, oxides, polymers, ceramics, etc.). Roughly, the electron density in RF discharges is of the order of 10^{15}-10^{17} m^{-3} and electron temperatures (T_e) in the range of 1- 4 eV, which of course depend on the dissipated power (typically 1-300 W) and on the gas mixture [1, 4].

Plasmas and Sheaths

A typical reactor for plasma process is a flat-bed or planar system in which the discharge is generated between two parallel plate electrodes (Fig. 2.1). In this system, one electrode is connected to the RF generator (RF / powered electrode or cathode) through an impedance matching network, which adapts the impedance of the system to 50 Ω, to ensure an optimal energy transfer to the discharge. The second electrode is usually connected to the ground (grounded electrode or anode). The choice of the electrode on which the substrate is mounted depends on the purpose of the process (deposition or etching), due to the difference in the energy of positive ions reaching the electrodes. The ion energy can be as high as $V_{RF}/2$ for symmetric systems and as high as V_{RF} at the powered electrode for asymmetric systems [1]. Therefore, the substrate is normally attached to the powered electrode for etching purposes, and to the grounded electrode for deposition.

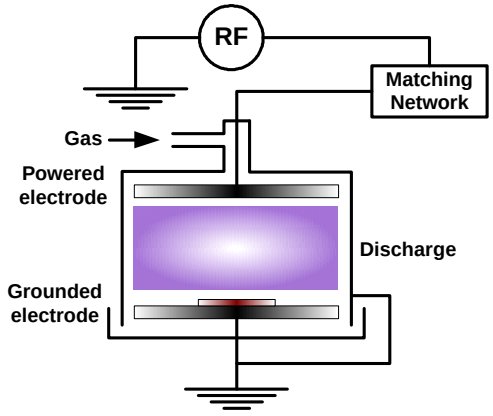

Fig. 2.1. Schematic diagram of a flat-bed or planar RF discharge reactor.

In RF discharges, because they are electrically driven and weakly ionized, the applied power preferentially heats the mobile electrons with respect to ions. Due to their higher mass, ions efficiently exchange their energy through collision processes with gas molecules. On the other hand, the electrons cannot share the energy gained from the electric field through elastic collisions with heavier ions or neutral species due to their small mass. Hence, the electrons

reach a much higher average energy than ions ($T_e >> T_i$). The electrons exchange their energy mainly through inelastic collision processes, such as excitation, dissociation and ionization. Therefore, the first step of plasma chemistry in RF discharges, the dissociation of gas molecules into radicals, is an electron driven process.

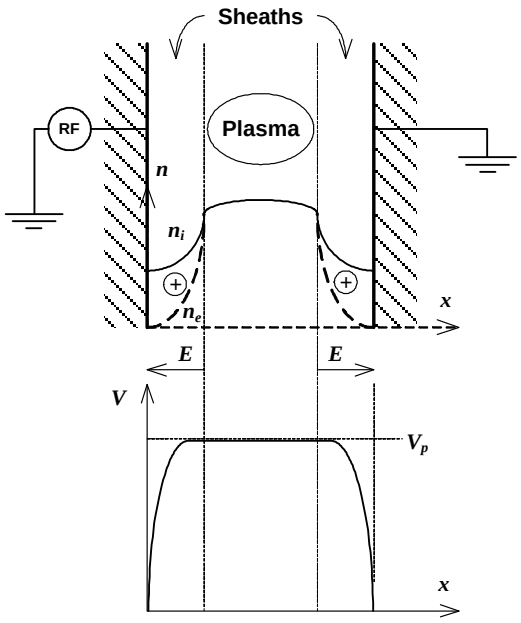

Fig. 2.2. Schematic diagram of average densities, electric field, and potential profiles after formation of the sheaths [1].

Sheaths are positively charged regions located between the bulk plasma (quasineutral, $n_i \approx n_e$) and the walls. These layers are formed due to the losses of fast-moving electrons to the walls; note that the thermal velocity of electrons is at least 100 times that of ions. Thus, on a very short time scale, the loss of electrons to the walls forms a region with a positive net charge density near the walls. This leads to a potential profile that is positive in the bulk plasma and falls sharply to zero near the walls (see Fig. 2.2). This profile confines the traveling electrons to the bulk plasma and accelerates or pushes out the ions that enter the sheaths. This potential is defined as the plasma potential V_p, which is positive anywhere in the plasma and can be regarded as the reference potential of the system. The potential on the powered electrode is also negative with respect to the plasma potential V_p. This can be explained by the charging effect due the large difference in mobility between electrons and ions in the plasma, that results in a leaky diode I-V characteristic as shown in Fig. 2.3a [5]. An applied RF voltage induces a large electron current towards the powered electrode during one-half of the cycle and a small ion current on the second half of the cycle. As a result, the capacitively coupled RF electrode gets negatively charged up to a certain self-bias V_{DC}, and finally the electron current induced by the positive voltage exceeding V_p on one-half of the

cycle becomes equal to the net ion current on the other half of the cycle, when the electrode potential is lower than V_p. Fig. 2.3b shows the spatial distribution of the average potential in a RF discharge reactor, where the sheath potential, V_s, is equal to V_{DC} + V_p on the powered electrode.

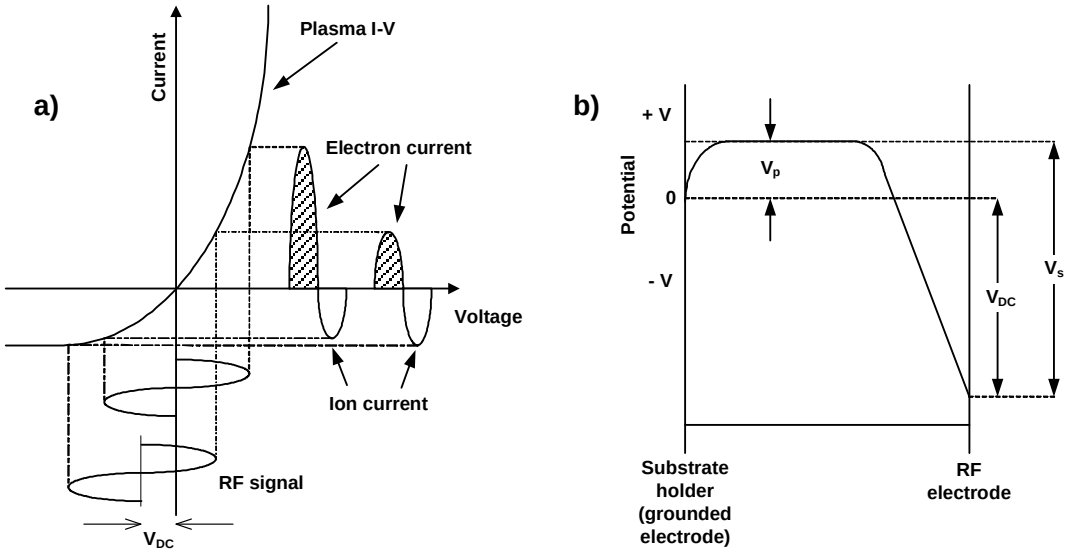

Fig. 2.3. Schematic diagram of a) generation of negative self-bias on the powered electrode in contact with RF plasma and b) spatial distribution of average potential in a RF glow discharge flat-bed reactor [6].

If we assume that the RF excitation is a perfectly sinusoidal wave, then we can derive a simple relation between the RF potential (V_{RF}), the plasma potential (V_p) and the self-bias potential (V_{DC}) [6]. Here, V_p is the most positive potential in the discharge by definition, then in the positive part of RF cycle we have

$$CV_{RF} + V_p \geq V_{RF} + V_{DC} \tag{2.1}$$

while in the negative part we have

$$-CV_{RF} + V_p \geq 0 \tag{2.2}$$

If we consider only the equality from equation 2.1 and 2.2, then by elimination we can obtain

$$V_p = \tfrac{1}{2}\left(V_{DC} + V_{RF}\right) \tag{2.3}$$

Equation 2.3 expresses a simple relation that can be used to estimate the plasma potential from observable potentials, which are easy to measure.

Deposition parameters and PLASMAT reactor

In the RF discharge deposition process we can measure and adjust several parameters which are important for the process control. Some of them are usually recorded as indicators,

such as the self-bias potential (V_{DC}) and the RF potential (V_{RF}). The other parameters can be categorized into i) adjustable parameters such as total pressure, partial pressure, gas flow rates, substrate temperature, RF power, plasma excitation frequency and ii) reactor geometry related parameters (distance between electrodes, electrodes diameter, and surface ratio of powered to grounded electrodes). By changing these parameters, we can optimize the deposition conditions to obtain materials with desired properties.

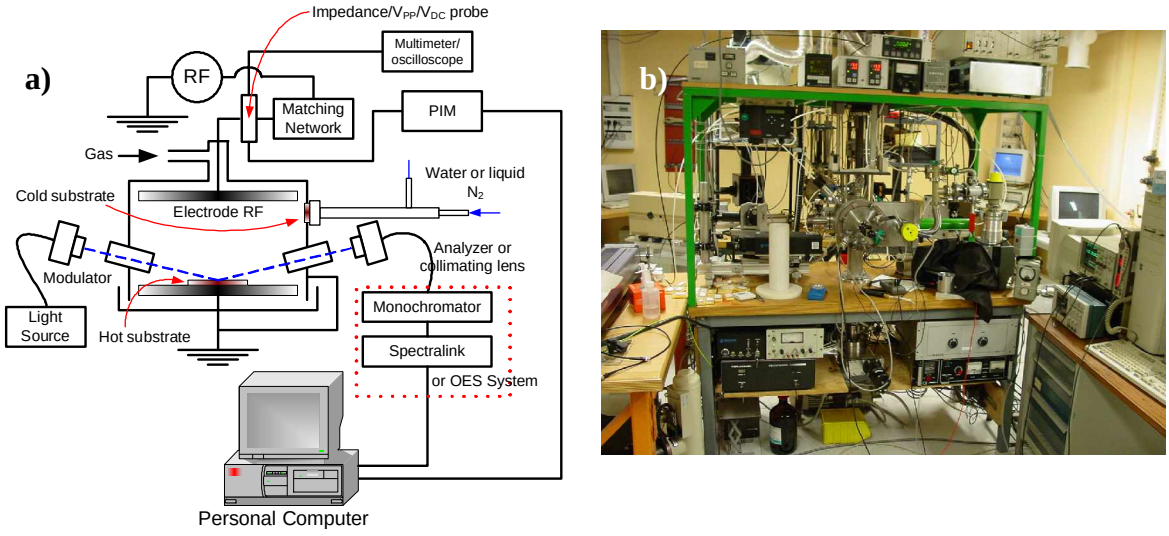

Fig. 2.4. PLASMAT reactor : a) a schematic diagram of installed in-situ diagnostic measurement systems, including a water or liquid nitrogen cooled substrate holder; b) front view of the reactor and the working environment.

In this work, we have used a flat-bed PECVD reactor (PLASMAT reactor), equipped with in-situ diagnostics providing information on the process itself: optical emission spectroscopy (OES), plasma impedance monitoring system (PIM), self-bias and RF potential measurements (Fig. 2.4), and on the material properties via a UV-Visible spectroscopic ellipsometer. This reactor preferentially works at a plasma excitation frequency of 13.56 MHz in the pressure range of 30-5000 mTorr. The temperature of each electrode can be independently adjusted in the range of 25-300 °C. The installed feed gases are H_2, Ar, He, SiH_4, CH_4, PH_3 diluted in H_2 and trimethylboron (TMB) diluted in H_2. The self-bias potential is measured using a low-pass filter connected to a voltmeter (multimeter), while the RF potential is measured through a calibrated dividing capacitor [7]. The details of other characterization techniques will be explained in the next sections.

2.2. Optical Emission Spectroscopy (OES)

Introduction

Optical emission spectroscopy (OES) of gas discharges has been long used for qualitative and quantitative analysis in plasma physics and chemistry. Information on the excited species in the plasma, including their intensity and relative changes with respect to other excited species can be obtained using this technique, which gives a rough idea of species concentration in the plasma. In practice, the excited species responsible for emission are not necessarily the most relevant for the deposition process. Measured OES quantities should therefore be considered as qualitative. To obtain quantitative information one must use more sophisticated methods such as actinometry and laser induced fluorescence, which are beyond the scope of this study.

In the plasma, electrons are responsible for almost all excitation and dissociation processes since they are much lighter than other species, which makes it easier for them to gain energy from the applied power. Moreover, ion bombardment, chemical reactive recombination, and metastable energy transfer can also contribute to the emission processes. Thus, plasma emission can result from following mechanisms:

a) electron impact excitation,

$$A + e^- \longrightarrow A^* + e^-$$
$$A^* \longrightarrow A + h\nu$$

b) electron impact dissociation,

$$AB + e^- \longrightarrow A^* + B + e^-$$
$$A^* \longrightarrow A + h\nu$$

c) ion impact processes,

$$A^+ + e^-(+M) \longrightarrow A^*(+M)$$
$$A^* \longrightarrow A + h\nu$$

d) chemiluminescent recombination reaction,

$$A + BC \longrightarrow AB^* + C$$
$$AB^* \longrightarrow AB + h\nu$$

where A, B and C are atoms or molecules, * indicates the excited (emitting) species, e^- is an electron and $e^-(+M)$ may be a neutral species, a negative ion, an electron plus a third body, or a surface (e.g. electrodes, reactor walls or particles in the plasma) [8].

Experimental setup and data treatment

The experimental setup for this technique is quite simple. It consists of i) a collimating system to collect the emission signal, ii) a optical fiber that brings the collected signal to the monochromator, iii) a high resolution monochromator with an adjustable entrance slit and iv) a photodetector. A detailed setup of this technique is explained elsewhere [5]. In practice, it is installed in our PECVD reactor (see Fig. 2.4a) with detail shown in Fig 2.5.

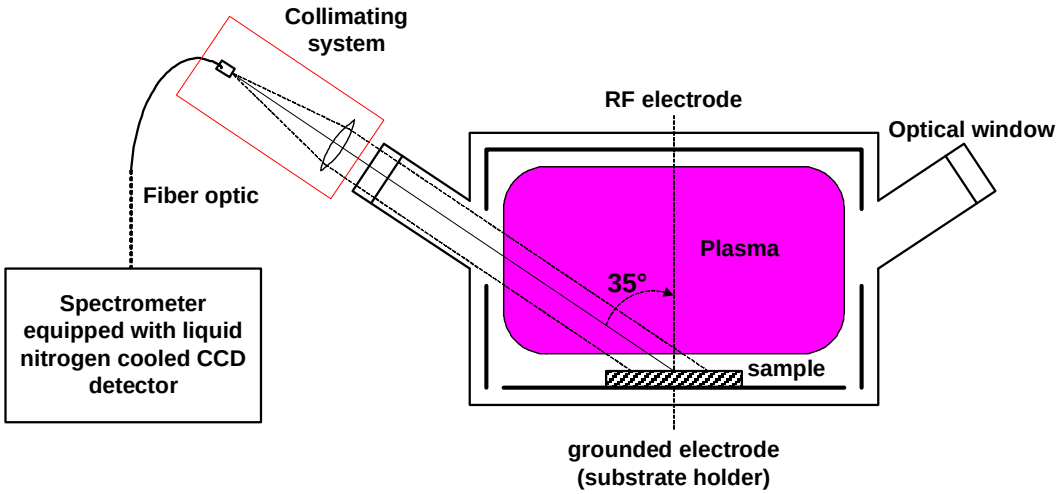

Fig. 2.5. Schematic of the setup for plasma optical emission spectroscopy (OES) measurements in PLASMAT reactor (see fig 4.24a). The optical window, also used for spectroscopic ellipsometry measurements, has a diameter of 0.8 cm and its axis is at 35° from the normal of substrate holder.

In this study, we used OES as a semi-quantitative technique to analyze the relative amounts of species in the plasma. Thus, we studied the evolution of the emission intensity of the species of interest, or the ratio of one species relative to another from one plasma condition to another. Each spectrum is baseline corrected with respect to the measurement background. Further, other data treatments are necessary as well, such as numerical integration to analyze the peak surface area (integrated intensity) and peak fitting using

Lorentzian function to obtain the full width at half maximum (FWHM) and other fitting parameters of the curves.

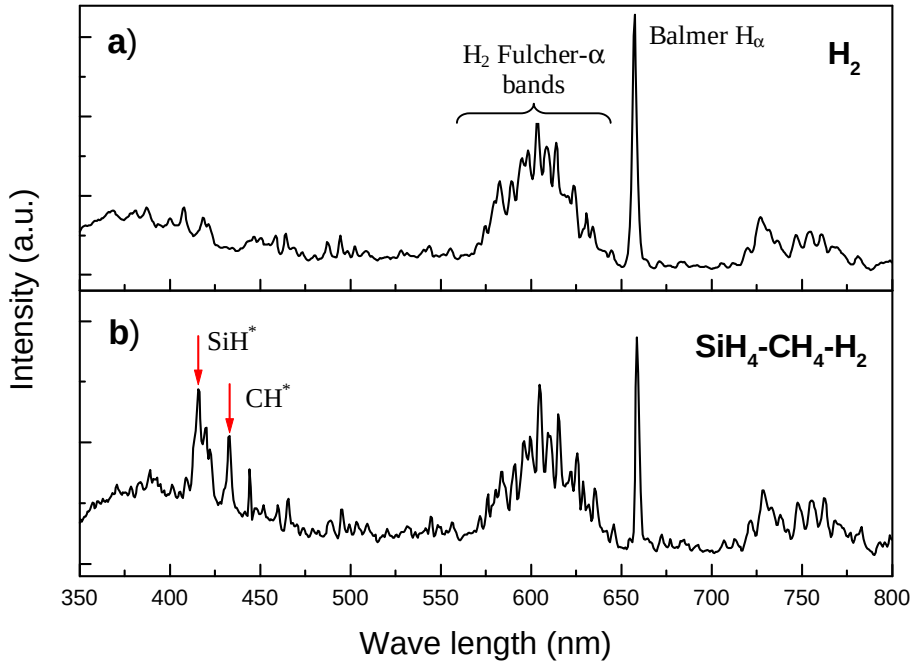

Fig. 2.6. Typical optical emission spectra of RF discharge plasmas with the emission lines of interest at 1600 mTorr for a) pure hydrogen and b) SiH_4-CH_4-H_2 mixture with an RF power of 10 and 20 W respectively. The temperature of both electrodes was set at 200 °C.

SiH_4-CH_4-H_2 glow discharge

Fig. 2.6 shows typical OES spectra from a RF glow discharge in pure hydrogen a) and a SiH_4-CH_4-H_2 mixture b). The emission lines of these systems are summarized in Table 2.1.

Table 2.1. Emission lines in SiH_4-CH_4-H_2 RF glow discharge system.

Line/band	Transition	Wave length (nm)	Note	Reference
Balmer H_α	$n'=3 \rightarrow n=2$	656.2	Balmer series: $\nu = R\left(1/2^2 - 1/n^2\right)$ n=3, 4, 5,…; R=Rydberg const.	5, 9, 10, 11, 13, 14
Balmer H_β	$n'=4 \rightarrow n=2$	486.1		
Balmer H_γ	$n'=5 \rightarrow n=2$	434.0		
SiH*	$A^2\Delta \rightarrow X^2\Pi$	414.2	Analogous to CH (A-X) system	5, 12, 13, 15
C_2 Swan	$d^3\Pi_g \rightarrow a^3\Pi_u$	516.5	Swan band of C_2	11, 14
CH*	$A^2\Delta \rightarrow X^2\Pi$	431.4	CH (A-X) system with Q (0,0) band head at 431.4 nm	9, 10, 11, 12, 14
H_2 Fulcher-α	$d^3\Pi_u \rightarrow a^3\Sigma_g$	570-640	Broad band consists of many lines centered at 602 nm	5, 10, 11, 14

2.3. Plasma Impedance Analysis

Introduction

Plasma impedance analysis is a sensitive and portable analysis method used to detect the present of nanometer size particles in capacitively coupled radio-frequency (RF) discharge at 13.56 MHz [16]. This method is based on the fact that the discharge is non-symmetric and capacitive-like, thus showing a non-linear relation between the RF voltage and the RF current in the sheaths [1]. This non-linearity induces the generation of harmonics in the discharge current that give significant information about the dynamics of ions and electrons in the plasma. When nanometer size particles are present in the plasma, the third harmonic (40.68 MHz) of RF current, J_3, has been shown to give the most significant changes as a function of time [16]. The abrupt changes on the amplitude ratio of the third harmonic of the RF current to the fundamental one (J_3/J_0) are also observed in the so-called α-γ' transition, which is accompanied by the appearance of particles and powders [13]. These abrupt changes are

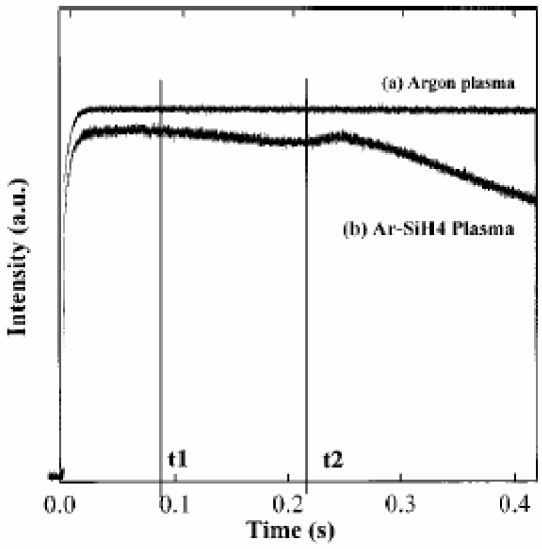

Fig. 2.7. Time evolution of the amplitudes of the third harmonic of the RF current for a) particle-free argon plasma and b) a powder-forming argon-silane plasma [16].

observed as a decrease of the amplitude ratio by one order of magnitude as the plasma changes from α to γ' mode, while the ratio between the first harmonic to the fundamental one almost does not change. The observed changes are related to the modification of the electron collision frequency in the discharge by the electron-particle collision process, which is proportional to the concentration and the collision cross section of particles. Moreover, the

particles in the plasma act as electron 'traps' through the electron attachment process [16, 13]. This process perturbs the electron-energy distribution function and self-sustaining electric field, which is observed as a decrease in the amplitude of J_3, related to the increase of plasma resistance. In the following, we use the amplitudes of the third harmonic of RF current as the observable parameter to monitor the presence of particles in the plasma, which we have confirmed by laser light scattering measurements in our reactor [17].

Particle growth monitoring

Fig. 2.7 shows the time evolution of the amplitudes of the third harmonic of the RF current, which represents the particles growth timeline in the plasma [16]. In general, this time evolution can be divided into 3 regions: i) gas decomposition region ($t_0<t<t_1$), which starts when the plasma is turned on and reaches a plateau; ii) particle formation and accumulation regime ($t_1<t<t_2$); and iii) coagulation regime or powder formation regime ($t>t_2$). In general, the experimental setup for this technique consists of i) an RF voltage probe, ii) an RF current probe, iii) an electronic board to process the measured signals, and iv) a personal computer with controlling applications to monitor and visualize the measured results. This

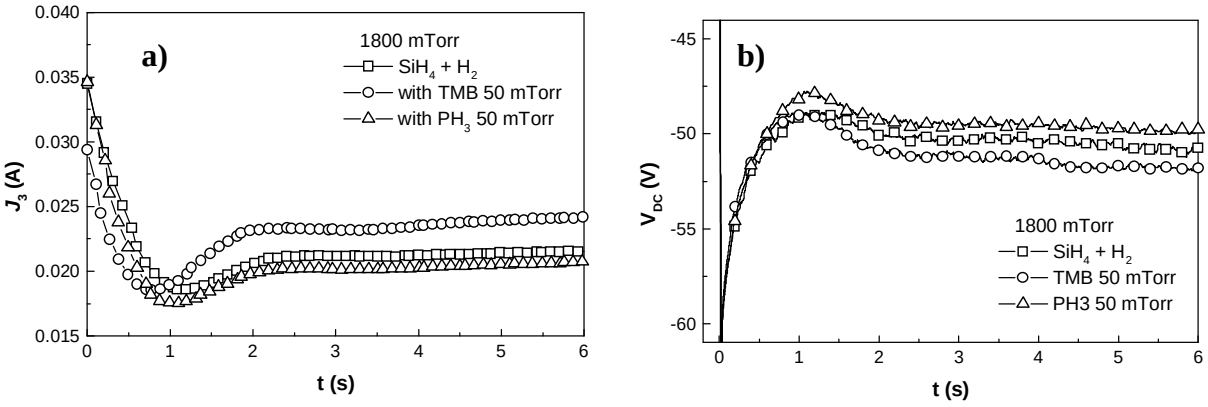

Fig. 2.8. The comparison between the time evolution of a) the amplitude of the thirdd harmonic of RF current (J_3) and b) the self-bias potential (V_{DC}) for a SiH_4-H_2 mixture plasma in the powder formation regime: 1800 mTorr with temperature of electrode of 200 °C and RF power of 22 W.

probing system is installed at the entry of the RF power in a PECVD reactor (between the matching network and the cathode) as shown schematically in Fig.2.4a. Recently, comparative studies between the time evolution of the self bias potential (V_{DC}) and the amplitude of the third harmonic of the RF current (J_3) have shown good [18]. Thus, we can use the evolution of V_{DC} instead of J_3 to monitor the formation of particles and powder in the

plasma. In Fig. 2.8 we compare the evolution of J_3 and V_{DC} for SiH_4-H_2 systems with and without doping gas in the powder formation regime at 1800 mTorr.

Materials Characterizations

2.4. Phase Modulated UV-Visible Spectroscopic Ellipsometry (SE)

Basic principle and experimental setup

Ellipsometry is a powerful technique for determining the thickness and optical properties of thin films [19, 20]. It is based on the principle that a fully polarized light changes its polarization state after reflection from or transmission through a thin film [21]. In general, ellipsometry can be used to measure both the index of refraction and the thickness of either transparent or absorbing materials. By examining the polarization state of the reflected light of known polarization, wavelength, and angle of incidence, we can obtain the information on the optical properties of thin films. Moreover, due to its non-perturbing nature, this technique is also very useful for in-situ studies during deposition.

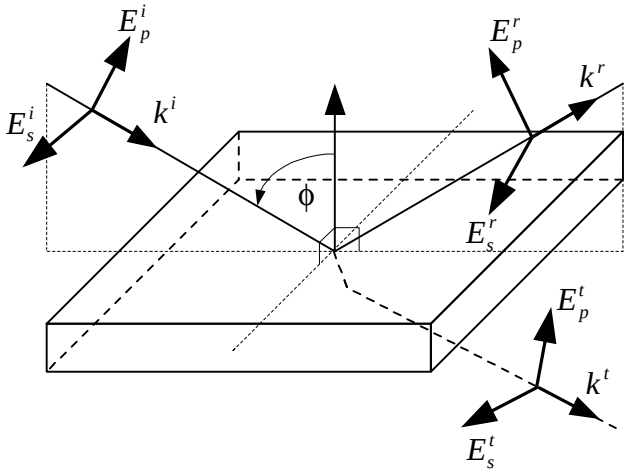

Fig. 2.9. Schematic diagram of incident, reflected and transmitted light on thin slab

The polarization state of the reflected light can be represented by the following complex number [21, 22]:

$$\rho = \frac{r_p}{r_s} = \tan(\psi)\exp(i\Delta) \tag{2.4}$$

where ψ and Δ are the ellipsometric angles. r_p and r_s are the parallel and perpendicular reflection coefficients (Fresnel coefficients):

$$r_p = \frac{E_p^r}{E_p^i} \tag{2.5}$$

$$r_s = \frac{E_s^r}{E_s^i} \tag{2.6}$$

where E_y^x are the electric field vectors as shown schematically in Fig. 2.9. ($x = i$ for the incident, $x = r$ for the reflected and $x = t$ for the transmitted waves respectively; $y = p$ for parallel component and $y = s$ for perpendicular component to incident plane).

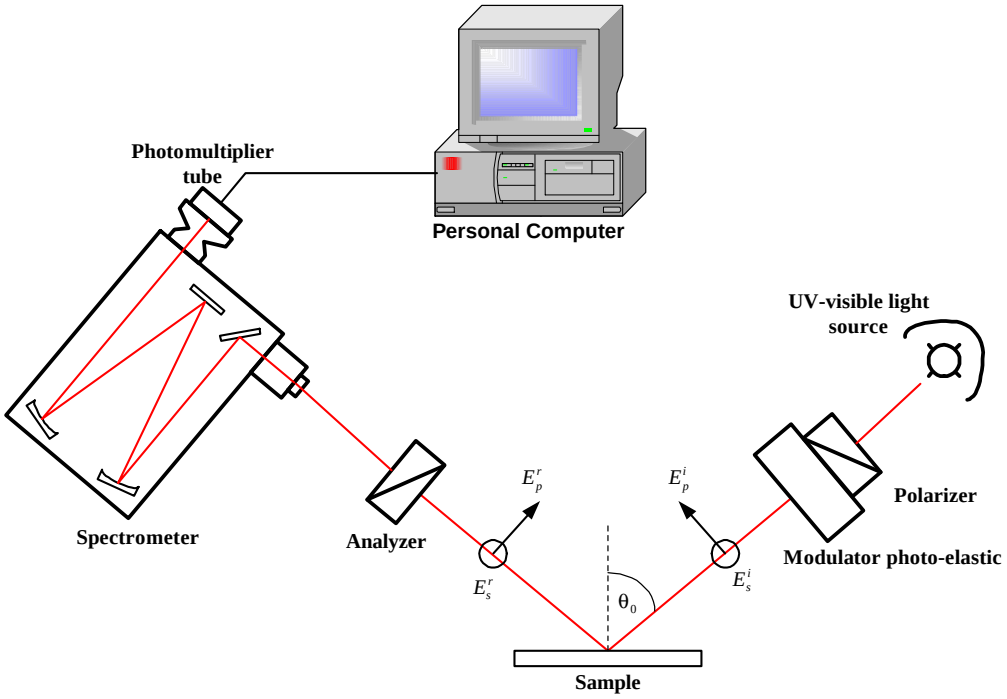

Fig. 2.10. Phase modulated UV-visible ellipsometer setup

The experimental setup of the phase-modulated UV-Visible spectroscopic ellipsometer (UVISEL) is represented schematically in Fig. 2.10. In this setup, the white light from the source is first modulated linearly by a polarizer then elliptically by a photo-elastic modulator. In this case the phase shift between component E_s and E_p is $\delta(t)$, can be expressed as

$$\delta(t) = A\sin(\omega t), \text{ where } \frac{\omega}{2\pi} = 50 \text{ kHz} \tag{2.7}$$

The reflected light is analyzed by a linear polarizer then its intensity is measured at selected wavelengths by a photodetector attached to a monochromator. The measured intensity I is defined as

$$I(\lambda, t) = I_0 + I_s \sin\delta(t) + I_c \cos\delta(t) \cong I_0 + 2J_1(A)I_s \sin\omega t + 2J_2(A)I_c \cos 2\omega t \tag{2.8}$$

where J_i is the ith order Bessel function. I_s and I_c are defined as,

$$I_s = \sin(2\psi)\sin\Delta = 2\,\mathrm{Im}\left(\frac{r_s r_p^*}{r_s r_s^* + r_p r_p^*}\right) \tag{2.9}$$

$$I_c = \sin(2\psi)\cos\Delta = 2\,\mathrm{Re}\left(\frac{r_s r_p^*}{r_s r_s^* + r_p r_p^*}\right) \tag{2.10}$$

By Fourier analysis of the signal, we can obtain directly the values of I_s and I_c, which relate to the Fresnel coefficients of the sample.

Data treatment and interpretation

In order to analyze quantitatively a spectroscopic ellipsometry measurement, we have to fit the experimental spectrum using an optical model. To obtain the best fit condition, we used the Levenberg-Marquardt algorithm to minimize globally the value of the biased estimator $\chi^2(\theta)$. Here $\chi^2(\theta)$ is a merit function that ensures the best fit of the SE data to the model at its global minimum. The biased estimator $\chi^2(\theta)$ is defined as

$$\chi^2(\theta) = \frac{1}{2N}\sum_{k=1}^{N} \frac{\left\|Is_{sim}(\theta,\lambda_k) - Is_{mes}(\lambda_k)\right\|^2}{\delta_k^2} + \frac{\left\|Ic_{sim}(\theta,\lambda_k) - Ic_{mes}(\lambda_k)\right\|^2}{\delta_k^2} \tag{2.11}$$

where δ_k is a statistic error that weights the value of the experimental spectrum [23].

In the general case of thin films, an optical model should contain information about: i) experimental parameters (angle of incidence, substrate, dielectric function of ambient), ii) film structure (how many distinguishable layers and their thickness), iii) layer structure (homogeneous, heterogeneous, isotropic, non-isotropic or gradual layer), and iv) dielectric function of each layer. The dielectric function of each layer can be expressed by the dielectric function of a single material or by a mixture of several materials, based on the effective medium theory. In general the effective medium theory can be expressed by the following equation [24]:

$$\varepsilon = \frac{\varepsilon_a \varepsilon_b + k\varepsilon_h \left(f_a \varepsilon_a + f_b \varepsilon_b \right)}{k\varepsilon_h + \left(f_a \varepsilon_b + f_b \varepsilon_a \right)}, \quad k = \left(\frac{1}{q} \right) - 1, \; 0 \le q \le 1 \tag{2.12}$$

where q is the screening parameter; ε, ε_h, ε_a and ε_b are the dielectric function of composite material, host material, component a and component b respectively; f_a and f_b are the volume fraction of components a and b respectively. In our case, we use Bruggeman effective medium approximation (BEMA), which is defined using eq. 2.12 with $\varepsilon_h = \varepsilon$ and $q = 1/3$ (or $k = 2$). The BEMA represents most likely an aggregate microstructure in which neither component can be viewed as the host material. The dielectric function of a single material can be expressed by a standard based on the experimental data or by a mathematical model whether it is derived theoretically (all involved parameters have physical meaning) or not (empirically, only a mathematical expression that allows to reproduce the experimental results).

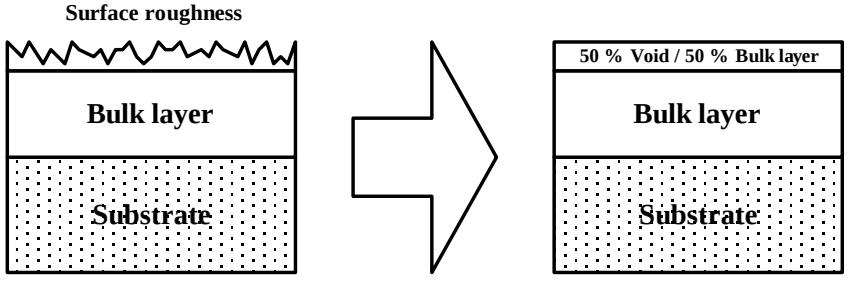

Fig. 2.11. Two-layers optical model of thin film, which consists of bulk layer and surface roughness.

In the case of amorphous silicon derived materials, the raw experimental data can be described by a two-layer model (ambient/surface roughness/bulk layer/substrate) as shown schematically in Fig. 2.11. From an optical point of view, the surface roughness (5-30 Å thick) is modeled by a layer with equivalent parallel-plane boundaries whose thickness is

equal to the characteristic roughness height parameter [21], and whose optical properties are described as a mixture of those of the bulk layer and ambient (void) according to the effective medium theory. In order to reduce the number of fitting parameters, we have kept the composition of the surface roughness constant (50 % void + 50 % bulk layer). Indeed, it has been shown empirically by Fujiwara et al [24] that in some cases we can replace this layer by a mixture of voids and bulk layer a fixed composition ratio of 1:1. The bulk layer is modeled as an homogeneous amorphous layer using the Tauc-Lorentz dispersion law [25]. This model combines Tauc's law for photon absorption above the band edge of amorphous semiconductors [26] and the standard quantum mechanical approach, thus the imaginary part of the dielectric function is expressed by the following equation:

$$\begin{aligned}\varepsilon_{2TL} &= \left[\frac{AE_0C\left(E-E_g\right)^2}{\left(E^2-E_0^2\right)^2+C^2E^2}\cdot\frac{1}{E}\right], \quad E>E_g,\\ &= 0 \qquad\qquad\qquad\qquad\qquad\quad E\le E_g\end{aligned} \tag{2.13}$$

Where A is the amplitude factor proportional to the density matrix of the material and the optical transition matrix elements, E_0 is the peak transition energy, C is the broadening parameter and E_g is the optical band gap. The real part of the dielectric constant is obtained by Kramers-Kronig integration, given by

$$\begin{aligned}\varepsilon_{1TL} &= \varepsilon_{1TL}(\infty)+\frac{AC}{\pi\zeta^4}\cdot\frac{a_{\ln}}{2\alpha E_0}\ln\left(\frac{E_0^2+E_g^2+\alpha E_g}{E_0^2+E_g^2-\alpha E_g}\right)-\frac{A}{\pi\zeta^4}\cdot\frac{a_{atan}}{E_0}\left[\pi-\operatorname{atan}\left(\frac{2E_g+\alpha}{C}\right)+\operatorname{atan}\left(\frac{-2E_g+\alpha}{C}\right)\right]\\ &+\frac{AE_0}{\pi\zeta^4\alpha}\cdot E_g\left(E^2-\gamma^2\right)\left[\pi+2\operatorname{atan}\left(2\frac{\gamma^2-E_g^2}{\alpha C}\right)\right]\\ &-\frac{AE_0C}{\pi\zeta^4}\cdot\frac{E^2+E_g^2}{E}\ln\left(\frac{\left|E-E_g\right|}{E+E_g}\right)+2\frac{AE_0C}{\pi\zeta^4}E_g\ln\left[\frac{\left|E-E_g\right|\cdot\left(E+E_g\right)}{\sqrt{\left(E_0^2-E_g^2\right)^2+E_g^2C^2}}\right]\end{aligned} \tag{2.14}$$

where

$$a_{\ln} = \left(E_g^2-E_0^2\right)E^2+E_g^2C^2-E_0^2\left(E_0^2+3E_g^2\right) \tag{2.15}$$

$$a_{atan} = \left(E^2-E_0^2\right)\left(E_0^2+E_g^2\right)+E_g^2C^2 \tag{2.16}$$

$$\zeta^4 = \left(E^2 - \gamma^2\right)^2 + \frac{\alpha^2 C^2}{4} \tag{2.17}$$

$$\alpha = \sqrt{4E_0^2 - C^2} \tag{2.18}$$

$$\gamma = \sqrt{E_0^2 - C^2/2}\,, \tag{2.19}$$

which adds another free parameter, the high frequency dielectric constant, $\varepsilon_1(\infty)$. Fig. 2.12a. shows the real and imaginary parts of the pseudo-dielectric function of a polymorphous silicon carbon alloy deposited on corning glass. The spectra are fitted considering a two-layer model. In this case, the dielectric functions are modeled using the Tauc-Lorentz model for the bulk layer and a 1:1 ratio of bulk material over void with BEMA the surface roughness, as

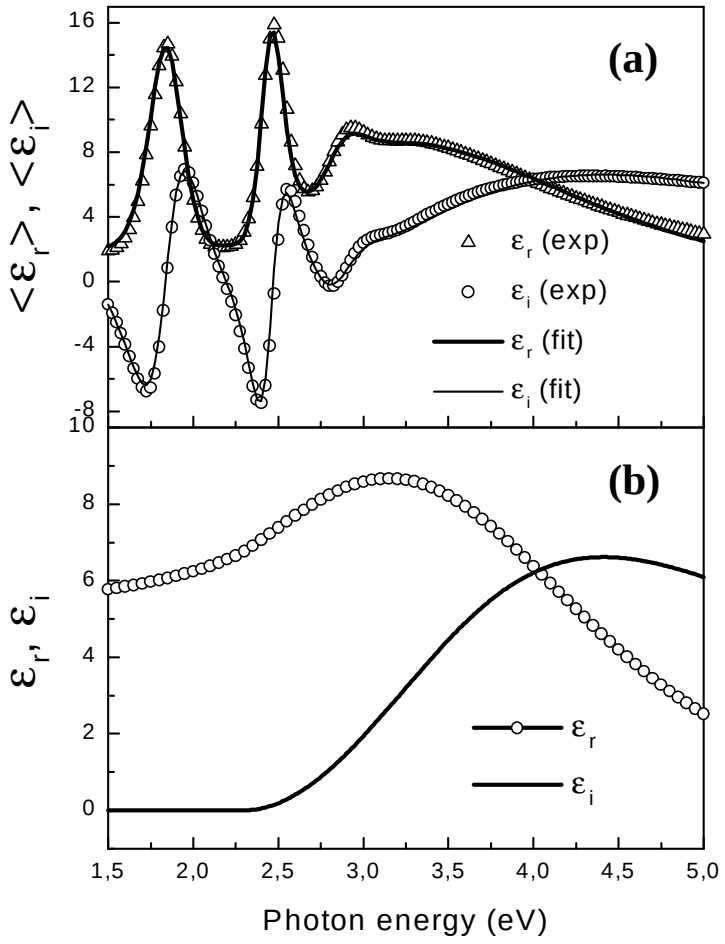

Fig. 2.12. Experimental and modeled real and imaginary parts of the pseudo-dielectric function of a *pm-$Si_{1-x}C_x$:H* film deposited at 3500 mTorr (200 °C), using a two-layers model with surface roughness consisting of 50 % of void and 50 % of bulk layer material (a) and extracted bulk layer dielectric function (b). The fitting parameters are: E_g=2.30 eV, $\varepsilon_1(\infty)$=1.82, A=127.22 eV, E_0=3.86 eV, C=3.57 eV and thickness of bulk layer of 2970 Å.

described above. The extracted dielectric function for bulk material, free of interference fringes due to multiple reflections and surface roughness effects, is shown in Fig. 2.12b. In this study, the deposition rate was determined from film thickness and deposition time by taking the assumption of an homogeneous constant film growth. For more detail on this technique, a review that covers general information and deeper discussions on in-situ studies of thin film growth can be found in ref. 19.

2.5. Raman Spectroscopy

Introduction

When photons interact with a molecule, they may be absorbed or scattered. Scattering itself is defined as a phenomenon in which photons change their direction and possibly also their energy after interaction with matter. Further, light scattering can be classified into elastic and inelastic processes, which describe the phenomena by which the photons are scattered without and with changes of their energy respectively. The inelastic scattering process is illustrated in Fig. 2.13a, where light incident with angular frequency ω_1 and wave vector $\mathbf{k}_1$ is scattered as a photon with frequency ω_2 and wave vector $\mathbf{k}_2$ by an excitation of the medium of frequency Ω and wave vector $\mathbf{q}$ [27]. This type of scattering can be mediated by many different types of elementary excitations in the matter. However, in the case of Raman

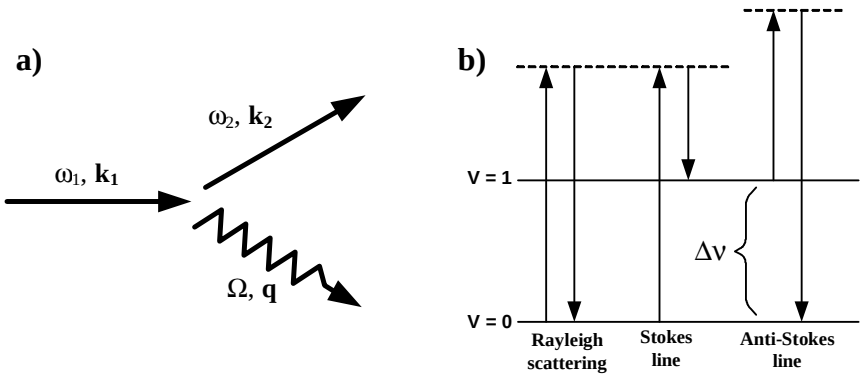

Fig. 2.13. Schematic diagram of a) inelastic scattering process and b) Stokes and anti-Stokes scattering.

scattering, we will consider only phonon mediated processes, which correspond to the energy difference in the vibrational and rotational energy levels. In this case, there is a similarity between Raman and infrared spectra, even though they are not the same due to the differences in the selection rules and relative band intensities. For a molecular vibration to be Raman

active, there must be a change in the induced dipole momentum as a result of a change in the polarizability of the molecule [28]. Therefore, even if there is no change in the dipole momentum or the molecule has no permanent dipole, it still can be Raman active as long as it has a change in the polarizability or in the induced dipole momentum due to vibrations or rotations. In general, the inelastic scattering can be divided in two generic types such: Stokes and anti-Stokes scattering (Fig. 2.13b). Stokes scattering corresponds to the emission of a phonon (scattered photons lose their energy), while anti-Stokes scattering corresponds to phonon absorption (scattered photons gain energy). Thus, with respect to the exciting photon energy, the light is shifted down in energy during a Stokes process and up in an anti-Stokes event.

Experimental setup and data treatment

A schematic diagram of a Raman setup equipped with a microscope for micro-Raman measurements with a HeNe laser (632.8 nm) as the source of excitation is shown in Fig. 2.14a. In this setup, the reflected part of the excitation light is cut off by a notch or edge filter instead of a second monochromator. The experimental spectra of Raman measurements were treated by fitting the data over the range of interest as a deconvolution of several Gaussian functions. From the fitting, we can obtain the area and the full width at half maximum (FWHM) for each peak, which provides information on each mode of vibration. Fig. 2.14b shows a typical Raman spectrum of hydrogenated amorphous silicon. We can observe the

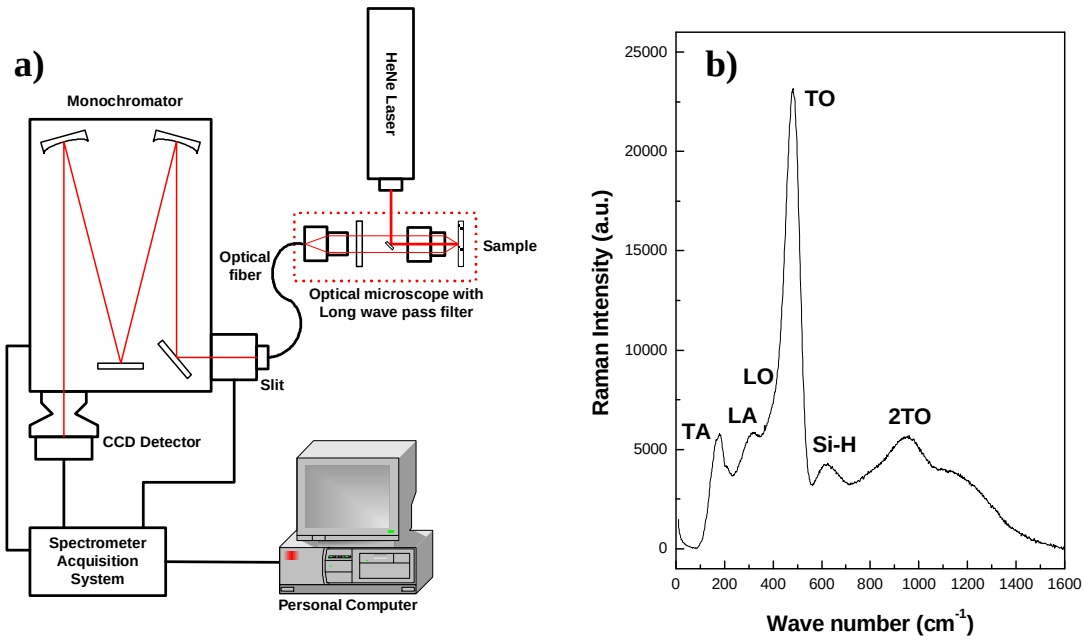

Fig. 2.14. a) A schematic diagram of a micro-Raman system and b) a typical Raman spectrum of a *pm-Si:H* film deposited at 600 mTorr, 250 °C, and 22 W of RF power.

principal phonons of amorphous silicon: i) transverse optic (TO) at 480 cm^{-1}, ii) longitudinal optic (LO) at 380 cm^{-1}, iii) longitudinal acoustic (LA) at 310 cm^{-1}, and iv) transverse acoustic (TA) at 150 cm^{-1} [28]. Moreover, the Si-H vibration mode at 640 cm^{-1} and the 2nd harmonic of the TO phonon at 960 cm^{-1} are also shown [29].

2.6. Infrared Spectroscopy

Introduction

The energy of a molecule can be divided into four parts, which are: a) translational energy, b) rotational energy, c) vibrational energy and d) electronic energy [28]. Electronic energy transitions normally are responsible for the absorption or emission in the UV and visible regions, while molecular vibrations give rise to the absorption through out most of the infrared region. When the frequency of a specific vibration is equal to the frequency of the IR radiation, the molecule will absorb the radiation with some selection rules. The simplest representation of a molecular vibration is the oscillation of a diatomic molecule, where its potential energy depends on the intermolecular distance. For a mode of vibration to be infrared active, there must be a change in the dipole moment of the molecule when it vibrates [28, 31]. Therefore, most symmetric stretching vibration modes of symmetric molecules are infrared inactive, while asymmetric modes are infrared active.

In this study, we used a Fourier-transform infrared spectrometer (FTIR), which measures the IR absorption in the range of 500-4000 cm^{-1} with a resolution of 2 cm^{-1}. This instrument consists of three basic components: a radiation source, an interferometer and a detector. The main difference in the setup between an FT and dispersive spectrometer systems is the replacement of the monochromator by an interferometer. The interferometer divides light into two beams, generates an optical path difference between them, then recombines them to produce repetitive interference signals as a function of optical path difference by a detector. In short, it produces interference signals that contain infrared spectral information generated after passing through the sample. A detailed description of the setup is explained elsewhere [31].

Data treatment and analysis

In order to analyze the data from FTIR measurements, first we have to eliminate the interference fringes from the raw data. In this study, we followed a quantitative method developed by Maley [32]. In this procedure, we fit the interference fringes of the spectra using

an optical model that considers a thin film on a semi-infinite substrate (c-Si) with multiple reflections (Fig. 2.15) as follows:

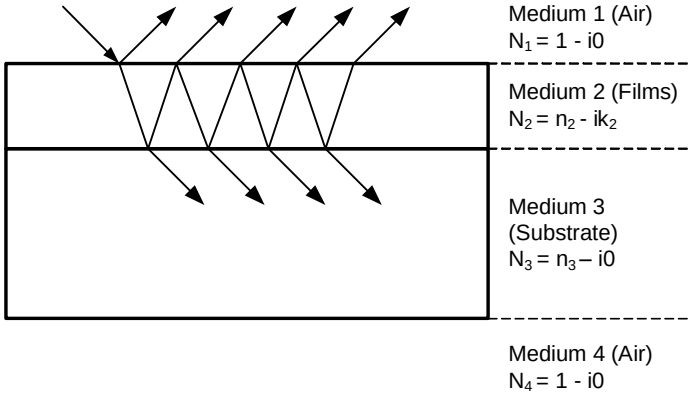

Fig. 2.15. Schematic diagram of the multiple reflections of an absorbing film on a non absorbing substrate. Here, the multi reflections in the substrate are omitted and the light is shown at non-normal angle of incidence for clarity [29].

$$T_{NA} = \frac{T_{34}T_{13}}{\left(1 - R_{31}R_{34}\right)} \tag{2.20}$$

in the coherent limit, we have

$$T_{13} = \left(n_3 / n_1\right)\left|\frac{t_{12}t_{23}P}{1 - P^2 r_{21}r_{23}}\right|^2 \tag{2.21}$$

$$R_{13} = \left|\frac{r_{12} + P^2 t_{12}t_{21}r_{23}}{1 - P^2 r_{21}r_{23}}\right|^2 \tag{2.22}$$

$$R_{31} = \left|\frac{r_{32} + P^2 t_{32}t_{23}r_{21}}{1 - P^2 r_{21}r_{23}}\right|^2 \tag{2.23}$$

where for $j = i \pm 1$

$$t_{ij} = \frac{2N_i}{N_i + N_j} \tag{2.24}$$

$$r_{ij} = \frac{N_i - N_j}{N_i + N_j} \tag{2.25}$$

$$R_{ij} = \left|r_{ij}\right|^2 \tag{2.26}$$

$$T_{ij} = \frac{n_j}{n_i\left|t_{ij}\right|^2} \tag{2.27}$$

$$P = \exp\left(-2\pi i N_2 d\omega\right) \tag{2.28}$$

$$N_i = n_i - k_i \tag{2.29}$$

By applying eqs. 2.20-2.29, we can fit the experimental data and obtain the base line with the interference fringes (Fig 2.16a). Here, we applied $n_3 = 3.42$ for the *c-Si* substrate, while n_2 of the films are pre-determined through spectroscopic ellipsometry measurement then extrapolated to low energy. These values of n_2 are included later on into the fitting parameter to obtain more precise values. Using the baselines obtained here, we can eliminate the interference fringes and obtain an interference-free transmission spectra (Fig. 2.16b).

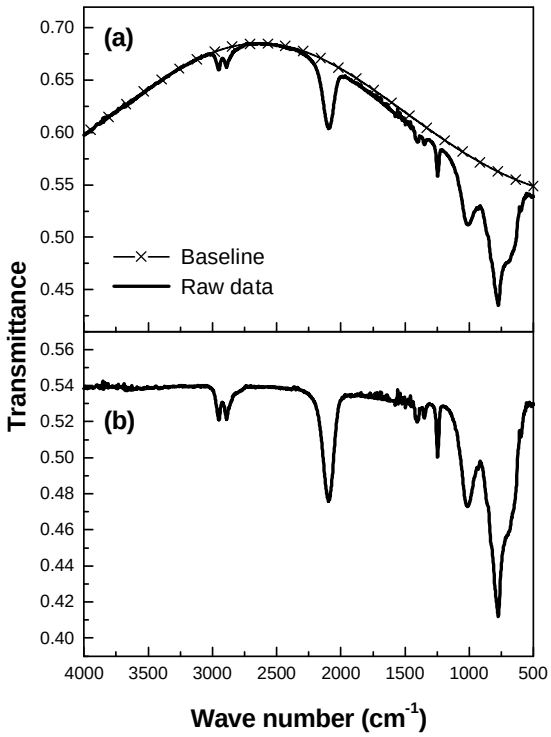

Fig. 2.16. Transmission spectra of *pm-*$Si_{1-x}C_x$ *:H* deposited at 800 mTorr with an RF power of 20 W : a) raw spectrum with baseline as fitting result of eq. 2.20 from ref. 29 and b) baseline corrected spectrum.

In order to calculate the absorption coefficient (α) from the interference-free transmittance, we followed the procedure proposed by Brodsky et. al. using the following relations [33]:

$$T = \frac{(1-R)^2 e^{-\alpha d}}{1-R^2 e^{-2\alpha d}} \tag{2.30}$$

where d is the film thickness and R is an empirically determined interface multiple reflection loss. Here, we determined R by setting $T = T_0 = 0.54$ as the absorption-free transmission of c-Si substrate when $\alpha = 0$ [32, 33], which yields

$$R = \frac{1-T_0}{1+T_0} \tag{2.31}$$

then by substituting eq. 2.31 into eq. 2.30, we can obtain

$$T = \frac{4T_0^2 e^{-\alpha d}}{(1+T_0)^2 - (1-T_0)^2 e^{-2\alpha d}} \tag{2.32}$$

which can be used to calculate α from the baseline corrected transmittance. We note that this procedure is still valid for samples with large index mismatch with respect to the c-Si substrate, such as pm-$Si_{1-x}C_x$:H thin films, as long as the interference elimination is applied with the exact equation of non-absorption transmittance as written in eq. 2.20. In principle, Maley's interference fringes elimination procedure transforms the raw data series which contains an unknown function $T_0 = f(\omega)$ as $T_0 = 0.54$ (see Fig. 2.16).

Further, using the data of IR absorption coefficient spectra, we can calculate the bond concentration for each type chemical bond in our films. The bond concentration for *X-Y* chemical bond (N_{X-Y}) is related to the integrated absorption of its peak by

$$N_{X-Y} = A\int \frac{\alpha(\omega)}{\omega} d\omega \tag{2.33}$$

where *A* is the proportionality factor or absorption strength and ω is the frequency or wave number in cm^{-1}[33-36]. The values of *A* for chemical bonds of interest in *pm-$Si_{1-x}C_x$:H* films are considered to be similar to these reported for *a-$Si_{1-x}C_x$:H* alloys and are tabulated in Table 2.2.

Table 2.2. IR absorption strength of chemical bonds in *pm-$Si_{1-x}C_x$:H* films.

Chemical bond	ω (cm^{-1})	*A* (cm^{-3})	References
Si-C	780-810	2.13×10^{19}	37, 38
Si-H	2000-2150	1.4×10^{20}	34, 35, 37, 38
C-H	2850-2950	1.35×10^{21}	37, 38

2.7. Photoluminescence (PL) Spectroscopy

Basic principle and experimental setup

In order to have a sample that emits photons, it has to be excited by some external source of energy. The method of excitation leads to a classification of the emission process. In the case of semiconductor materials, one possible method is the injection of electrons and

holes via an external current, resulting in *electroluminescence*. Another common method is the excitation by photons with energy higher than that of the band gap, resulting in *photoluminescence*, characterized by the emission of photons with lower energy than that of the excitation. The emission of radiation induced by the heating of the sample is known as thermoluminescence, while the process induced by electron bombardement is called *cathodoluminescence*.

Photoluminescence spectroscopy is an important method to study and develop electroluminescent devices, such as light-emitting-diodes (LED) and lasers. The basis of this technique is to detect the emission spectra of samples excited by a monochromatic light source. In most cases, the emission efficiency is quite low; therefore, a high intensity light source and a highly sensitive detector are required.

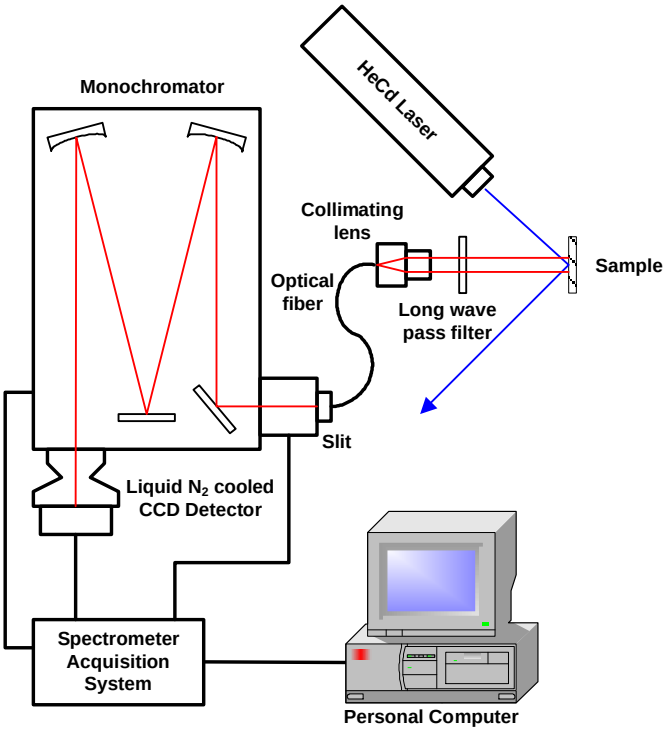

Fig. 2.17. Experimental arrangement used for the observation of photoluminescence spectra. The sample is excited using a light source (HeCd laser : 325 or 441.6 nm) with energy of photons higher the band gap. The reflected laser signal is blocked by the long wave pass filter, while the luminescence signal passes through and is collected by the collimating system. The collected signal is recorded using a computer controlled spectrometer and detector.

The standard experimental setup of this method consists of a monochromatic excitation light source (e.g. lasers or Na lamp), a collimating system to collect the luminescence signal (a complex optical setup which can be replaced by a simple optical fiber fitted with a collimating lens), a high pass wavelength filter, a spectrometer and a detector (liquid nitrogen

cooled CCD camera). In many cases, a cryostat or another temperature controllable sample holder also becomes an important part of this technique. Fig. 2.17 shows schematically a PL spectroscopy setup used in this study. Typical PL spectra for *pm-$Si_{1-x}C_x$:H* samples are shown in Fig. 2.18a. The spectrum from a GaAs wafer is also given as a reference for the peak position. To determine the reliability of our setup, we checked our results against these measured at the *Laboratoire d'Optique des Solides*, as shown in Fig. 2.18b [39].

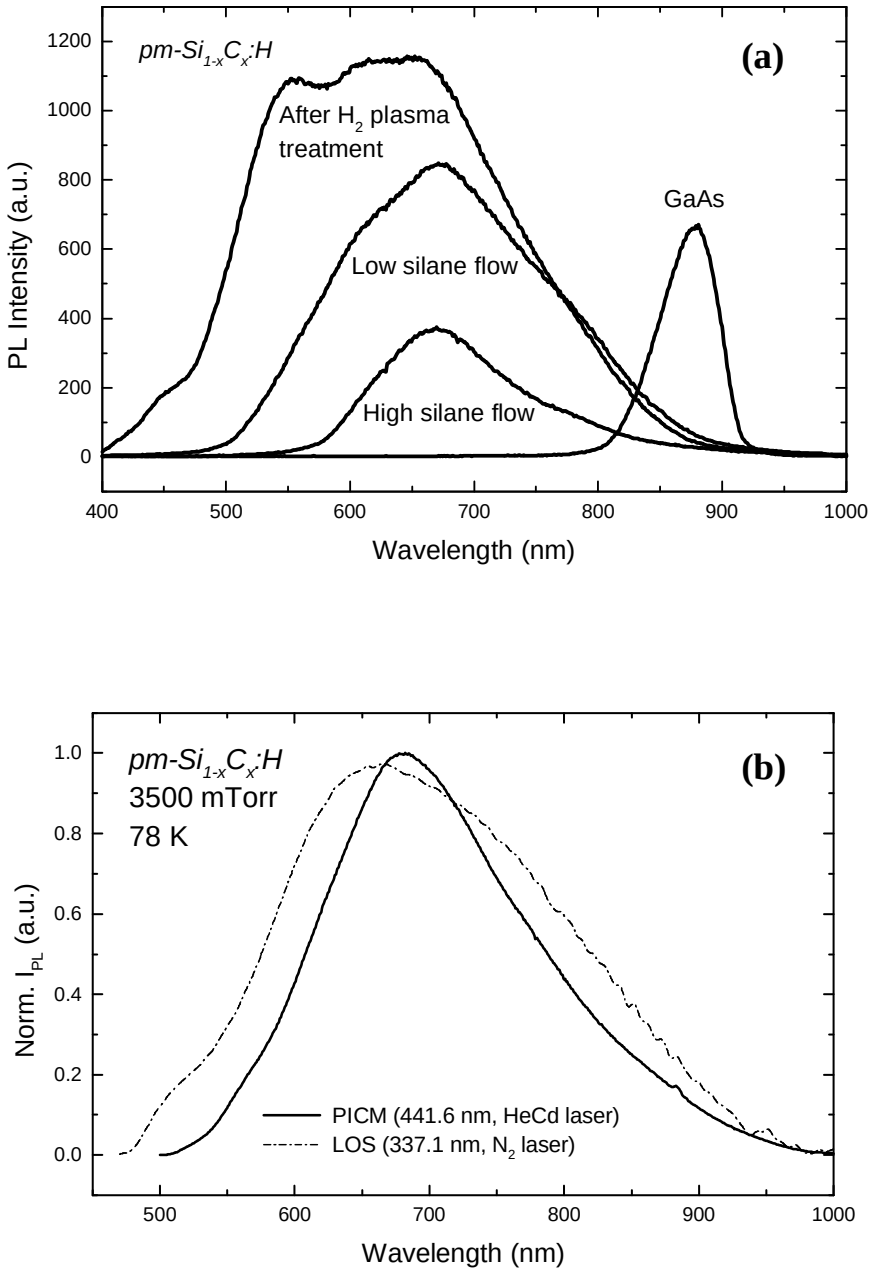

Fig. 2.18. a) Typical PL spectra for *pm-$Si_{1-x}C_x$:H* samples with GaAs PL emission peak as a reference. All the samples were measured at ambient temperature under the same measurement conditions ($\lambda_{exc.}$ = 325 nm). b) Comparison of PL spectra of the same sample measured at 78 K with the PL setup at PICM (full line) and at LOS (dash-dot line).

Reliability studies

Before going further into the analysis of PL data, it is important to check our PL measurement setup. Two lines of a HeCd laser at 325 and 441.6 nm were used as the excitation source. The excitation light intensity was adjusted by using neutral density filters and measured using a wattmeter. PL measurements were carried out at room temperature on *pm-*$Si_{1-x}C_x$*:H* samples deposited under the following standard conditions, unless mentioned otherwise : 3500 mTorr, 33.4 sccm of CH_4, 20 W of RF power and a substrate temperature of 200 °C.

Fig. 2.19 shows the effect of the power of the excitation light on the PL emission intensity. It shows that the PL emission intensity increases linearly with the power of the excitation light. The inset of Fig 2.19a shows the linear relation between the integrated PL intensity and the laser power in a log-log scale. It indicates that by the increase of the electron-hole pair formation, the number of pairs that recombines radiatively increases in a linear way. Moreover, the variation of the excitation light power does not change the shape of the PL spectra as shown in Fig 2.19b. Thus, within our experimental conditions, the effect of laser power is simply to increase the PL intensity.

Fig. 2.20 shows that the increase of laser excitation energy from 2.8 eV (441.6 nm) to 3.8 eV (325 nm) does not change the shape of the PL spectra. Here, the measurement was carried out on the sample deposited at 3500 mTorr with 10 W of RF power, which we also used for the fabrication of EL diodes. Both emission lines have enough energy to excite all the PL centers of interest due to their higher energy with respect to the optical band gap of the materials (< 2.7 eV). The difference of intensity between the spectra is due to the difference in the laser power, where the blue line (441.6 nm) has approximately 10 times higher intensity than the UV line (325 nm). However, as depicted in Fig. 2.20, the excitation at shorter wavelength has an advantage, as we get half of PL intensity with only one tenth of the laser excitation power. In other words, the PL intensity is higher when using the UV line, which might be due to the increase of the absorption coefficient with photon energy (see chapter 5).

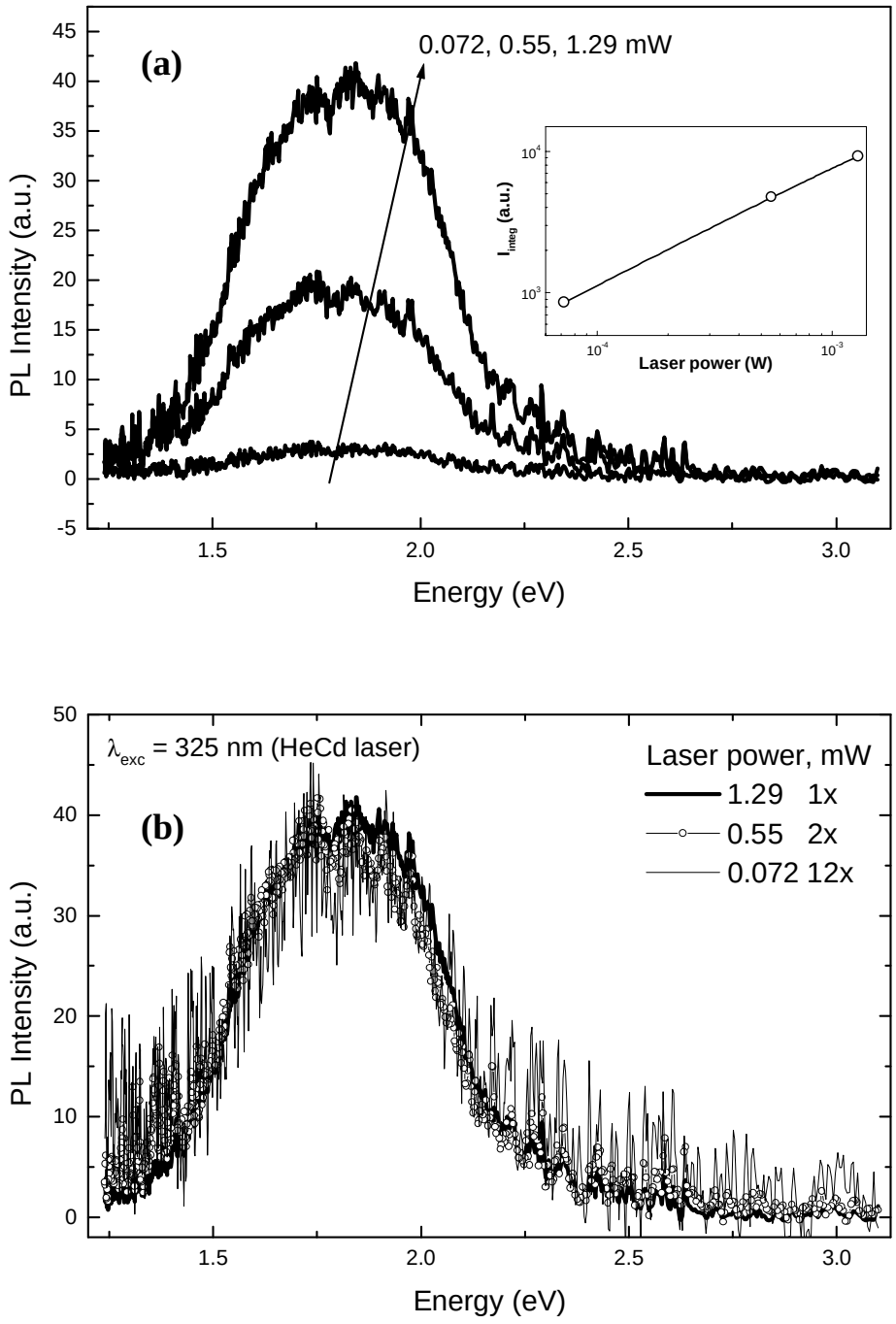

Fig. 2.19. The effect of the laser power on a) the intensity and b) the shape of PL spectra of *pm-*$Si_{1-x}C_x$ *:H* films deposited at 3500 mTorr with a substrate temperature of 200 °C and RF power of 20 W. The samples were excited using a HeCd laser at 325 nm (3.8 eV) and measured at ambient temperature. The inset shows the excitation intensity dependence of the integrated PL intensity of the same sample.

Another important issue is the effect of surface oxidation on the PL spectra, which could play an important role on the reproducibility of the results. In this work we have used UV and blue lines from a HeCd laser, which have a quite low penetration depth (~20 nm for λ_{exc} = 325 nm) due to the high absorption coefficient. In other words, the PL spectra are mostly due to the excitation and the radiative recombination of carriers near the film surface. Therefore, it is necessary to check the effect of air exposure on the PL of our films.

We therefore deposited two similar samples with the same thickness, one coated with 20 nm of amorphous silicon and the other not. The amorphous silicon layer acts as a protection layer against oxidation of the film beneath. First, the sample covered with amorphous silicon is measured immediately after deposition, while the other sample is kept in open air for 3 weeks before measurement. The presence of the amorphous silicon layer will perturb the shape of the PL spectrum. Thus, in order to compare the PL spectra between samples, we also deposited 20 nm of amorphous silicon on the top of second sample. Fig. 2.21 shows the spectra of the as-deposited sample (open circles) and that of the sample left for 3 weeks in open air sample (thick line). Neither the shape nor the intensity of the spectra change with the treatment, which leads us to the conclusion that the air exposure of our films has no influence on the PL spectra of dense polymorphous silicon carbon thin films. Thus, PL measurements can be used to obtain reliable information on sample properties.

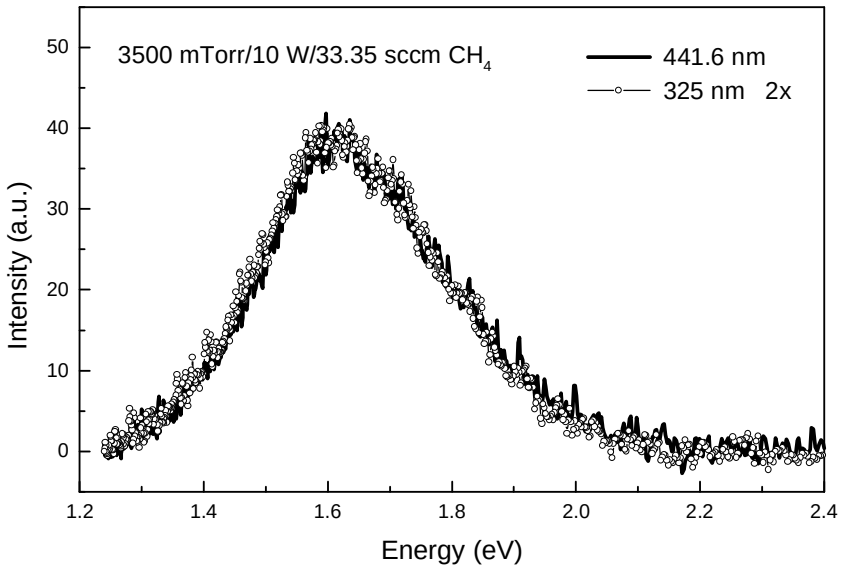

Fig. 2.20. The effect of the laser wavelength on the PL spectra of *pm-$Si_{1-x}C_x$:H* films deposited at 3500 mTorr with a substrate temperature of 200 °C and an RF power of 10 W.

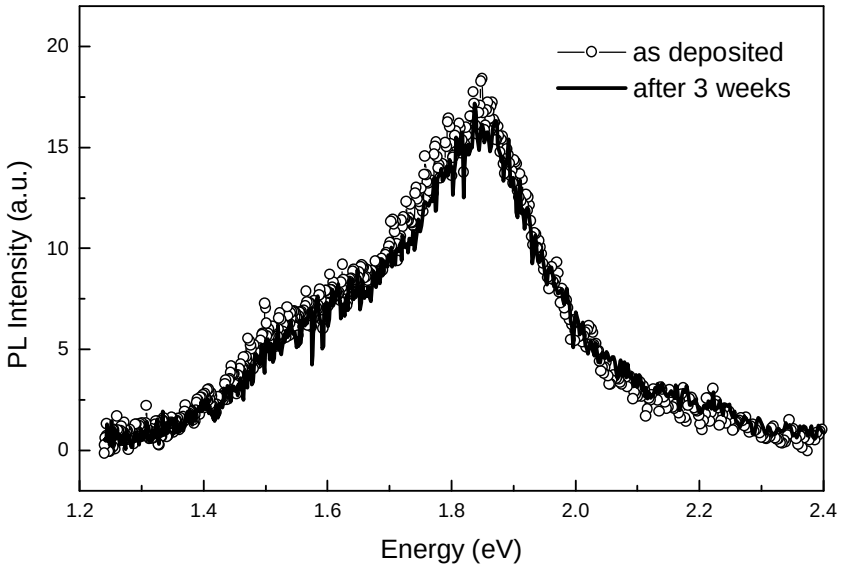

Fig. 2.21. The room temperature PL spectra of *pm-$Si_{1-x}C_x$:H* films as deposited and after being left for 3 weeks in open air at ambient temperature.

Several variations of the basic PL spectroscopy have been developed over the years, such as photoluminescence excitation (PLE) spectroscopy, photoluminescence resonant spectroscopy and time-resolved photoluminescence spectroscopy [26]. In time-resolved PL spectroscopy, the sample is excited with a very short light pulse and the emission is recorded as a function of time. In this technique, the decay of the luminescence intensity can be observed and studied. The decay spectra can be obtained using the same setup as show in Fig. 2.17 but with a different excitation source and detector. An ultra fast pulse laser is necessary as the excitation source, and lasers emitting pulses shorter that 1 ps are now available in the market. Thus, the time resolution is usually limited by the response time of the detector. Time resolutions down to ~100 ps can be obtained using a photomultiplier tube (PMT), while resolutions down to 1 ps or better are possible using a streak-camera or up-conversion techniques. The decay spectrum gives direct information about the carrier relaxation and recombination mechanisms, and allows to measure the radiative lifetimes.

2.8. Electroluminescence Measurements

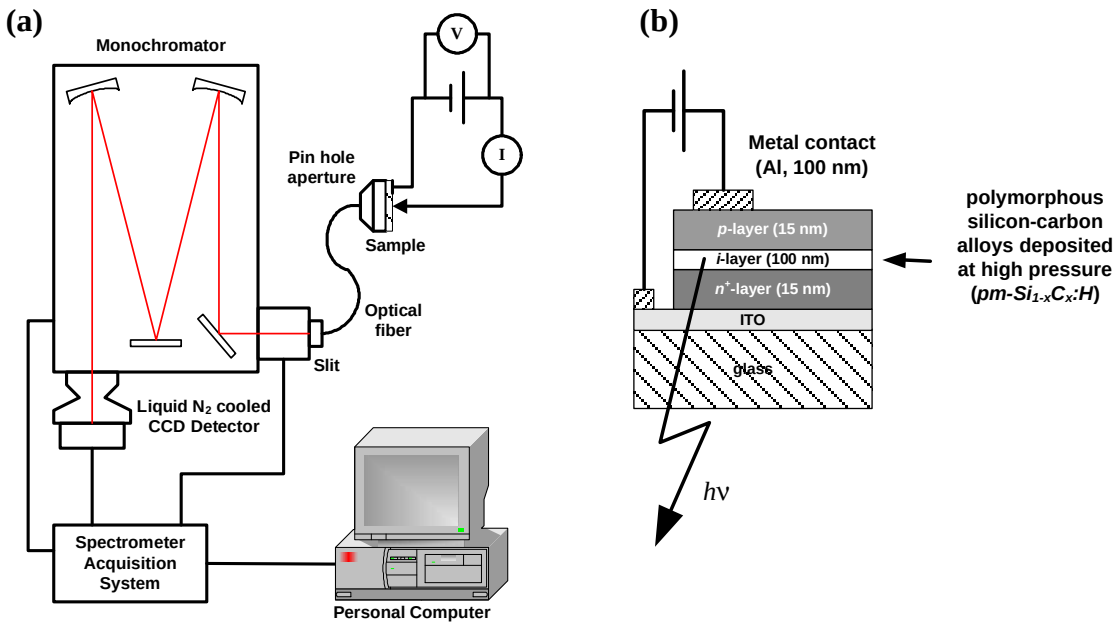

Fig. 2.22. Schematic of a) the experimental setup for electroluminescence measurement that includes the *J-V* acquisition system and b) the structure of electroluminescence diode.

In principle, the electroluminescence measurement (EL) is similar to the PL measurement, except for the excitation source. In EL measurements, the injection of charge carriers (electrons and holes) replaces the external photons to obtain electrons in the excited

state (conduction band). The experimental setup of this technique is practically the same as for the PL spectroscopy, but the excitation light source is replaced by an electric power supply (controllable current/voltage source). In this setup, we also installed a voltmeter and an ammeter in the loop of the cell in order to record the current-voltage (*J-V*) characteristic of the sample for each measurement (see Fig. 2.22a). The emission spectra for each applied voltage or current and also the total emission intensity-current/voltage (I_{PL}-*J* and I_{PL}-*V*) relations were recorded, as they are very important for device fabrication. The main difference between EL and PL measurement is in the sample preparation. We can measure any sample with PL spectroscopy technique just after synthesis or deposition without any other preparation. On the contrary, in the case of EL measurements, electrical contacts suitable to inject electrons and holes into the emissive layer are required (see Fig. 2.22b). This has been achieved by using *p*-type and *n*-type *a-Si:H* layers, even though their optimization is still under development.

2.9. High Resolution Transmission Electron Microscopy (HRTEM)

Introduction

In a conventional transmission electron microscope (TEM), a thin sample (5-100 nm, 10 nm is ideal) is irradiated by an electron beam with uniform current density. For routine measurement purposes, the acceleration voltage is in the range of 80-120 kV, while the medium-voltage instrument works in the range of 200-500 kV. Basically, this setup consists of 1) an electron gun (either emitted by thermionic, Schottky or field emission), 2) a two- or three-stage condenser-lens system that permits to vary the illumination aperture and the illuminated area of the specimen, 3) an imaging system consisting of three- or four-stage lenses system, and 4) an image recording system (either by a direct exposure of a photographic emulsion plate or digitally using a fluorescent screen coupled by a fiber-optic plate to a CCD camera. The setup, details of the technique including theory and data interpretations, are well-explained elsewhere [40].

TEM allows two kinds of image contrast. The bright-field contrast is produced either by intercepting the electrons scattered through angles larger than the objective aperture (scattering contrast) or by interference between the scattered wave and the incident wave at the image point (phase contrast). Dark-field contrast is obtained by tilting the primary beam or by hollow-cone illumination, so that the primary beam falls on the objective diaphragm. In the samples that contain a crystalline phase, the use of the primary beam (bright-field) or the

on axis Bragg-reflected beam (dark-field) gives rise to diffraction contrast which is important for crystal imaging.

In principle, TEM can provide high resolution imaging because elastic scattering is an interaction process that is highly localized to the region occupied by the screened Coulomb potential of an atomic nucleus. The angular distribution of inelastically scattered electrons is concentrated within a smaller scattering angle than that of elastically scattered ones. Most of the inelastically scattered electrons normally pass through the objective diaphragm in the bright-field mode, even though they do not contribute to high-resolution image details due to their less localized nature. Thus, by energy filtering transmission electron microscopy, it is possible to have a narrower inner-shell ionization and resolution of lattice periodicities around 0.3-0.5 nm due to the increase of energy loss [40].

Sample preparation

In this study, most of samples were directly deposited on copper microscope grid covered by a thin carbon membrane. This method is relatively easy and time saving, because by adjusting the deposition time we can control the thickness of films quite precisely and make them thin enough for TEM analysis. However, when the TEM analysis are also accompanied with chemical analysis, we need to deposit samples on the microscope grid without support (no carbon membrane). In this case, we deposited samples on NaCl or Al foil substrates, which later on were dissolved in water or HCl solution respectively. After the substrate removal, we can catch the thin film floating on the solution surface using a copper microscope grid without a carbon membrane and dry it before measurement.

2.10. X-ray Energy Dispersive Spectroscopy (XEDS)

The principle of x-ray energy dispersive spectroscopy (XEDS) or x-ray microanalysis is based on the fact that the x-ray generated by a focused electron beam that penetrates the sample carries information about the elements present in the sample. X-ray microanalysis in TEM setup mainly relies on energy-dispersive Si(Li) or highly pure germanium detectors, though instruments have been constructed with wavelength-dispersive spectrometers as used in x-ray microanalyzers.

Fig. 2.23 shows the schematic instrument setup of XEDS installed inside a TEM. The detection system consists of a collimator placed in front of the detector crystal (see Fig. 2.23). The collimator protects the detector against the entry of undesired radiation from the stage

region of the microscope; it defines the collection angle of the detector and the average take-off angle of x-rays entering the detector. Ideally, the collimator should be built of a high-Z material such as W, Ta or Pb, then coated externally and internally with a low-Z material such as Al, C or Be. The low-Z coating will minimize the production of x-rays from any backscattered electrons and the high-Z material will absorb any high-energy bremsstrahlung radiation.

In principle, the preparation of samples for XEDS measurements is similar to the preparation of samples for TEM. The differences are only in the thickness of the samples, which is ~ 50 nm for XEDS.

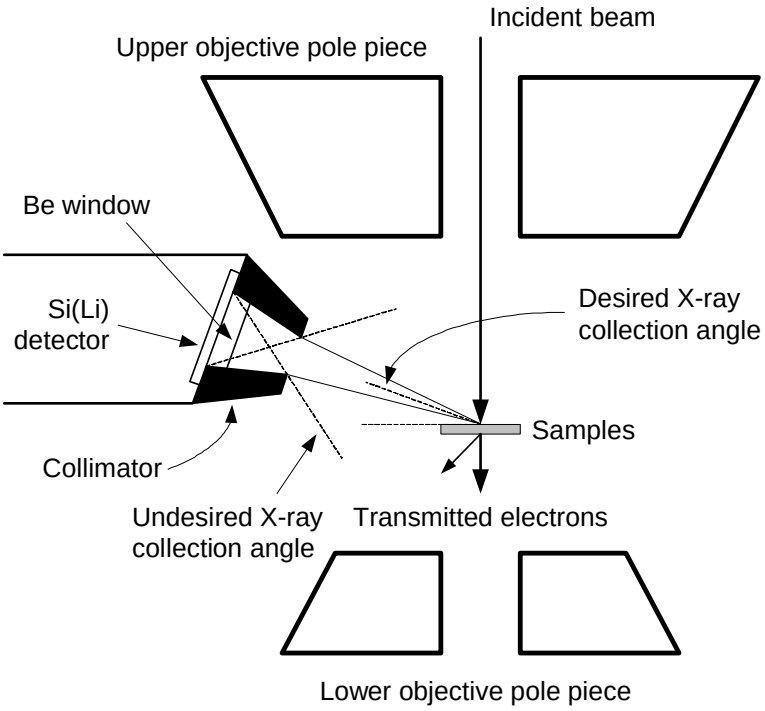

Fig. 2.23. Schematic of X-ray energy dispersive spectroscopy (XEDS) arrangement inside a transmission electron microscope setup [41].

Transport Characterization

2.11. Dark Conductivity Measurements

The dark conductivity measurements were carried out inside a small chamber that permits us to have a primary vacuum in order to reduce the parasitic conductance due to absorption of molecules (water, oxygen, etc.) on the sample surface. Inside the measurement chamber, we fix the sample on the temperature controllable substrate holder, where we can vary its temperature between –25 and 170 °C. In this experiment, we measure the current as a function of the temperature for a fixed applied voltage using a two-contact method with coplanar configuration. This experimental setup consists of four main components: 1) measurement chamber (includes pumping system and pressure gauge); b) temperature controllable substrate holder (includes heating element, cooling system with liquid N_2, temperature controller and electrical measurement probes); c) controllable DC voltage source; and d) picoammeter. In practice, this setup is computer controlled with programmable routines for temperature scanning measurements.

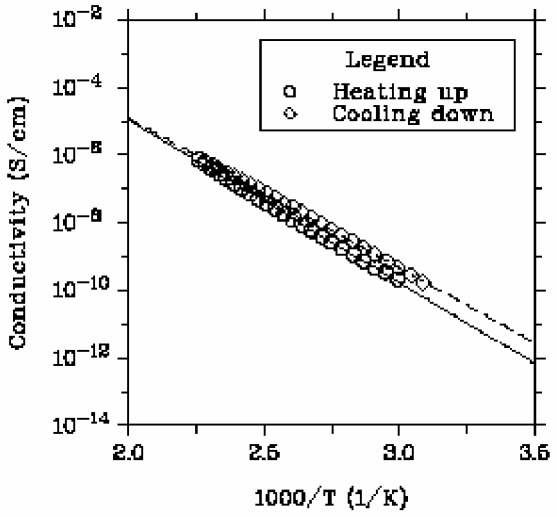

Fig. 2.24. Temperature dependence of the dark conductivity for a *pm-*$Si_{1-x}C_x$*:H* film and the fitting results according to the Arrhenius model for heating up and cooling down process.

In order to determine the activation energy, the conductivity data are fitted using the common Arrhenius equation:

$$\sigma = \sigma_0 e^{-\frac{E_a}{kT}} \qquad (2.34)$$

Where E_a is activation energy in eV, k is the Boltzmann constant and T is temperature in Kelvin. Fig. 2.24 shows the experimental conductivity data and the fitting results for *pm-*$Si_{1-x}C_x$*:H* films.

2.12. *J-V* Characteristic Measurements

J-V characteristic measurements were carried out on the same experimental setup as for dark conductivity measurement. In this case, we just change the measurement option to the constant temperature mode and then measure the current as a function of the applied voltage.

References

[1] M. A. Liebermann, A. J. Lichtenberg, *Principles of Plasma Discharges And Materials Processing*, John Wiley & Sons, Inc., New York, 1994.

[2] W. Luft, Y. S. Tsuo, *Hydrogenated Amorphous Silicon Alloy Deposition Processes*, Marcel Dekker, Inc, New York, 1993.

[3] F. F. Chen, *Introduction to Plasma Physics*, Plenum Press, New York, 1974.

[4] W. J. Goedheer, *Plasma Sources Sci. Technol.* **9**, 507 (2000).

[5] M. Hirose, in: J. I. Pankove, (Ed.), *Semiconductors and Semimetals*, Vol. 21A, Academic Press, Inc., Orlando, 1984.

[6] H. S. Butler, G. S. Kino, *The physics of fluids* **6**, 1346 (1963).

[7] P. Roca i Cabarrocas, *Science des matériaux et technique du réacteur dans le dépôt par procedé plasma RF de photopiles et d'autres dispositifs en silicium amorphe hydrogéné*, Thesis disertation, Université de Paris VIII, UFR de Physique, 1988.

[8] V. M. Donnelly, in: O. Auciello and D. L. Flamm (Eds.), *Plasma Diagnostics: Discharge Parameters and Chemistry*, Vol. 1., Academic Press, Inc., San Diego, CA, 1989.

[9] X. Zhao, T. Okazaki, A. Kasuya, H. Shimoyama, Y. Ando, *Jpn. J. Appl. Phys.* **38**, 6014 (1999).

[10] I. Géraud-Grenier, V. Massereau-Guilbaud, A. Plain, *Eur. Phys. J. AP* **8**, 53 (1999).

[11] I. Géraud-Grenier, V. Massereau-Guilbaud, A. Plain, *29th EPS Conference on Plasma Phys. and Contr. Fusion Montreux*, 17-21 June 2002 ECA Vol. **26B**, P-4.125 (2002).

[12] J. L. Andújar, E. Pascual, G. Viera, E. Bertran, *Thin Solid Films* **317**, 120 (1998).

[13] C. Böhm, J. Perrin, *J. Phys. D: Appl. Phys.* **24**, 865 (1991).

[14] M. Heintze, M. Magureanu, M. Kettlitz, *J. Appl. Phys.* **92**, 7022 (2002).

[15] S. Stamou, D. Mataras, D. Rapakoulias, *Chem. Phys.* **218**, 57 (1997).

[16] L. Boufendi, J. Gaudin, S. Huet, G. Viera, M. Dudemaine, *Appl. Phys. Lett.* **79**, 4301 (2001).

[17] A. V. Kharchenko, V. Suendo, P. Roca i Cabarrocas, *Thin Solid Films* **427**, 236 (2003).

[18] L. Boufendi, P. Roca i Cabarrocas, A. V. Kharchenko, Private discussions, 2002.

[19] B. Drévillon, *Prog. Cryst. Growth Charact. Mater.* **27**, 1 (1993).

[20] D. U. Fluckiger, *J. Opt. Soc. Am. A* **15**, 2228 (1998).

[21] R. M. A. Azzam, N. M. Bashara, *Ellipsometry and Polarized Light*, North-Holland, Amsterdam, 1977.

[22] P. Yeh, Optical Waves in Layered Media, John Wiley & Sons, Inc., New York, 1988.

[23] G. E. Jellison, Jr., *Appl. Opt.* **30**, 3354 (1991).

[24] H. Fujiwara, J. Koh, P. I. Rovira, R. W. Collins, *Phys. Rev. B* **61**, 10832 (2000).

[25] G. E. Jellison, Jr., F. A. Modine, *Appl. Phys. Lett.* **69**, 371 (1996); *Appl. Phys. Lett.* **69**, 2137 (1996).

[26] R. Tauc, R. Grigorovici, A. Vancu, Phys. Stat. Sol. **15**, 627 (1966).

[27] M. Fox, *Oxford Master Series in Condensed Matter Physics*: *Optical Properties of Solids*, Oxford University Press, Oxford, 2001.

[28] N. B. Colthup, L. H. Daly, S. E. Wiberley, *Introduction to Infrared and Raman Spectroscopy*, Academic Press Inc., New York, 1964, Ch1.

[29] G. Viera, S. Huet, L. Boufendi, *J. Appl. Phys.* **90**, 4175 (2001).

[30] A. Zwick, R. Carles, *Phys. Rev. B* **48**, 6024 (1993).

[31] C. –P., Sherman Hsu, in: F. Settle (Ed.), *Handbook of Instrumental Techniques for Analytical Chemistry*, Prentice-Hall Inc., New Jersey, 1997.

[32] N. Maley, *Phys. Rev. B* **46**, 2078 (1992).

[33] M. H. Brodsky, M. Cardona, J. J. Cuomo, *Phys. Rev. B* **16**, 3556 (1977).

[34] A. A. Langford, M. L. Fleet, B. P. Nelson, W. A. Lanford, N. Maley, *Phys. Rev. B* **45**, 13367 (1992).

[35] E. C. Freeman, W. Paul, *Phys. Rev. B* **18**, 4288 (1978).

[36] R. Reitano, G. Foti, *Solid State Communications* **115**, 375 (2000).

[37] W. K. Choi, S. Gangadharan, *Materials Science and Engineering B* **75**, 174 (2000).

[38] X. Redondas, P. Gonzalez, B. Leon, M. Pérez-Amor, *Surface and Coatings Technology* **100-101**, 160 (1998).

[39] We thank Carlos Barthou for his help with PL measurement at LOS. In this case we used the same setup as described elsewhere in his publication, i.e.: C.-C. Kao, C. Barthou, B.

Gallas, S. Fisson, G. Vuye, J. Rivory, *Materials Science and Engineering B* **105**, 226 (2003).

[40] L. Reimer, *Transmission Electron Microscopy: Physics of Image Formation and Microanalysis*, Springer Series in Optical Science, 4th Edition, Springer-Verlag, Berlin, 1997.

[41] D. B. Williams, C. B. Carter, *Transmission Electron Microscopy: A textbook for Materials Science, Vol. 4: Spectrometry*, Plenum, New York, 1996.

Chapter 3

Deposition of hydrogenated polymorphous silicon

3.1. Introduction

Hydrogenated polymorphous silicon (*pm-Si:H*) is a nanostructured material that attracts much attention due to its unique structure, which is intermediate between those of hydrogenated amorphous silicon (*a-Si:H*) and microcrystalline silicon (μ*c-Si:H*) [1, 2]. The term polymorphous refers to a material with various crystalline structures, which is the case of polymorphous silicon thin films which consist of nanometer sized silicon crystallites embedded in a matrix of *a-Si:H*-like material [3, 4]. The crystallites adopt various structures (diamond, hexagonal close packed, face center cubic,..) depending on the deposition conditions [5]. The presence of embedded nanocrystals improves the order of the amorphous matrix and results in a more relaxed structure with some medium range order (MRO) in comparison to *a-Si:H* [3]. Moreover, this material shows excellent properties such as: low defect density of the order of 5×10^{14} cm^{-3} V^{-1}, hole diffusion lengths larger that 200 nm [6, 7], and more important, a higher stability with respect to *a-Si:H* under illumination (less than 10 % of degradation in solar cell efficiency) [8]. Thus, this material is an interesting alternative to *a-Si:H* for applications to large area electronic devices such as solar cells, thin film transistors, detectors, etc.

Polymorphous silicon is produced from the dissociation of silane (SiH_4) highly diluted in hydrogen (H_2) (10 sccm of SiH_4 in 90 sccm of H_2) by the standard RF glow discharge method in the pressure range of 1-2.5 Torr and at high RF power (typically 0.21 W/cm^2). As shown in previous studies, the dependence of the deposition rate on the deposition pressure can be used to identify the deposition regime in the SiH_4/H_2 system [9, 10], thus we can distinguish four deposition regimes as a function of pressure: 1) microcrystalline silicon growth, 2) nanocrystal formation, 3) agglomeration and 4) powder formation regimes (Fig. 3.1). Below 1000 mTorr, we obtain μ*c-Si:H* thin films, which result from the reaction of SiH_x and H radicals on the surface and subsurface (microcrystalline growth regime). Above 1000

mTorr, we obtain polymophous silicon (*pm-Si:H*) materials with different properties with respect to standard *a-Si:H.* The nanocrystal formation regime begins just after the microcrystalline growth regime at slightly higher pressure, where the building blocks for the growth are both silicon radicals and nanocrystals produced in the plasma phase. In this regime, we observe a linear increase of deposition rate with pressure. Above 1600 mTorr, there is a drastic increase of deposition rate, corresponding to the so-called α–γ' transition [11]. In this regime, the deposition involves radicals, nanocrystals and their agglomerates. Further, in the powder formation regime, the growth and agglomeration rates are very fast, which yields powders that get charged negatively. These particles are confined in the plasma due to their charge and cannot contribute to deposition; when they became too large to be confined in the plasma, they are pumped out by the gas flow. Therefore, in this regime, the deposition rate reaches saturation and starts to decrease.

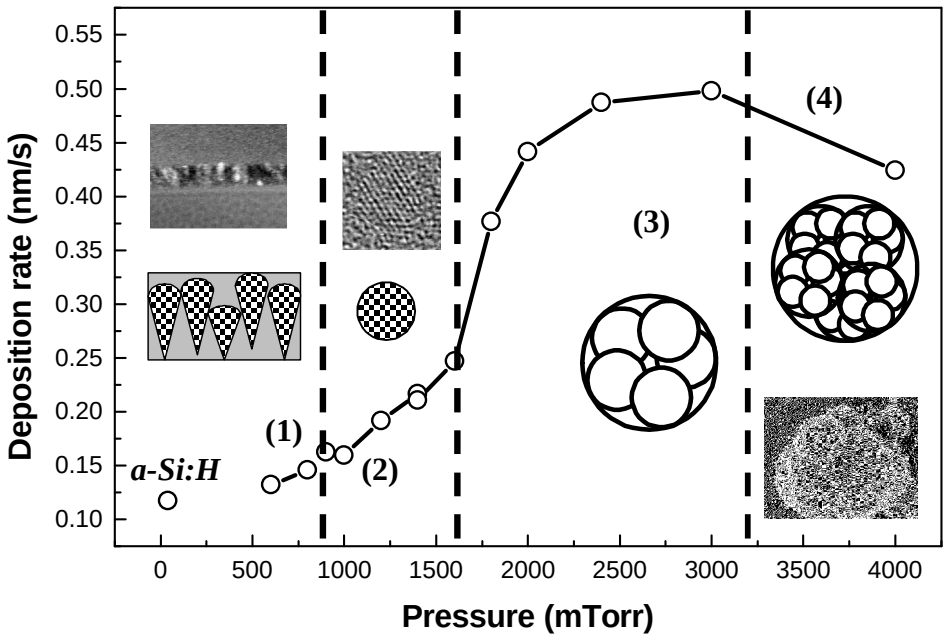

Fig. 3.1. Deposition rate as a function of deposition pressure for silane highly diluted in hydrogen at 13.56 MHz. At low pressure (40 mTorr), the deposition rate of standard amorphous silicon is given as a reference.

In the following sections, the effects of the excitation frequency on the deposition rate and properties of the films are presented and discussed. Moreover, we present the effect of dopants on the dynamics of powder formation and film properties at various pressures, which demonstrates the possibility to produce both *n*- and *p*-type doped *pm-Si:H.*

~ *Overview of previous studies on α–γ' transition* ~

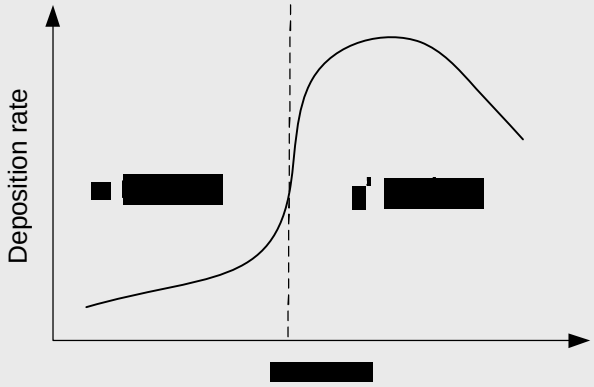

α–γ' transition is characterized by an abrupt increase in the deposition rate as a function of pressure in SiH_4-H_2 RF plasma.

A. V. Kharchenko, V. Suendo, P. Roca i Cabarrocas, *Thin Solid Films* **427**, 236 (2003).

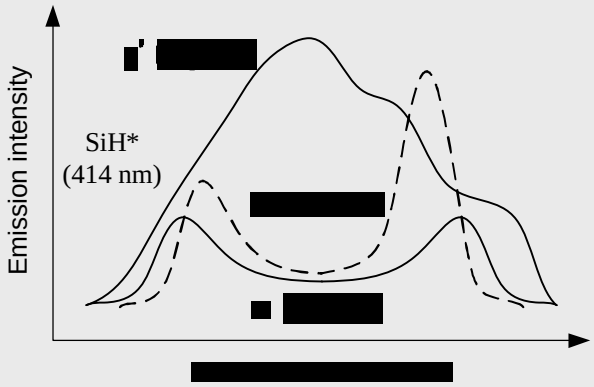

α–γ' transition is characterized by the transition of the spatial distribution of light emission SiH* (414 nm) in SiH_4 RF plasma from sheath to bulk dominant.

J. Perrin, C. Böhm, R. Etemadi, A. Lloret, *Plasma Sources Sci. Technol.* **3**, 252 (1994).

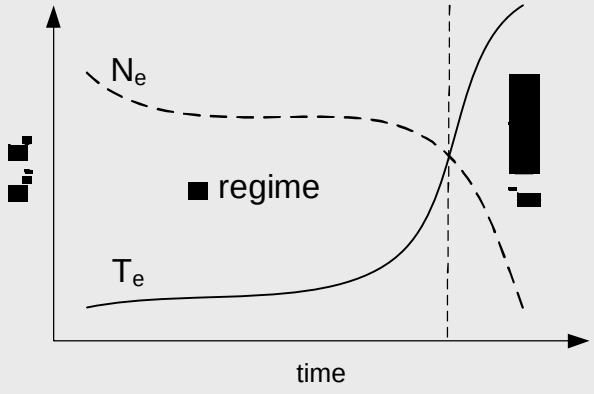

The high rate of electron attachment to large agglomerates stimulates the α–γ' transition, which is charaterized by a strong decrease in the electron density and a remarkable increase in the electron temperature.

A. A. Fridman, L. Boufendi, T. Hbid, B. V. Potapkin, A. Bouchoule, *J. Appl. Phys.* **79**, 1303 (1996).

3.2. The effects of RF excitation frequency

An important issue in the deposition of thin film semiconductor materials is the determination of process conditions which produce device quality films at high deposition rate, to achieve a high throughput and low production costs. In the case of standard *a-Si:H*, deposition at low pressure and low RF power yields a high quality material but at low deposition rate (see Fig. 3.1). Many efforts have been carried out to increase the deposition rate by optimizing the process parameters in terms of total gas pressure, RF power, coupling technique, substrate temperature and excitation frequency [12]. Ideally, those efforts should increase the deposition rate without sacrificing the film quality, but this is not an easy task to

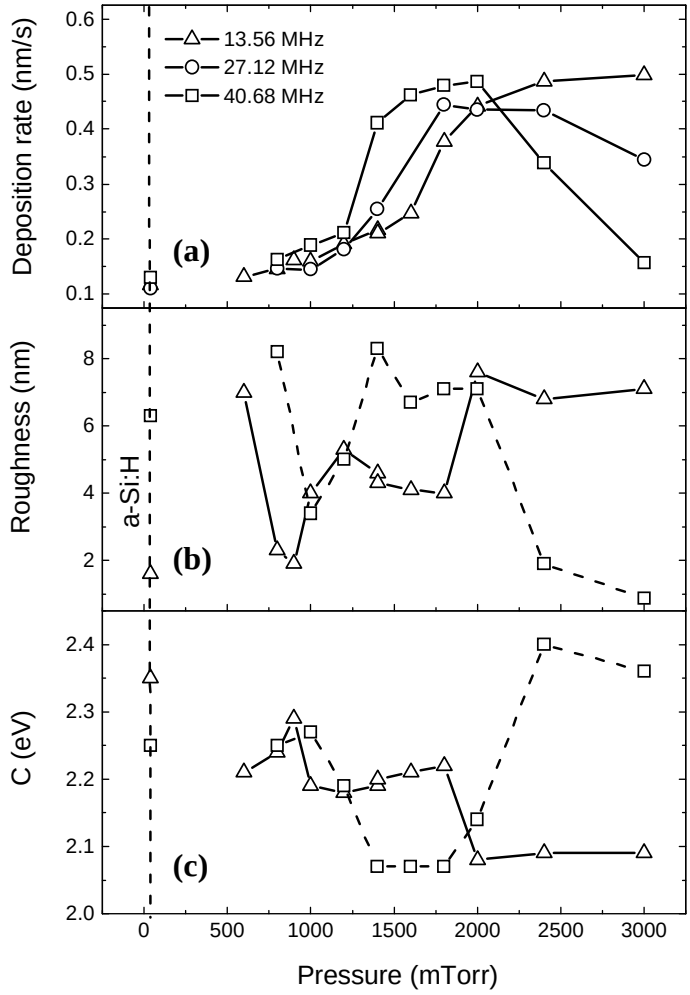

Fig. 3.2. (a) Deposition rate, (b) surface roughness and (c) broadening term of the TL model, C, as functions of the deposition pressure for samples deposited at various frequencies. The values for a standard a-Si:H are also given as a reference. The lines are provided as guides to the eye. Error bars are of the same order as the size of the symbols.

accomplish. In general, an increase of the deposition rate results in a decrease of the film quality. For example, high deposition rates can be simply achieved by increasing the total gas pressure or the RF power, but the properties of the films tend to deteriorate due to the powder formation and/or the bombardment by high energy ions [13]. Among the process parameters, an increase of the excitation frequency has often been suggested as a way to achieve higher deposition rates while maintaining device quality *a-Si:H* films [13, 14]. Therefore, we have performed a detailed study of the effect of RF excitation frequency on deposition rate and film properties.

Fig. 3.2a. shows the effect of the total pressure on the deposition rate for three excitation frequencies (13.56, 27.12 and 40.68 MHz). The deposition rate of standard *a-Si:H* films deposited at 40 mTorr from pure silane at low RF power (0.03 W/cm^2) is also given as reference, and found independent of the excitation frequency. For samples deposited from the dissociation of silane-hydrogen mixtures at high RF power (0.21 W/cm^2), we observed that the pressure at which the α–γ' transition takes place is shifted towards lower pressure as the excitation frequency increases. Thus, one can conclude that for a given pressure, an increase of the excitation frequency results in an increase of deposition rate (for example at 1600 mTorr as shown in Fig 3.2). However, the maximum deposition rate for a fixed RF power is independent of the excitation frequency and, overall, increasing the excitation frequency does not produce any substantial increase in deposition rate. Moreover, at higher pressure, we observe saturation in the pressure dependence of the deposition rate, followed by a decrease in the deposition rate, particularly at 27.12 and 40.68 MHz. The decrease can be attributed to the formation of large particles or powders that get negatively charged and trapped in the plasma, and therefore cannot contribute to the deposition.

The increase in deposition rate at high pressure is associated with an increase in the surface roughness, as shown in Fig. 3.2b for films deposited at 13.56 and 40.68 MHz. As explained in the previous section, the films deposited at pressures lower than 1000 mTorr are microcrystalline and thus have a larger surface roughness due to the columnar structure of crystallites. At 13.56 MHz, for films deposited in the low deposition rate regime ($1200<P<1800$ mTorr), the surface roughness is quite low (~3 nm) and sharply increases along with the deposition rate for $P>1800$ mTorr. Above this pressure, both deposition rate and surface roughness reach a saturation value and remain constant. A similar behavior can be observed for samples deposited at 40.68 MHz. We observe an increase in the surface roughness at $P\sim1200$ mTorr, which corresponds to the α–γ' transition for this excitation frequency. Then the surface roughness and the deposition rate remain constant in the pressure

range 1200<*P*<2000 mTorr and finally for pressures above 2000 mTorr, the decrease in deposition rate is accompanied by a decrease in the surface roughness. The above results can be related to the contribution of nanocrystals/clusters and their agglomerates to the deposition. Below the α–γ' transition, the density of nanocrystals/clusters is too low for them to agglomerate in the gas phase. Thus, in the low pressure regime, only nanocrystals and/or nanoclusters contribute to deposition, thus resulting in a smooth surface. As pressure increases, the density of particules exceeds a critical value for agglomeration to take place. In this regime, agglomerates with sizes up to 10 nm contribute to deposition and thus the surface roughness increases. Further increase of pressure leads to the coalescence of the agglomerates and to the formation of larger particles or powders which are negatively charged due to the attachment of electrons on their surface, and thus they cannot contribute to deposition as they are confined to the plasma. As a result, the deposition rate (Fig. 3.2a) and the surface

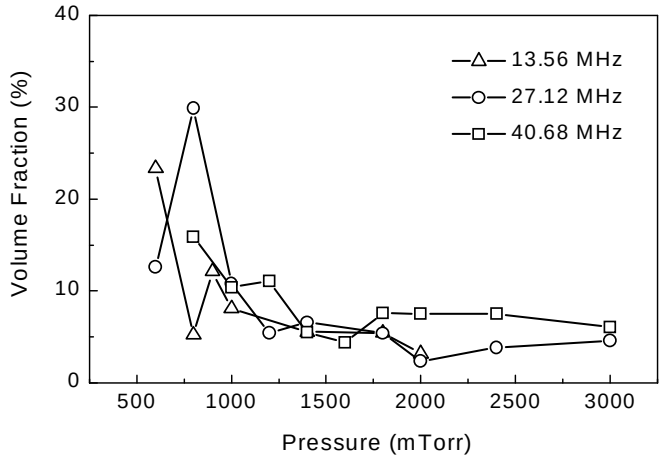

Fig. 3.3. The effect of deposition pressure on the crystalline volume fraction deduced from Raman analysis for samples deposited at various excitation frequencies.

roughness (Fig. 3.2b) decrease.

Fig. 3.2c shows the effect of the deposition pressure on the broadening term (*C*) obtained from the Tauc-Lorentz (TL) model, which represents the disorder of the material. We found that more ordered materials, which have smaller *C* values, are deposited in the pressure range of 2000-3000 mTorr for an excitation frequency of 13.56 MHz, while the minimum is shifted to lower pressure (1400-2000 mTorr) for films deposited at 40.68 MHz. Thus, compared to standard *a-Si:H* films we obtained for *pm-Si:H* conditions an important decrease of the broadening parameter, related to the contribution of nanocrystals and their

agglomerates to deposition. Interestingly, the lowest values of the broadening parameter are achieved in the regime where the deposition rate and the surface roughness are the highest. Thus, with respect to previous studies [3], the above results show that it is the incorporation of nanometer size clusters, nanocrystals and particularly of their agglomerates with sizes up to 10 nm, which produces a more ordered material. This mechanism is well demonstrated by the deposition of films at 40.68 MHz and for pressures above 2000 mTorr. In this regime, clusters are consumed in the formation of large particles and/or powders that cannot contribute to deposition, thus resulting in a decrease of the deposition rate and surface roughness, but an increase on the material disorder. Therefore, the most ordered *pm-Si:H* films are obtained at

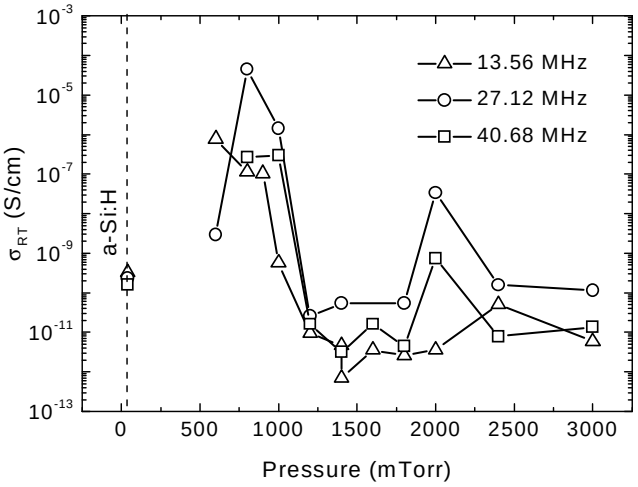

Fig. 3.4. Deposition pressure dependence of the dark conductivity at room temperature for samples deposited at various RF excitation frequencies.

high pressure and at the highest deposition rate, just before the onset of powder formation.

Fig. 3.3 shows the volume fraction of the crystalline phase in the films deduced from the analysis of their Raman spectra (see Ch. 2). The figure shows a general trend for the crystalline fraction: a decrease with increasing deposition pressure. These measurements show that microcrystalline silicon films are obtained at pressures below 1000 mTorr, while polymorphous silicon above this pressure, independently of the excitation frequency. This trend is also supported by the evolution of room temperature dark conductivity (σ_{RT}) with deposition pressure as shown in Fig. 3.4. For pressures below 1000 mTorr, the conductivity is in the range of 10^{-5}-10^{-7} S/cm corresponding to that of intrinsic μ*c-Si:H* films, while at pressures above, the crystalline fraction decreases below the percolation threshold (~30 %) [15]. Thus, at pressures above 1000 mTorr, the conductivity strongly decreases with pressure until it reaches values of 10^{-10}-10^{-12} S/cm corresponding to those of polymorphous silicon.

In the polymorphous deposition regime, the conductivity of samples is almost independent of pressure (Fig. 3.4). The conductivity of samples deposited at 13.56 and 40.68 MHz is quite similar, while that of the sample deposited at 27.12 MHz is approximately one order of magnitude higher in the whole pressure range. Moreover, we found a local maximum at 2000 mTorr for the films deposited at higher frequencies, while this maximum is less pronounced and shifted to higher pressure for the 13.56 MHz samples. Note that the conductivity of the sample deposited at 2000 mTorr and 27.12 MHz is close to that of μ*c-Si:H* films. This suggests that at this pressure we are depositing an important amount of nanocrystals produced in the gas phase. The reason for such optimum could be the increase of the nanocrystals fraction and the lower energy of the ions at 27.12 and 40.68 MHz.

3.3. Effects of dopants on the dynamics of powder formation and film properties

The availability of doped *a-Si:H* is well-known and widely used for many applications. On the other hand, the possibility of obtaining doped *pm-Si:H* is still in question. Until now, for device applications of *pm-Si:H,* the doped layers are based on (*a-Si:H* or *a-*$Si_{1-x}C_x$*:H*). The different deposition conditions between *pm-Si:H* and *a-Si:H* are reflected in their interface quality and device properties such as low efficiency in *p-i-n* solar cells. Thus, it is preferable to have doped *pm-Si:H* layers for both *p*- and *n*-layers.

The process of cluster and powder formation in silane plasmas is still a subject of research [16]. So far, no study has shown the effects of dopants in this process, even though one may expect that the addition of impurities affects the charging process of clusters and thus the dynamics of their agglomeration. In order to study these effects, we monitored the evolution of the amplitude of the third harmonic of the RF current (J_3), which has been found to be very sensitive to the different phases of powder formation [17]. In this study, we used trimethylboron (TMB or $[CH_3]_3B$) and phosphine (PH3) as dopants to obtain *p*- and *n*-type materials respectively.

Firstly, in order to study the influence of the doping gas on the plasma, we measured the evolution of J_3 for different concentrations of dopants as shown in Fig. 3.5. Here, we fixed the total pressure at 1600 mTorr, i.e. at the α–γ' transition (see Fig. 3.1). The analysis of J_3 has

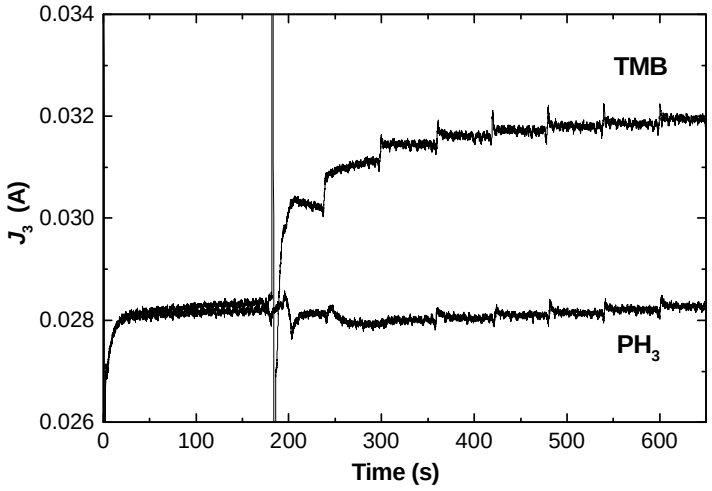

Fig. 3.5. Time evolution of the amplitude of the third harmonic of the RF current (J_3) at 1600 mTorr with the increase of doping gas partial pressure of 7 mTorr each minute.

confirmed that for the intrinsic case, i.e. for a dopant partial pressure equal to zero, the silane-hydrogen plasma at 1600 mTorr contains silicon nanoclusters, nanocrystals and/or their agglomerates [9]. We switched on the RF power at t = 0, then we observed the evolution of J_3. In the first 3 minutes, we observe that J_3 increases and reaches a steady–state value. After 3 minutes, we introduce the doping gas mixture (2 % TMB or PH_3 diluted in H_2) and increase its partial pressure by 7 mTorr each minute. At the same time, we keep the total pressure constant by decreasing the flow rate of hydrogen, in order to suppress the effect of pressure on J_3. As shown in Fig. 3.5, the addition of TMB leads to an increase of J_3, while the addition of PH_3 has no significant effect. Further, we prepared a series of experiments, where long-term measurements were carried out. Here, we measured the steady-state value of J_3 for each value of dopant partial pressure. In this case, we observed that after ignition of the plasma, J_3 displays a transient behavior characteristic of the formation of clusters. Depending on the process conditions, J_3 will reach a steady-state with a value that characterizes the amount of clusters or powder in the plasma. A lower value of J_3 indicates a higher concentration of powders that trap electrons in the plasma and thus decreases the current [9]. Fig. 3.6 shows the steady-state values of J_3 as a function of doping gas partial pressure. These results and

those of Fig. 3.5 indicate that with respect to the condition without dopants, the addition of TMB has a strong effect on the saturation value of J_3, while the addition of PH_3 has no significant effect. This suggests that boron (or carbon) incorporation changes the electronic properties of the particles, i.e. on average they become less trapped. Thus one can expect a similar structure or morphology for *n*-type and intrinsic, while *p*-type films should be different.

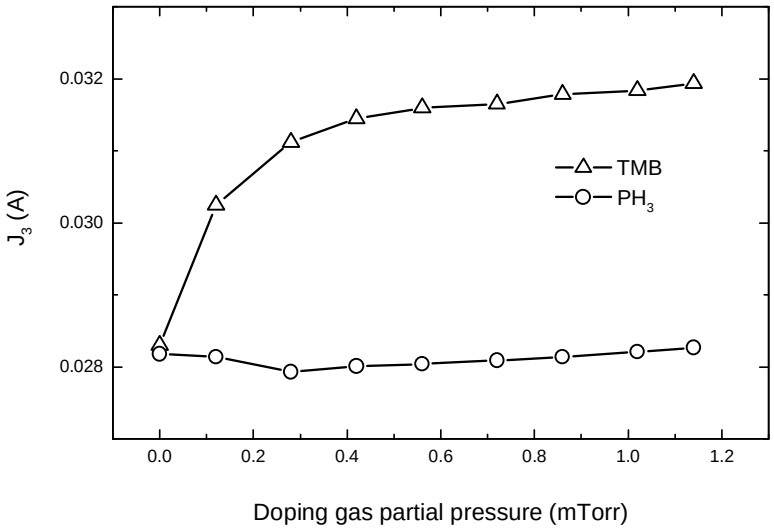

Fig. 3.6. Steady-state values of J_3 as a function of dopant mixture partial pressure. A partial pressure equal to zero corresponds to the growth of undoped films at 13.56 MHz under a total pressure of 1600 mTorr.

Several series of samples with and without dopants were deposited. The partial pressure of each doping gas was optimized by selecting the conditions for which the dark conductivity of the material is maximum. In our case, we used 4.5 sccm for TMB and 1 sccm for PH_3, which corresponds to a dopant/silane ratio of 5.4×10^{-3} and 2×10^{-3} respectively. Fig. 3.7a shows the pressure dependence of the deposition rate for intrinsic and doped films. The evolution of the deposition rate of *i*- and *n*-type films is the same as expected from the analysis of J_3, while the deposition rate of *p*-type films is significantly higher in the whole pressure range. This result is in good agreement with previous studies on the effect of boron on the deposition of *p*-type *a-Si:H* using diborane (B_2H_6) as doping gas [18]. Moreover, the presence of dopants does not shift significantly the α–γ' transition regime. Fig. 3.7b shows the evolution of the surface roughness with deposition pressure. A sharp increase of the surface roughness was observed just after the α–γ' transition, corresponding to the

agglomeration of clusters and nanocrystals, this increase being more pronounced in the case of *n*-type samples. These results suggest that the increase of surface roughness is due to the contribution of small agglomerates of nanoclusters and/or nanocrystals. Thus, the smaller roughness in the case of p-type samples can be attributed to the inhibition of the agglomeration process by the presence of boron, which is in agreement with the results of J_3 analysis as shown in Fig 3.6. This fact might be due to the formation of positively charged particles, which tend to be accelerated to the electrodes by the plasma potential before they can grow larger. As a result, the addition of TMB increases the deposition rate while the

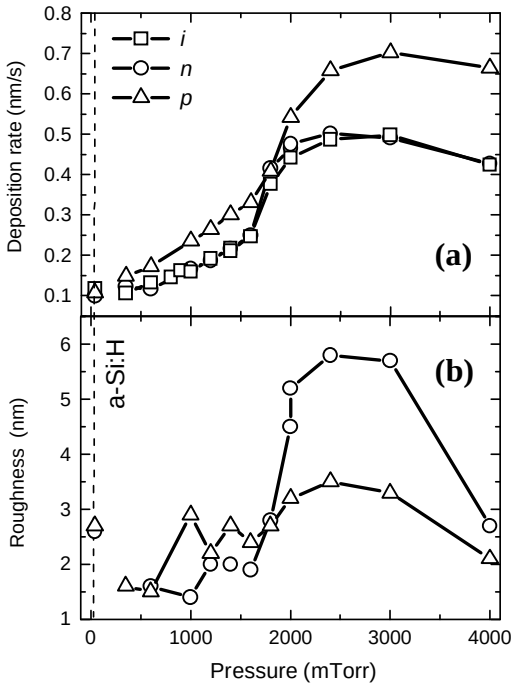

Fig. 3.7. (a) Deposition rate and (b) surface roughness as functions of the deposition pressure for doped films

surface roughness does not change much compared to doped *a-Si:H* as depicted in Fig. 3.7.

The effect of the deposition pressure on the broadening parameter (*C*), deduced from ellipsometry data for undoped and doped samples, is presented in Fig 3.8. It shows that the presence of dopants generally increases the material disorder without significantly changing the pressure dependence. Indeed, the three series show the same minimum value of C for deposition pressures in the range between 2000 and 3000 mTorr. The parameter *C* represents the broadening of the absorption edge according to Tauc's law due to material disorder. Thus, it is expected that by introducing dopants into the materials, the defects will increase and

directly broaden the absorption edge. Moreover, the addition of phosphorous is more efficient at increasing the disorder, which is consistent with its higher doping efficiency from the dark conductivity measurement results (Fig. 3.9). Interestingly, even though the value of the parameter *C* increases with the presence of dopants, they still show the same trend in their evolution with pressure as shown in Fig. 3.8.

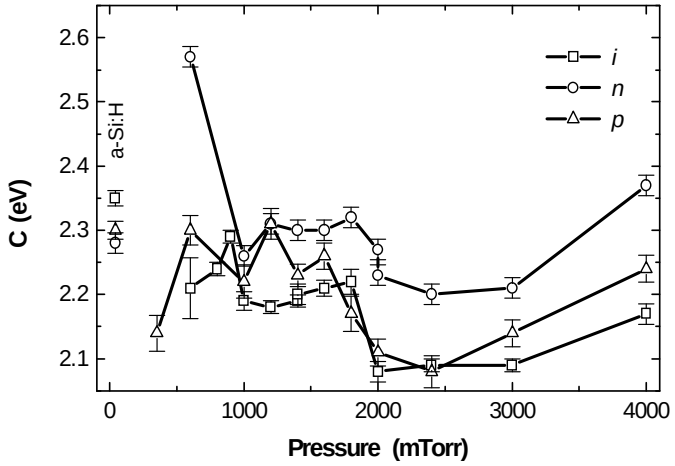

Fig. 3.8. The pressure dependence of broadening parameter (C) for intrinsic, *n*- and *p*-type doped films.

The results of dark conductivity measurements for intrinsic and doped films are presented in Fig. 3.9. It is shown that the transport properties of doped *pm-Si:H* are comparable to those of standard *a-Si:H*. The *n*-type *pm-Si:H* films show higher conductivity compared to *p*-type films, in a similar way for standard *a-Si:H* given as a reference. We note here that for *i*- and *n*-type materials, in the pressure range between 300 and 1000 mTorr, the films are μ*c-Si:H*, which explains their higher value of conductivity and low activation energy. However, in the case of *p*-type materials, both conductivity and activation energy are of the same order of magnitude for the whole pressure range, which is consistent with the fact that we could not detect any crystalline fraction either by spectroscopic ellipsometry or by Raman measurements.

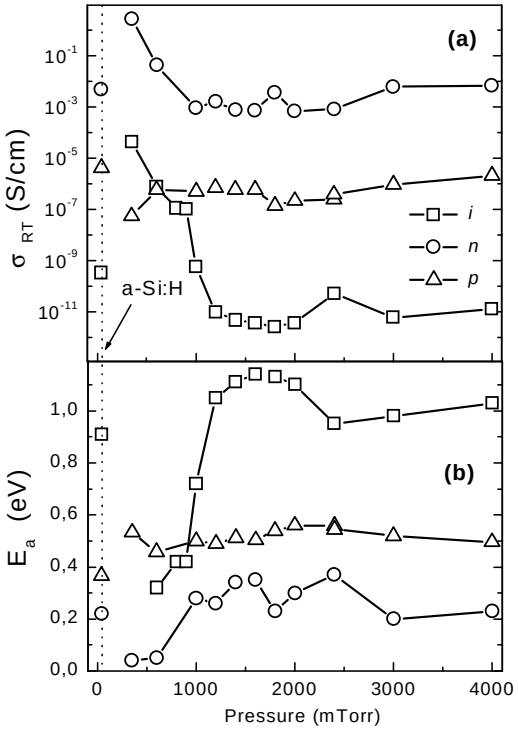

Fig. 3.9. (a) Room temperature dark conductivity and (b) activation energy for intrinsic and doped films as functions of the deposition pressure at 13.56 MHz.

3.4. Photonic applications

The presence of nanocrystals in *pm-Si:H* films has improved their properties, making them suitable for many optoelectronic applications. Moreover, the possibility of doping the material and varying its properties by changing the excitation frequency, as described above, gives further flexibility for device optimization. However, until know, we have not yet used the characteristic of the embedded nanocrystals, such as their associated quantum confinement effects. Since Canham discovered strong visible luminescence from porous silicon [19], the quantum confinement properties of silicon-based materials became an important issue for photonic applications [20, 21]. In the case of polymorphous silicon, we have to consider not only the presence of silicon nanocrystals but also the matrix of amorphous silicon. It is well-known that amorphous silicon is not a good candidate for photonic applications, although it gives better luminescence than its crystalline counterpart [22, 23], from the radiative recombination of band-tail electrons and holes [22-26]. In these studies, it has been shown that the PL efficiency of *a-Si:H* strongly depends on the deposition conditions, which of course determines the defect density in the films. Therefore, we have to

take into account the effect of amorphous silicon matrix on the luminescence properties of embedded nanocrystals in *pm-Si:H*.

In principle, we should be able to observe two main luminescence peaks from a *pm-Si:H* sample. A peak in the near infrared region (~1.3 eV), which corresponds to the radiative recombination of carriers that are trapped in shallow defect levels near the band edge as in hydrogenated amorphous silicon, and a second peak at higher energy, related to the radiative recombination in the silicon nanocrystals. Considering that the luminescence efficiency of silicon nanocrystals is higher than that of amorphous silicon and that their emission wavelength is in the visible region [19-21], we will focus on the luminescence from silicon nanocrystals, which is more interesting for photonic applications.

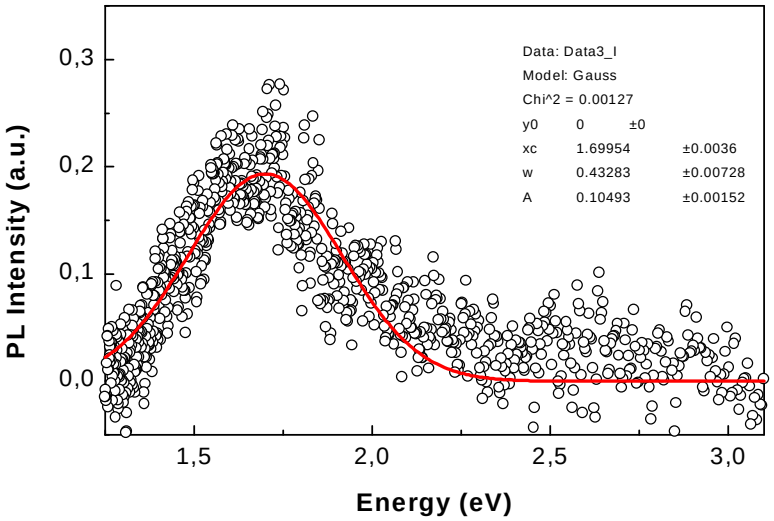

Fig. 3.10. Room temperature photoluminescence (PL) spectrum of a polymorphous silicon thin films deposited at 200 °C under total pressure of 3000 mTorr. PL was excited with a HeCd laser line at 325 nm (3.8 eV) with a power of 4 mW for an illumination area of 0.03 cm^2.

Fig. 3.10 shows the room temperature PL spectrum of a *pm-Si:H* film deposited at 3000 mTorr, in the powder formation regime. It gives a symmetric Gaussian type peak centered at around 1.7 eV, which is a typical PL emission energy for medium size silicon nanocrystals [27]. The PL intensity is so low that it cannot be observed by the naked eye even in a dark room. Thus the radiative recombination process in silicon nanocrystals is inefficient in *pm-Si:H*. The low efficiency might be due to i) the competition between the radiative recombination process in the nanocrystals and the nonradiative one in the matrix or at the surface of nanocrystals, ii) insuficient confinement, as the gap difference between *a-Si:H* and silicon nanocrystals is small, and iii) absorption of the emitted light by the *a-Si:H* matrix.

Thus, to improve photoluminescence, we should improve the matrix material, where an amorphous high band gap semiconductor with a low defect density should be used instead of hydrogenated amorphous silicon. The matrix material must be able to passivate the surface of embedded nanocrystals and have a higher band gap than them to confine the carriers. Spatially confined carriers in nanosized semiconductors exhibit a quantum size or confinement effect (QSE or QCE), which increases the band gap energy and the radiative recombination probability. Moreover, the high band gap material also provides a transparent matrix for PL emission in the visible region.

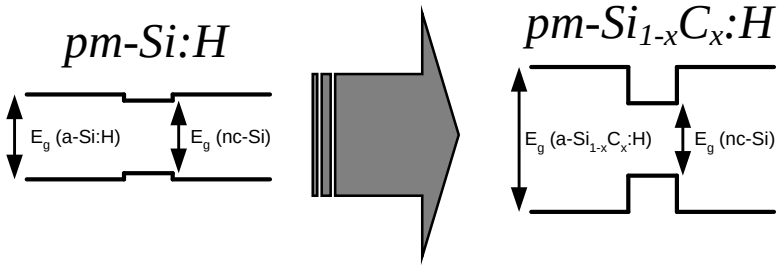

Fig. 3.11. Schematic diagram of the approach to improve the carrier spatial confinement by replacing *a-Si:H* as the matrix material in *pm-Si:H* with *a-$Si_{1-x}C_x$:H* in *pm-$Si_{1-x}C_x$:H*.

Many studies have been devoted to the synthesis of silicon nanocrystals embedded in a SiO_2 matrix, which gives an excellent passivation and confinement effect [28]. Moreover, the SiO_2 matrix also gives a high transparency for emission in visible region. However, as described by Polman, the insulating nature of the SiO_2 matrix makes it difficult to inject carriers into the nanocrystals, and thus efficient light-emitting diodes are difficult to realize [29]. Our approach is presented schematically in Fig. 3.11, where the matrix material is based on amorphous silicon carbon alloys (*a-$Si_{1-x}C_x$:H*). The reasons for choosing *a-$Si_{1-x}C_x$:H* as a matrix material are: a) *a-$Si_{1-x}C_x$:H* is a high band gap material with a possibility to tune its band gap energy by varying the concentration of carbon, hydrogen, and sp^3/sp^2 bond ratio; b) *a-$Si_{1-x}C_x$:H* can be doped; c) *a-$Si_{1-x}C_x$:H* is known as a luminescence material among amorphous semiconductors [30-36]; d) Si-C bond in the amorphous phase is well-known to be compatible with the surface of crystalline silicon [20]; and e) this material is easy to synthesize by PECVD with a wide range of properties and applications [25, 31, 32-36]. Thus, in the following we will focus on the *pm-$Si_{1-x}C_x$:H* instead of *pm-Si:H* for the application of electroluminescent devices.

References

[1] P. Roca i Cabarrocas, S. Hamma, S. N. Sharma, G. Viera, E. Bertran, J. Costa, *J. Non-Cryst. Solids* **227-230**, 871 (1998).

[2] C. Longeaud, J. P. Kleider, P. Roca i Cabarrocas, S. Hamma, R. Meaudre, M. Meaudre, *J. Non-Cryst. Solids* **227-230**, 96 (1998).

[3] A. Fontcuberta i Morral, H. Hofmeister, P. Roca i Cabarrocas, *J. Non-Cryst. Solids* **299-302**, 284 (2002).

[4] A. Fontcuberta i Morral, R. Brenot, E. A. G. Hamers, R. Vanderhaghen, P. Roca i Cabarrocas, *J. Non-Cryst. Solids* **266-269**, 48 (2000).

[5] G. Viera, M. Mikikian, E. Bertran, P. Roca i Cabarrocas, L. Boufendi, *J. Appl. Phys.* **92**, 4684 (2001).

[6] J. P. Kleider, C. Longeaud, M. Gauthier, M. Meaudre, R. Meaudre, R. Butté, S. Vignoli and P. Roca i Cabarrocas, *Appl. Phys. Lett.* **75**, 3351 (1999).

[7] O. Saadane, C. Longeaud, S. Lebib, P. Roca i Cabarrocas, *Thin Solid Films* **427**, 241 (2003).

[8] Y. Poissant, P. Chatterjee, P. Roca i Cabarrocas, *J. Non-Cryst. Solids* **299-302**, 1173 (2002).

[9] A. V. Kharchenko, V. Suendo, P. Roca i Cabarrocas, *Thin Solid Films* **427**, 236 (2003).

[10] V. Suendo, A. V. Kharchenko, P. Roca i Cabarrocas, *Thin Solid Films* **451-452**, 259 (2004).

[11] J. Perrin, C. Böhm, R. Etemadi, A. Lloret, *Plasma Sources Sci. Technol.* **3**, 252 (1994).

[12] W. Luft, Y. S. Tsuo, *Hydrogenated Amorphous Silicon Alloy Deposition Processes*, Marcel Dekker, Inc., New York, 1993, pp. 124-144.

[13] T. Takagi, K. Takeuchi, Y. Nakagawa, Y. Watanabe, S. Nishida, *Vacuum* **51**, 751 (1998).

[14] R. Platz, S. Wagner, C. Hof, A. Shah, S. Wieder, B. Rech, J. Appl. Phys. 84, 3949 (1998).

[15] S. Hamma, P. Roca i Cabarrocas, *Solar Energy Mater. Solar Cells* **69**, 217 (2001).

[16] A. Bouchoule (Ed.), *Dusty Plasmas*, Wiley, New York, 1999.

[17] L. Boufendi, J. Gaudin, S. Huet, G. Viera, M. Dudemaine, *Appl. Phys. Lett.* **79**, 4301 (2001).

[18] J. Perrin, Y. Takeda, N. Hirano, Y. Takeuchi, A. Matsuda, *Surf. Sci.* **210**, 114 (1989).

[19] L. T. Canham, *Appl. Phys. Lett.* **57**, 1046 (1990).

[20] P. Ball, *Nature* **409**, 974 (2001).

[21] L. Canham, *Nature* **408**, 411 (2000).

[22] R. A. Street, J. C. Knights, D. K. Biegelsen, *Phys. Rev. B* **18**, 1880 (1978).

[23] D. J. Dustan, F. Boulitrop, *Phys. Rev. B* **30**, 5945 (1984).

[24] F. Boulitrop, D. J. Dustan, *Phys. Rev. B* **28**, 5923 (1983).

[25] L. R. Tessler, I. Solomon, *Phys. Rev. B* **52**, 10962 (1995).

[26] C. Tsang, R. A. Street, *Phys. Rev. B* **19**, 3027 (1979).

[27] G. Ledoux, O. Guillois, D. Porterat, C. Reynaud, F. Huisken, B. Kohn, V. Paillard, *Phys. Rev. B* **62**, 15942 (2000).

[28] L. Pavesi, L. Dal Negro, C. Mazzoleni, G. Franzo, F. Priolo, *Nature* **408**, 440 (2000).

[29] A. Polman, *Nature Materials* **1**, 10 (2002).

[30] W. Siebert, R. Carius, W. Fuhs, K. Jahn, *Phys. Stat. Sol.* (*b*) **140**, 311 (1987).

[31] C. Palsule, S. Gangopadhyay, D. Cronauer, B. Schröder, *Phys. Rev. B* **48**, 10804 (1993).

[32] D. Engemann, R. Fischer, J. Knecht, *Appl. Phys. Lett.* **32**, 567 (1978).

[33] S. V. Chernyshov, E. I. Terukov, V. A. Vassilyev, A. S. Volkov, *J. Non-Cryst. Solids* **134**, 218 (1991).

[34] V. A. Vasil'ev, A. S. Volkov, E. Musabekov, E. I. Terukov, V. E. Chelnokov, S. V. Chernyshov, Yu. M. Shernyakov, *Sov. Phys. Semicond.* **24**, 445 (1990).

[35] I. Solomon, M. P. Schmidt, H. Tran-Quoc, *Phys. Rev. B* **38**, 9895 (1988).

[36] I. Solomon, *Appl. Surf. Sci.* **184**, 3 (2001).

Chapter 4

Deposition of hydrogenated polymorphous silicon carbon alloys

4.1. Introduction

As explained at the end of the previous chapter, the deposition conditions of hydrogenated polymorphous silicon carbon alloys (*pm-$Si_{1-x}C_x$:H*) are derived from those used for hydrogenated polymorphous silicon (*pm-Si:H*), a bridge material between microcrystalline silicon (μ*c-Si:H*) and amorphous silicon (*a-Si:H*) [1]. Thus, *pm-$Si_{1-x}C_x$:H* has some characteristics that resemble those of *pm-Si:H*, particularly its microstructure, consisting of silicon nanocrystals/nanoclusters embedded in the amorphous matrix [2]. The idea behind the synthesis of *pm-$Si_{1-x}C_x$:H* is to enlarge the band gap of the matrix by introducing carbon atoms that form Si-C bonds, which facilitate a better confinement of the embedded nanocrystals and chemically provide a better surface passivation [3]. Moreover, the matrix becomes more transparent in the PL emission spectral range of silicon nanocrystals due to the widening of the gap, and thus reduces the absorption of emitted light. To produce *pm-$Si_{1-x}C_x$:H*, we added methane (CH_4) to the SiH_4-H_2 mixture. As a result, we can obtain films that contain silicon nanocrystals/nanoclusters embedded in the *a-$Si_{1-x}C_x$:H* matrix. Further, by varying the CH_4 concentration and the other deposition parameters, we were able to adjust the gap and the properties of the films, as shwon in the next sections of this chapter.

Fig. 4.1 shows the optical gap of *a-Si* (amorphous silicon) nanoclusters [4] and *nc-Si* (silicon nanocrystal) [5, 6] as a function of their size. The insets schematically show the change of the optical gap of nanocrystals with dot size in the case of *pm-Si:H* and *pm-$Si_{1-x}C_x$:H*. In the case of an *a-Si* nanocluster or quantum dot (QD), the relation between band gap energy E_g and dot size a is given by:

$$E_g \text{ (eV)} = E_0 + 2.40/a^2 \ (E_0 = 1.56) \qquad (4.1)$$

which is obtained by fitting the experimental data using effective mass theory [7]. Here, the value of E_0 is close to that of the gap of amorphous silicon (1.6-1.7 eV) [4]. In the case of *nc-Si*, the curves were obtained for two cases using the confinement model:

i) without crystalline lattice correction [5]:

$$E_g \text{ (eV)} = E_0 + 3.73/a^{1.39} \qquad (4.2)$$

and ii) with crystalline lattice correction due to the reducing size [6]:

$$E_g \text{ (eV)} = E_0 + 3.73/a^{1.39} + 0.881/a - 0.245 \qquad (4.3)$$

with E_0 = 1.17 eV for bulk *c-Si*. These curves show that the effect of quantum confinement on the gap widening of nanostructured silicon is very important. As shown by the hatched area in Fig. 4.1, the quantum confinement effect gives a blue shift to the gap of bulk crystalline silicon (*c-Si*) from around 1.17 eV to 1.5-2.8 eV depending on the size, while this effect on the *a-Si* QD is slightly less pronounced. As a consequence, the gap of nanocrystals can be slightly smaller or even larger than the gap of the *a-Si:H* matrix (1.6-1.7 eV), as shown schematically in the inset of Fig. 4.1. Thus, in order to have enough confinement effect of the carriers by the matrix, we should surround the nanocrystals with a higher gap material such as *a-*$Si_{1-x}C_x$*:H* (2.2-2.4 eV) as in the case of *pm-*$Si_{1-x}C_x$*:H*.

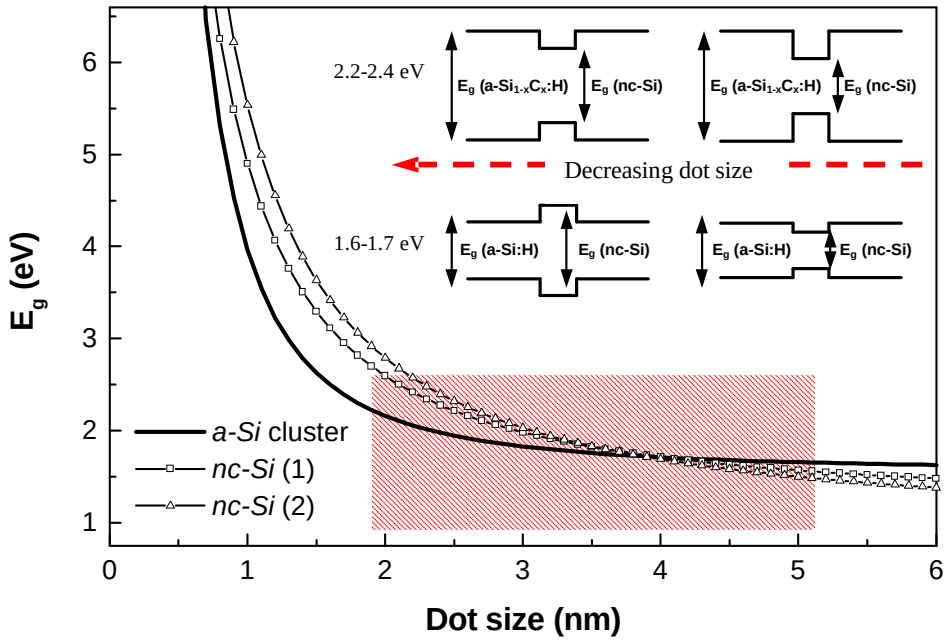

Fig. 4.1. Photoluminescence peak energy of nanostructured silicon as a function of the dot size. The thick line was obtained empirically by fitting experimental data using effective mass theory for a-Si QD (Ref. 4). The squares (1) and triangles (2) dotted lines were obtained using quantum confinement model without (Ref. 5) and with lattice correction (Ref. 6) respectively.

This approach, combining silicon nanocrystals and a wide band gap matrix (*a-*$Si_{1-x}C_x$*:H*) has given a first important result. Indeed by using *a-*$Si_{1-x}C_x$*:H* as matrix, we have been able to observe photoluminescence signal by naked eyes at room temperature as shown in chapter 1

(Fig. 1.1). Fig. 4.2. shows the PL spectrum for a *pm-Si$_{1-x}$C$_x$:H* film deposited at high pressure (3500 mTorr). This spectrum can be separated into several peaks, each one representing a group of nanocrystals according to its size and defect state [2]. For comparison, the PL spectrum of *pm-Si:H* deposited at 3000 mTorr is shown in the inset of Fig. 4.2. In both cases, the PL measurement setup and acquisition conditions are the same. Thus the PL intensity of both curves can be used as a semi-quantitative parameter to compare the luminescence efficiency. Therefore, by changing the matrix with a higher gap material, the efficiency of the radiative recombination process has increased enormously. Moreover, the appearance of multi peaks and the shift of the main peak towards high energy are interesting features of *pm-Si$_{1-x}$C$_x$:H* with respect to *pm-Si:H*.

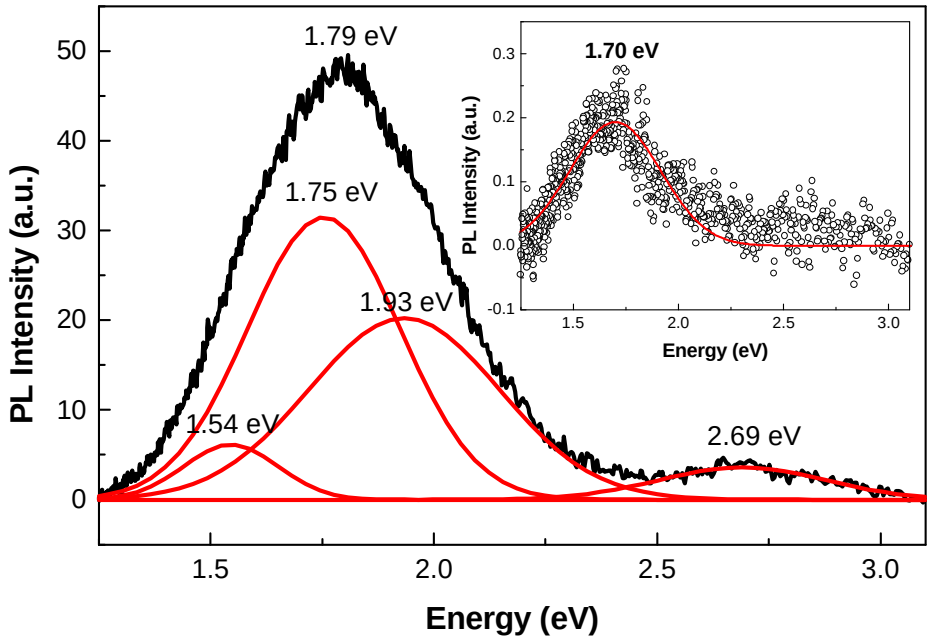

Fig. 4.2. The room temperature photoluminescence (PL) spectrum of *pm-Si$_{1-x}$C$_x$:H* deposited at 200 °C with total pressure of 3500 mTorr and an RF power of 0.21 W/cm^2. For the comparison, the room temperature PL spectrum of *pm-Si :H* deposited at 200 °C with total pressure of 3000 mTorr and an RF power of 0.21 W/cm^2 is shown in the inset. In both cases, HeCd laser line at 325 nm (3.8 eV) was used as the excitation source with power of 4 mW for an illumination area of 0.03 cm^2.

In the next sections, the deposition conditions of *pm-Si$_{1-x}$C$_x$:H* and their influence on film properties will be discussed in detail, along with the results of plasma studies and material characterizations. The material characterizations include the chemical analysis and the determination of film structure and morphology by various methods. The luminescence (PL and EL) properties will be discussed in the next chapter.

4.2. Deposition of hydrogenated polymorphous silicon carbon alloys

A common issue in the deposition of thin film materials (semiconductors, insulators, dielectrics, etc.) is to obtain deposition conditions with high deposition rate while maintaining the quality of the films [8]. This is not a simple task to accomplish considering the number of parameters (pressure, substrate temperature, RF power, …) that have to be taken into account to obtain such condition. The deposition rate is an important parameter for general case, while the film quality has to be defined with respect to a given application. In the case of

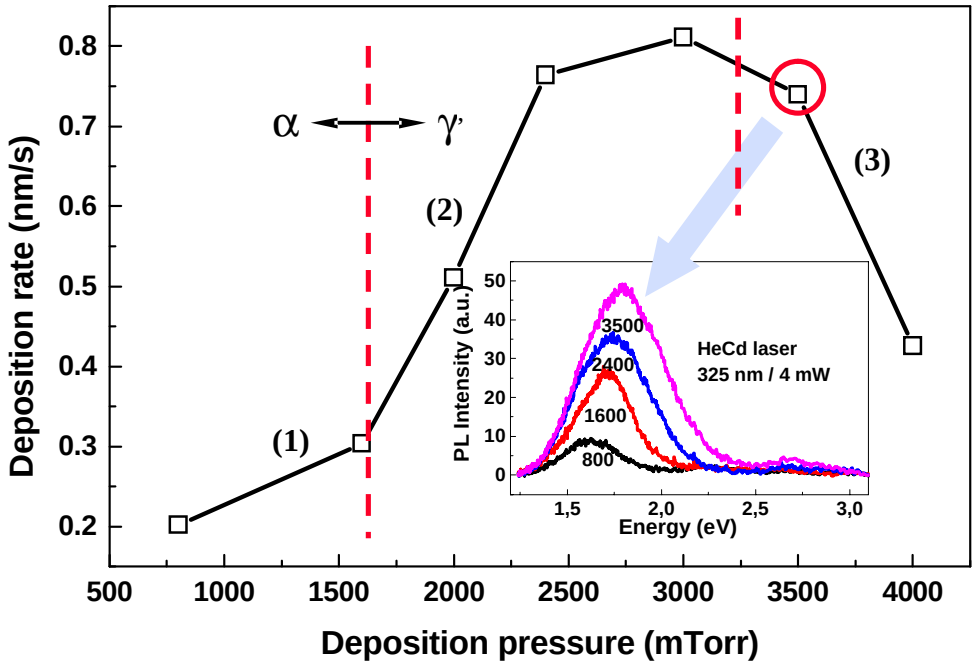

Fig. 4.3. A typical pressure dependence curve of the deposition rate for *pm-Si$_{1-x}$C$_x$:H* at 200 °C and RF power of 20 W (0.21 W/cm^2). The inset shows the effect of deposition pressure on the PL spectra of *pm-Si$_{1-x}$C$_x$:H* thin films deposited in the same conditions.

hydrogenated polymorphous silicon carbon alloys, the photoluminescence is the property of interest, and will be considered as the principal parameter to improve. In this study, *pm-Si$_{1-x}$C$_x$:H* is deposited from the decomposition of SiH_4-CH_4-H_2 mixtures using the standard RF glow discharge technique (PECVD). The parameters that we have varied to control the film properties are: deposition pressure (800-5000 mTorr), RF power (10-30 W (0.105-0.316 W/cm^2)), methane flow rate (0-40 sccm) and substrate temperature (100-300 °C), while the flow rate of silane and the total flow rate were kept constant at 10 and 133 sccm, respectively.

Fig. 4.3. shows a typical curve of deposition rate of *pm-$Si_{1-x}C_x$:H* as a function of the total pressure, which resembles to that of *pm-Si:H*, except for the microcrystalline regime, which is not observed even at low pressure (Fig. 3.1). We can distinguish three regimes in the deposition rate pressure dependence curves for both cases [2]. Each regime, corresponds to the incorporation of different film precursors: (1) nanocrystals formation regime ($P \leq 1600$ mTorr), (2) agglomeration regime ($1600 \leq P \leq 3000$ mTorr) and (3) powders formation regime ($P \geq 3000$ mTorr). In the nanocrystals formation regime (1), we deposit a film that consists of nanometer size silicon crystallites embedded in the *a-$Si_{1-x}C_x$:H* matrix. In the agglomeration regime (2), the increase of pressure leads the nanocrystals formed in the plasma to agglomerate and form a larger "blackberry" like structures, consisting of nanocrystals that stick to each other, and are covered with an amorphous shell, as deduced from darkfield images of TEM analysis. In the powder formation regime (3), the agglomeration process continues and leads to the formation of very large powders. They do not contribute to the deposition because they are negatively charged and remain confined in the plasma until they are pushed away to the outside of reactor by the pumping flow. This results in the saturation and then the decrease of the deposition rate.

In general, the formation of powders during deposition of amorphous silicon thin films can give unwanted results such as columnar growth, voids, and pin-holes in devices, as well as the deterioration in material properties (i.e.: higher light-induced degradation) [9]. However, in the case of *pm-$Si_{1-x}C_x$:H*, the high pressure deposition regime does not only favor high deposition rate, which is important for film fabrication, but also favors an increase of the PL intensity as shown in the inset of Fig. 4.3. Thus, by increasing the pressure, we can deposit material with strong PL intensity at high deposition rate. Moreover, considering the decrease of the mean free path of ions, high pressure conditions also reduce the effects of high energy ion bombardment, which is very important in the device fabrication regardless the effect of powders [10].

The pressure dependence of deposition rate for two values of the RF power is shown in Fig. 4.4. For both values of the RF power, the increase of pressure leads to the same pressure dependence of the deposition rate. However, the difference of deposition rate becomes more pronounced in the high pressure regime ($P > 3000$ mTorr). As explained in the previous chapter, the decrease of deposition rate in the high pressure regime is mainly due to the powder formation process. By increasing the RF power, one could expect that the formation of reactive species through the collisions with electrons in the plasma becomes more

important, thus the growth of particles should increase in this condition resulting on a more pronounced decrease of the deposition rate. However, we have to consider also other aspects of the increase of RF power which favor the neutralization of formed particles, as an example, photo-detachment can decrease the negative charge on the particles and favor their deposition.

Fig 4.5a shows the effect of the methane flow rate on the growth rate in the high pressure regime at high power (20W). The increase of methane flow rate results in a linear

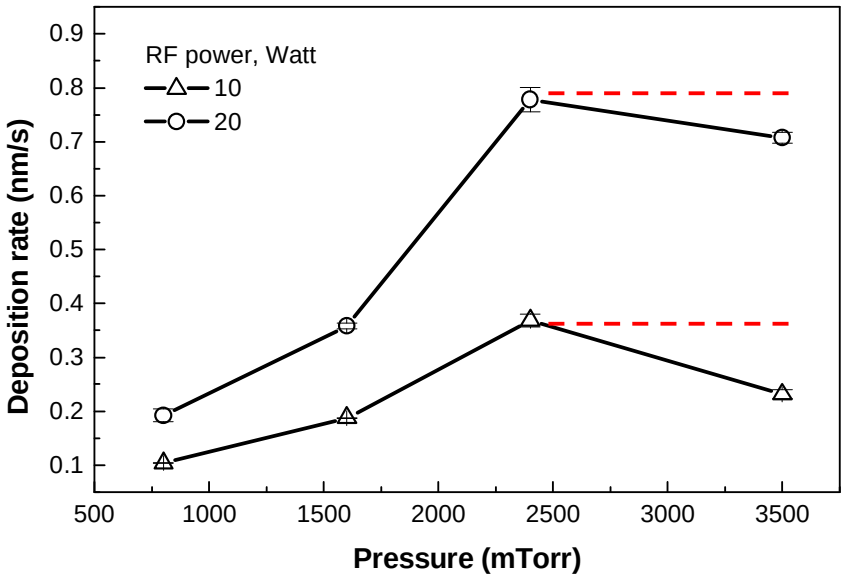

Fig. 4.4. Deposition rate as a function of total pressure for *pm-*$Si_{1-x}C_x$*:H* samples deposited at 200 °C with 10 (0.105) and 20 W (0.21 W/cm^2) of RF power (power density).

increase of the deposition rate, which means that the contribution of methane to deposition should be considered as a first order process [11]. It is well-known that methane is more difficult to dissociate than silane, which leads to a different mechanism of carbon incorporation between depositions carried out at low [12, 13] and high [14] RF power regimes. In the low RF power regime (i.e.: 0.06 W/cm^2), methane molecules are practically not dissociated, thus we can imagine that they act like a buffer gas and give contribution to deposition only through the reaction with the active species produced by the plasma decomposition of silane [12]. Thus, this condition leads to the deposition of device quality *a-*$Si_{1-x}C_x$*:H* films with a low density-of-states, where the incorporation of carbon, mostly in the form of methyl groups, is limited to less than 40 at. %. In this condition, the deposition rate, V_d, is roughly proportional to the concentration of silane [SiH_4] and to the density of electrons, N_e [12]:

$$V_d \approx N_e[SiH_4], \qquad (4.4)$$

This is quite different from our results shown in Fig. 4.5a. In this case, the deposition rate increases linearly with the methane flow rate. Thus the deposition rate kinetic equation may be written:

$$V_d \approx N_e[SiH_4]^n[CH_4], \qquad (4.5)$$

where n is the reaction order of silane which is not considered equal to unity due the participation of secondary reactions of silane to deposition. On the other hand, in the high RF power regime, one can obtain *a-*$Si_{1-x}C_x$*:H* films with any proportion of silicon and carbon

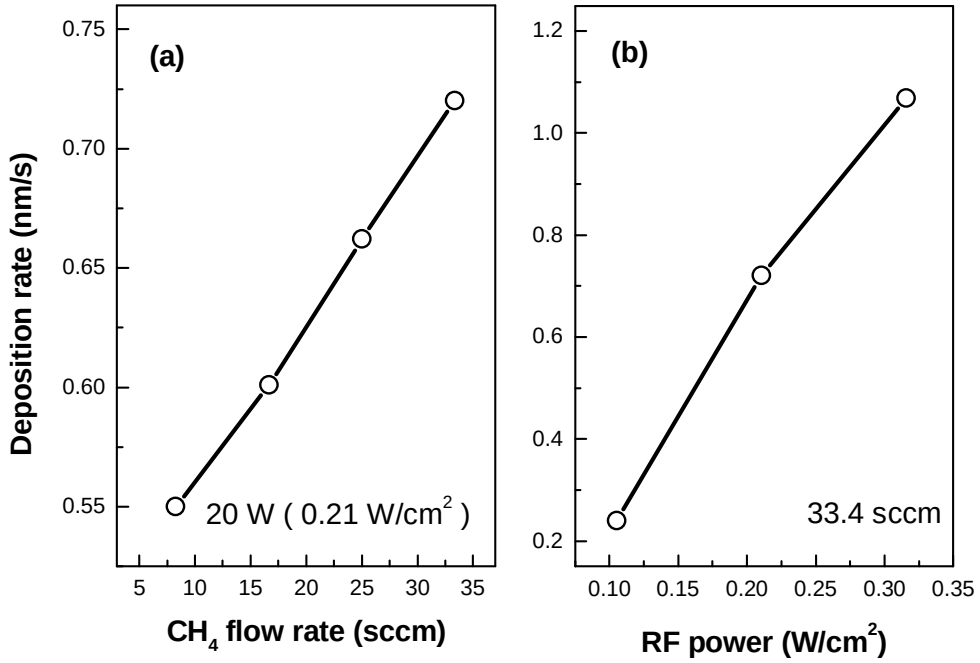

Fig. 4.5. The effects of methane flow rate (a) and RF power density (b) on the deposition rate of *pm-*$Si_{1-x}C_x$ *:H* for samples deposited at 3500 mTorr, 200 °C.

which depends on the deposition condition, and makes it difficult to control the properties of films [15]. Other problems also appear due to the presence of an important amount of carbon with sp^2 hybridization in films deposited at high RF power [13]. The formation of graphitic or carbon-carbon sp^2 bonds relaxes the films but makes it difficult to predict the band gap energy. However, as reported recently [14], device quality *a-*$Si_{1-x}C_x$*:H* films can be grown in the high RF power regime (50-300 W or 0.33-1.95 W/cm^2) and high pressure (1700 mTorr) and temperature (400°C). These conditions produce chemically ordered *a-*$Si_{1-x}C_x$*:H* films

where carbon content, band gap energy and room temperature PL peak position increase with the RF power.

In our case, for the deposition of *pm-$Si_{1-x}C_x$:H*, we have used a high power (but lower than that of ref. 14), in between low and high power regimes [12-14]. Moreover, we deposited our materials at much higher pressure, which preserves a mild deposition condition as previously explained. Let us recall that one of the important aspects to consider in the synthesis of thin film semiconductors is the possibility to use them in large area electronic, photonic or optoelectronic devices. In this case, we have to consider not only the quality of the materials but also the influence of the synthesis process on the device properties: deterioration of doped layers in case of p-i-n structure fabrication for example.

Further, if we look at the effect of RF power on the deposition rate in the pressure regime of interest (at 3500 mTorr) which gives the highest PL intensity (inset Fig. 4.3), we can see that the deposition rate increases linearly with RF power (see Fig. 4.5b). If we suppose a simple homogeneous capacitively coupled discharge system, where the total time-average power per unit area absorbed by the electrons depends linearly on the electron density or vice versa [16], then we can simply explain the RF power influence on the deposition rate using equation 4.5. In this case, the deposition rate will be determined by the electron density as one of the reactants in the simplified deposition chemical reaction with reaction order equal to unity. However, the actual situation is not as simple due the deposition in the α–γ' transition and powder formation regimes. Thus, we have to consider the contribution of RF power (or electron density) into deposition at least through two different ways: a) deposition of radicals or ions (surface reaction process) and b) formation and deposition of nanocluster/nanocrystals and their agglomerates (plasma reaction process).

Another aspect that will be discussed here is the effect of substrate temperature on the deposition rate of *pm-$Si_{1-x}C_x$:H*. It is well-known that the substrate temperature has a strong influence on the film properties. This can be explained by the annealing-like or cross linking processes, as observed in the deposition of amorphous silicon thin films [17] and in molecular dynamics simulation in the case of *a-SiC* thin film [18], as well as by the modification of surface reactivity [19-21]. In the case of amorphous silicon, the evidences of this effect are the increase of medium range order (MRO) [22], the decrease of hydrogen content [19, 20, 23] and of the band gap energy [23] with the increase of substrate temperature. During deposition, the increase of the substrate temperature favors the elimination of hydrogen and the surface diffusion of atomic hydrogen that induces the reconstruction of the amorphous network. Moreover, in the case of polymorphous silicon deposition, we also have to consider the gas

heating effect by electrodes regarding the high pressure and close distance between electrodes (approx. 2.5 cm).

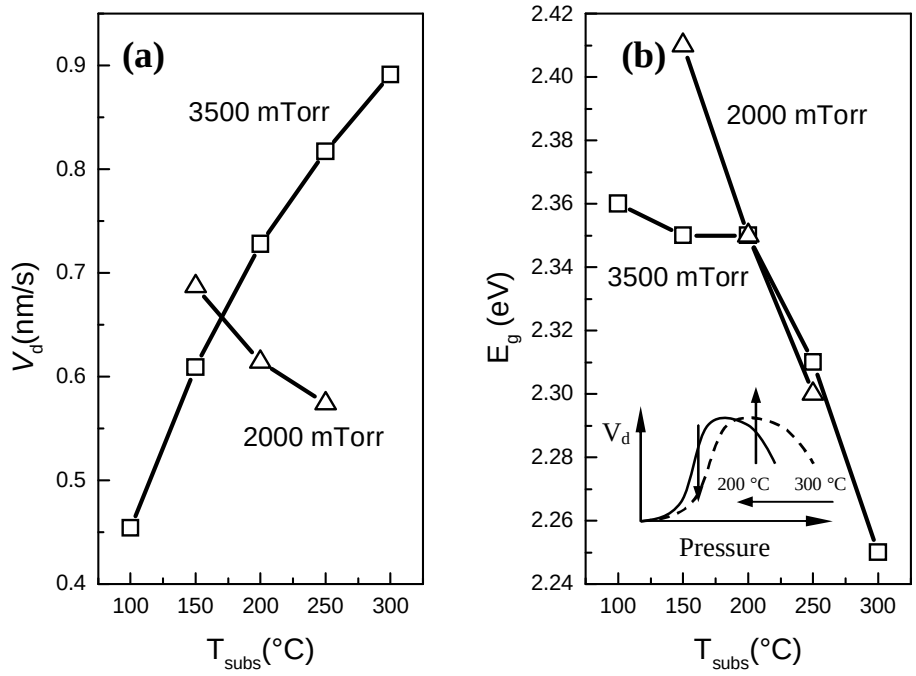

Fig. 4.6. Substrate temperature dependence of the deposition rate (a) and band gap energy (b) of *pm-Si$_{1-x}$C$_x$:H* samples deposited at 2000 (circles) and 3500 (squares) mTorr and 20 W of RF power. The inset shows the shift of the α–γ' transition towards high pressure with the increase of temperature.

Here, we note that the temperature of electrodes refers to the temperature of substrate, which is located on the grounded electrode due to the parallel heating of both electrodes. Fig. 4.6a shows the substrate temperature dependence of deposition rate for samples deposited at 2000 and 3500 mTorr with 20 W of RF power. The figure shows that the deposition rate decreases with substrate temperature for samples deposited at 2000 mTorr, while the opposite behavior was observed for samples at 3500 mTorr. Let us recall that these pressures corresponds to the agglomeration and powder formation regimes respectively, for deposition of *pm-Si$_{1-x}$C$_x$:H* at 200 °C (see Fig. 4.3). Moreover, as observed in silane-argon plasmas, the increase of gas temperature delays the phase of particle formation [24]. Thus, the opposite substrate temperature dependence of deposition rate can be explained by the shift of α–γ'transition due to different temperature influence on the plasma phase particle formation on two mentioned regimes (see the inset of Fig. 4.6b). Here, the presence of particles was confirmed by TEM studies for samples deposited in both regimes at 200 °C, where both

samples deposited on the cold finger and the heated substrate holder showed trapped particles and embedded clusters respectively. The temperature dependence of deposition rate shown here is found to be different with respect to surface reaction model for deposition such as in *a-Si:H* and *a-$Si_{1-x}C_x$:H* depositions, where the value of sticking coefficient of deposition precursors is relatively constant with temperature [23].

Now, if the increase of substrate temperature induces important changes in the gas phase by delaying the powder formation, it should also induce changes on the plasma electron density, which is detectable by the plasma electrical measurements. The detail of the effects of particle formation on the plasma electrical parameters will be discussed in section 4.3. The experimental results show that the increase of temperature from 150 to 250 °C at 2000 mTorr changes the values of V_{DC}/V_{PP} from -55 V/752 V to -65 V/808 V, which might indicate the increase of electron density by the increase of temperature. As the particle formation is delayed, the attachment of electrons to the particles is also reduced, which leads to the increase of the self bias and RF voltage. At 3500 mTorr, this effect cannot be detected easily due to the measurement in the saturation regime (see Fig 4.7). Therefore, the increase of substrate temperature from 100 to 250 °C gives almost no change in V_{DC}, while in V_{PP} only a slight increase (the values of V_{DC}/V_{PP} change from -20.7 V/552 V to -20.1 V/560 V).

Moreover, we suggest that the temperature induced rearrangement process of the films also plays role on deposition. Fig. 4.6b gives an evidence of the network rearrangement process, where the increase of deposition rate is accompanied by the decrease of the band gap energy due to the decrease of hydrogen content [23]. The modification of the band gap by Si-H bonds contribution is well explained by tetrahedron model and Bruggemann Effective Medium Theory (BEMA) for optical dielectric function of amorphous silicon [25]. Thus, the decrease of band gap energy is directly related to the network rearrangement, where the films contain less hydrogen and have a more compact structure. Another evidence of this rearrangement process is the increase of parameter *A* of Tauc's Lorentz model (see Ellipsometry section in Ch. 2) that is related to the increase of materials density as the substrate temperature increases. Fig. 4.6b shows a different temperature dependence of the Tauc's band gap E_g between samples deposited at 2000 and 3500 mTorr. The contrast is observed for temperatures lower than 200 °C, while for higher temperatures they show approximately the same behavior. If we correlate the decrease of E_g with the decrease of hydrogen content or to a thermally induced hydrogen desorption process, a different mechanism must be responsible for samples deposited at each pressure. The difference might be due to the difference in the plasma phase. Samples deposited at 2000 mTorr show a

decrease in E_g with a linear tendency, while samples deposited at 3500 mTorr show similar values for samples deposited below 200 °C, and the same tendency as 2000 mTorr samples for temperatures higher than 200 °C. We suggest that the constant value of E_g for samples deposited at 3500 mTorr is due to the presence of deposited particles in aggregate or agglomerate form.

We have given a short description of the deposition conditions of *pm-*$Si_{1-x}C_x$*:H* films related to their properties and deposition rate. In order to have a better understanding about this deposition system, further studies are necessary. Especially, a study by a direct method that is able to provide information about active species (radicals, ions, nanocrystals/clusters and their agglomerates) that contribute to the deposition.

4.3. Monitoring particle growth by the evolution of plasma electrical parameters

Historically, active research on particle formation in low pressure glow discharges was triggered by the concern of particles contamination in industrial plasma reactors used for material processing such as deposition and etching processes [26-29]. The formation of powder in the plasma produces significant changes in plasma parameters such as the electron density, the electron temperature and the plasma composition, which leads to the changes of electrical observable parameters such as the impedance of the discharge, the self-bias voltage on the powered electrode [26, 27] and peak-to-peak RF voltage. Therefore, we can use these parameters to monitor the growth of particles in the plasma. Plasma or discharge impedance analysis is a very sensitive and well developed method to monitor the presence of nanometer size particles in the plasma [24]. Each step of the powder formation process is observed by monitoring the evolution on the discharge impedance, admittance, current, voltage, phase change and their harmonics as a function of time. The third harmonic of the RF current (J_3) is the most widely used to study the powder formation in RF plasma (see Ch. 2.). At the beginning (t=0), we can observe a sharp increase followed by a characteristic transient which depends on the plasma conditions before reaching steady-state. The steady-state value of J_3 is proposed to represent the equilibrium condition of the observed system, which is responsible for the properties of deposited materials. Therefore, in most cases, the steady-state value of J_3 becomes a parameter to compare one deposition condition with another. Moreover, further studies about this subject lead us to the conclusion that this method can be replaced by monitoring the steady-state value of the self-bias potential (V_{DC}), which shows similar trends as J_3 [30]. Thus, for the daily monitoring of the plasma reactor for industrial purposes, this

method is a good alternative with several strong points such as: high sensitivity, relatively cheap, and easy installation and data treatment.

Fig. 4.7. shows the evolution of the steady-state values of the peak-to-peak RF potential (V_{PP}) and of the self bias potential (V_{DC}) with the increase of total pressure for different values of the RF power. We observe the same tendency independent of the RF power, where V_{PP} decreases and V_{DC} increases with pressure. They begin with smooth changes, followed by a saturation in the high pressure regime. In the case of V_{PP}, the increase of RF power shifts up the curve monotonically without changing its shape. In other words, there is no transition regime shift due to the increase of the RF power, except for 30 W as shown by the constant values at low pressure (Fig. 4.7a.). On the other hand, the evolution of V_{DC} follows the same trend as a function of pressure for three values of RF power. Fig. 4.7b. shows clearly that the effect of RF power is more significant in the low pressure regime up to transition regime.

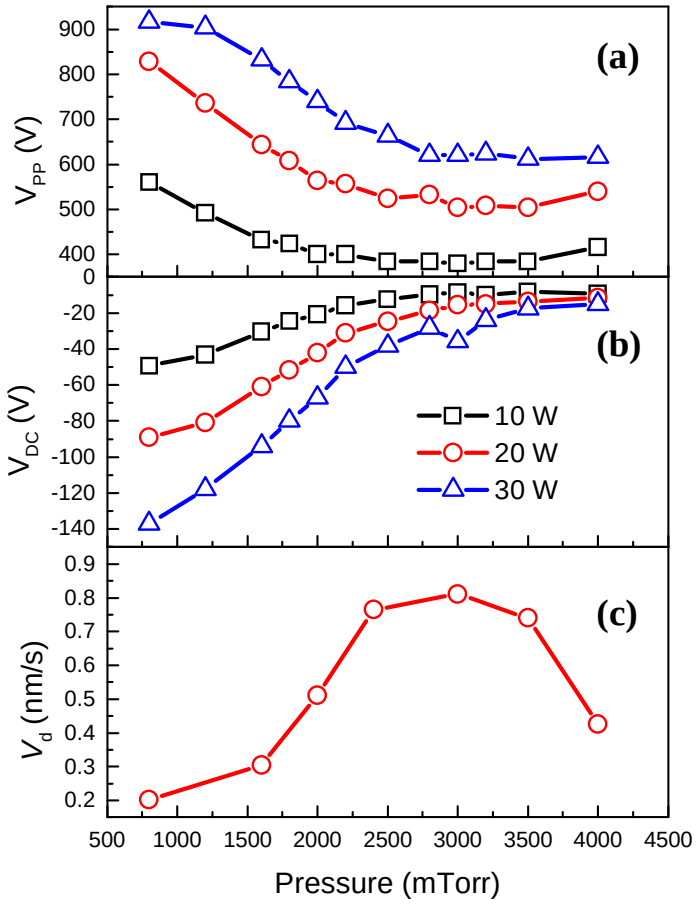

Fig. 4.7. Pressure dependence of peak-to-peak RF voltage (V_{PP}) (a) and DC self-bias (V_{DC}) (b) in SiH_4-CH_4-H_2 plasmas used for *pm-*$Si_{1-x}C_x$*:H* deposition, measured at different values of the RF power. Pressure dependence of deposition rate for samples deposited at 20 W is shown as well for comparison (c).

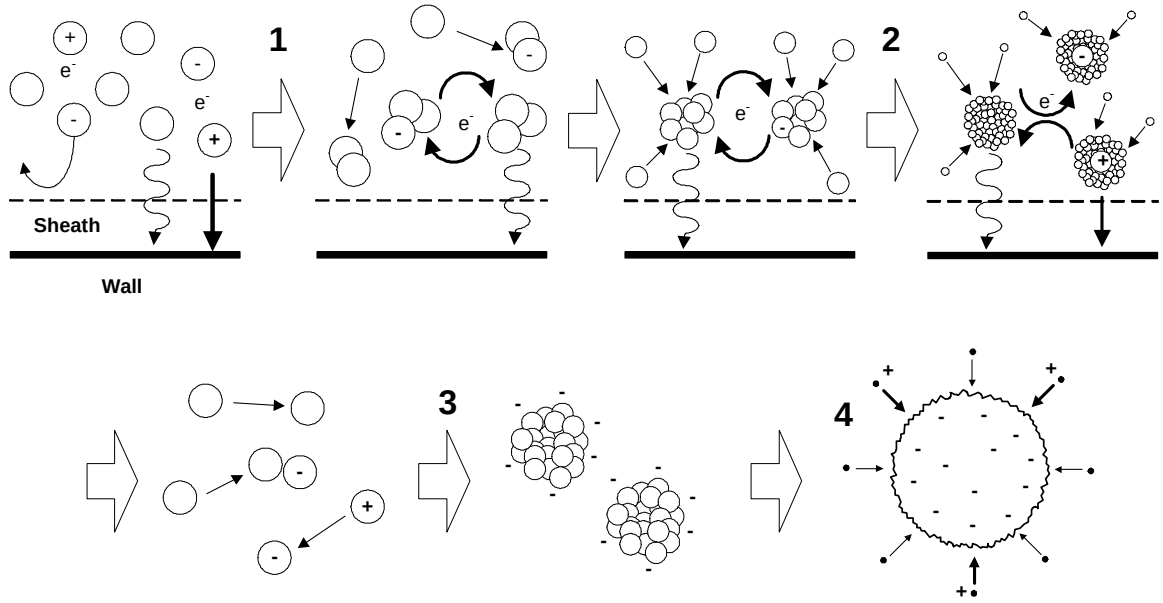

Fig. 4.8. Schematic illustration of particles growth from atomic level to macroscopic particle. It consists of four following steps : 1)Formation of primary clusters, 2)Nucleation and cluster growth, 3)Coagulation and 4)independent growth of trapped multiple charged macroscopic particles by radicals [31].

Before going further into the discussion of our results, let us consider the process of particles growth in silane plasmas. After Perrin [31], the growth of particles can be described schematically by four steps: 1) formation of primary clusters, 2) nucleation and cluster growth, 3) coagulation and 4) growth of trapped multiple charged macroscopic particles (see Fig. 4.8). This scenario begins with the formation of primary clusters of atoms up to a critical size where the nucleation takes place, followed by the growth of small particles by avalanche condensation (r_p < 5 nm), then continued by the agglomeration or coagulation into macroscopic particles (r_p < 50 nm), and finally their growth as isolated multiple charged particles by condensation. During the growth and nucleation stage or before coagulation stage, the particles are either neutral or singly charged and undergo charge fluctuations. After coagulation, the particles bear a multiple negative charge and remain trapped in the plasma. The particles become negatively charged after coagulation due to the electron attachment explained by the increase of electron capture cross section with particle size [31]. Moreover, the presence of particles will increase the resistive part of the impedance through the modification of the electron collision frequency [24]. Thus, the increase (or decrease of the absolute value) of V_{DC} can be explained by the decrease of the electron flux to the electrodes due to the attachment of electrons on the particles and to the electron-particle collisions.

As we discussed previously, the important indication of the deposition condition for polymorphous silicon is the α–γ' transition, which can be observed simply by plotting the deposition rate as a function of deposition pressure [8]. If we look back to Fig. 4.7 and compare the pressure dependence of V_{DC} to that of the deposition rate, we can observe a transition when the deposition rate increase steeply, before it reaches a saturation, which corresponds to the α–γ' transition. When the value of V_{DC} increases, it corresponds to the beginning of nanocrystals/clusters formation regime or primary cluster formation regime in Perrin's model. In this regime, the presence of particles (nanocrystals/clusters) starts to disturb the flux of electrons that arrive to the electrode surface through electron-particle collisions. Then, deposition will enter the agglomeration regime, which consists of the nucleation and cluster growth, then followed by the coagulation process. In this regime, the particles start to stick together and form bigger particles with large surface area due to the agglomeration of many small particles.

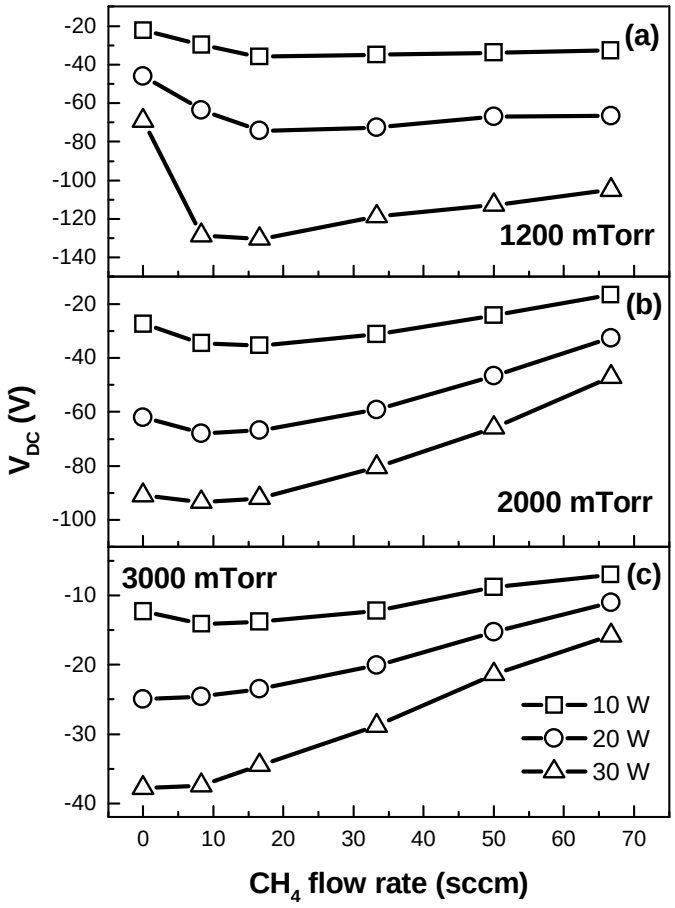

Fig. 4.9. Effect of methane flow rate on the steady-state values of V_{DC} in SiH_4-CH_4-H_2 plasmas, measured at 1200 (a), 2000 (b) and 3000 mTorr of total pressure and 200 °C for 10, 20 and 30 W of RF power.

The presence of agglomerates disturbs the plasma more than the nanoparticles. As the particle diameter increases, the probability to have collisions between particles and electrons increases, or in other words the particle-electron collision cross section increases. Moreover, small (2-10 nm) particles undergo charge fluctuations due to electron attachment. In this situation, the particles are either neutral or single charged. It explains why we observe a smooth increase in V_{DC} as the pressure increases. Later on the particles continue to grow and become multiple negatively charged, which corresponds to the maximum in the deposition rate or the beginning of saturation in V_{DC} curves. These particles are trapped in the plasma due to the sheath potential and continue to grow. Finally, when the particles become too large to be held by the sheath potential (powder formation), they start to be flushed away by the pumping, and drift outside the reactor, and do not contribute anymore to deposition. Thus, we observe an important decrease on deposition rate at higher pressure (Fig. 4.7c). In V_{DC}

evolution curves, this transition is difficult to observe, we only can see that the value of V_{DC} reaches a saturation value close to zero. It is well-known that if we go further until the powder regime, the plasma can go off for a few moments due to the electron attachment where there is not enough current to maintain the discharge. The evidence of large particle formation (powder) was confirmed by the deposition of samples at 4500 mTorr or above, where we obtained opaque films which indicate a very rough surface due to the deposition or sticking of powders during deposition. In this case, the surface roughness is beyond the roughness level that can be analyzed using UV-Visible spectroscopic ellipsometry.

The methane flow rate dependence of V_{DC} for three different pressure regimes and RF powers is shown in Fig. 4.9. Each pressure corresponds to a specific regime as we mentioned before in Fig. 4.3. In all conditions, the methane flow rate dependence of V_{DC} shows a similar tendency, where the addition of a small amount of methane into the reactive plasma decreases the value of V_{DC}. However, increasing the methane flow rate decreases the absolute value of V_{DC}. This indicates that the addition of methane inhibits the powder formation process at small quantity, but favors it at high flow rate. In general, this phenomenon explains the growth mechanism of particles in the plasma, which corresponds as well to the surface reaction on the substrate but with some restrictions mainly due to the particle size (i.e. deposition rate increases with methane flow rate). In general, the absolute value of V_{DC} has a tendency to decrease with the presence of particles and/or powders in the plasma due to the interaction between particles and electrons as explained above. However, in the case of SiH_4-CH_4-H_2 plasmas, we have to take into account that the physico-chemical properties of the two gases and the deposited films are different. It is well-known that methane is harder to dissociate and that *a-C:H* films present the hydrogen terminated surface with stronger bonds (C-H) compared to silicon (Si-H). The strength between these two types of bonds (C-H and Si-H) also varies with the size of clusters, where it can be seen from the activation energy of hydrogen elimination reaction for each type of cluster that varies with cluster size in different manner. The activation energy decreases with the increase of size in the case of silicon clusters, while it shows the opposite behavior for carbon clusters [21]. Moreover, from atomic point of view, carbon has a higher electron affinity (-123.4 kJ/mol) and first ionization energy (1086.4 kJ/mol) compared to silicon (electron affinity: -135.0 kJ/mol, first ionization energy: 786.4 kJ/mol), which are responsible for its lower reactivity [32].

In Fig. 4.9, we can observe that the increase of V_{DC} in absolute value by the addition of a small amount of methane is more pronounced in the low pressure regime (1200 mTorr), in particular at high RF power (30 W). Moreover, we notice that the minimum is shifted to lower

methane flow rate by the increase of RF power. In general, the presence of methane in the plasma will induce the surface deactivation of small clusters in the system due to their coverage by C-H bonds, which leads to the suppression of particle growth. As the particles cannot grow up too large, the main influence on the plasma electrical parameters is only due to the electron-particle collision. Furthermore, regarding the difference of electron affinity and ionization potential between silicon and carbon atoms, we can imagine that the presence of a small amount of carbon on the cluster surface can make the cluster to become less reactive to interact with electrons. In this case, we propose that the change on the surface state of clusters due to presence of carbon atoms reduces the electron attachment, even though they can reach a critical size to facilitate this process. Thus, these lead to a smaller influence of particles on the plasma electrical parameters. As a comparison, in the condition without methane, the silicon clusters can grow up to a certain size without any suppression and reach a larger average cluster size than with the presence of small amount of methane. Thus, the particles can grow up to the size which is enough to facilitate the electron attachment process.

On the other hand, a further increase of methane flow rate can promote the formation of new particle seeds due to the partial surface deactivation by carbon termination. We can imagine this process by comparing the activation energy of hydrogen elimination reaction between carbon and silicon clusters necessarily for the growth, where the formation of new silicon seeds should be more preferable than to continue the growth on carbon contaminated silicon clusters. We assume that silicon clusters are always formed first, which is deduced from the higher silane reactivity [33] and the lower activation energy for the hydrogen abstraction reaction [21]. The formation of more particle seeds in the plasma results in the increase of total number of particles with smaller size in the steady state system. We consider that in the low pressure regime the influence of particles on V_{DC} is mainly because of the electron-particle collision process due to their small size. Thus, it will reduce the absolute value of V_{DC} only by increasing the electron-particle collision frequency. As the RF power increases, each reaction process will become faster due to the higher electron flux. A severe competition occurs between the suppression of particles growth accompanied with the changes on the particles surfaces by carbon termination that increases the absolute value of V_{DC} and the formation of new particle seeds that decreases it. This could be the reason for the shift of V_{DC} minimum with the RF power as shown in Fig. 4.9a.

Furthermore, in order to analyze the effect of methane flow rate at higher pressure, we have to consider the difference on the structure of particles formed at low and high pressure regimes. At low pressure, the particles are formed as single units, while at high pressure those

particles start to agglomerate and form large particles, which favor electron attachment. Thus, the value of V_{DC} in the presence of particles will be determined by two factors: a) electron-particle collision and b) the electron attachment process. Based on the assumption of a steady-state condition with a constant gas flow, the number of particles should increase with pressure due to the decrease of gas mean-free-path (favoring the formation of new seeds), while their average size should decrease. As the particles start to agglomerate, their number decreases but their size increases. The increase of their size increases the cross-section of collision with electrons and allows electrons to attach on their large surface. Thus, the particles will interact in two ways in this regime resulting in a more pronounced decrease of the absolute value of V_{DC}, where the presence of methane only gives a small increase of V_{DC} absolute value in small quantity (Fig 4.9b) or even gives no suppression effect at all for high pressure and RF power condition (Fig 4.9c). The addition of more methane in the reactive plasma decreases the absolute value of V_{DC}. This can be explained by inducing the agglomeration of less reactive particles that form a chain-like structure as will be shown later (Fig. 4.19). In such structure, the open surface on the agglomerates that can interact with electrons will increase with respect to the agglomerates with a globular structure as observed in *pm-Si:H* deposition (see Fig. 3.1). Moreover, the increase of RF power favors a faster formation of new particles, which results in a further decrease of V_{DC} absolute value.

4.4. Study of reactive species by optical emission spectroscopy

The study of reactive species in the plasma is necessary for its control and reproducibility. We can analyze the presence of reactive species simply by observing their emission using optical emission spectroscopy (OES). Even though the emissive species do not always correspond to the reactive species of interest, the deposition precursors in our case, the information obtained from this technique is still very important to study the plasma during deposition (*in-situ*) due to its non-perturbative characteristic.

In the *pm-*$Si_{1-x}C_x$*:H* deposition system, we will discuss three emission lines, which represent emissive species form each gas: a) SiH^* ($A^2\Delta \rightarrow X^2\Pi$) system at 414.2 nm, b) CH^* ($A^2\Delta \rightarrow X^2\Pi$) system at 431.5 nm and c) the Balmer atomic hydrogen emission line H_α at 656.2 nm [34-36]. Furthermore, the Fulcher molecular hydrogen emission band α ($d^3\Pi_u \rightarrow a^3\Sigma_g$) [34, 36, 37], which consists of many lines dispersed between 570-640 nm, will also be discussed as complementary information to the plasma assisted deposition and

powder formation processes. A typical optical emission spectrum is shown in Fig 4.10 for a plasma with an RF power of 0.21 W/cm^2 at 1600 mTorr. The emissive species, SiH* and CH* excited radicals, are the direct result from the dissociative excitation by electron collision processes with SiH_4 and CH_4 molecules [35]. Thus, we can correlate their intensity to the relative concentration of dissociated species, including the deposition precursors such as SiH_3 and CH_3 radicals.

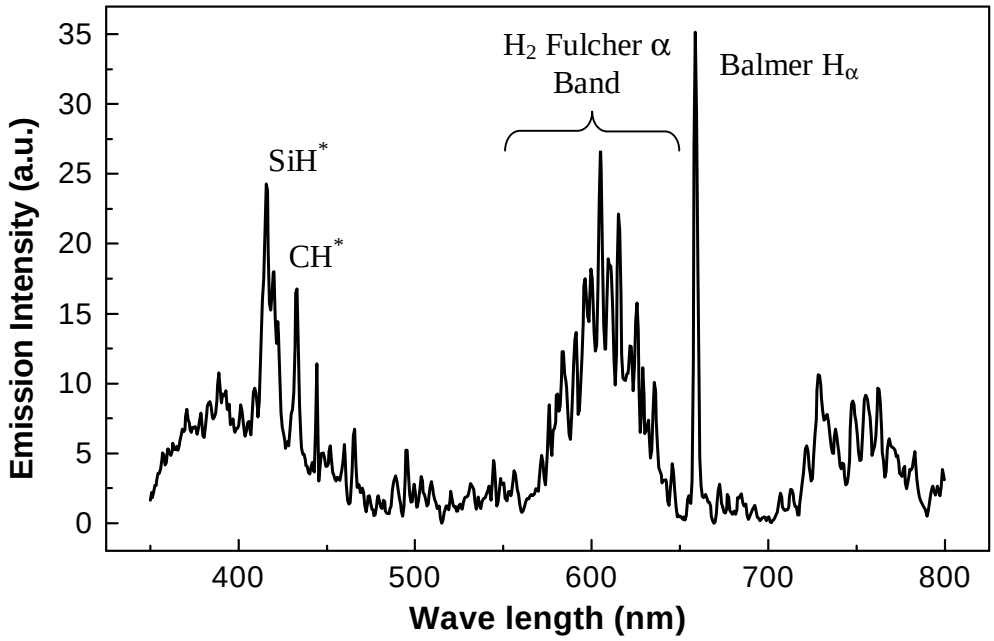

Fig. 4.10. Optical emission spectrum from a SiH_4-CH_4-H_2 glow discharge with an RF power of 0.21 W/cm^2 at 1600 mTorr. Both electrodes were heated at 200 °C.

Fig. 4.11 shows the effect of RF power on the optical emission spectrum for different total gas pressures: a) 800, b) 2000 and c) 3000 mTorr, which represent the three pressure regimes previously discussed. In the low pressure regime (800 mTorr), the emission spectra show no difference in their shape or intensity with the increase of RF power (Fig 4.11a). However, a careful analysis shows that the SiH*/CH* intensity ratio decreases from 1.25 to 0.97 with the increase of RF power from 10 (0.105) to 30 W (0.32 W/cm^2). This indicates an increase of dissociated methane species in the plasma, which is not observed at higher pressure regimes, for which the intensity of SiH* peak is always higher than that of CH*. In particular, at 3000 mTorr, SiH* becomes dominant with respect to CH* (see Fig.4.11c). The most characteristic feature shown in Fig. 4.11 is that the intensity of Fulcher molecular hydrogen band increases compared to the intensity of Balmer atomic hydrogen emission line (H_α) with the increase of

RF power at high pressure regimes. Moreover, if we compare the spectra from this three pressure regimes, it is obvious that the Fulcher band shows a unique characteristic or "finger print" that strongly depends on pressure. In addition, at 3000 mTorr, it is accompanied by a continuum band (350-470 nm) that corresponds to the emission from molecular hydrogen ($2s^3\Sigma \rightarrow 2p^3\Sigma$) [34].

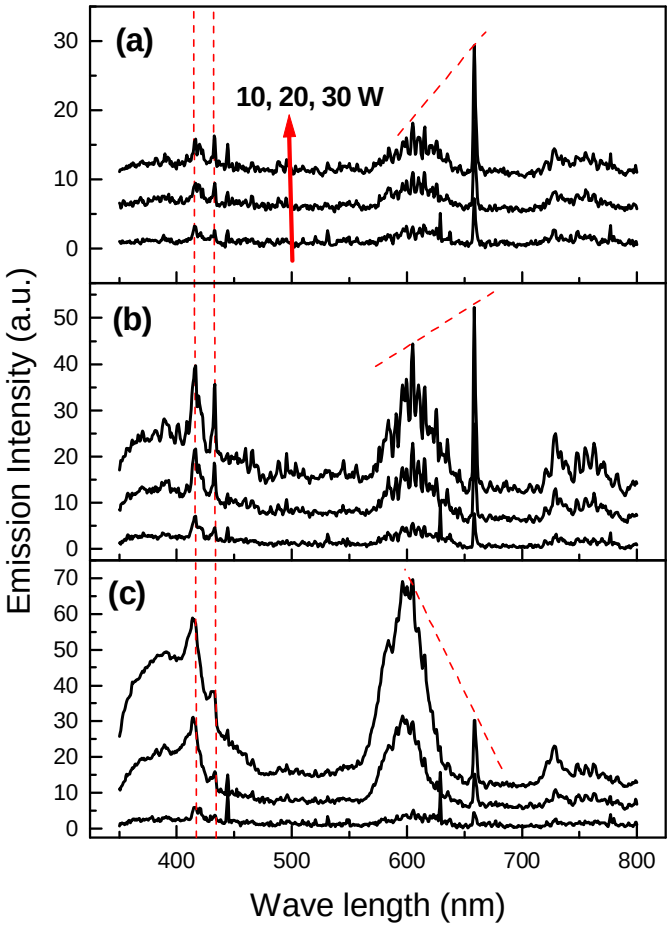

Fig. 4.11. Optical emission spectra of SiH_4-CH_4-H_2 glow discharge system at various total gas pressure: a) 800, b) 2000 and c) 3000 mTorr with RF power of 10, 20 and 30 W and gas flow rate : 10, 33 and 90 sccm for SiH_4, CH_4 and H_2 respectively.

Further, in order to analyze the effect of pressure on the deposition of *pm-*$Si_{1-x}C_x$*:H*, the emission intensities of SiH*, CH* and Balmer H_α were analyzed as a function of pressure. Fig. 4.12 shows the results of this analysis. We obtain a similar tendency regardless of the species and RF power, where their intensity tends to decrease with pressure except between 800 and 1200 mTorr where an abrupt increase was observed. This abrupt increase is suggested to be related to the transition from the plasma without particles to the nanocrystals formation regime. Moreover, the increase of RF power results in an increase of the emission

intensity for all species, which can be explained by the increase of interaction between gas molecules and electrons through collision process due to higher electron density. The decrease of emission intensity of all species with the increase of pressure may be due to the decrease the electron temperature, related to the decrease of mean-free-path. However, the emission from SiH* and CH* also shows a local maximum between 2000 and 3500 mTorr, which is not observed for H_α emission or in particle free plasma such as in pure hydrogen. Further information on the plasma characteristics can be obtained by calculating the ratio between the emission intensity of excited radicals and H_α ($I_{SiH^*}/I_{H\alpha}$ and $I_{CH^*}/I_{H\alpha}$). The evolution of each ratio indicates the changes on the average plasma chemical composition during deposition, which should correlate with the material properties as proposed to be highly dependent on pressure for polymorphous silicon based materials [8]. Particularly, the ratio between the intensity of SiH* and CH* (I_{SiH^*}/I_{CH^*}) that has been used in *a-$Si_{1-x}C_x$:H* deposition to monitor the silicon-carbon ratio in the plasma and correlate it with the film composition [35].

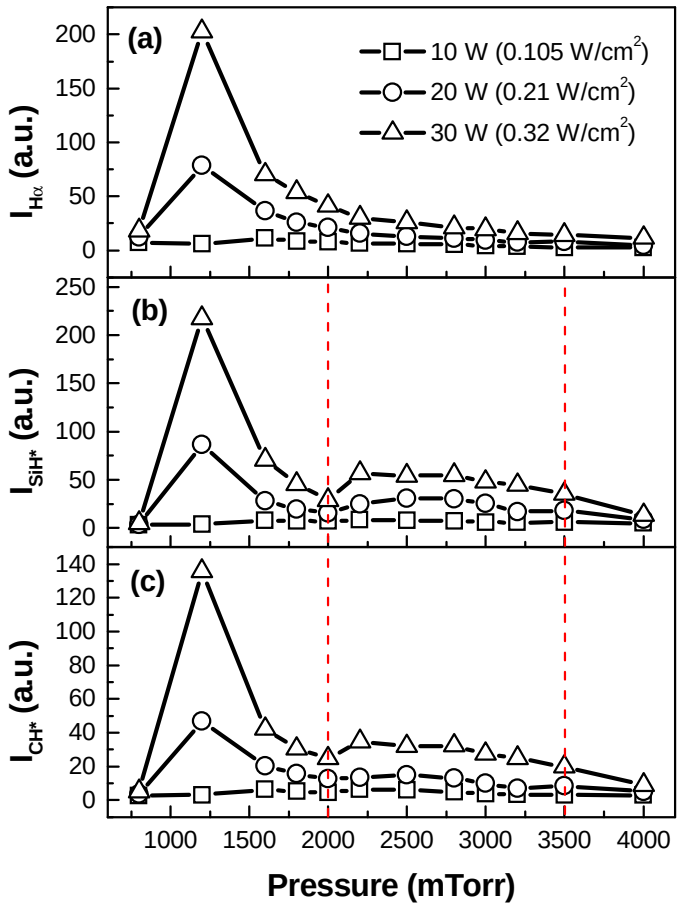

Fig. 4.12. The evolution of emission intensity of a) Balmer H_α atomic hydrogen line, b) SiH* radical, c) CH* radical with the increase of pressure at various RF power of 10, 20 and 30 W. Error bars are of the same order as the size of the symbols.

Fig. 4.13a-b shows three steps transition on the excited radicals/H_α ratios, the first transition is located around 1000 mTorr, while the second and the third ones are located around 2000 and 3500 mTorr, respectively. At 10 W, the transition is less pronounced, especially for $I_{SiH^*}/I_{H\alpha}$ one, where it increases linearly with pressure. It can be related to a lower particle formation or agglomeration at low RF power as observed by the less abrupt transition in the pressure dependence of deposition rate (Fig. 4.4). The first transition is suggested to correspond to the transition between free-particle plasma to the nanocrystal formation regime as described by the first stage of particle formation in Perrin's model (see Fig. 4.8). Here, the increase of emission intensity might be due to the increase of electron temperature by the presence of particles. Further increase of pressure, will decrease the size of particles that reduce the process cross-section for the electron-particle interactions, and as a consequence reduce their effect on the excitation process for radiative transitions indicated by the decrease of the ratio until it reaches a local minimum at 2000 mTorr. As mentioned before, the intensity of excited radicals is the indication of the presence of the precursors in the system. This assumption is based on the consideration that the energy needed for the formation of the emissive species from the collision between gas molecules and electrons is higher than for the formation of precursors. For example, it needs an electron with energy more than 10.33 eV to dissociate a SiH_4 molecule and form a SiH* excited radical, while for the formation of a SiH_3 radical we need only 8.75 eV [38]. At 2000 mTorr, we observe a drastic increase in the emission intensity ratios followed by a maximum at 3000 mTorr for RF powers of 20 and 30 W. We attribute the drastic increase around 2000 mTorr to the onset of agglomeration, while further increase of pressure leads to another transition at ~3500 mTorr due to powder formation located. The third transition is signified by the decrease in intensity ratio, in particular at 30 W of RF power.

Let us look more in detail Fig. 4.13a. The evolution of $I_{SiH^*}/I_{H\alpha}$ at 20 and 30 W has a similar behavior, while at 10 W we observe a linear increase with pressure. Thus, at 10 W the increase of pressure does not change drastically the dissociation of silane which leads to the formation of emissive species. It might indicate that the perturbation by plasma formed particles is small. Notice that the local minimum of the emission intensity at 1200 mTorr is not observable. At 20 and 30 W, the perturbation by the plasma formed particles becomes more important. On the other hand, the evolution of $I_{CH^*}/I_{H\alpha}$ in Fig 4.13b shows a clear transition at 2000 mTorr. At 10 and 20 W, they show a steep increase then followed by a plateau, without any decrease at 3500 mTorr, while at 30 W is followed by a maximum before

a drastic drop around 3500 mTorr. The contrast between $I_{CH*}/I_{H\alpha}$ and $I_{SiH*}/I_{H\alpha}$ evolutions could be due to the different reactivity between methane and silane, where it is well-known that methane is less reactive than silane and thus requires higher electron temperature for dissociation. The transitions at 10 W can be observed easier in the case of $I_{CH*}/I_{H\alpha}$. This might be due to the same reason as the presence of particles can aid the dissociation process by the increasing of electron temperature [39]. A pressure that corresponds to a certain particle density is needed to have high enough electron temperature to dissociate methane. Fig. 4.13c shows the evolution of I_{SiH*}/I_{CH*} ratio as a function of pressure for 10, 20 and 30 W of RF power. In this figure, we see that the I_{SiH*}/I_{CH*} ratio for 10 W plasma shows no important changes, while 20 and 30 W plasmas show a maximum between 1000 and 2000 mTorr. At 20 W, we can observe another maximum around 3000 mTorr, while at 30 W a plateau is observed for pressures higher than 2000 mTorr.

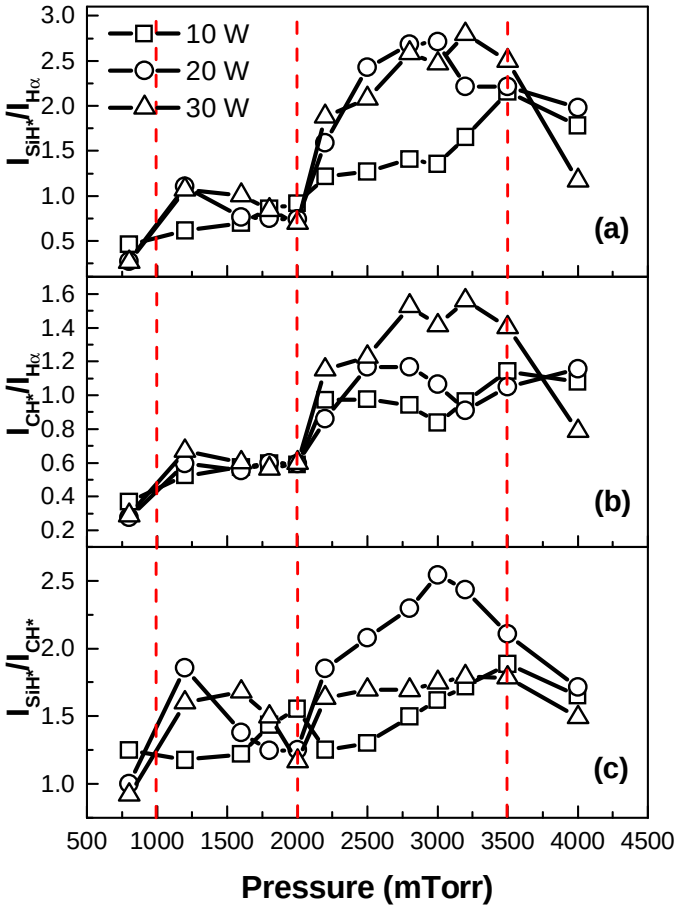

Fig. 4.13. The evolution of emission intensity ratios between the excited species in the SiH_4-CH_4-H_2 glow discharge system as a function of total pressure at various RF powers.

Another clear signature for the transition in plasma processes is the drastic change in the full-width at half maximum (FWHM) value of Balmer H_α line with the increase of pressure. Fig. 4.14 shows the evolution of FWHM of H_α emission line as a function of pressure for various values of the RF power. A sharp transition appears at 2000 mTorr, as observed for the intensity ratio in Fig. 4.13. The width of the emission line might correspond to the Doppler widening determined by the gas temperature [40, 41] and other broadening mechanisms, such as ion bombardment to the electrode surface, electron impact dissociation processes [41], and interruption by collision [42]. Among them, the interruption by collision is usually the most important factor at high pressure for the visible spectral range [42], such the observation of Balmer H_α emission line in the *pm-*$Si_{1-x}C_x$*:H* deposition condition.

The evolution of FWHM shown in Fig. 4.14 follows the same trend regardless of the RF power, which is in good agreement with the deposition rate pressure dependence as shown in Fig. 4.4, where the position of transition does not change significantly with the increase of RF power. Fig. 4.14 shows a local maximum around 1200 mTorr, followed by an abrupt increase between 2000 and 2200 mTorr and finally a decrease for higher pressures. Surprisingly, the most abrupt increase in transition around 2000 mTorr and the steepest decrease is presented by the 10 W plasma. In the case of 20 W plasma, we observe a fairly constant value of FWHM after the abrupt increase at around 2000 mTorr. In order to analyze the pressure effect on the evolution of FWHM, first let us neglect the Doppler broadening by the gas temperature. Here, we consider the gas temperature determined by the electrodes heating and gas flow, considering the high working pressure and the small electrode distance (2.5 cm). Thus, with the increase of pressure, the FWHM should change through the collision processes, which may form hydrogen excited species with larger energy distribution due to the inelastic collisions. Let us recall the deposition condition of polymorphous silicon where the particles are formed in plasma phase and evolve in both size and structure with pressure. Thus, the collisions with particles most likely occur in the plasma.

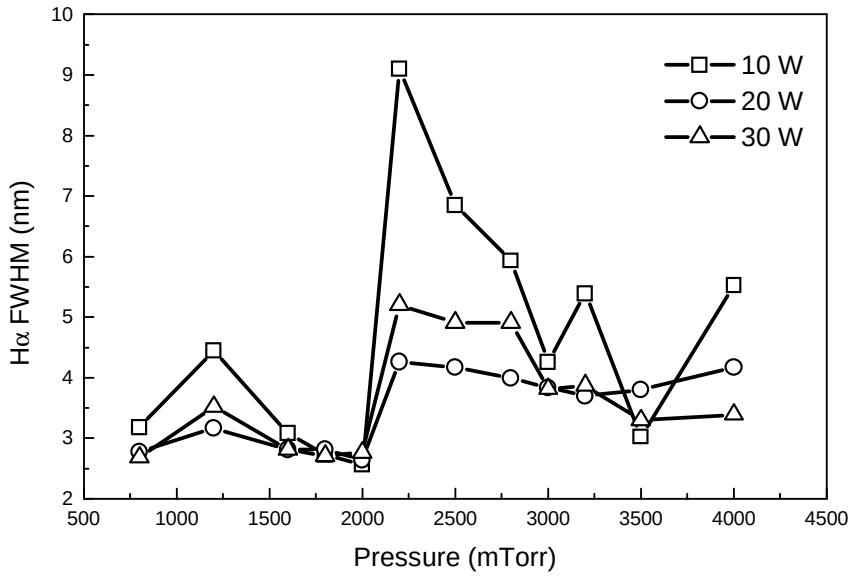

Fig. 4.14. The full width at half maximum (FWHM) of H_α emission peak as a function of total pressure at various RF power.

As pressure increases, particles start to form in the plasma (nanocrystal formation regime) and induce the broadening of the Balmer H_α emission line through the collision processes of excited species with particles. This is observed as a maximum in the FWHM of Balmer H_α as function of pressure at 1200 mTorr (Fig. 4.14). Further increase of pressure leads to the increase of the number of particles, but decreases their average size. Note that the collision frequency increases with the increase of particle diameter and their number. As a consequence, the decrease of the particle average size decreases the collision process probability, which has more significant effect than the increase of the number of particles. Thus, one can expect a decrease in the value of FWHM as observed between 1200 and 2000 mTorr in Fig. 4.14. At 2000 mTorr, when the number of particles reaches a critical value, they start to agglomerate and form large particles with an abrupt increase in their size. Thus, the transition at 2000 mTorr is associated to the agglomeration process where one can expect the abrupt increase of the FWHM of Balmer H_α line. Moreover, the presence of large particles perturbs the plasma in two ways, through the collision of excited species with particles and the electron attachment process. Further increase of pressure will lead to the growth of larger particles, which decreases the particle density and proposed to result in a lower collision frequency. The decrease of collision frequency as a consequence reduces the value of FWHM.

Moreover, the increase of pressure also reduces the power consumed by ions and increases the coupling efficiency to electrons [43], which facilitates electron impact excitation. Note that the electron impact excitation produces narrow emissions with the Doppler width, which depends only on the gas temperature.

Another interesting feature that could be observed in the plasma during the transition sequences from nanocrystal formation regime to agglomeration and powder formation regimes is the increase of Fulcher α band emission intensity (see Fig. 4.11). Here, the increase of intensity is also accompanied with the broadening of the overtone peaks, which can be observed by the disappearance of the fine structure of this band at high pressure and RF power. Moreover, the increase of the Fulcher α band emission intensity is observed to be important. Fig. 4.15a shows the effect of pressure on the ratio of the Balmer H_α line with respect to the Fulcher α band emission intensity ($I_{H\alpha}/I_{Fulcher}$) at various RF powers. We can observe that there are two transitions on the evolution of $I_{H\alpha}/I_{Fulcher}$ as a function of pressure. The first transition at ~1200 mTorr is associated with transition from particle-free plasma to the nanocrystal formation regime, while the second transition at ~2000 mTorr corresponds to the agglomeration process of plasma formed particles as already discussed. The second transition is also marked by a drop of the ratio value to less than unity. Interestingly, we could not observe such behavior in a pure hydrogen plasma as depicted in Fig. 4.15b, even if we vary the pressure and RF power. Thus, this fact supports our assignment of the various regimes in the plasma to the presence of particles.

Fig. 4.15a shows that the ratio $I_{H\alpha}/I_{Fulcher}$ provides a clear cut between the accumulation and agglomeration regimes, which are hardly noticeable in the evolution of the observable electrical parameters of the discharge such as V_{PP} and V_{DC} (see Fig. 4.7). Such transition should be related to the change in the size of particles from individual nanocrystals to larger agglomerates that induces the increase of the electron temperature [39]. The increase in electron temperature leads to a more energetic plasma with a higher density of excited species as observed by the increase of the integrated emission intensity of hydrogen as shown in Fig. 4.11. To understand the abrupt changes displayed in Fig. 4.15a, let us consider the main reactions responsible for H_α and for Fulcher α emission bands [44-46]:

$$e + H_2(X) \xrightarrow[E>16.6\,eV]{} H_2^* + e \rightarrow H(n=3) + H(n=1) + e \qquad (4.6a)$$

$$e + SiH_4(X) \xrightarrow[E>16.1\,eV]{} SiH_4^* + e \rightarrow H(n=3) + SiH_3(X) + e \qquad (4.6b)$$

$$e + H(n=1) \rightarrow H(n=3) + e\ (E_{th} = 12.06\ eV, \sigma_{\max} = 1.3\times10^{-17}\ cm^2)$$
$$H(n=3) \rightarrow H(n=2) + h\nu\ \ (H_\alpha, 656.2\ nm). \qquad (4.6c)$$

$$e + H_2(X^1\Sigma_g) \rightarrow H_2(d^3\Pi_u) + e\ (E_{th} = 15\ eV, \sigma_{\max} = 2\times10^{-18}\ cm^2),$$
$$H_2(d^3\Pi_u) \rightarrow H_2(a^3\Sigma_g) + h\nu\ \ (Fulcher\ \alpha\ band, 570-640\ nm). \qquad (4.7)$$

The higher cross section and lower threshold energy for H_α transition (eq. 4.6) are responsible for the higher emission intensity of H_α with respect to Fulcher α band at low pressure. Because of the lower cross section for second reaction (eq. 4.7), the increase of the electron temperature alone cannot account for the decrease of the $I_{H\alpha}/I_{Fulcher}$ at high pressure shown in Fig. 4.15a. Therefore, we propose that the observed transition in the $I_{H\alpha}/I_{Fulcher}$ is due to the recombination of atomic hydrogen on the surface of the particles. When agglomeration starts the cross section of this process increases abruptly and thus atomic hydrogen is consumed, leading to the sharp decrease in H_α emission. Moreover, the molecular hydrogen is formed and excited to give the increase of the intensity of the Fulcher molecular hydrogen α band and thus to the transition in the $I_{H\alpha}/I_{Fulcher}$ ratio.

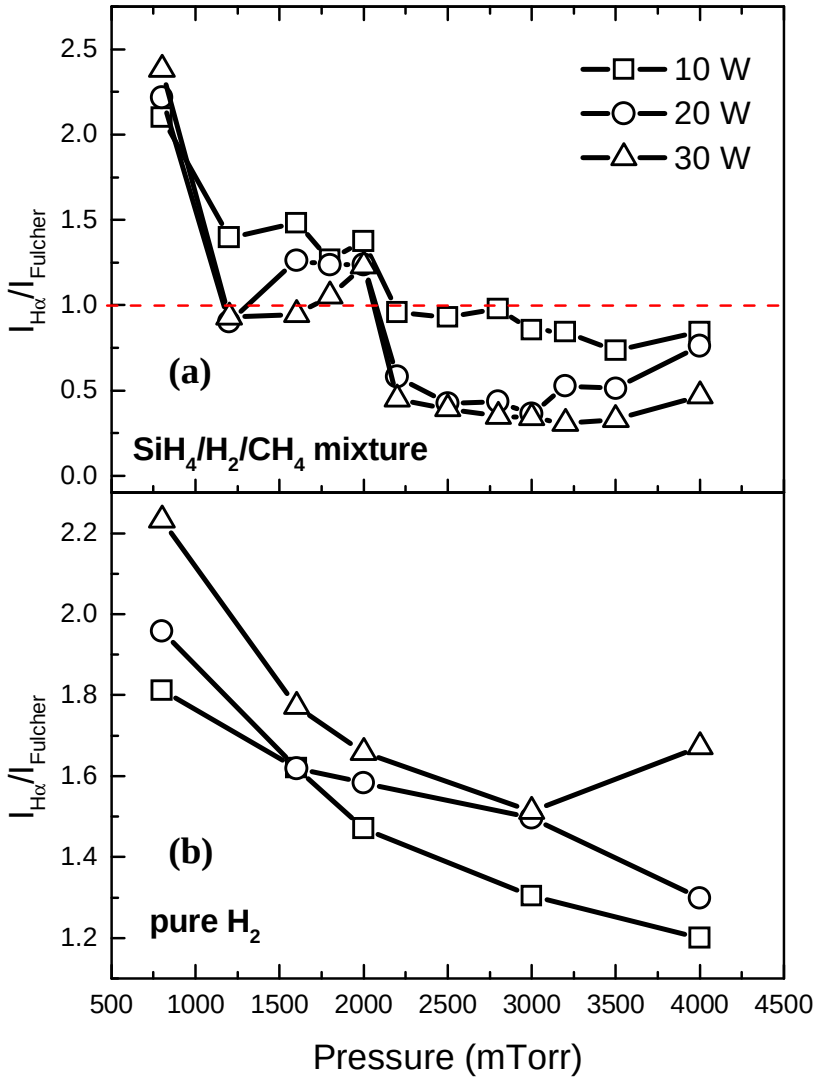

Fig. 4.15. Effect of pressure on the intensity ratio between Balmer H_α and Fulcher band α ($I_{H\alpha}/I_{Fulcher}$) in the case of a $SiH_4/H_2/CH_4$ plasma a) and of a pure hydrogen plasma b), for three values of the RF power.

Fig. 4.16 shows the evolution of intensity of several optical emission lines as a function of the RF power for the values of the total pressure: 800, 2000 and 3500 mTorr, corresponding to the three deposition regimes discussed above: nanocrystals formation, agglomeration and powder formation regimes, respectively. As in the case of pressure, we can see that the RF power has different effects on the plasma optical emission spectra, which differ for each emissive species. As predicted in a discharge model proposed by Novikova for pure hydrogen plasma, the increase of pressure leads to a higher amount power transferred to electrons and to the decrease of the power consumed by ions [43].

Fig. 4.16a shows the evolution of the emission intensity of the Balmer H_α line as a function of RF power. The H_α emission intensity has a particular behavior at 2000 mTorr (agglomeration regime) compared to other regimes. It shows a stronger dependence on RF power. The RF power effect on SiH^* emission intensity is shown in Fig. 4.16b. The emission intensity shows no power dependence at 800 mTorr, while a strong increase is observed at 2000 and 3000 mTorr. Moreover, Fig 4.16b also shows that at 2000 mTorr (agglomeration regime) and at 3000 mTorr (powder formation regime) the SiH* has the same evolution below 15 W while above this value the effect of the RF power is much more important at 3000 mTorr. The evolution of the emission intensity of CH^* shows a similar behavior to that of SiH* at 800 mTorr. At 2000 and 3000 mTorr, we observe approximately the same behavior. The difference between CH* and SiH* behavior can be related to the lower reactivity of methane, which needs higher electron temperature to produce CH* that can be achieved with the presence of particles at high pressure. The emission intensity ratio between SiH^* and CH^* is shown in Fig. 4.16d. The evolutions of I_{SiH*}/I_{CH*} with RF power at 800 and 2000 mTorr give approximately the same tendency. The increase of pressure, from nanocrystals formation regime to the agglomeration regime leads to a plasma richer in silane reactive species, signified by the shift of I_{SiH*}/I_{CH*} evolution curve to the higher value. However, a totally different behavior is observed at 3000 mTorr. The I_{SiH*}/I_{CH*} increases significantly with RF power up to 20 W, and is followed by a decrease for higher pressure.

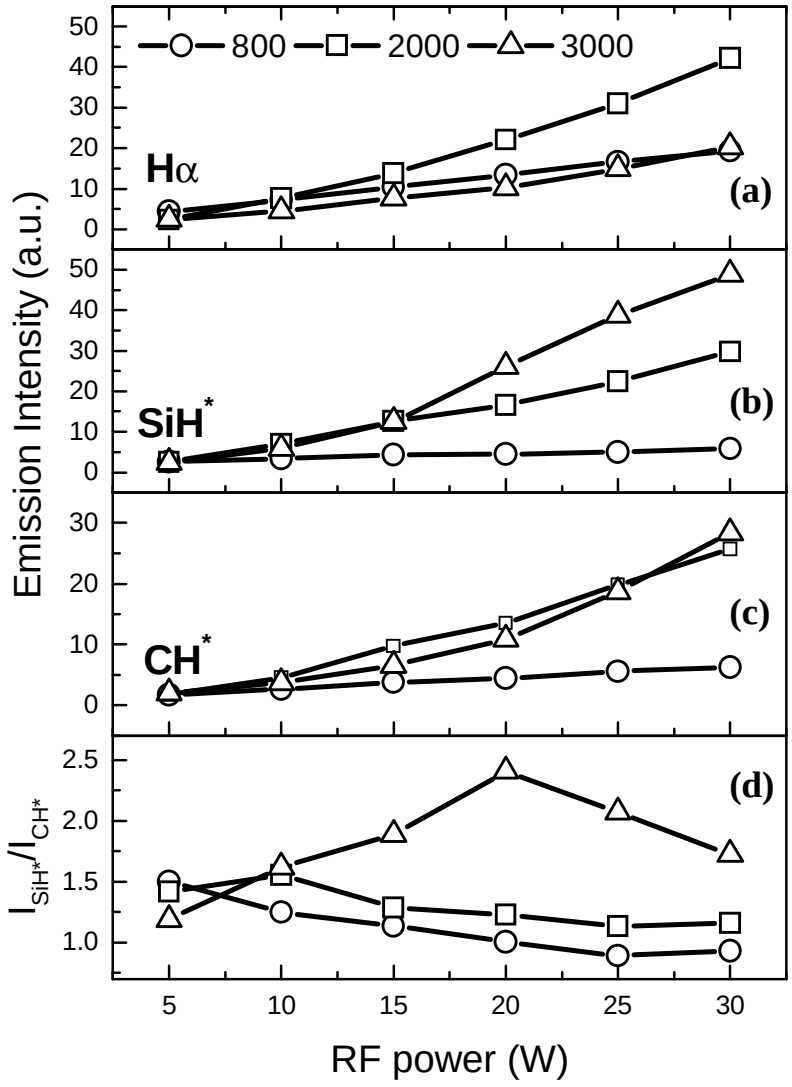

Fig. 4.16. The evolution of optical emission intensity of a) H_α, b) SiH^*, c) CH^* lines and d) emission intensity ratio between SiH^* and CH^* lines as functions of RF power at various pressures.

4.5. Chemical analysis of thin films

The chemical composition of the samples was studied by Fourrier transform infrared (FTIR) spectroscopy and energy dispersive (EDX) X-ray spectroscopy. The concentration of chemical bonds (Si-H, C-H and Si-C) was extracted from FTIR analysis, while the silicon/carbon ratio was deduced from EDX analysis. In both cases, the results represent the bulk chemical composition due the measurement by transmission method.

Fig. 4.17 shows the base-line corrected IR spectra from FTIR measurements as the absorption coefficient spectra for samples deposited at various pressures with 20 W of RF power. The base-line corrections, including the elimination of interference fringes and absorption by the substrate, were carried out using a method proposed by Maley [47] (see Ch. 2). Clear changes of features in the spectral range from 500 to 1200 cm^{-1} as the total pressure increases are observed. With increasing pressure, some less pronounced peaks at 800 mTorr appear and become clear at higher pressure. The figure shows another interesting feature: the narrowing of the peak with the increase of pressure all over the range, i.e. the Si-H_n stretching mode around 2100 cm^{-1} reduces the value of FWHM from 92 to 82 cm^{-1} with the increase of pressure from 800 to 3500 mTorr.

The assignment of the observed peaks to the infrared vibration modes is listed in Table 4.1. Here, the absorption peaks were extracted by fitting the experimental spectra using Gaussian-Lorentzian mixture curves (SGL) for each spectral regime separately. Then, we can calculate the bond concentration using eq. 2.33, by introducing the fitting result and the absorption strength value for certain chemical bond as listed in Table 2.2.

Fig. 4.18a shows the evolution of Si-H bond concentration as a function of deposition pressure deduced from the peak corresponding to Si-H_n stretching vibration modes (~2000 cm^{-1} for monohydride and ~2100 cm^{-1} for polyhydride bonds) of IR absorption spectra for samples deposited at 10 and 20 W. The figure shows a local minimum, which is shifted towards low pressure with the increase of RF power. We suggest that the local minimum might correspond to the transition between nanocrystal formation and agglomeration regime, observed as an abrupt increase in deposition rate pressure dependence. The deposition of particles in the form of agglomerates of individual nanocrystals should lead to the increase of the hydrogen concentration in the film. Moreover, the observed shift on the local minimum might be due to delayed particle formation at low RF power. Fig. 4.18b shows the pressure dependence of C-H bond concentration deduced from the CH_n groups stretching vibration modes (2700 – 3200 cm^{-1}). As pressure increases, the C-H bond concentration tends to

decrease until it reaches a minimum. The increase of the RF power increases the C-H bond concentration without changing its variation with pressure. The evolution of Si-C bond concentration deduced from Si-C stretching vibration mode (~780 cm^{-1}) shows a slight decrease with increasing pressure as depicted in Fig. 4.18c. The increase of RF power from 10 to 20 W does not have much influence on Si-C bond concentration; it slightly increases the Si-C bond concentration for samples deposited at high pressure but not for 800 mTorr samples. The FTIR analysis shows that the particle formation induced transition, observed by plasma measurements (both electrically and optically) and on the evolution of deposition rate, reflects on the chemical composition of the films. However, we cannot conclude this problem simply by relying on FTIR analysis which cannot detect Si-Si and C-C bonds.

Table 4.1. Assignment of the infrared modes observed in polymorphous silicon carbon alloys

ω (cm^{-1})	Assignment	Reference
~640	Si-H_n wagging	48-51
~780	Si-C stretching	48-51
~835	Si-H_2 wagging	48-51
~870	Si-H_2 scissoring	48-51
~900	Si-H_2 bending	48-51
~1000	C-H wagging	48-51
1300–1600	C-H_n, n=2, 3 bending	48, 51, 52
~1273	C-H_3 symmetric bending in Si-CH_3	48, 51, 52
~1345	C-H_3 symmetric bending	48, 51, 52
~1406	C-H_3 asymmetric bending	48, 51, 52
2000–2100	Si-H_n complexes stretching	48-51
2700–3200	C-H_n groups stretching	48, 51, 52
~2883	C-H_3 symmetric stretching	48, 51, 52
~2955	C-H_3 asymmetric stretching	48, 51, 52

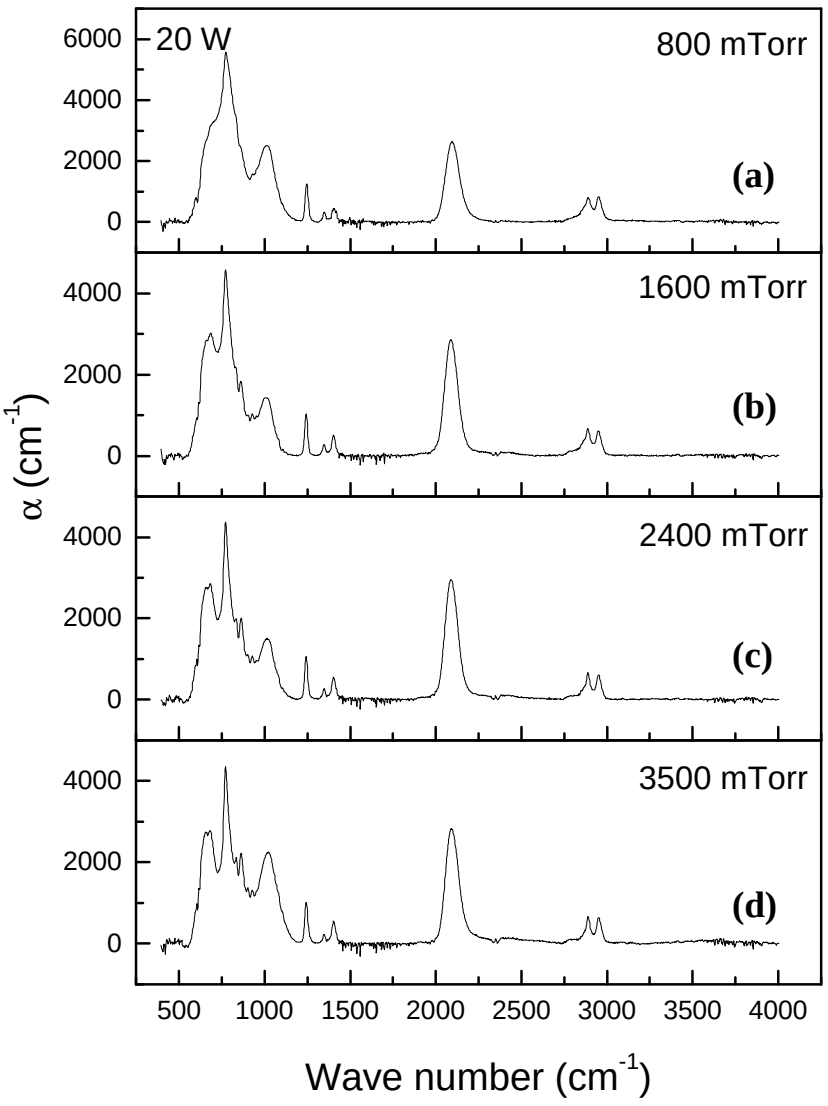

Fig. 4.17. The infrared absorption spectra for *pm-$Si_{1-x}C_x$:H* samples deposited at various pressures from (a) 800, (b) 1600, (c) 2400 and (d) 3500 mTorr with 20 W of RF power.

. Fig. 4.18d shows the evolution of the ratio of Si/C as a function of deposition pressure for *pm-$Si_{1-x}C_x$:H* thin films deposited at 20W deduced from EDX measurements. Interestingly, the evolution of Si/C ratio shows a similar behavior as the evolution of Si-H bonds concentration depicted in Fig. 4.18a. Based on these results, we can deduce that most silicon and carbon deposited at high pressure (agglomeration and powder formation regimes) are hydrogenated, therefore the change in the ratio between these two constituents give an obvious effect on the concentration of chemical bonds with hydrogen. Moreover, we can also correlate the increase of optical band gap (see Ch. 5) while the Si-C bond concentration decreases with higher contribution of nanocrystals and hydrogen content.

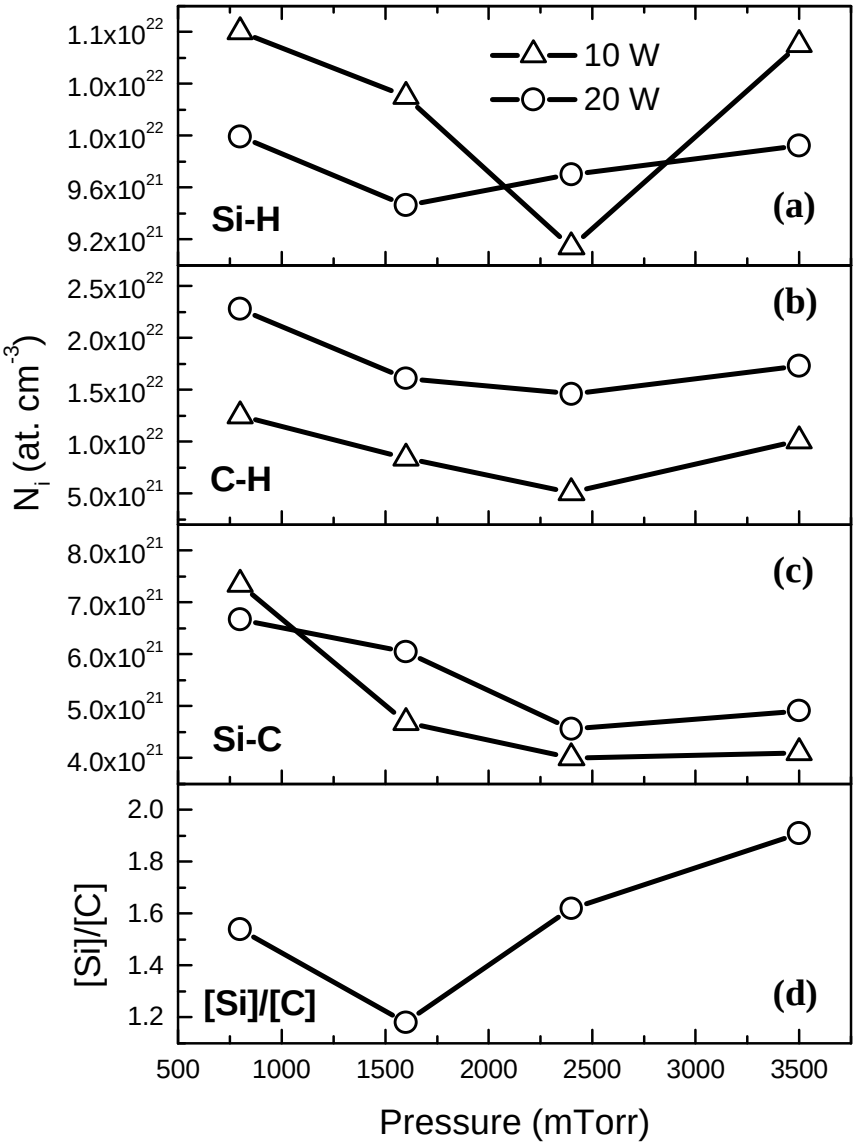

Fig. 4.18. The bond concentration deduced from FTIR analysis for a) Si-H, b) C-H and c) Si-C bonds, respectively for samples deposited at 10 and 20 W of RF power. d) The atomic concentration ratio deduced from EDX analysis between silicon and carbon for 20 W samples.

4.6. Structure and morphology of thin films

Transmission electron microscopy (TEM) analysis

Fig. 4.19 shows that the change of deposition rate as a function of pressure is accompanied by the evolution of the structure of the particles. Here, the particles were collected on the liquid nitrogen cooled substrate holder thanks to the thermophoresis force due to the temperature gradient between the plasma and the substrate. Because of the low temperature, we can assume that the trapped particles are frozen, i.e. they reflect their structure in the plasma. In this case, we deposited the particles produced in the plasma directly on the amorphous carbon covered copper grid for TEM analysis.

As we can see in the enlarged TEM images at the bottom of Fig. 4.19, the shape and the size of the particles depend on the total pressure. At 800 mTorr, we deposited nothing except radicals which form a thin film. The increase of pressure to 1600 mTorr leads to the formation of thin chain-like particles. Each chain consists of many spherical particles that stick together. Further increase of pressure to 2400 and 3500 mTorr leads to the formation of larger agglomerates. Here, the particles still have spherical shape, but their size is much larger than at 1600 mTorr. The shape of the particles formed at 2400 and 3500 mTorr is similar, only differs in their average size and size distribution. As the pressure increases from 2400 to 3500 mTorr, the average size decreases from 34 to 31 nm and the size distribution becomes slightly larger, characterized by the increase of the FWHM of the distribution value from 20 to 22 nm.

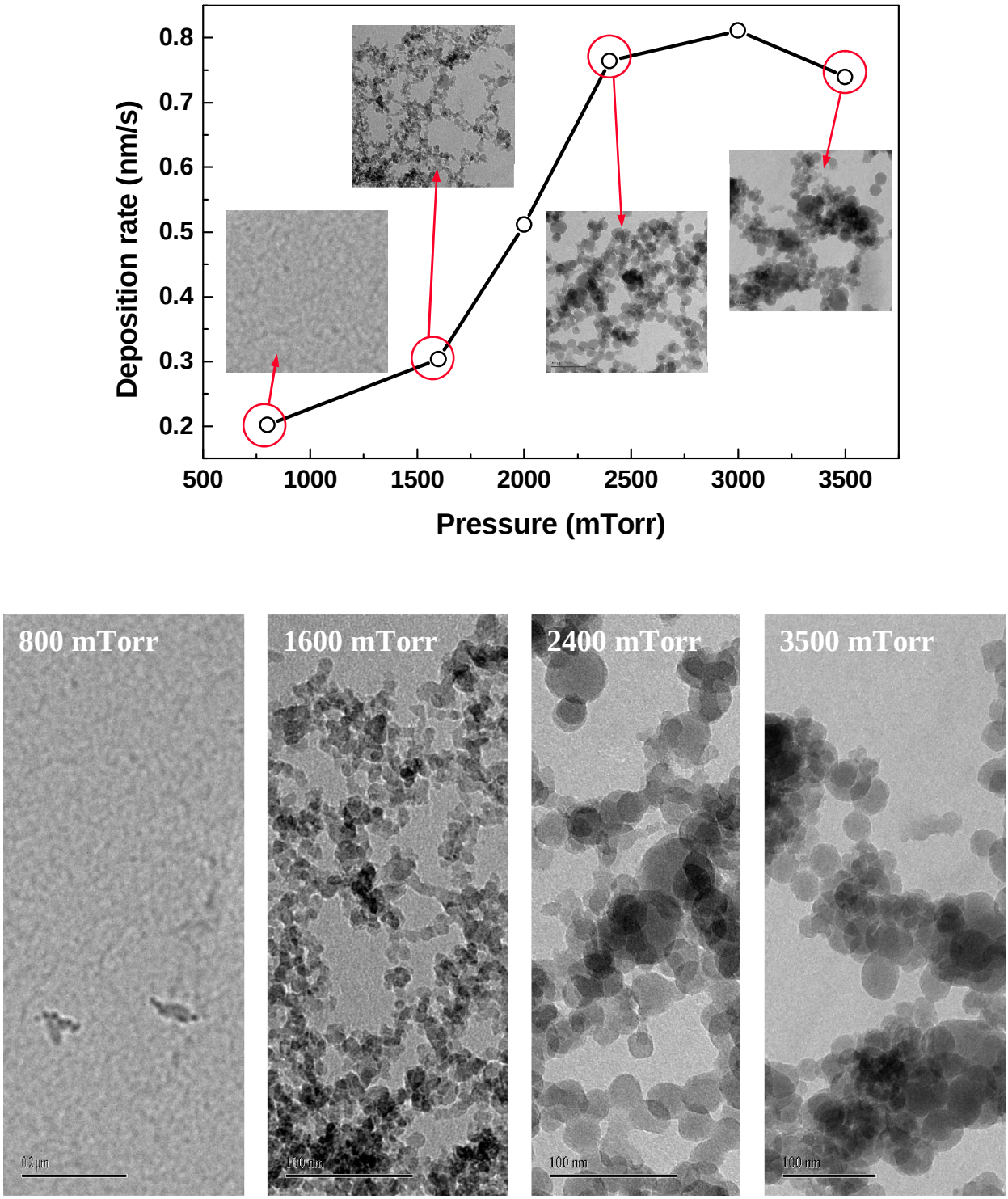

Fig. 4.19. The evolution of deposition rate as a function of the deposition pressure and related changes in the plasma formed particles (above). TEM images of the particles trapped on the cold substrate (below).

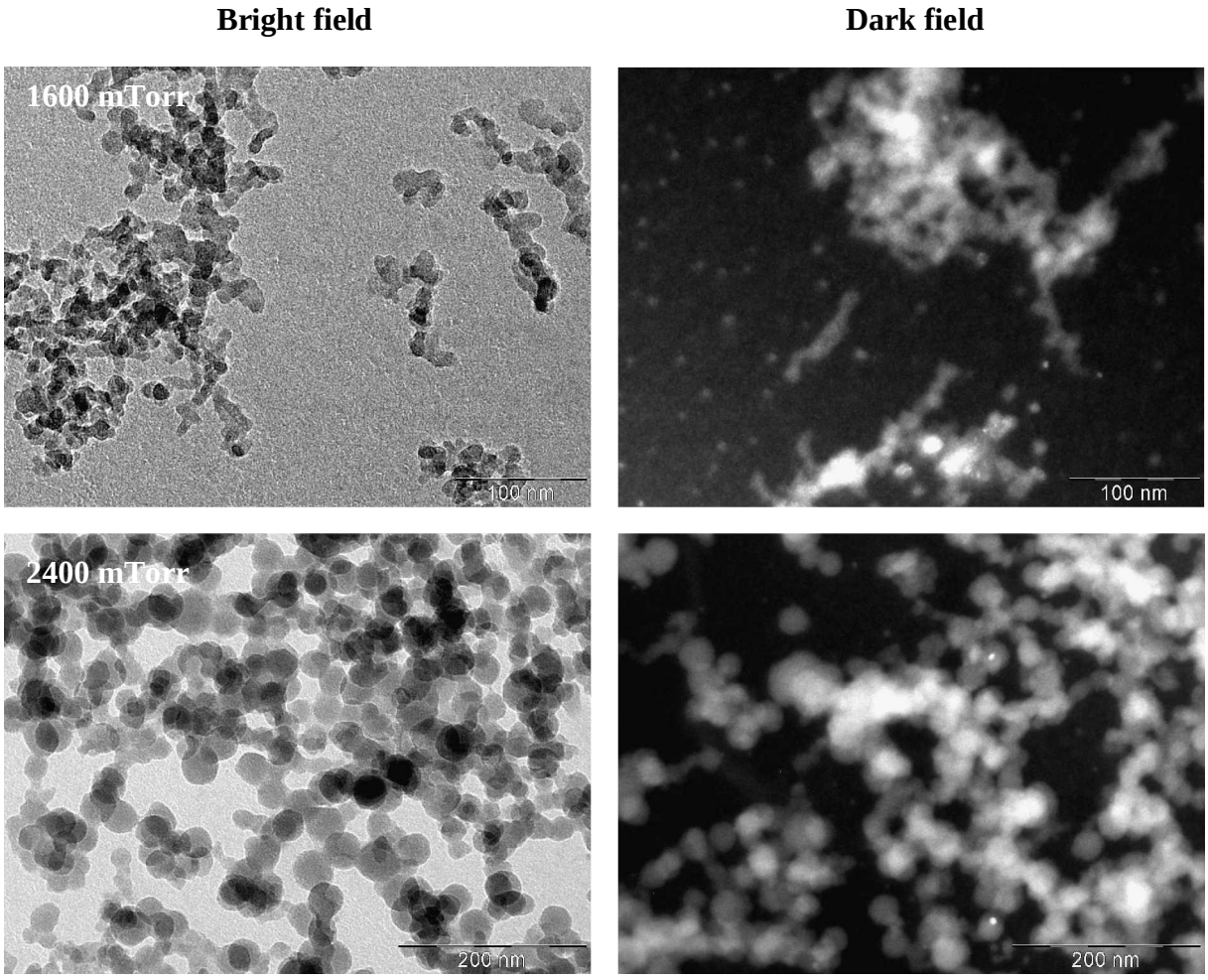

Fig. 4.20. TEM images of particles trapped on the cold substrate in two image modes: bright field (left column) and dark field (right column) for *pm-*$Si_{1-x}C_x$*:H* samples deposited at 1600 (upper row) and 2400 (lower row) mTorr.

In the study of material synthesis for luminescent applications, the presence of silicon nanocrystals is a very important issue. In the case of polymorphous silicon carbon alloys, the room temperature luminescence is clearly observed, but its origin is not defined yet. To demonstrate the presence of nanocrystals in the plasma, we performed bright field and dark field TEM measurements of powder samples collected on the liquid nitrogen cooled sutbstrate and produced at two pressures. Fig. 4.20 shows the TEM images of particles trapped at two different conditions (1600 and 2400 mTorr) in both image modes. In bright field images we can observe the change on shape, size and number of spherical particles with the increase of pressure. In dark field images, we can observe tiny bright objects, which indicate the presence of silicon nanocrystals in agglomerate form.

To see whether the same nanocrystals are deposited on the hot substrate we also performed TEM measurements of *pm-*$Si_{1-x}C_x$*:H* thin films deposited under the same

conditions as the powder samples described above. Fig. 4.21 shows the TEM images of *pm-$Si_{1-x}C_x$:H* films deposited on the hot substrate. The images show the presence of dark objects corresponding to the embedded silicon nanocrystals, which have a higher density than the matrix due to their partly crystallized structure. From the bright field images we cannot distinguish the differences the samples produced at various pressures, even though the increase of pressure has a strong effect on the PL intensity (inset of Fig. 4.3 and Ch. 5 for detail). However, the inset in Fig. 4.21 shows clearly the presence of 2-3 nm sized nanocrystals inside the agglomerates in dark field mode for the sample deposited at 3500 mTorr.

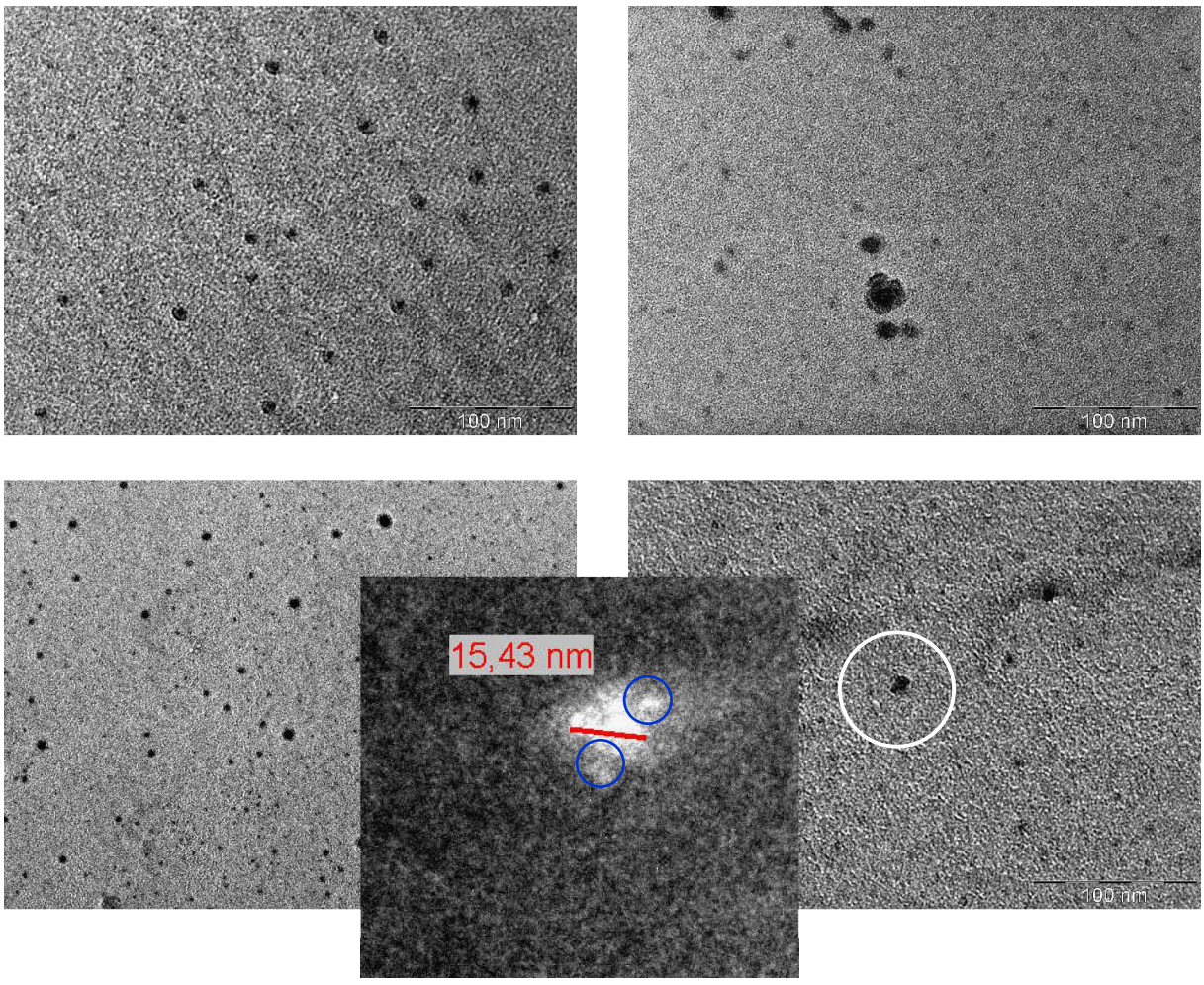

Fig. 4.21. TEM images of particles deposited on the hot substrate at various deposition pressures in bright field mode. The inset shows a detail in dark field mode of a particle deposited as a packet of many individual particles in size range of 2-3 nm for a sample deposited at 3500 mTorr.

Fig. 4.22 shows the effect of RF power on the structure of films deposited on the hot substrate. The particles are similar as in the samples of the pressure series (Fig. 4.21). The increase of RF power does not produce any significant change in film structure as deduced from bright field mode TEM images (left column). However, in dark field mode (right column), the presence of bright spots increases significantly with the increase of RF power. This is closely related to the increase of the PL intensity with RF power.

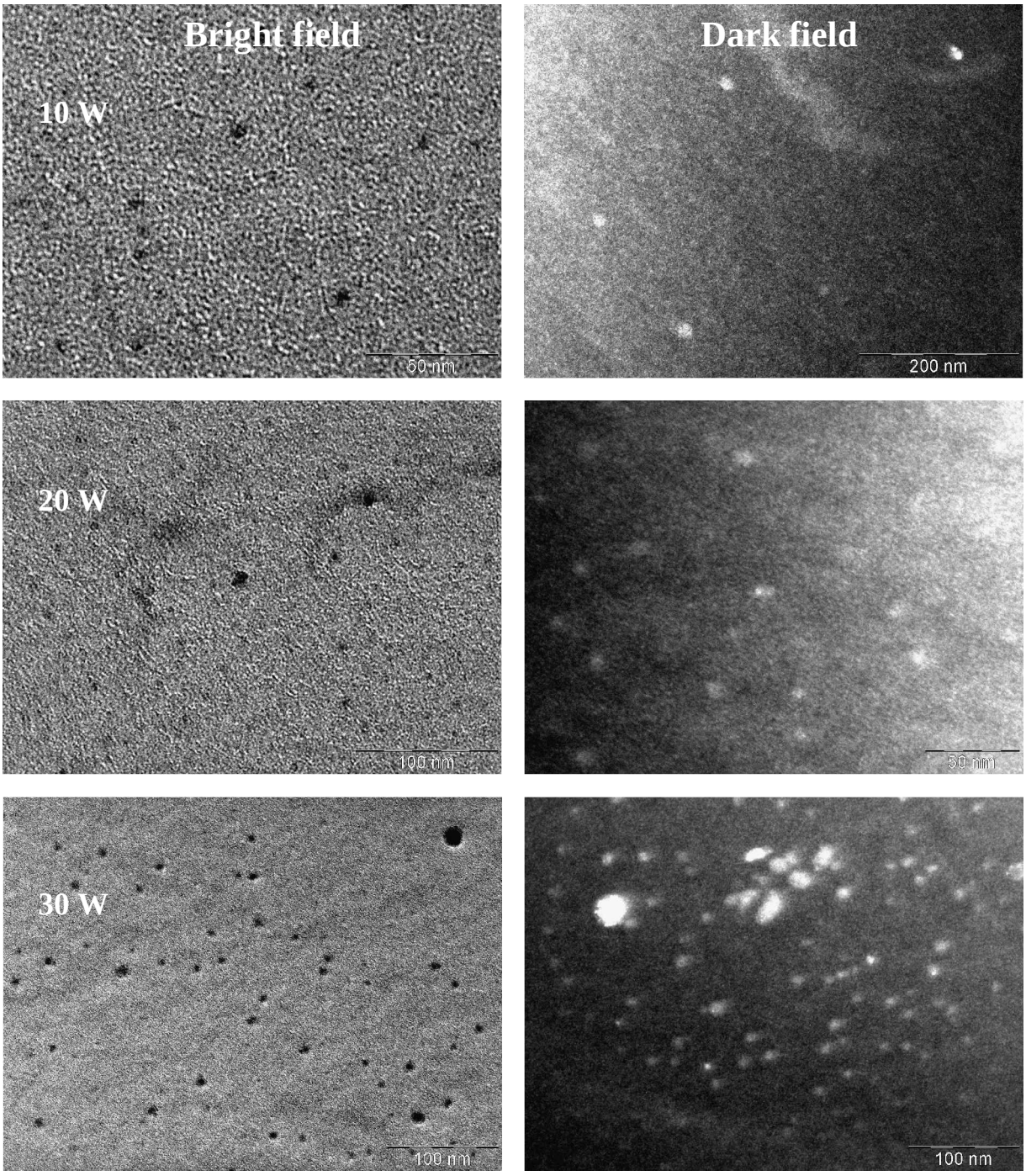

Fig. 4.22. TEM images of particles deposited on the hot substrate in two image modes: bright field (left column) and dark field (right column) for *pm-*$Si_{1-x}C_x$*:H* samples deposited at 3500 mTorr for various values of the RF power.

Raman spectroscopy Analysis

Fig. 4.23 shows the Raman spectra and the fitting results for *pm-$Si_{1-x}C_x$:H* samples deposited at various pressures. Here, the experimental spectra have been deconvoluted into several modes corresponding to the hydrogenated amorphous silicon or its alloys with carbon, such as: transverse optic (TO) ~480 cm^{-1}, longitudinal optic (LO) ~380 cm^{-1} [53], Si-H vibration ~640 cm^{-1}[54], and 2nd harmonic of TO phonon (2TO) ~960 cm^{-1}[54, 55] and Si-C vibration ~780 cm^{-1} [56]. The spectrum of a c-Si wafer is given as a reference for the TO peak position at 520 cm^{-1}. The overlap among bands makes the deconvolution by fitting necessary to analyze them, i.e., to separate TO and LO bands. In this study, we fitted the experimental spectra with six bands defined as gaussian peaks as shown in Fig. 4.23. Among them, five bands are well-known for the amorphous silicon carbon alloys system as mentioned above: LO, TO, Si-H vibration, 2TO and Si-C vibration bands. Moreover, we have added a broad band centered around 1200-1400 cm^{-1}, which is necessary to obtain a good fit of the experimental spectra. The Si-C vibration band weakly appears near 760 cm^{-1} due to its low Raman efficiency [57]. The band position is shifted slightly towards low energy, indicating the increase of disorder compared to the crystalline peak. In contrast, the presence of Si-H and 2TO bands is easier to observe in this system. Note that in our samples the Raman band for C-C vibration as the D and G bands in graphite are not detected, indicating the low C-C concentration in the film.

The results of the analysis of the spectra are shown in Fig. 4.23. The width of the peaks is represented by their full width at half maximum (FWHM), and their values are listed in Table 4.2. The relative intensity of each band to the Si-Si TO band (~480 cm^{-1}) is represented by the peak area ratio as given in Fig. 4.24. The figure shows the evolution of A_{LO}/A_{TO}, A_{Si-H}/A_{TO}, A_{Si-C}/A_{TO}, and A_{2TO}/A_{TO} values as functions of deposition pressure.

Let us see the evolution of convoluted peaks in Fig. 4.23, where the deposition pressure affects not only the relative intensities but also their bandwidths. Table 4.2 shows that the value of FWHM regardless of the peaks evolves in the same manner, except for Si-H (~640 cm^{-1}) and 2TO bands. Their general tendency is to decrease with pressure until entering the powder formation regime. In this regime the increase of pressure leads to an increase the value of FWHM. The Si-H band shows a slightly different behavior, as it is practically constant before increases when enters the powder formation regime. In contrast, the 2TO band shows an increase with deposition pressure with a plateau in agglomeration or α–γ‘ transition regime.

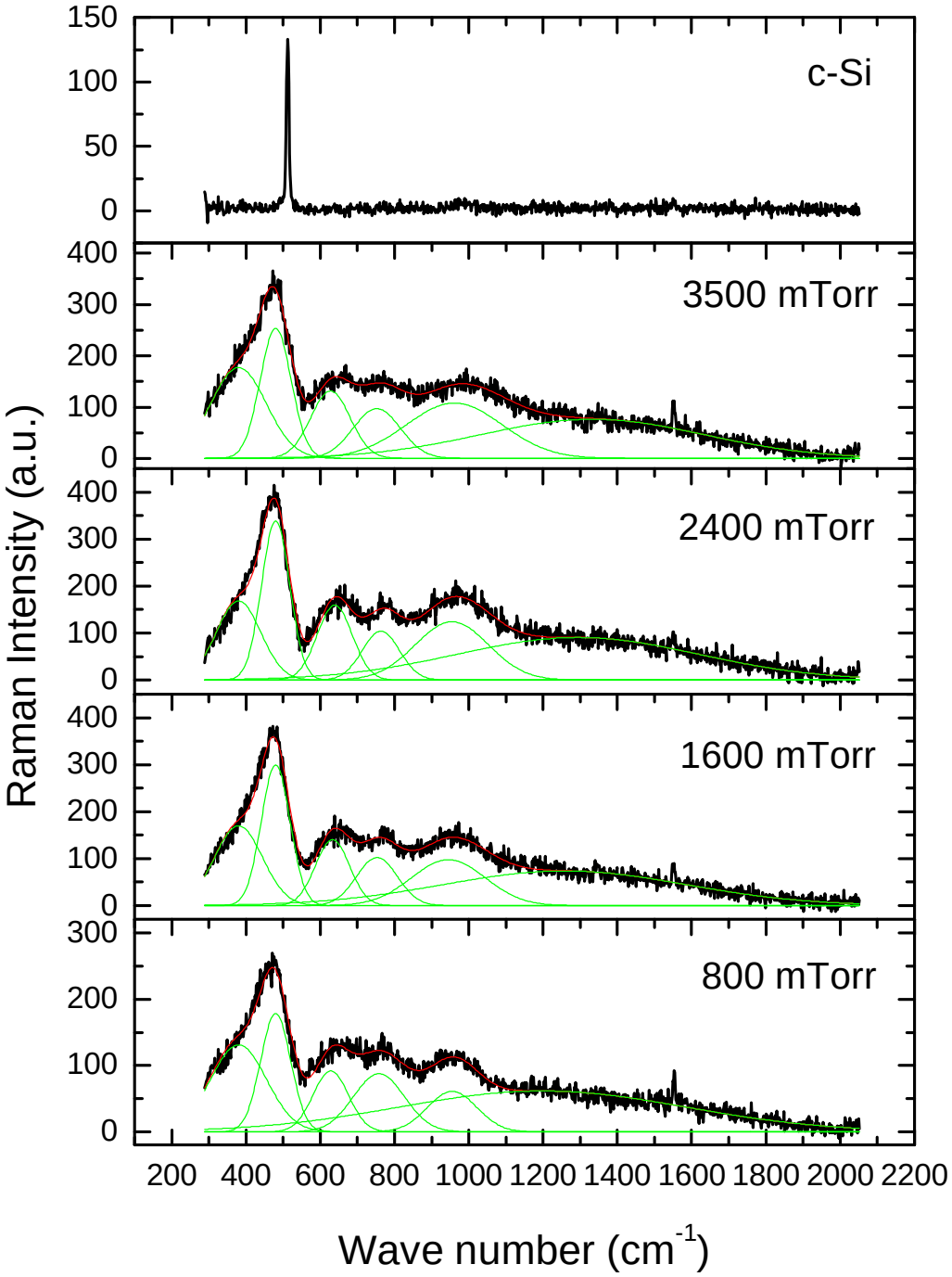

Fig. 4.23. The experimental Raman spectra and the fitting results of *pm-*$Si_{1-x}C_x$*:H* samples deposited at various pressure. The spectra of c-Si sample is also shown here as a reference for the Si-Si TO peak position. The gaussian curves are used here to represent the convoluted peak in spectrum fitting.

We assume that the increase of pressure modifies the material structure by changing its disorder, which affects the Raman active vibration modes. In this case the value of FWHM of first order Raman signal contains the response of the disorder induced by the chemical bond vibrations relative to the same mode in their crystalline counterpart, i.e. broadening and red shift of TO-like band in amorphous silicon and its alloys [57]. Let us return to the results in Table 4.2, showing the narrowing tendency of first order Raman modes with pressure before entering the powder formation regime. We suggest that the decrease of FWHM might indicate the increase of nanocrystals contribution which induces the average material orderness as reported elsewhere [22, 58]. In contrast, the samples deposited at 3500 mTorr may consist of rather different types of plasma formed particles. In this condition, the particle formation is very fast, which reduces the probability for rearrangement or crystals formation. Thus, even though the number of nanocrystals embedded in the film increases because we deposit more agglomerates, actually the morphology inside the agglomerate might be different. Moreover, the faster deposition process also facilitates the increase of the disorder during deposition as discussed previously. The FWHM of 2TO bands shows the same tendency to increase with pressure as TO bands. The second order optic band widening is one of the indications of the decrease in the size of embedded nanocrystals [55], which is in good agreement with the result of PL spectroscopy.

Fig. 4.24 shows the ratio of the peak area of several Raman bands with respect to the TO band as a function of deposition pressure. The squares curve represents the evolution of A_{LO}/A_{TO}, showing a decrease with pressure up to 2400 mTorr then followed by a significant increase, which is similar to the FWHM. A similar behavior is also observed for $A_{Si\text{-}C}/A_{TO}$, represented by up triangles curve. The increase of A_{LO}/A_{TO} indicates the increase in material disorder as observed in amorphous silicon by the increase of LO band intensity [57]. This result is in a good agreement with the broadening of Raman bands represented by the FWHM. The $A_{Si\text{-}C}/A_{TO}$ evolution is suggested to represent the decrease of Si-C contribution with pressure as also shown by its IR counter part (see Fig. 4.18). In contrast, the $A_{Si\text{-}H}/A_{TO}$ shows practically constant values with the increase of pressure, which suggests the presence of the hydrogenated embedded nanocrystals in our films. Moreover, the monotone increase of A_{2TO}/A_{TO} value with pressure represented by down triangle curve follows the same behavior as the FWHM. This behavior indicates the decrease of nanocrystals size or the increase of amorphous contribution in the system.

Table. 4.2. The full width at half maximum of the Raman spectral peaks of *pm-$Si_{1-x}C_x$:H* samples.

Pressure (mTorr)	FWHM (cm^{-1})*				
	380 cm^{-1} LO	480 cm^{-1} TO	640 cm^{-1} Si-H	760 cm^{-1} Si-C	960 cm^{-1} 2TO
800	176	95	112	162	156
1600	152	91	108	130	234
2400	141	89	111	118	231
3500	176	98	125	150	304

*)Fitted as gaussian peaks.

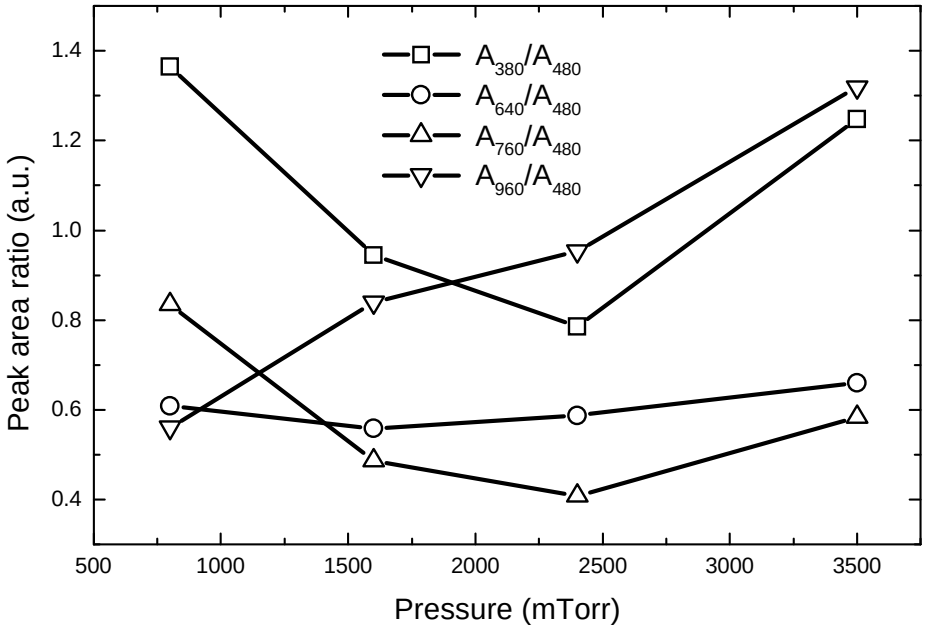

Fig. 4.24. The peak area ratio of Raman spectra for several peak of interest on *pm-$Si_{1-x}C_x$:H* samples: A_{LO}/A_{TO} or A_{380}/A_{480} (squares), A_{Si-H}/A_{TO} or A_{640}/A_{480} (circles), A_{Si-C}/A_{TO} or A_{760}/A_{480} (up triangles) and A_{2TO}/A_{TO} or A_{960}/A_{480} (down triangles).

Atomic force microscopy (AFM) analysis

Fig . 4.25 shows the AFM images for polymorphous silicon carbon alloys deposited at 800 and 2000 mTorr, which represent the samples deposited in the particle-free plasma and in the agglomeration regime, respectively. The sample deposited at 800 mTorr displays a smooth surface with very low roughness. In contrast, the sample deposited agglomeration regime shows a much rough surface. Here, the images show many large bright spots, the characteristic of deposited particles on the film surface, with diameters up to 80 nm. These results confirm that the transition from nanocrystals formation regime to agglomeration regime changes the surface roughness drastically due to the deposition of plasma formed particles as agglomerates of nanocrystals, as in the case of pm-Si:H films deposited from SiH_4/H_2 plasma [59].

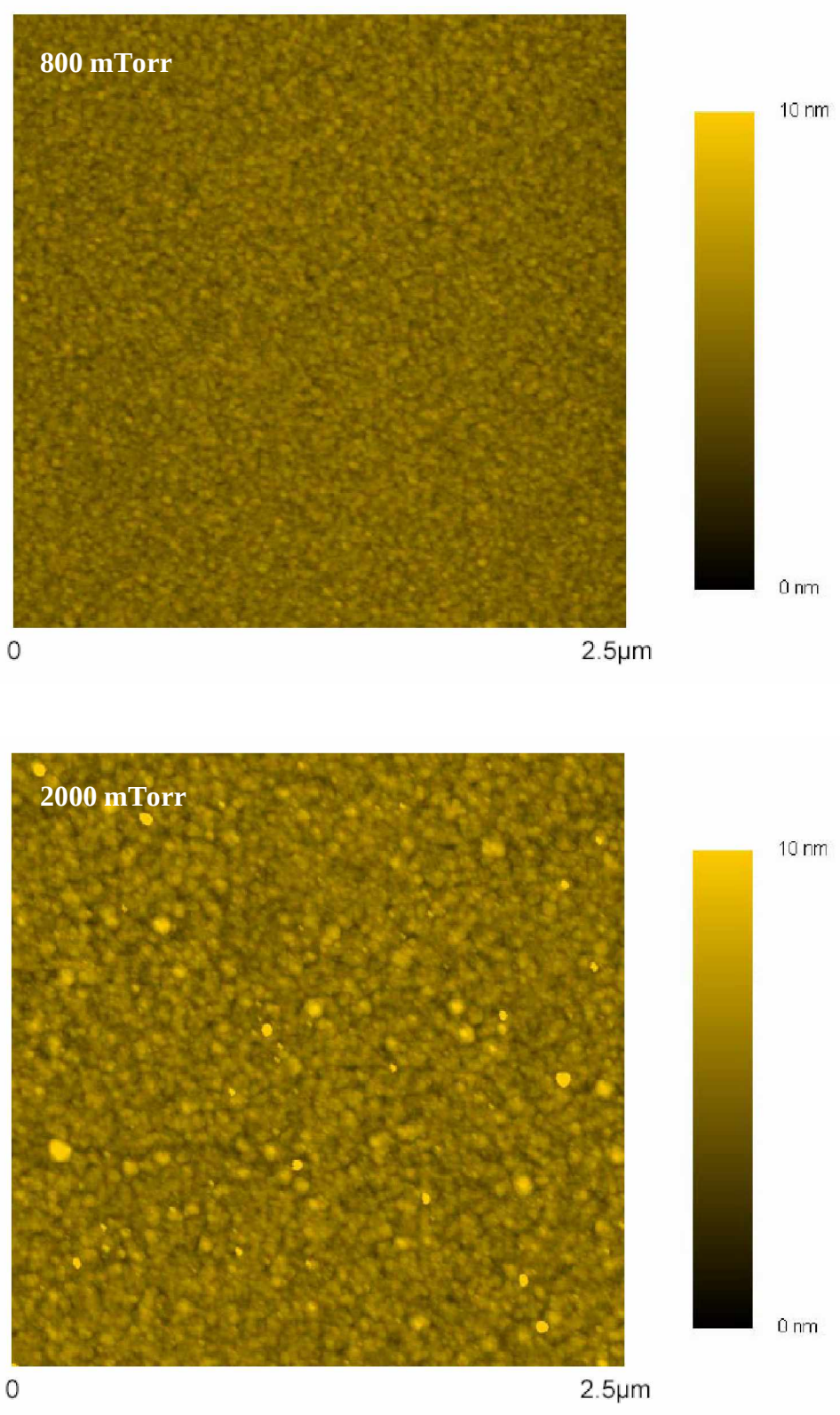

Fig. 4.25. Atomic force microscopy images of the surface of *pm-$Si_{1-x}C_x$:H* samples deposited at 800 and 2000 mTorr, corresponding to the nanocrystal formation and agglomeration regimes respectively.

4.6. Summary and conclusions

The analysis of the deposition rate as a function of deposition parameters such as pressure, RF power, methane flow rate and substrate temperature, shows that the growth of *pm-*$Si_{1-x}C_x$*:H* follows the same mechanisms as in the case of *pm-Si:H*. A better material is always found in the deposition regime after α–γ' transition, which shows the importance of the presence of particles in deposition. Further, the presence of the particles formed in the plasma and their contribution to deposition were also observed by the plasma electrical measurements and TEM analysis.

The optical emission spectroscopy (OES) measurements show that the same transition observed by the plasma electrical measurements (V_{DC}, J_2,…) can also be observed optically. Interestingly, the plasma perturbation by the presence of particles induces many observable parameters such as the intensity of SiH* and CH* emissions, the FWHM of H_α and the intensity ratio between Balmer H_α and Fulcher band α, which can be observed independently. Moreover, the evolution of $I_{H\alpha}/I_{Fulcher}$ and the FWHM of Balmer H_α provide a clear cut for detail feature of transition, such as between the nanocrystal formation and agglomeration regimes, which is hardly noticeable in the evolution of V_{PP} and V_{DC}. The chemical analysis based on FTIR and EDX measurements shows that the deposited films are hydrogenated and rich in silicon. The concentration of silicon increases significantly for samples deposited at high pressure, in the agglomeration and powder formation regimes. This results are in a good agreement with the OES result of I_{SiH*}/I_{CH*} ratio, which shows an important increase at high pressure regimes. Further, the evolution of Si-H bond concentration is also observed to follow the same trend as Si/C concentration ratio evolution with pressure. A similar behavior is also observed by Raman spectroscopy, where the evolution of the area ratio between TO and Si-H peaks is nearly constant with pressure.

The TEM analysis of particles trapped in the cold substrate shows that the size and shape of particles evolve with deposition conditions. On the heated substrate, similar particles were also detected. In both cases, silicon nanocrystals were observed inside large particles by the darkfield image mode. Here, the large particles consist of agglomerates of silicon nanocrystals, which concentration increases with pressure and RF power. Moreover, these results have also been verified by AFM analysis for the drastic increase of film roughness for the transition from the nanocrystal formation regime to the agglomeration regime.

References

[1] P. Roca i Cabarrocas, S. Hamma, S. N. Sharma, G. Viera, E. Bertran, J. Costa, *J. Non-Cryst. Solids* **227-230**, 871 (1998).

[2] V. Suendo, G. Partriarche, P. Roca i Cabarrocas, Optical Materials (2004).

[3] X. T. Zhou, R. Q. Zhang, H. Y. Peng, N. G. Shang, N. Wang, I. Bello, C. S. Lee, S. T. Lee, *Chem. Phys. Lett.* **332**, 215 (2000).

[4] N.-M. Park, C.-J. Choi, T.-Y. Seong, S.-J. Park, *Phys. Rev. Lett.* **86**, 1355 (2001).

[5] C. Delerue, G. Allan, M. Lannoo, *Phys Rev. B* **48**, 11024 (1993).

[6] G. Ledoux, O. Guillois, D. Porterat, C. Reynaud, F. Huisken, B. Kohn, V. Paillard, *Phys. Rev. B* **62**, 15942 (2000).

[7] J. M. Ferreyra, C. R. Proetto, *Phys. Rev. B* **60**, 10672 (1999).

[8] V. Suendo, A. V. Kharchenko, P. Roca i Cabarrocas, *Thin Solid Films* **451-452**, 259 (2004).

[9] W. Luft, Y. S. Tsuo, *Hydrogenated Amorphous Silicon Alloy Deposition Processes*, Marcel Dekker Inc., New York, 1993, p15-16, 139-140.

[10] W. Luft, idem, p16-17.

[11] J. I. Steinfeld, J. S. Francisco, W. L. Hase, *Chemical Kinetics and Dynamics*, Prentice Hall Inc., New Jersey, 1989, p3-8.

[12] I. Solomon, M. P. Schmidt, H. Tran-Quoc, *Phys. Rev. B* **38**, 9895 (1988).

[13] L. R. Tessler, I. Solomon, *Phys. Rev. B* **52**, 10962 (1995).

[14] G. Ambrosone, V. Ballarini, U. Coscia, S. Ferrero, F. Giorgis, P. Maddalena, A. Patelli, P. Rava, V. Rigato, *Thin Solid Films* **427**, 279 (2003).

[15] I. Solomon, Appl. Sci. Surf. 184, 3 (2001).

[16] M. A. Lieberman, A. J. Lichtenberg, *Principles of Plasma Discharges and Materials Processing*, John Wiley & Sons, Inc., New York, 1994, Ch 11.

[17] S. Ray, C. Das, S. Mukhopadhyay, S. C. Saha, *Solar Energy Materials & Solar Cells* **74**, 393 (2002).

[18] J.-Y. Kim, B.-W. Lee, H.-S. Nam, D. Kwon, *Thin Solid Films* **467**, 294 (2004).

[19] W. M. M. Kessels, J. P. M. Hoefnagels, P. J. van den Oever, Y. Barrell. M. C. M. van de Sanden, *Surface Science* **547**, L865 (2003).

[20] W. M. M. Kessels, A. H. M. Smets, D. C. Marra, E. S. Aydil, D. C. Schram, M. C. M. van de Sanden, *Thin Solid Films* **383**, 154 (2001).

[21] K. Sato, H. Haruta, Y. Kumashiro, *Phys. Rev. B* **55**, 15467 (1997).

[22] P. M. Voyles, J. E. Gerbi, M. M. J. Treacy, J. M. Gibson, J. R. Abelson, *J. Non-Crystalline Solids* **293-295**, 45 (2001).

[23] W. Luft, idem, p124-129.

[24] L. Boufendi, J. Gaudin, S. Huet, G. Viera, M. Dudemaine, *Appl. Phys. Lett.* **79**, 4301 (2001).

[25] K. Mui, F. W. Smith, *Phys. Rev. B* **38**, 10623 (1988).

[26] A. Bouchoule (Ed.), *Dusty Plasma*, John Wiley & Sons, Inc., New York, 1999, p162-165, 245-257.

[27] J. Perrin, C. Böhm, R. Etemadi, A. Lloret, *Plasma Sources Sci. Technol.* **3**, 252 (1994).

[28] G. S. Selwyn, J. E. Heidenreich, K. L. Haller, *J. Vac. Sci. Technol.* **A 9**, 2817 (1991).

[29] K. G. Spears, R. P. Kampf, T. J. Robinson, *J. Phys. Chem.* **92**, 5297 (1988).

[30] L. Boufendi, P. Roca i Cabarrocas, A. V. Kharchenko, private discussions, 2002.

[31] J. Perrin, C. Hollenstein, In : A. Bouchoule (Ed.), *Dusty Plasma*, John Wiley & Sons, Inc., New York, 1999, p77-180.

[32] D. D. Ebbing, *General Chemistry*, 3rd Edition, Houghton Mifflin, 1990.

[33] J. P. M. Schmitt, *J. Non-Crystalline Solids* **59-60**, 649 (1983).

[34] M. Hirose in J. I. Pankove (Ed.), *Semiconductor and Semimetals* **Vol. 21** : *Hydrogenated Amorphous Silicon* **Part A** : *Preparation and Structure*, Academic Press, Inc., Orlando, 1984, p13-17.

[35] J. L. Andùjar, E. Pascual, G. Viera, E. Bertran, *Thin Solid Films* **317**, 120 (1998).

[36] I. Géraurd-Grenier, V. Massereau-Guilbaud, A. Plain, *Eur. Phys. J. AP* **8**, 53 (1999).

[37] M. Heintze, M. Magureanu, M. Kettlitz, *J. Appl. Phys.* **92**, 7022 (2002).

[38] M.Takai, T. Nishimoto, M. Kondo, A. Matsuda, *Science and Technology of Advanced Materials* **2**, 495 (2001).

[39] J. P. Boeuf, *Phys. Rev. A* **46**, 7910 (1992).

[40] A. Okada, K. Kijima, *Vacuum* **65**, 319 (2002).

[41] V. M. Donnelly in O. Auciello and D. L. Flamm (Eds.), *Plasma Diagnostics: Discharge Parameters and Chemistry*, **Vol. 1**., Academic Press, Inc., San Diego, CA, 1989.

[42] J. H. Van Vleck, V. F. Weisskopf, *Rev. Mod. Phys.* **17**, 227 (1945).

[43] T. Novikova, B. Kalache, P. Bulkin, K. Hassouni, W. Morscheidt, P. Roca i Cabarrocas, *J. Appl. Phys.* **93**, 3198 (2003).

[44] A. Gicquel, M. Chenevier, Kh. Hassouni, A. Tserepi, M. Dubus, *J. Appl. Phys.* **83**, 7504 (1998).

[45] T. Makabe, F. Tochikubo, M. Nishimura, *Phys. Rev. A* **42**, 3674 (1990).

[46] B. Xiao, S. Kado, S. Kajita, D. Yamazaki, *Plasma Phys. Control. Fusion* **46**, 653 (2004).

[47] N. Maley, *Phys. Rev. B* **46**, 2078 (1992).

[48] P. I. Rovira, F. Alvarez, Phys. Rev. B 55, 4426 (1997).

[49] H. D. Fuchs, M. Stutzmann, M. S. Brandt, M. Rosenbauer, J. Weber, A. Breitschwerdt, P. Déak, M. Cardona, *Phys. Rev. B* **48**, 8172 (1993).

[50] R. Saleh, L. Munisa, W. Beyer, *Thin Solid Films* **426**, 117 (2003).

[51] F. Vivet, A. Bouchoule, L. Boufendi, *J. Appl. Phys.* **83**, 7474 (1998).

[52] G. Fanchini, P. Mandracci, A. Tagliaferro, S. E. Rodil, A. Vomiero, G. Della Mea, *Diamond Relat. Mater.* **14**, 928 (2005).

[53] G. Viera, S. Huet, L. Boufendi, *J. Appl. Phys.* **90**, 4175 (2001).

[54] A. Zwick, R. Carles, *Phys. Rev. B* **48**, 6024 (1993).

[55] P. Mishra, K. P. Jain, *Phys. Rev. B* **64**, 073304 (2001).

[56] Z. Hu, X. Liao, H. Diao, G. Kong, X. Zeng, Y. Xu, *J. Cryst. Growth* **264**, 7 (2004).

[57] J. S. Lannin in J. I. Pankove (Ed.), *Semiconductor and Semimetals* **Vol. 21** : *Hydrogenated Amorphous Silicon* **Part B** : *Optical Properties*, Academic Press, Inc., Orlando, 1984, p159-195.

[58] A. Foncuberta i Morral, H. Hofmeister, P. Roca i Cabarrocas, *J. Non-Crystalline Solids* **299-302**, 284 (2002).

[59] V. Suendo, A. V. Kharchenko, P. Roca i Cabarrocas, *Thin Solid Films* **451-452**, 259 (2004).

Chapter 5

Optoelectronic properties of *pm-$Si_{1-x}C_x$:H* A material for photonic applications

5.1. Introduction

The synthesis of hydrogenated polymorphous silicon carbon (*pm-$Si_{1-x}C_x$:H*) films is based on deposition conditions derived from polymorphous silicon (*pm-Si:H*). Thus, the structure of *pm-$Si_{1-x}C_x$:H* films consists of nanocrystals and/or their agglomerates embedded in an amorphous matrix, which resembles the structure of *pm-Si:H* (see Fig. 4.21). By adding methane to the reactive plasma, we obtain a higher deposition rate and a wider optical band gap with respect to *pm-Si:H*, which are important parameters for optoelectronic applications. Interestingly, we have observed a strong luminescence at room temperature on this material, which can be even seen by naked eye (see Fig. 1.1). Our studies show that the luminescence properties depend on the deposition conditions and are stronger when particles are present in the plasma. The origin of the luminescence is still unclear due to the complex structure of the material. Indeed, the luminescence center can be the *a-$Si_{1-x}C_x$:H* matrix, the silicon nanocrystals, or even the interfaces between them. Another important property of *pm-$Si_{1-x}C_x$:H* alloys is their low defect density even at high carbon content, which should reduce non-radiative recombination.

In this chapter, we focus on the optoelectronic properties of *pm-$Si_{1-x}C_x$:H*. From the analysis of the film properties, we try to understand the relationship between the deposition conditions and optoelectronic properties. Further, by correlating with the structural characterization in Ch. 4 and comparing with some standard *a-$Si_{1-x}C_x$:H* alloys, the origin of the luminescence in this material is discussed.

5.2. Optical properties of polymorphous silicon carbon alloys

Absorption coefficient and optical gap

In this section, we present the effect of the deposition conditions on the optical properties of *pm-$Si_{1-x}C_x$:H*. The methane flow rate was kept constant at 33 sccm. Optical properties were extracted from SE measurements in the photon energy range from 1.5 to 5 eV by fitting the experimental data using Tauc-Lorentz (TL) model as explained in Ch. 2 (see Fig. 2.10).

Effect of pressure

The total pressure was varied in a wide range from 800 up to 3500 mTorr. Fig. 5.10 shows the absorption coefficient spectra extracted from SE data. It shows that the increase of the total pressure does not produce a monotonous trend. Indeed, at low energy (2-3 eV), the absorption coefficient is shifted towards high energy as the deposition pressure increases.

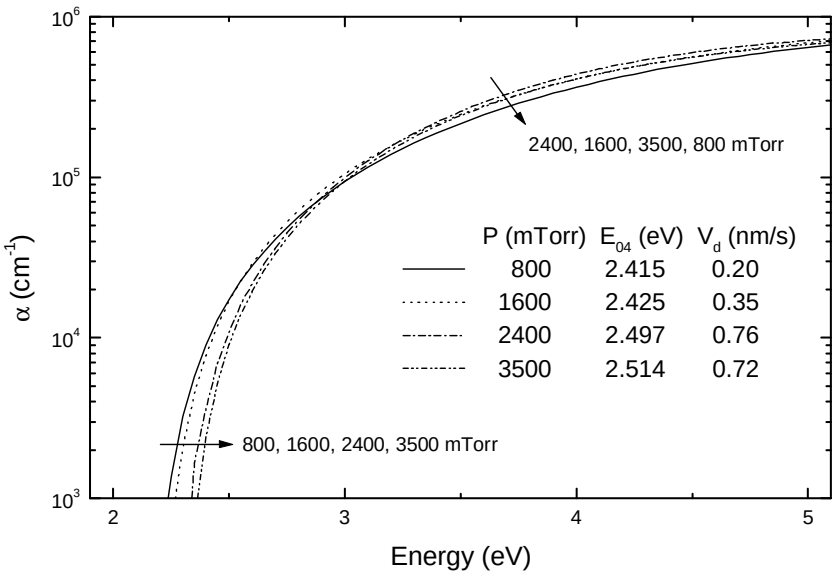

Fig. 5.10. Effect of the deposition pressure on the absorption coefficient of *pm-$Si_{1-x}C_x$:H* films deposited at 200 °C, 20 W of RF power and with gas flow rate of 33, 10 and 90 sccm for CH_4, SiH_4 and H_2 gases respectively.

Here, we can observe a slight nonlinearity on the spectral shift with the increase of pressure, which might correspond to the same transition observed in the pressure dependence of the deposition rate discussed in Ch. 4 (see Fig. 4.3). On the other hand, in the high energy range,

the value of the absorption coefficient decreases in the following order of deposition pressure: 2400, 1600, 3500 and 800 mTorr.

The legend in Fig. 5.10 shows the effect of pressure on the optical band gap (E_{04}), which provides quantitative information of the shift of the absorption spectra at low energy. As the deposition pressure increases, the value of E_{04} increases slightly between 800 and 1600 mTorr, followed by a sharp increase between 1600 and 2400 mTorr, and again a slight increase between 2400 and 3500 mTorr. As indicated above, the sharp increase in E_{04} can be related to the transition in deposition rate due to the change in the nature of species contributing to deposition.

Effect of RF power

The RF power was varied between 10 and 30 W (0.105 – 0.315 W/cm^2). The increase of RF power gives a monotonous trend on the absorption coefficient for all energy range (see Fig. 5.11). In the low energy part, α is shifted towards high energy with the increase of RF power as shown by the evolution of E_{04} given in the legend of Fig 5.11. This shift might correspond either to the increase of carbon, hydrogen, nanocrystallites or their combination.

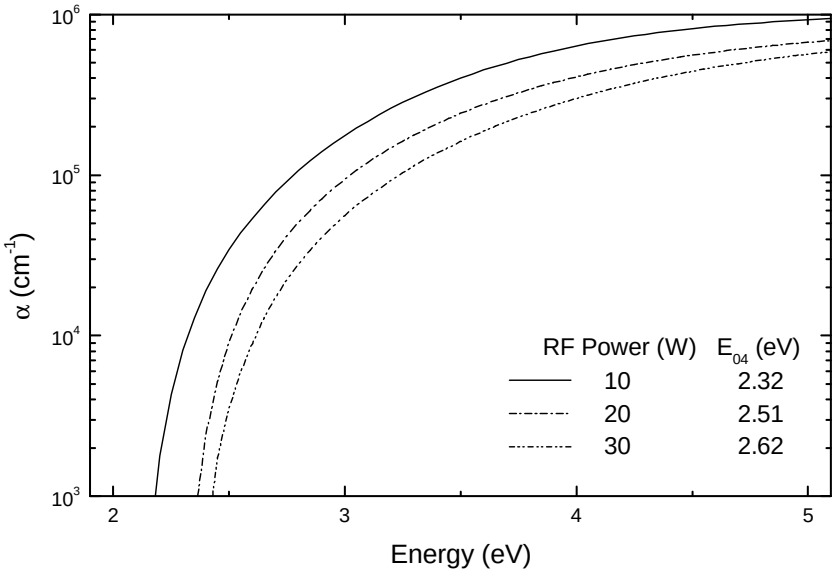

Fig. 5.11. The effect of RF power on the absorption coefficient of *pm-Si$_{1-x}$C$_x$:H* films deposited at 200 °C and 3500 mTorr.

Effect of methane flow rate

The methane flow rate was varied from 8 up to 33 sccm, in order to increase the band gap of films, which is strongly related to their luminescence properties. Fig. 5.12 shows the absorption coefficient for samples deposited under 3500 mTorr of total pressure with 20 W of RF power and 200 °C of substrate temperature, a condition optimized for a strong luminescence. Here, the absorption coefficient spectra are shifted towards high energy with the increase of the methane flow rate as previously reported in literature [1-7]. This shift corresponds to the increase of the band gap of the material as shown by the value of E_{04} given in the legend of Fig. 5.12. As in the case of the RF power, we observe a monotonous trend with the change of methane flow rate. In the low energy part, it shows a shift towards high energy due to the increase of the band gap, while at high energy, a decrease of amplitude is observed with the increase of methane flow rate.

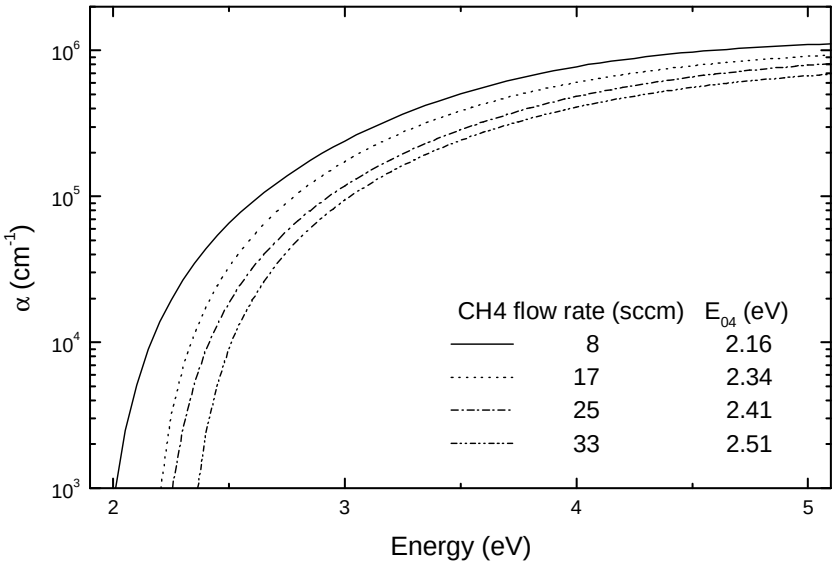

Fig. 5.12. The effect of methane flow rate on the absorption coefficient of *pm-$Si_{1-x}C_x$:H* films deposited at 200 °C, 3500 mTorr and 20 W of RF power.

Effect of substrate temperature

The substrate temperature was varied from 100 up to 300 °C at two different pressures (2000 and 3500 mTorr) which represent deposition regimes before and after the maximum in the pressure dependence of deposition rate at 200 °C (see Fig 4.3). In principle, there is a significant difference between these two presures in the species contributing to deposition, due to powder formation at 3500 mTorr. At 200 °C, the agglomeration of nanocrystals formed in the plasma phase occurs at 2000 mTorr, while large agglomerates and powders are trapped in the plasma at 3500 mTorr. However, the increase of substrate temperature affects the powder formation process [8]. As shown in Ch. 4, the increase of the temperature will shift the α–γ' transition towards higher pressure, which will result changes in the film precursors and thus the material properties for a fixed pressure (see Fig 4.6).

Fig. 5.13a and b show the absorption coefficient for samples deposited at various substrate temperatures at 2000 and 3500 mTorr, respectively. For both pressures, the increase of the substrate temperature gives the same general trend: a shift of the absorption spectra towards low energy along with an increase in the value of the absorption coefficient. As the temperature increases, the spectra at 2000 mTorr are shifted linearly towards low energy and their high energy part shows a monotonous increase of amplitude (Fig. 5.13a). On the other hand, at 3500 mTorr, in the powder formation regime, the behavior is quite different. A nonlinear shift of the spectrum towards low energy is observed, characterized by a slight shift between 100 and 200 °C, and an abrupt shift between 200 and 300 °C (Fig. 5.13b). At high energy, the increase of the amplitude with substrate temperature follows a monotonous trend as shown in Fig. 5.13b. The different behavior for the two series of samples is clearly shown in in Fig. 5.14, where E_{04} is plotted as a function of substrate temperature. It linearly decreases as temperature increases for samples deposited at 2000 mTorr. On contrary, for deposition at 3500 mTorr, a nonlinear evolution is observed, characterized by a slight decrease between 100 and 200 °C and a steep decrease for higher temperature.

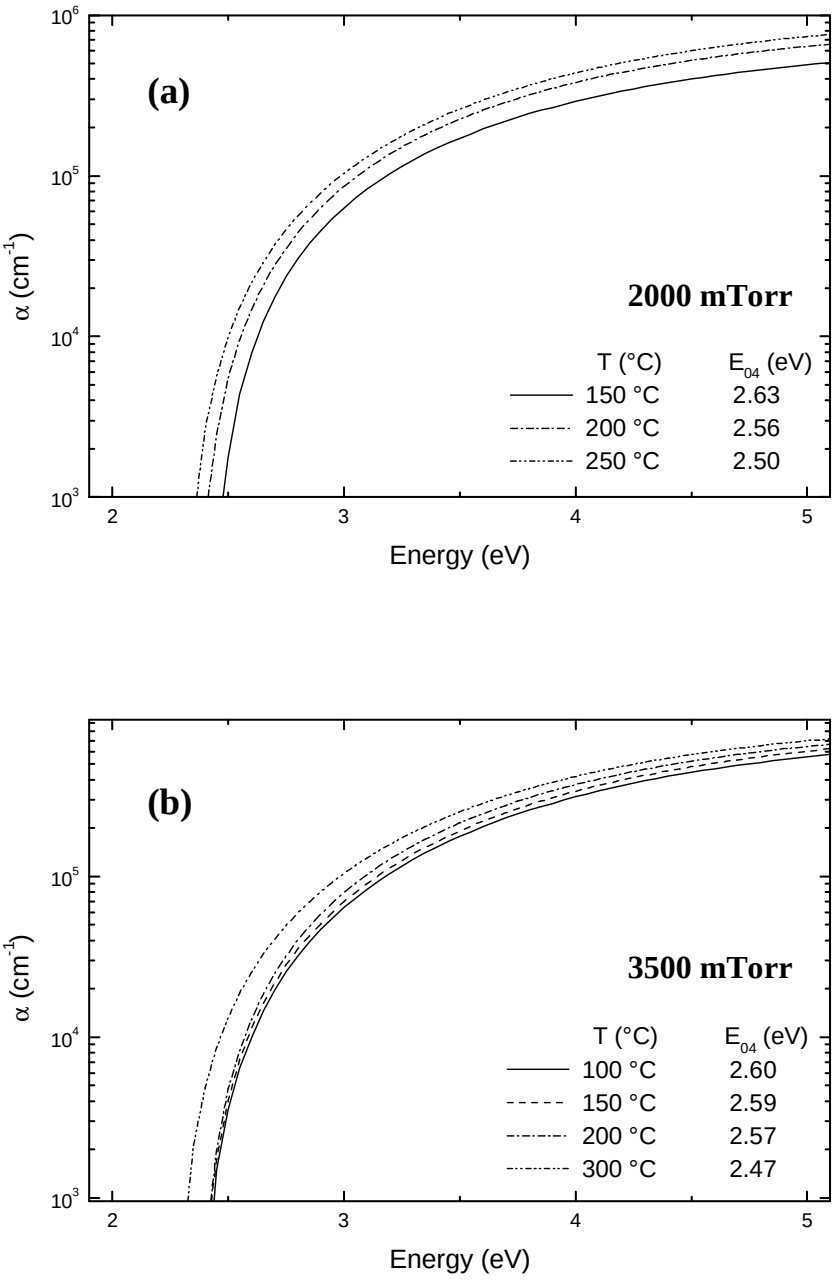

Fig. 5.13. The effect of the substrate temperature on the absorption coefficient of *pm-*$Si_{1-x}C_x$:*H* films deposited at a) 2000 and b) 3500 mTorr with 20 W of RF power.

The distinct dependence of the optical gap as a function of substrate temperature between samples deposited at 2000 and 3500 mTorr can be related to the differences in the structure of deposited particles, which induces dissimilar hydrogen desorption processes. Note that a fast deposition of hydrogenated aggregates at 3500 mTorr will be quite different from a slow deposition of individual nanocrystals. Then, let us recall that the concentration of incorporated hydrogen in amorphous silicon and its alloys, determines the optical gap of materials [1]. Thus, it can be one explanation why the optical gap evolves differently between these two cases. Besides the incorporation of silicon nanocrystals and their agglomerates with different characteristics, the size and the number of deposited individual particles will affect the absorption coefficient as well. Note that we measure an average absorption coefficient of the film which takes into account the absorption coefficient of incorporated particles.

The increase of substrate temperature inhibits the particle formation through gas

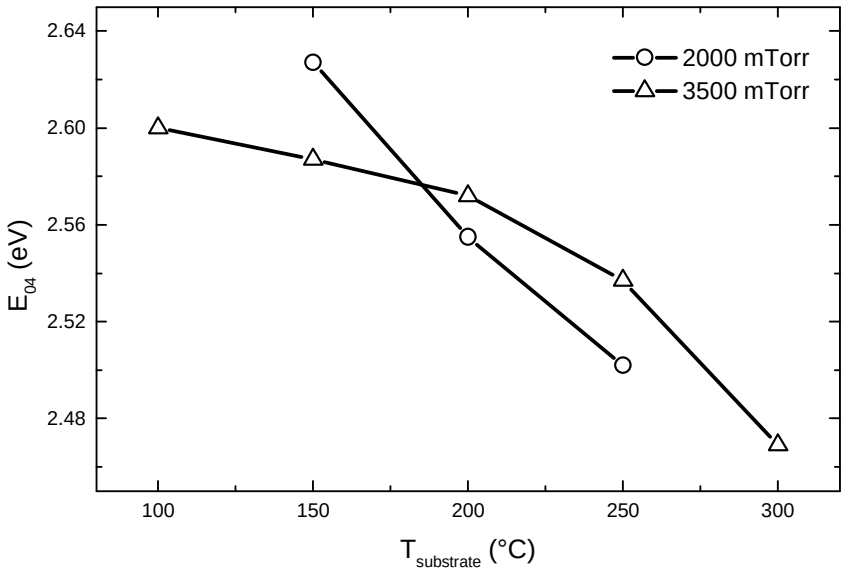

Fig. 5.14. The effect of substrate temperature on optical band gap, E_{04}, for of *pm-*$Si_{1-x}C_x$ *:H* films deposited at 2000 and 3500 mTorr with a RF power of 20 W.

heating, as observed in the deposition of polymorphous silicon [8]. Moreover, the increase of the substrate temperature in the range of 100-300 °C may affect the surface rearrangement and cross-linking reactions leading to hydrogen desorption, but it does not affect the sticking probability on the surface [9]. Therefore, the increase of substrate temperature might affect the change of optical gap mainly through the changes in the structure of deposition building

blocks and hydrogen content of resulting films. The structure of building block also determines other processes responsible for the gap determination such hydrogen desorption.

Tauc-Lorentz model fitting parameters from SE data

In the same way as in the previous section, here we show the results of the analysis of the SE data, related to the interpretation of the Tauc-Lorentz model. The changes in the parameters of the model used to fit the SE data are studied as function of the controllable experimental parameters such as pressure, RF power, methane flow rate, and substrate temperature.

Effect of pressure

Fig. 5.15 shows pressure dependence of the Tauc-Lorentz model parameters used to analyze the SE data. As pressure increases, the widening of E_g is characterized by a nonlinearity between 1600 and 2400 mTorr, even though less pronounced than for E_{04} (Fig. 5.10).

The broadening parameter C decreases and reaches a minimum value with the increase of deposition pressure as shown in Fig. 5.15b. This parameter reflects the broadening of the optical transition state, which normally corresponds to the defects that increase the density of states in the band edge. Even though the TL model cannot provide the information on tail states in the band edge, the broadening parameter can be considered as a quantity that represents these states since by fitting we took the average value of the absorption edge. The peak transition energy E_0 tends to decrease monotonically as pressure increases (Fig. 5.15c), which shows an opposite behavior with respect to the optical band gap. This result tells us that the increase of pressure does not increase the average energy difference between VB and CB, but only reduces the defect states, leading to the narrowing of the tails. Overall, this narrowing results in the increase of the optical band gap energy, i.e. E_{04} and E_g.

The amplitude factor A tends to increase with pressure. Fig 5.15d, shows a sharp increase between nanocrystal formation and agglomeration regimes which then achieves a saturation. This parameter correlates with the electronic density of the materials and it can be used as an indicator to compare their density. This method should be valid as long as applied among materials which have similar chemical composition. Thus, the results shown in Fig. 5.15d suggest the increase of material density with pressure. However, we also observe the evolution with pressure of another parameter that correlates with the density of material, the

refractive index at 632.8 nm ($n_{632.8}$) as shown in Fig 5.15e. This parameter shows a different tendency with respect to the amplitude factor *A*, especially at high pressures where the agglomerates are present.

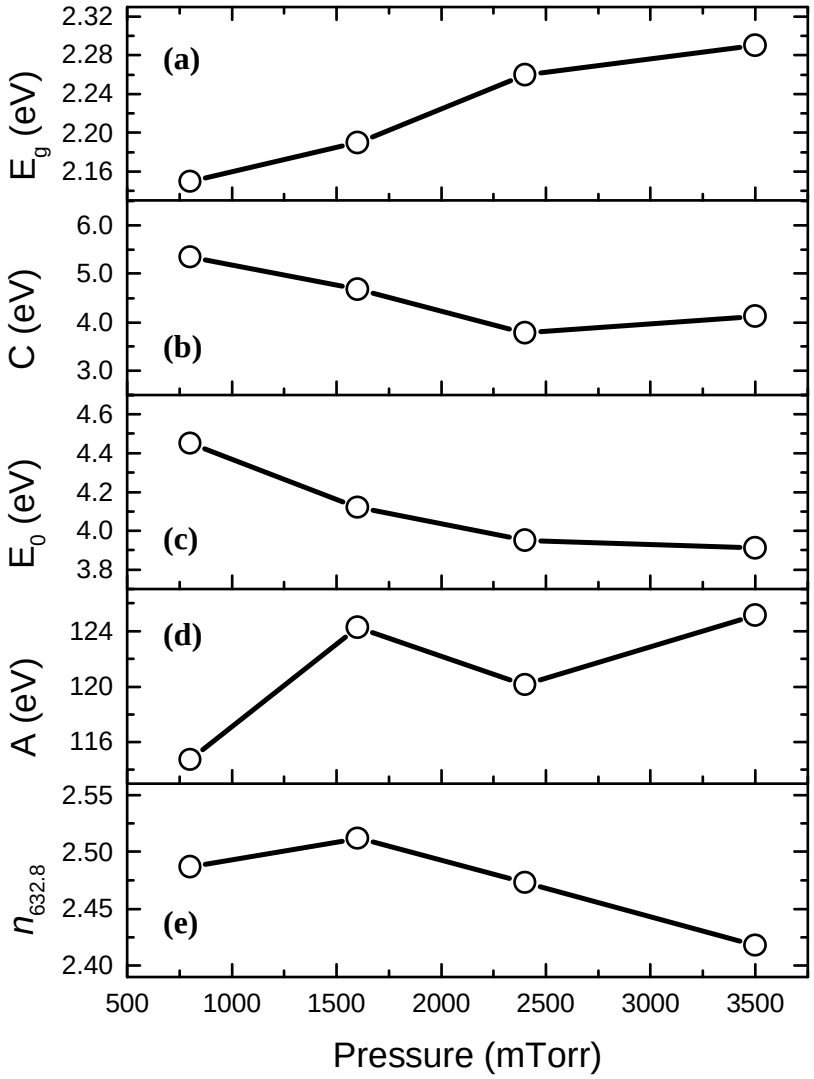

Fig. 5.15. The pressure dependence of a) Tauc's band gap energy (E_g), b) broadening parameter (C), c) transition peak energy (E_0), d) amplitude factor (A) and e) refractive index at 632.8 nm ($n_{632.8}$) of *pm-*$Si_{1-x}C_x$ *:H* films deposited at 200 °C with an RF power of 20 W.

Effect of RF power

The increase of RF power gives a linear dependence for all fitting parameters of the Tauc-Lorentz model as shown in Fig. 5.16. All fitting parameters have the same tendency to increase with RF power except for amplitude factor A and refractive index $n_{632.8}$. The increase of RF power corresponds to the increase of the amount of energy injected into the plasma system, which increases the electron density, their energy and as a consequence the dissociation rate of SiH_4 and CH_4 molecules. Owing to the difference in cross section for dissociation of SiH_4 and CH_4, the CH_4 molecules are more difficult to dissociate than SiH_4. Thus, the increase of RF power enhances the dissociation of CH_4, which increases the carbon content and the band gap of the films. Therefore, we can observe the increase of Tauc's band gap E_g with RF power. The increase of the broadening parameter C might be due to the increase of carbon content which is well-known to induce compositional disorder in the amorphous structure [1-7]. Another kind of disorder, due to defects might be related to ion bombardment, which becomes more severe by increasing the RF power. Here, the increase of the band gap can refer to the "true" band gap widening, which is reflected by the increase of both the Tauc's band gap E_g and the peak transition energy E_0 (see Fig. 5.16a and c). As mentioned before, the peak transition energy corresponds to the energy where the transition between VB and CB occurs with the maximum probability [10]. In other words, if the value of E_0 increases, it means that the average probability of transition is shifted towards high energy.

However, it is clear that even though both E_g and E_0 increase with RF power, they do not follow the same trend (Fig 5.16a and c). As RF power increases, the increase of E_0 is mainly due to the contribution of different composition of chemical bonds, which determines the structure of the bands. Each type of chemical bond will contribute to the shape of the band, based on their bonding and anti bonding molecular orbital states. Here, we emphasize on four types of chemical bonds Si-Si, Si-H, Si-C and C-C sp^3, which represent the chemical structure of *pm-*$Si_{1-x}C_x$*:H*. The Si-Si bond is the main chemical bond for all *a-Si:H* based alloys, which includes *pm-*$Si_{1-x}C_x$*:H*. As the other three chemical bonds concentration increases in the alloys, their band gap energy tends to increase. The increase of band gap energy here refers to the shift of interband transition, which is due to the overlapping of bonding and anti-bonding states among different types of chemical bonds. The value of E_0 can reflect this situation. If we look back, E_g represents the gap energy between lowest states in

CB and the highest states in VB, which in practice takes into account the defect states near the band edge [10]. Fig 5.16d shows that the amplitude factor *A* decreases with RF power linearly, which indicates the decrease in density. It is in a good agreement with the fact that the deposition rate increases linearly with RF power as well as the contribution of nanocrystals/clusters and their agglomerates (see Fig 4.5b). Thus, the decrease of amplitude factor or density may be due to the deposition of large building blocks with the lack of time for rearrangement on the film surface leading to a porous film. The similar behavior was also observed on the evolution of refractive index shown in Fig. 5.16e. Overall, the increase of RF power leads to the expected evolution of optical parameters.

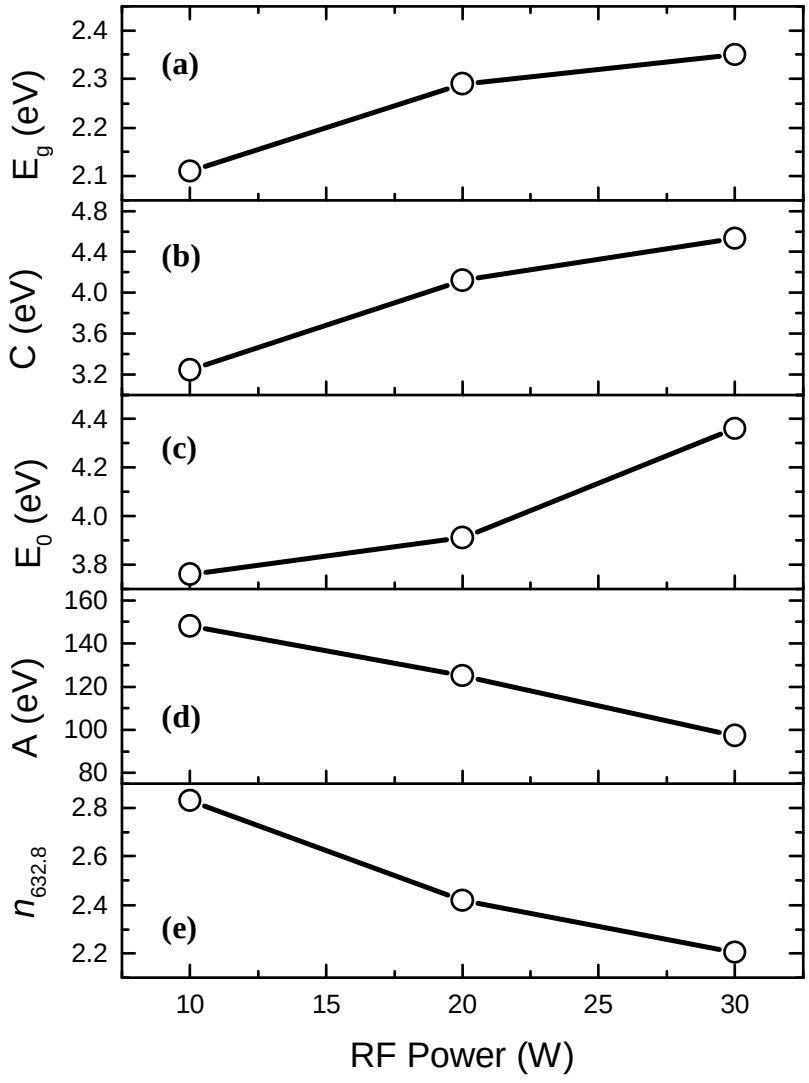

Fig. 5.16. The RF power dependence of a) Tauc's band gap energy (E_g), b) broadening parameter (C), c) transition peak energy (E_0), d) amplitude factor (A), and e) refractive index at 632.8 nm ($n_{632.8}$) of *pm-*$Si_{1-x}C_x$*:H* films deposited at 200 °C under total pressure of 3500 mTorr.

Effect of methane flow rate

The main purpose of varying of the methane flow rate is to adjust the optoelectronic properties of the films by alloying silicon with carbon. In the case of *a-*$Si_{1-x}C_x$*:H* alloys, the most evident effect of the increase of carbon content is the increase of optical band gap energy [1-7]. In some optoelectronic applications such as solar cells, optical filters and electroluminescent devices, materials with higher gap than *a-Si:H* are needed. Thus, alloying is necessary to fulfill this demand. For luminescence applications, the control of the band gap energy is very important because it determines the wavelength of the emitted light, where the radiative process is the band-to-band and tail-to-tail transitions in most amorphous semiconductors.

Fig. 5.17 shows the methane flow rate dependence of Tauc-Lorentz fitting parameters. In general, all fitting parameters tend to increase with methane flow rate except for the amplitude factor *A* and the refractive index $n_{632.8}$. Fig 5.17a shows that the increase of CH_4 flow rate increases the Tauc's band gap E_g as expected from the increase of carbon content [1-7]. This increase is followed as well by the increase of the broadening term *C*, which represents the increase of disorder due to alloying (Fig 5.17b). However, the peak transition energy (Fig 5.17c) increases in a different manner, thus suggesting that the change in E_g is mostly like due to the increase of hydrogen content rather than to the contribution of carbon. As the methane flow rate continues to increase, E_0 increases abruptly, which might be due to the formation of Si-C bonds that widen the gap.

The abrupt transition observed for E_0 can be observed in the evolution of the amplitude factor *A* as shown in Fig 5.17d. If we correlate this parameter with the density of the material, then it tells that the films density decreases abruptly when CH_4 flow rate increases from 17 to 25 sccm. As previously discussed, at high deposition rate, the density of the films tends to be low due to the lack of time for the rearrangement of the arriving constituents. Another reason for the decrease of density might be the effect of alloying with carbon, which does not favor a compact structure. If we look back at Fig. 4.5b, which shows a linear increase of deposition rate with methane flow rate at 3500 mTorr, then the abrupt decrease in amplitude factor or density cannot be explained by the building block packing problem due to the different rearrangement duration only. However, as discussed as well in Ch. 4, based on the observation of electrical parameters of the plasma, a small amount methane tends to retard the particle formation, while a large amount favors it. Thus, if we correlate the effect of adding

methane with the evolution of amplitude factor *A*, it gives a good agreement. At low methane flow, we deposit most likely small particles, while at high methane flow rate the large particles are deposited, thus leading to the abrupt decrease in density.

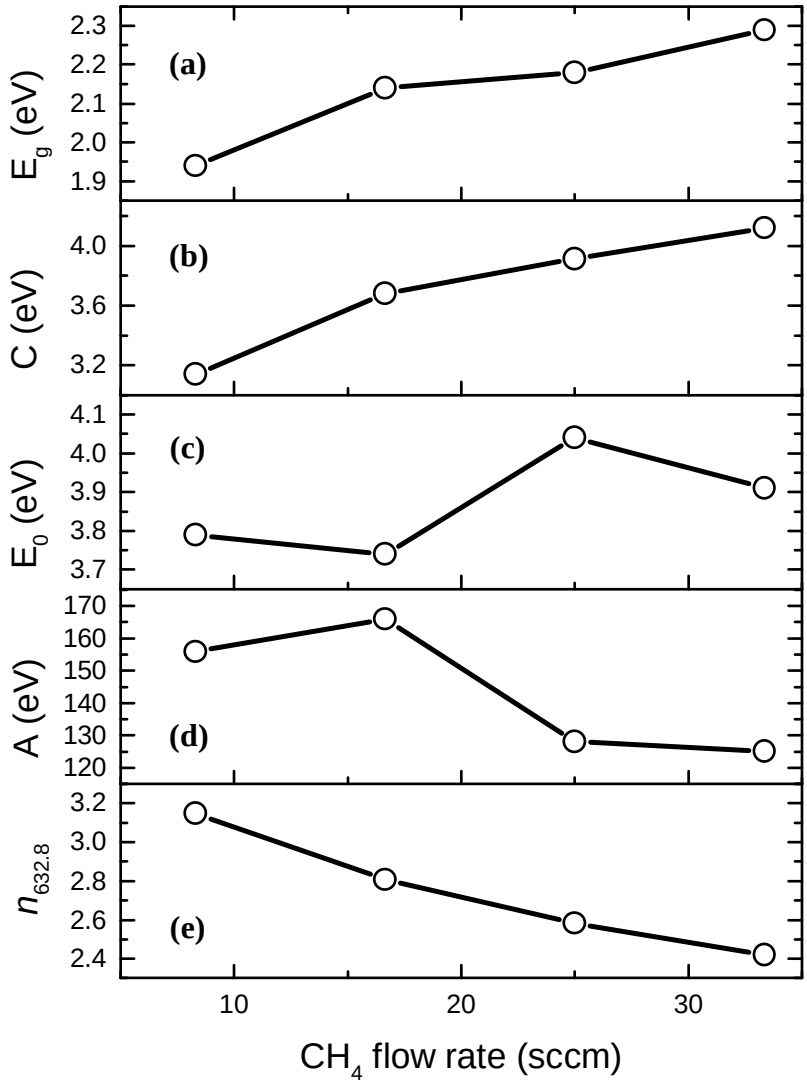

Fig. 5.17. The CH_4 flow rate dependence of a) Tauc's band gap energy (E_g), b) broadening parameter (C), c) transition peak energy (E_0), d) amplitude factor (A), and e) refractive index at 632.8 nm ($n_{632.8}$) of *pm-*$Si_{1-x}C_x$:*H* films deposited at 200 °C under total pressure of 3500 mTorr and 20 W of RF power.

In *a-*$Si_{1-x}C_x$*:H* alloys, it is well-known that the refractive index decreases as the concentration of carbon and optical band gap increase [1, 5, 7, 11]. The decrease of the refractive index can be correlated to the decrease of the density of materials (Fig. 5.17e).

Here, we can analyze the decrease of density from two different points of view. First, as mentioned in Ch. 4, the increase of methane flow rate facilitates an important increase in deposition rate (see Fig 4.5a), which induces the decrease of the material density due to a lack of time for rearrangement process during deposition. Second, due to the contribution of carbon atoms, we obtain a less dense structure with heterogeneous chemical bonds. Further, the contribution of carbon also increases the band gap of materials due to the formation of chemical bonds with higher transition energy between bonding and anti-bonding states such as Si-C or C-C sp^3.

Effect of substrate temperature

Fig. 5.18a shows the effect of the substrate temperature on E_g. For samples deposited at 2000 mTorr, the band gap energy decreases linearly with the increase of substrate temperature. On the other hand, the E_g of the samples deposited at 3500 shows an almost constant value up to 200 °C, followed by a decrease with the same trend as the samples deposited at 2000 mTorr. A similar feature can be observed for the broadening parameter *C*, as shown in Fig. 5.18b, where the samples deposited at 3500 mTorr show small changes for temperatures below 200 °C but not for 2000 mTorr samples. The samples deposited at 2000 mTorr show an important decrease of *C* between 150 and 200 °C, while it becomes constant for temperature higher than 200 °C. An opposite behavior between samples deposited at 2000 and 3500 mT is observed on the evolution of the peak transition energy E_0 as shown in Fig 5.18c. For samples deposited at 2000 mTorr, the peak transition energy increases linearly with substrate temperature, while E_0 decreases for samples deposited at 3500 mTorr. The interesting feature observed for 3500 mTorr samples is the transition around 200 °C. Fig 5.18d shows the evolution of the amplitude factor *A* as a function of substrate temperature, which has the similar tendency to increase for both pressures. However, the value of the amplitude factor *A* of samples deposited at 2000 mTorr still increases for temperature beyond 200 °C, while for the samples deposited at 3500 mTorr starts to saturate. This increase might be due to the rearrangement induced by temperature accompanied by the hydrogen desorption that leads to the film densification. We suggest that the different behavior between the two pressure regime is due to the different hydrogen incorporation, types of particles and rearrangement process during deposition at different substrate temperature. Moreover, regarding the evolution of E_g between samples deposited at 2000 and 3500 mTorr, we also can suggest that the hydrogen is bonded stronger at 3500 than at 2000 mTorr.

The increase of substrate temperature gives a linear increase in refractive index at both pressures, 2000 and 3500 mTorr as shown in Fig 5.18e. However the increase is more pronounced at 2000 mTorr. This indicates that the growth process of samples deposited at 2000 mTorr is more sensitive to thermal rearrangement and maybe to the hydrogen desorption process as well. In other words, the samples deposited at 3500 mTorr are more stable thermally than 2000 mTorr samples. This feature expresses the difference in deposition process between these two pressure regimes, which might be due to the different phases of particle formation in the plasma. Here, we have to see the effect of substrate temperature on both plasma and surface process. As discussed previously in Ch. 4, the increase of substrate

temperature tends to shift the α–γ' transition towards high pressure. Thus, the evolutions shown in Fig 5.18 can be interpreted as the effect of the shift of the α–γ' transition as well. At 2000 mTorr, we leave the agglomeration regime and enter the particle formation as the temperature increases. On the other hand at 3500 mTorr, we leave the powder formation regime and enter the agglomeration regime with the increase of temperature.

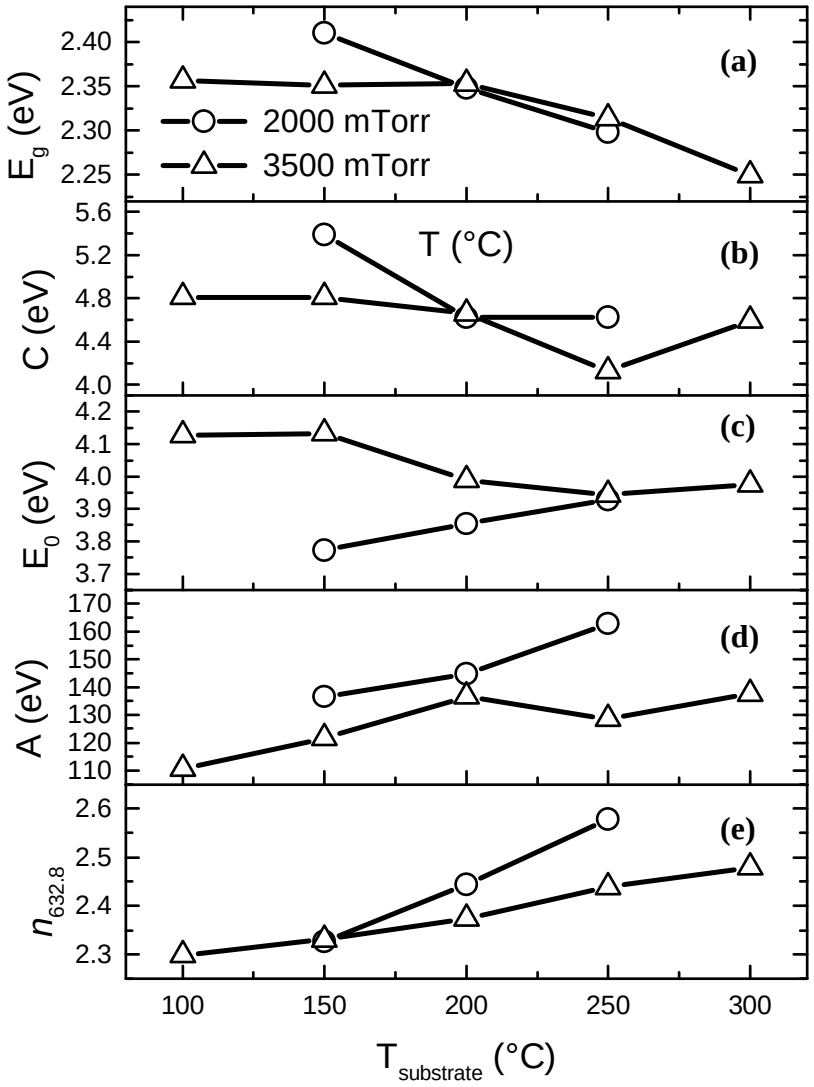

Fig. 5.18. The substrate temperature dependence of a) Tauc's band gap energy (E_g), b) broadening parameter (C), c) transition peak energy (E_0), d) amplitude factor (A) and e) refractive index at 632.8 nm ($n_{632.8}$) of *pm-Si$_{1-x}$C$_x$:H* films deposited at 20 W of RF power.

Defect density

In order to understand the contribution of the defect states inside the gap on the luminescence properties of hydrogenated polymorphous silicon carbon alloys, we performed photo-thermal deflection spectrometry (PDS) measurements which give access to very low values of the absorption coefficient as complementary to SE. Some of the results have been published [12].

Effect of pressure

Fig. 5.19 shows the absorption coefficient as a function of the photon energy for various values of the deposition pressure. Here, the absorption edge is shifted towards high energy with increasing pressure which indicates the increase of band gap energy. Besides that, the absorption coefficient inside the gap and band tails tends to decrease, indicating a lower defect density for materials deposited at higher pressure. The energy position of the features inside the gap (at around 1.5, 1.7 and 2.3 eV) as discussed in detail in [12], remains practically constant and only their intensity decreases. This suggests that with increasing pressure there is no formation of new type of states inside the gap. Note that the increase of pressure is accompanied by the increase of deposition rate.

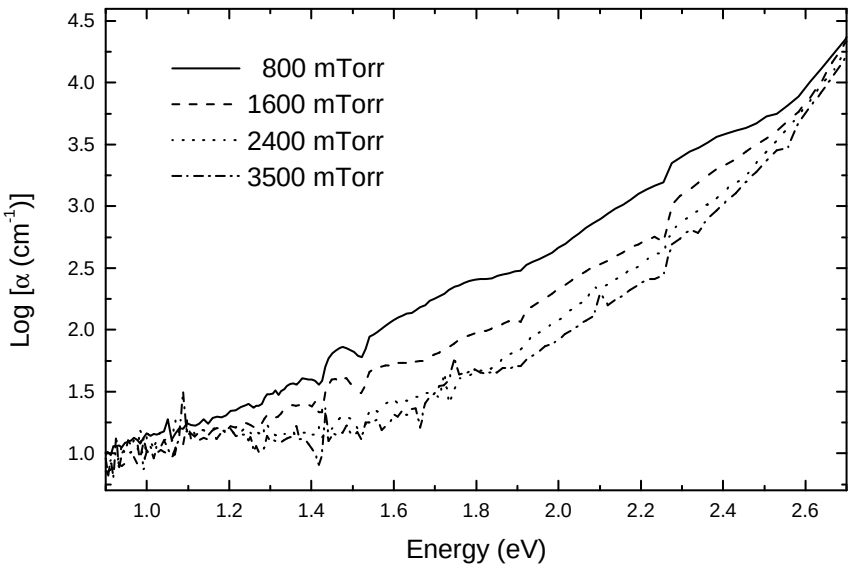

Fig. 5.19. Absorption coefficient for *pm-$Si_{1-x}C_x$:H* films deposited at various pressures with a substrate temperature of 200 °C and a RF power of 20 W.

Effect of RF power

The effect of RF power on the absorption coefficient is more pronounced for features in the band edge than inside the gap as shown in Fig. 5.20. The increase of RF power shifts the absorption edge towards high energy. Here, we observe that the decrease of the feature at 2.3 eV, is very pronounced, in particular between 10 and 20 W. Further increase in RF power yields more decrease in absorption coefficient at the band edge, while the absorption inside the gap remains constant. Thus, these results are in contrast with the general effect of increasing the RF power, namely an increase of the density of states and Urbach energy [13]. Here, the decrease in the absorption coefficient can be correlated with the decrease of the defect density and the contribution of different types of chemical bonds leading to the increase of the optical band gap [12]. Both, the decrease of the density of states and the increase of E_g enhance the radiative recombination process in the material, which is consistent with the results on PL measurements presented later on.

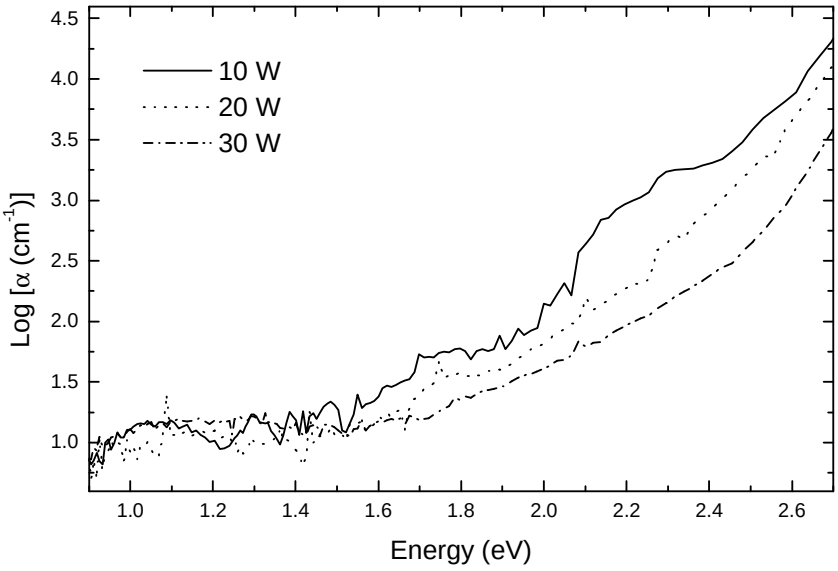

Fig. 5.20. Absorption coefficient for *pm-*$Si_{1-x}C_x$*:H* films deposited at 3500 mTorr, for various values of the RF power, at a substrate temperature of 200 °C.

Effect of methane flow rate

In general, the increase of the carbon content in *a-$Si_{1-x}C_x$:H* increases the density of states in the band edge, indicated by the increase of the Urbach energy, which represents the weak bonds due to the material disorder [1-7]. However, this is not the case for *pm-$Si_{1-x}C_x$:H* where we observed the opposite behavior, i.e., the intensity of the absorption coefficient near the absorption edge and inside the gap tends to decrease with the increase of methane flow rate. More interestingly, Fig. 5.21 shows that the strong feature around 2.3 eV decreases significantly with the increase of methane flow rate. As discussed elsewhere [12], this feature might be due to the overlap of several transition bands of different chemical bonds, which leads to a condition where the determination of the Urbach energy is not reliable in the case of *a-$Si_{1-x}C_x$:H* alloys. The disappearance of the feature at 2.3 eV is accompanied with a decrease in the intensity of the feature in the range of 1.8–2.2 eV and of the broad feature centered at 1.5 eV, which even disappears with the increase of methane flow rate.

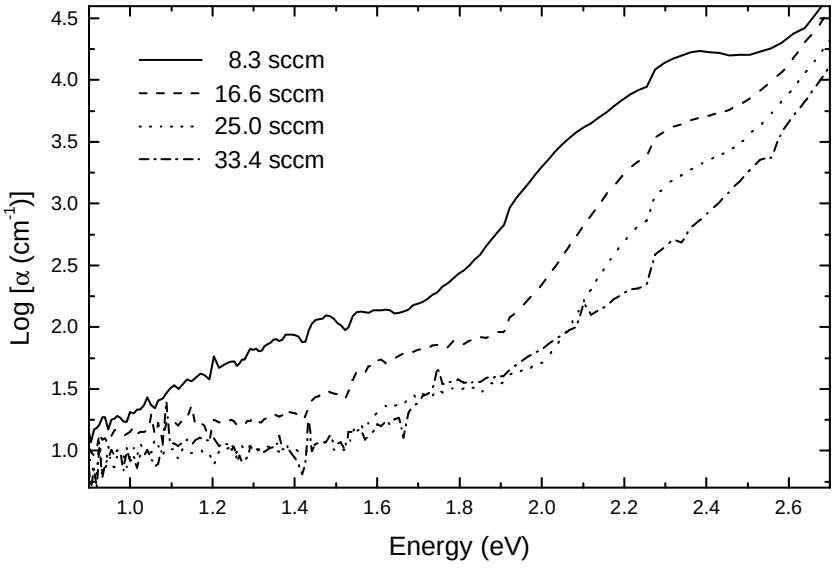

Fig. 5.21. Absorption coefficient for *pm-$Si_{1-x}C_x$:H* films deposited at 3500 mTorr for various methane flow rates with substrate temperature of 200 °C and 20 W of RF power.

5.3. Photoluminescence of polymorphous silicon carbon alloys

In this section, we discuss the effect of deposition parameters on the characteristics of the PL spectra of *pm-$Si_{1-x}C_x$:H*. As shown in the previous sections, these parameters are responsible for the changes in film properties. Thus, they should also affect the characteristics of the PL spectra. We focus on the PL feature between 1.2 and 2.4 eV, but not the weak feature at around 2.6 eV which might be due to the presence of an oxide layer on the films.

Effect of pressure

The deposition pressure plays an important role in the synthesis of polymorphous materials which deposition is closely related to the formation of particles in the plasma. Fig. 5.22 shows that the intensity of PL increases with deposition pressure. As for the film properties, we can see an important increase on PL intensity between 800 and 1600 mTorr

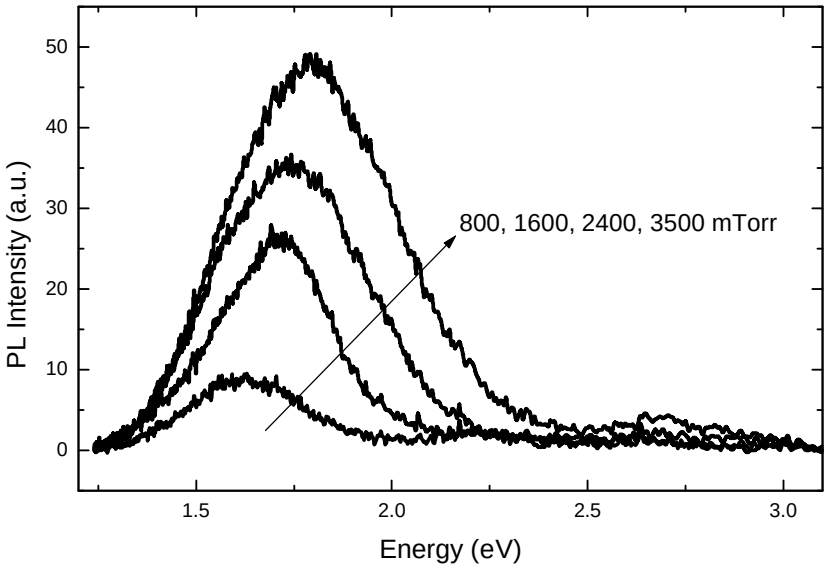

Fig. 5.22. The room temperature PL spectra of *pm-$Si_{1-x}C_x$:H* films deposited at 200 °C with 20 W of RF power for various total pressure between 800 and 3500 mTorr. The samples were excited using a HeCd laser at 325 nm (3.8 eV).

corresponding to the α–γ‘ transition. As shown in Table 5.1, it gives a strong increase of about 200 % in PL intensity. Between these regimes, the concentration of particles in the plasma increases significantly. At low pressure the particles are kept separated individually during growth until they reach a critical concentration, above which they start to agglomerate. The size of individual particles (nanocrystals) decreases with the increase of pressure, while

the the size of agglomerates increases and forms much larger particles. As a consequence, the number of deposited individual particles significantly increases in the α–γ' transition and results in the strong increase in both deposition rate and PL intensity. Further increase of pressure will induce the formation of larger agglomerates and powders, which of course will increase the concentration of deposited particles and of PL intensity. However, the increase of PL intensity is less pronounced above 1600 mTorr as shown in Table 5.1.

Table 5.1. Effect of deposition pressure on the PL spectra characteristics of *pm-*$Si_{1-x}C_x$*:H* samples

Pressure (mTorr)	E_{PL} (eV)	FWHM (eV)	$I_{PLinteg}$ (a.u.)	$E_{04} - E_{PL}$ (eV)
800	1.63	0.37	3.36	0.78
1600	1.70	0.38	10.08	0.72
2400	1.74	0.46	17.30	0.75
3500	1.80	0.51	25.81	0.71

The size of individual particles plays an important role to determine the PL emission energy. As explained in Appendix A, the PL emission energy of nanostructured silicon depends strongly on its size based on QSE. As pressure increases, we propose that the size of individual nanocrystals decreases, thus leading to a blue shift in PL spectra based on the QSE prediction. The experimental results (Fig 5.22) are in good agreement with our polymorphous silicon deposition model, where the size of nanocrystals decrease with pressure. The energy shift can be analyzed quantitatively based on their peak position as summarized in Table 5.1, which shows a linear trend with pressure.

Fig. 5.22 shows that the increase of pressure not only shifts the spectrum towards high energy but also enlarges the shape of spectrum. The quantitative representation of this enlargement is given by the value of FWHM. The evolution of FWHM is also interesting, as it follows the same trend as the evolution of PL intensity, and might be due to the widening of particle size distribution. The enlargement of the size distribution of agglomerates present in the plasma was observed when we increase the deposition pressure from 2400 to 3500 (see Ch. 4). We suppose that not only the size distribution of the agglomerates increases but also the size distribution of the individual particles. However, a direct probing method is necessary for further analyze these results.

Based on the value of PL emission energy, we can conclude that the radiative recombination occurs inside the gap. As listed in Table 5.1, the differences between band gap energy and the maximum of PL emission energy range between 0.71 and 0.78 eV for the

pressure series, which is a quite narrow value compared to “low-power” *a-Si*$_{1-x}$*C*$_x$*:H* (0.6-1.2 eV)[7]. The values of E_{04}-E_{PL} tend to decrease with the increase of pressure, which indicates that the blue shift of PL emission peak maximum is more important than the blue shift of the optical band gap. This result is in a good agreement with the deposition condition where the flow of methane was kept constant in this series. Thus, the increase of pressure mostly reduces the size of nanocrystals and increases their concentration, which leads to the blue shift of the PL emission peak.

Effect of RF power

The increase of RF power has an important effect on both the increase of PL intensity and emission energy. Fig. 5.23 shows that the PL spectra shifts towards high energy with increasing RF power and also leads to a strong increase of the PL intensity. If we compare with other deposition parameters such as total pressure or methane flow rate, we can see that RF power gives a stronger effect on PL intensity. The increase of RF power directly increases the electron density in the plasma, which accelerates the dissociation process of gases and leads to a faster particle formation. The increase of RF power may increase the PL properties of deposited materials as long as the effect of powder formation does not disturb the deposition process and the acceleration of particles to the deposition landing surface does not destroy their structure [14].

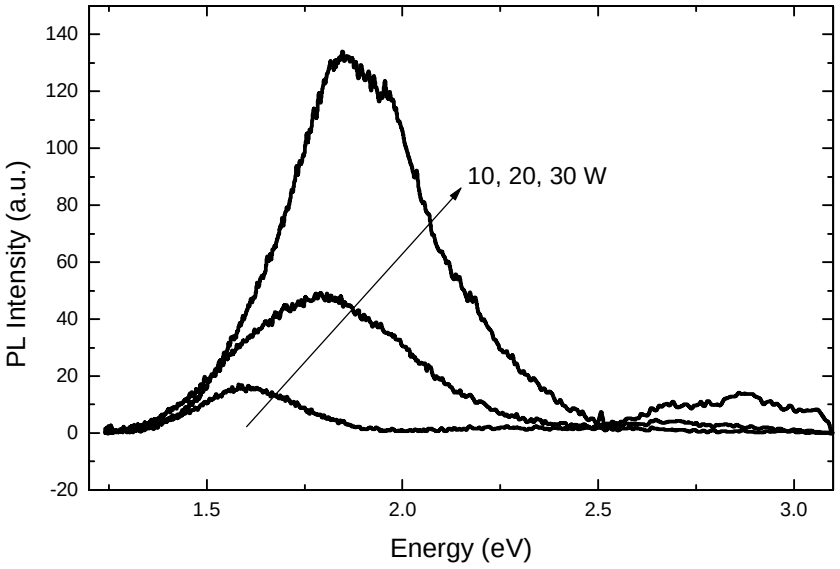

Fig. 5.23. Room temperature PL spectra of *pm-$Si_{1-x}C_x$:H* films deposited at 3500 mTorr with a substrate temperature of 200 °C for three values of the RF power. The samples were excited using a HeCd laser at 325 nm (3.8 eV).

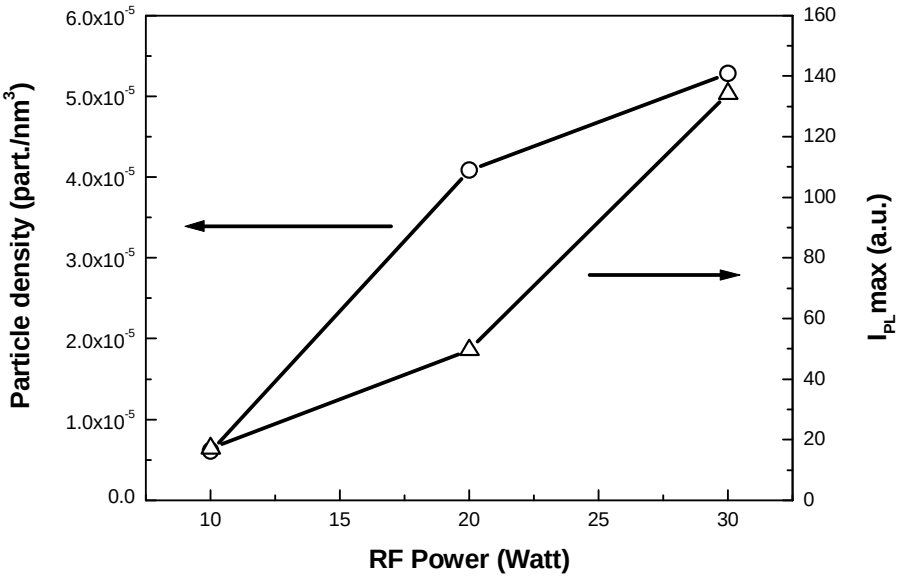

Fig. 5.24. The density of nanocrystals in the films (left) and the maximum intensity of PL spectra (right) as functions of RF power for *pm-$Si_{1-x}C_x$:H* samples deposited at 200 °C and 3500 mTorr with 33.4 sccm of methane. The particle density was deduced from TEM images.

Table 5.2. Effect of RF power on the characteristics of PL spectra *pm-$Si_{1-x}C_x$:H* samples

RF power (W)	E_{PL} (eV)	FWHM (eV)	$I_{PLinteg}$ (a.u.)	$E_{04} - E_{PL}$ (eV)
10	1.61	0.32	5.19	0.71
20	1.80	0.51	25.81	0.71
30	1.89	0.45	62.20	0.73

At high pressure, the nanocrystals are deposited in the form of large agglomerates, the number of embedded nanocrystals being proportional to the number of deposited agglomerates. Thus, the increase of PL intensity correlates with the increase of the density of embedded Si nanocrystals with increasing RF power (see Fig. 5.24). As the concentration of particles in the plasma increases, their size decreases also due to the fast formation process. This leads to the blue shift on the PL emission energy. Moreover, it is followed by the opening of the optical gap due to the transition from intermediate to high-power regime, which increases the carbon content significantly. Looking at the evolution of E_{04}-E_{PL}, we remark that the gap opening goes in the same pace as the blue shift of PL emission energy. The significant increase of PL intensity not only reflects the more efficient QSE by reducing size but also the increase of film transparency due to gap opening.

Effect of methane flow rate

Fig. 5.25 shows the effect of methane flow rate on the PL spectra of *pm-$Si_{1-x}C_x$:H* samples. A nonlinear increase is observed for the PL intensity, quantitatively shown in Table 5.3. First, the PL intensity increases significantly between 8 and 17 sccm, followed by a moderate increase up to 25 sccm and finally a steep rise for the increase of flow rate to 33 sccm. The same behavior is observed on the evolution of PL emission energy (E_{PL}) and FWHM with methane flow rate.

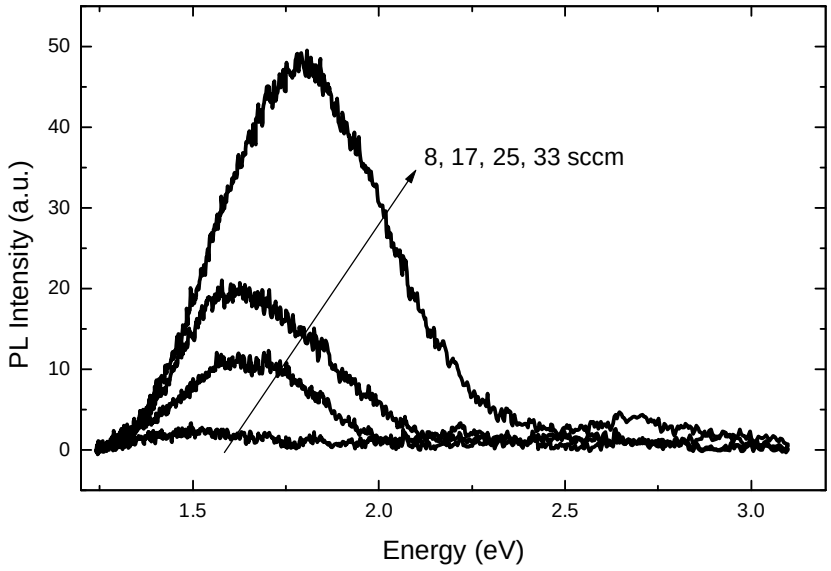

Fig. 5.25. The room temperature PL spectra of *pm-$Si_{1-x}C_x$:H* films deposited at 200 °C, 3500 mTorr and 20 W of RF power for different methane flow rates. The samples were excited using HeCd laser at 325 nm (3.8 eV).

The value of the difference between optical band gap and PL peak position energy (E_{04}-E_{PL}) tends to decrease with the increase of the methane flow rate. It indicates that the gap opening is less important than the blue shift of E_{PL} or might indicate independent origins for those two parameters. This behavior contrasts with that of *a-$Si_{1-x}C_x$:H* alloys, where the value of E_{04}-E_{PL} follows the same trend as the FWHM, the Urbach energy and the E_{PL}, namely to increase with carbon content [1]. If we consider the presence of silicon nanocrystals inside the film as observed by TEM, then we could suggest that the incorporation of carbon mostly induces the increase of band gap of matrix, while the increase of E_{PL} is due to the decrease of nanocrystal size induced by methane.

Table 5.3. PL spectra characteristics of *pm-$Si_{1-x}C_x$:H* samples at various CH_4 flow rates

CH_4 flow rate (sccm)	E_{PL} (eV)	FWHM (eV)	$I_{Plinteg}$ (a.u.)	$E_{04} - E_{PL}$ (eV)
8	1.53	0.37	0.88	0.88
17	1.65	0.41	4.90	0.78
25	1.67	0.43	9.14	0.83
33	1.80	0.51	25.81	0.71

Effect of substrate temperature

As shown in Fig 5.26a and b, the general effect of increasing the substrate temperature is to shift the PL emission energy towards low values, independently of the deposition pressure. The raw data were analyzed and the fitting results are summarized in Table 5.4, where we can observe as well a narrowing of PL spectra indicated by the decrease of FWHM and the increase of the value of E_{04}-E_{PL}.

Table 5.4. PL spectra characteristics of *pm-*$Si_{1-x}C_x$*:H* samples at various temperatures

T_{subs} (°C)	E_{PL} (eV)	FWHM (eV)	$I_{Plinteg}$ (a.u.)	$E_{04} - E_{PL}$ (eV)
2000 mTorr				
150	1.80	0.58	40.37	0.83
200	1.67	0.54	28.92	0.88
250	1.60	0.40	28.04	0.91
3500 mTorr*				
100	1.79	0.47	1.25	0.81
150	1.77	0.36	0.73	0.82
200	1.71	0.43	0.83	0.86
300	1.66	0.43	0.83	0.81

*) due to different optical setup, the absolute value of PL intensity cannot be compared

The red shift of the PL suggests that the increase of substrate temperature induces the deposition of larger silicon nanocrystals. The narrowing of PL spectra might correlate with two different aspects related to the size of silicon nanocrystals. First, the size itself, where as the crystal size decreases not only E_{PL} shifts towards high energy but the peak also becomes narrower as indicated by the decrease of FWHM [15]. The second point is the nanocrystal size distribution, which is directly responsible for the width of PL spectra. In this case, the spectral narrowing is related to the decrease of the nanocrystal size distribution because this is not followed by the blue shift of PL spectra. Then, by recalling the evolution of E_{04} as a function of substrate temperature (Fig 5.14), the increase of E_{04}-E_{PL} indicates that the decrease of E_{PL} is faster than that of E_{04} with the increase of substrate temperature. In other words, the increase of particle size by the shift of α–γ transition (in plasma phase) and/or by the "annealing like" rearrangement process (on the surface) gives a significant effect on the decrease of the particles effective gap (E_{PL}). This effect is even more important than the

substrate temperature effect on the optical gap of material (E_{04}), as can be seen from the increase of E_{04}-E_{PL} values with temperature. This argument can be explained by the $d^{-1.39}$ law based on the LCAO (linear combination of atomic orbital) technique used to calculate the electronic structure of silicon nanocrystals [15, 16], which we used to analyze the size of nanocrystals from their PL spectra. Note that according to this law, the confinement energy varies significantly depending on the nanocrystal size. The confinement energy follows the relation $\Delta E = (A/d^{1.39})$, where A is a constant (4.122 for *nc-Si*) and d is the diameter of the particle.

In Fig. 5.26, we also observe that the effect of the temperature on samples deposited at 2000 mTorr is more significant than on samples deposited at 3500 mTorr, as shown by the spectral red shift. Interestingly, this behavior is also observed in the evolution of other optical parameters such as E_g, $n_{632.8}$, etc. Thus, let us evaluate the effect of substrate temperature from the point of view of deposition process. The increase in substrate temperature delays the powder formation and shifts the α–γ‘ transition towards high pressure [8]. As previously mentioned, 2000 and 3500 mTorr correspond to different particle formation regimes at 200 °C. At 2000 mTorr, we are in the agglomeration regime, while 3500 mTorr corresponds to the powder formation regime. Therefore, at 2000 mTorr, with the increase of the substrate temperature, the plasma will leave agglomeration regime and enter the nanocrystals formation regime. On the other hand, it will enter the agglomeration regime from the powder regime for deposition pressure of 3500 mTorr. In the first case, we should observe a significant change on the deposited particle structure, including their size, while not for later case. We assume that the difference between the particles in the agglomeration regime and in the powder formation regime is mainly in their size. Moreover, in both regimes, particle formation is very fast and accompanied with agglomeration process that reduces the large variation of particle size. In addition, if we take into account the annealing process on the surface, the treatment of individual particles should be more efficient than that of agglomerates.

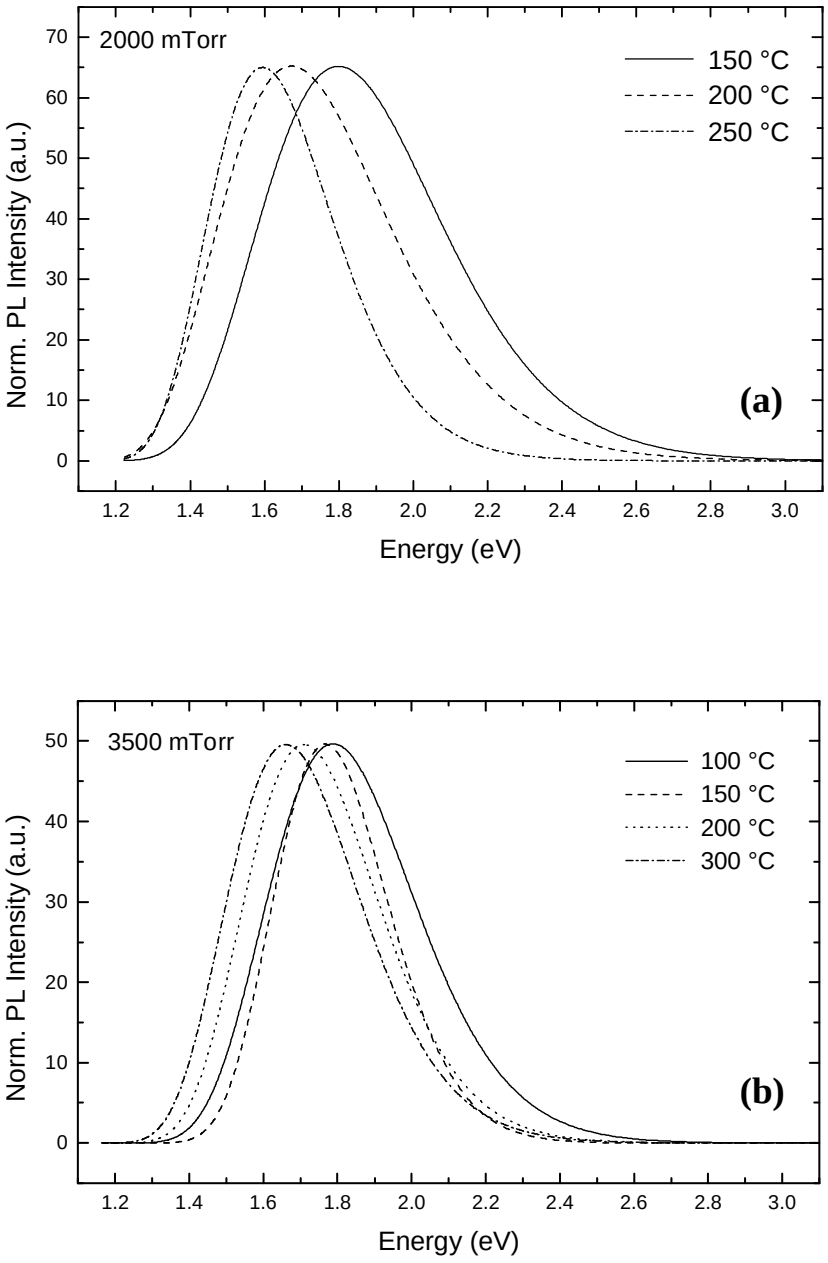

Fig. 5.26. The normalized PL spectra of *pm-*$Si_{1-x}C_x$*:H* films deposited at a) 2000 and b) 3500 mTorr for different substrate temperatures and an RF power of 20 W. PL was excited using HeCd laser at 325 nm (3.8 eV) and measured at room temperature.

Other deposition regimes

Low silane flow rate

Fig. 5.27 shows the effect of deposition pressure on PL spectra for samples deposited at a low silane flow rate of 5 sccm, which is 50 % of the standard flow rate used so far. This deposition condition gives some distinct features. First, we observed a smooth increase in deposition rate without any abrupt transition. Second, in this condition we can go to higher pressures than at 10 sccm, without reaching the powder formation regime. Third, we can obtain materials with higher optical gap (E_g~2.4-2.5) than the standard ones (E_g~2.1-2.3 eV). Finally, the PL intensity increases smoothly with deposition pressure, as observed for the deposition rate, and is accompanied with a blue shift on the spectra. Note that the average PL intensity here is much higher than in any other *pm-*$Si_{1-x}C_x$*:H* films, see for example the PL spectra in Fig 5.28 measured under the same conditions.

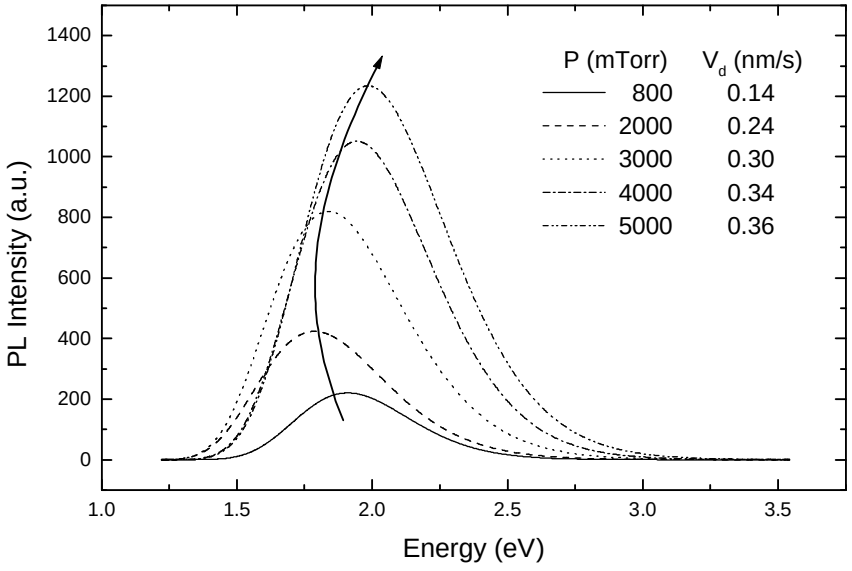

Fig. 5.27. Room temperature PL spectra of *pm-*$Si_{1-x}C_x$ *:H* films deposited at different pressures at 200 °C with an RF power of 20 W and low silane flow rate (5 sccm). The samples were excited using HeCd laser at 325 nm (3.8 eV) and measured at room temperature. The values of the deposition rate are shown in the legend.

These results indicate that the deposition occurs in nanocrystal formation regime rather than in agglomeration regime. In nanocrystal formation regime, we can deposit individual

nanocrystals which are well separated, surface passivated and encapsulated by the matrix, which is more efficient for the radiative recombination process with respect to the deposition of agglomerates. Fig. 5.27 also shows that the PL spectra tend to shift towards high energy with the increase of pressure, except for samples at 800 mTorr. As previously mentioned, this blue shift may express the decrease in nanocrystals size with increasing pressure. The increase of pressure will reduce the size of individual particles but increase their number. That is the reason why we find no drastic increase in PL intensity with pressure. Moreover, the enhancement of PL intensity of samples in this condition might be also the result from the high transparency of the films due to their high optical gap. Thus, the deposition condition in this regime shows many advantages with respect to its application in EL devices.

Powder formation regime

Fig. 5.28 shows the pressure dependence of PL spectra at pressures above 3000 mTorr or powder formation regime (low pressure deposited samples also shown as references). As pressure increases, the plasma changes from particle free conditions and enters the nanocrystals formation regime, which is followed by the agglomeration and powder formation regimes. If we follow the evolution of PL spectra in Fig 5.28, we can see that the PL intensity increases significantly between 800 and 2000 mTorr, then continues to increase up to 3000 mTorr before it reaches saturation and starts to decrease. This behavior can be observed as well in the evolution of the deposition rate as a function of pressure. Interestingly, the highest PL intensity is achieved at the highest deposition rate. Thus, these results again confirm that the presence of nanoparticles is strongly related with the PL characteristics of films.

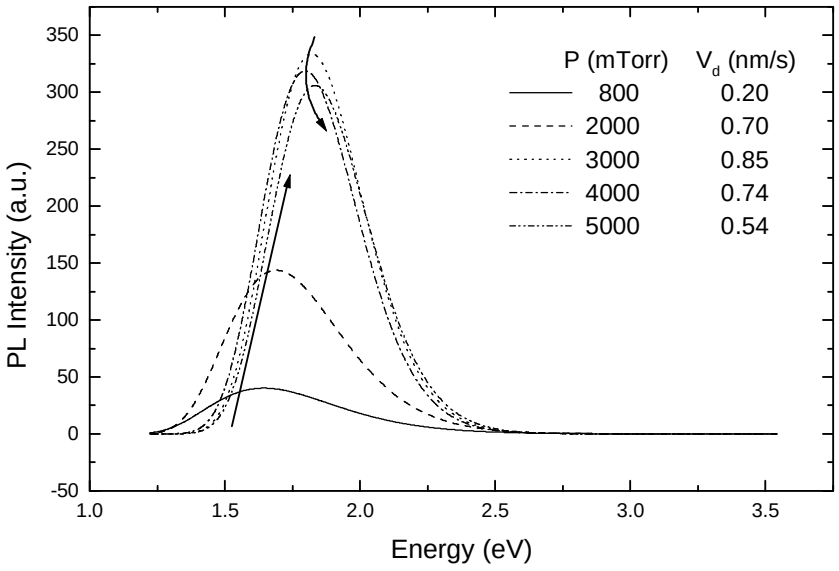

Fig. 5.28. Effect of the total pressure on the room temperature PL spectra of *pm-*$Si_{1-x}C_x$ *:H* films deposited at 200 °C with an RF power of 20 W. The samples were excited using a HeCd laser at 325 nm (3.8 eV) and measured at room temperature. The values of deposition rate are shown in the legend.

Time resolved photoluminescence

We measured the decay characteristics of PL intensity at various temperatures for *pm-$Si_{1-x}C_x$:H* samples deposited under a total pressure of 3500 mTorr, with an RF power of 20 W and a flow rate of 33.4 sccm of CH_4 at 200 °C. The measurements were carried out at LOS (*Laboratoire d'Optique des Solides*), Paris, using a liquid N_2 cooled vacuum cryostat in the temperature range between 78 and 300 K. The emission was detected at a wavelength of 640 nm, while the excitation is at 337.1 nm. The excitation light source was provided by a N_2 laser with a pulse width of 0.6 ns and an energy of 1.4 mJ/pulse. In this study, we analyze the fastest decay component, related to the slow PL S-band in porous silicon [17, 18]. The common fast component for porous silicon samples, which lies in the time range of 10^{-9} sec [17, 19] was not observed in our *pm-$Si_{1-x}C_x$:H* films. The PL decays were characterized by a "strecthed-exponential" relation law given by:

$$I(t) = I(0)\exp\left[-\left(\frac{t}{\tau}\right)^{\beta}\right], \quad 0 < \beta < 1 \tag{5.23}$$

where τ is a lifetime and β is a dispersion factor [36, 37]. Tsang and Street proposed that the total PL intensity, $I(t)$, is composed of an infinite number of pure exponentials weighted by a recombination rate distribution, $G(\tau)/\tau$, which can be written as [20]:

$$I(t) = const.\int_0^{\infty} \tau^{-1} G(\tau) e^{-(t/\tau)} d\tau \tag{5.24}$$

where $G(\tau)$ can be obtained from the following relation [18]:

$$G(\tau) \approx const.I(\tau)\left(\frac{d[\ln I(\tau)]}{d(\ln \tau)}\right) = const.\frac{\beta}{\tau_0^{\beta}}\tau^{\beta} e^{-(\tau/\tau_0)^{\beta}} \tag{5.25}$$

We analyzed quantitatively the effect of temperature on the PL life time using two parameters that represent the lifetime distribution $\tau G(\tau)$ statistically, those are the lifetime at the maximum of the distribution τ_{max} and the average lifetime $<\tau>$. They are defined as [18]:

$$\tau_{max} = \left(1 + \beta^{-1}\right)^{1/\beta}\tau_0 \tag{5.26}$$

$$<\tau> = \frac{\int \tau G(\tau) d\tau}{\int G(\tau) d\tau} \tag{5.27}$$

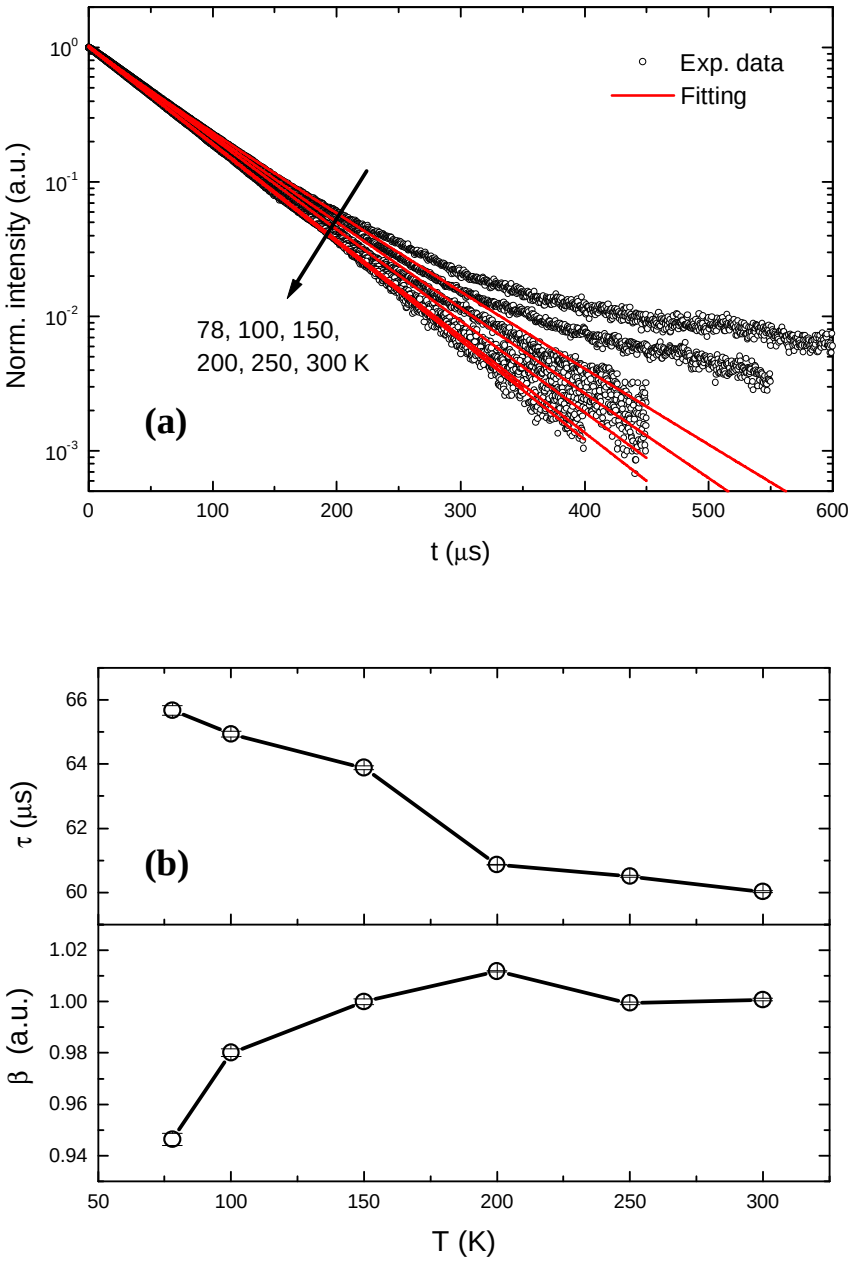

Fig. 5.29. (a) The semi-logarithmic plots of the experimental PL decay (circles) and the fitted PL decay (full lines) evaluated by eq. 5.23 in the temperature range between 78 and 300 K. The PL was detected at 640 nm and excited at 337.1 nm (1.4 mJ/pulse, 0.6 ns pulse). (b) the fitting parameters of stretched-exponential relaxation law (eq. 5.23) as functions of temperature.

The semi-logarithmic plots of PL decays at various temperatures and their fitting results are shown in Fig. 5.29a. The figure shows that the increase of temperature tends to shift the transient to faster decays. Note that the fitting represents well the fastest components but not the slower ones, which disappear or become faster with the increase of temperature. Let us recall that the goal of this study is to synthesize a material with luminescent properties for device applications at room temperature. Thus, the component that can maintain its characteristics at room temperature, in this case the fastest component, is more interesting to develop. Fig. 5.29b shows the temperature dependence of the two fitting parameters, τ and β, from the "strecthed-exponential" relation. It shows that τ tends to decrease slightly with temperature, i.e., the decay is faster, while the value of the dispersion parameter β tends to increase and reach saturation with a value near to unity as the temperature increases from 78 K up to room temperature. Based on this observation, we can say that the value of β is not really affected by temperature. On the other hand, the effect of temperature on τ is more pronounced but not as important as in porous silicon [17, 18] and *nc-Si* in SiO_2 [21]. The saturation of β can be an indication of a very efficient detrapping of excited carriers, i.e. a dynamics typical of extended states [17].

Using equations 5.26 and 5.27, we calculate the value of the average lifetime $<\tau>$ and the lifetime at the maximum of the distribution τ_{max} shown in Fig. 5.30. These parameters represent the PL transient better than τ, because they take into account the dispersion factor β, or basically represent statistically the lifetime distribution $G(\tau)$. As shown in Fig. 5.30, both parameters display the same trend: a decrease with increasing temperature and a saturation above 200 K. The trends are approximately the same, because they represent the same distribution. If we compare the value of these parameters with τ, we find a quite large difference which tells us that the lifetime is widely spread with a distribution determined by the dispersion factor β. As β increases, the lifetime distribution becomes narrower. Fig. 5.31 shows the normalized lifetime distribution $\tau G(\tau)$ in a semi-logarithmic plot for various temperatures, derived from our experimental data. Here, we can see that the increase of temperature shifts the lifetime distribution to faster decays. Note that the effect of temperature is more pronounced for the slower components than for the faster ones, which can be an indication of a distribution narrowing due to the increase of β. Further, if we look back to the average lifetime values and try to fit them with an Arrhenius like equation, then we can obtain an activation energy for carriers intersystem transfer process, i.e. detrapping or single-triplet transition [18]. In this case, we obtain an activation energy of 1.61 meV, which is one order of

magnitude smaller than the one to be considered as the exchange splitting energy [17, 18, 22, 23]. Even at 78 K, where the thermal energy, kT = 6.72 meV, the presence of this activation energy can be neglected and lead us to a single preferable state.

Here, we consider our system (*pm-*$Si_{1-x}C_x$*:H*) as an analogy to the *nc-Si* in SiO_2 system, just by replacing the SiO_2 matrix with *a-*$Si_{1-x}C_x$*:H*. Note that we have confirmed that the lifetime τ of PL in our system is of the order of 60 μs for room temperature emission at 640 nm (see Fig. 5.29b), which is close to the reported PL S-Band in porous silicon (32-45 μs for 600-700 nm emission) [24] and for *nc-Si*/SiO_2 system (25 μs at 850 nm) [25]. This result is supported by the HRTEM analysis showing the presence of nanocrystals embedded in amorphous matrix (see Ch. 4). Moreover, this lifetime range is quite far from PL lifetime of other plausible luminescent sources, such as *a-*$Si_{1-x}C_x$*:H* (0.3 μs at 77 K[1] and 0.8-14.5 ns at 25 K [2]) or *nc-SiC* (200 ps and 1 ns at room temperature [26]). Even though the *a-Si:H* that might be present in the agglomerates can still contribute to the luminescence, due to the wide lifetime distribution (from 10^{-2} to 10^{4} μs) [20], the strong quenching behavior at room temperature discards its contribution to PL. Thus, the essential difference of PL in *pm-*$Si_{1-x}C_x$*:H* compared to other well-known systems is in the nanocrystals-matrix interface. We found that the problem is not as simple as just replacing the SiO_2 matrix with *a-*$Si_{1-x}C_x$*:H* and considering a different electronic environment at nanocrystals-matrix interface, i.e. dielectric constant of surrounding matrix. In particular, we observed a different behavior of the PL decays as a function of temperature with respect to *nc-Si*/SiO_2 [23]. Thus, we have to consider other aspects to explain the temperature dependence of the PL decay. The matrix seems to favor the radiative recombination process in the embedded nanocrystals.

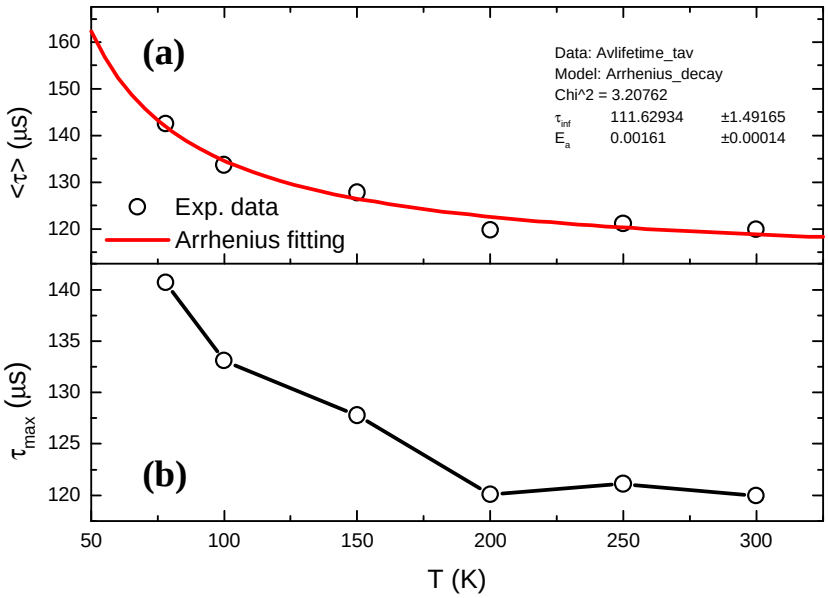

Fig. 5.30. (a) The average lifetime calculated from the experimental data (circles) and the fitted (full lines) by Arrhenius-like and (b) the life time at the maximum of distribution as a function of temperature in the range between 78 and 300 K.

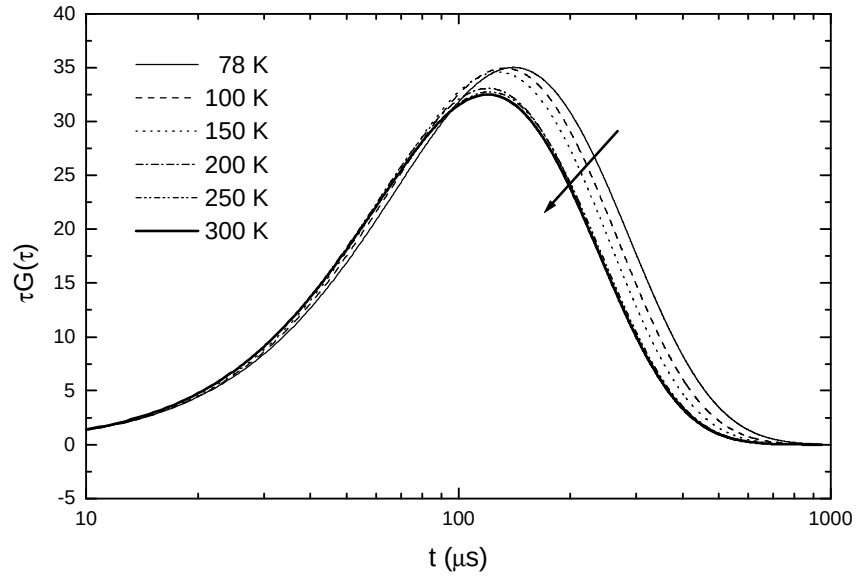

Fig. 5.31. The normalized lifetime distribution τG(τ) derived from the fitted PL decay shown in Fig 5.29a for temperature between 78 and 300 K.

Therefore, the results of the temperature dependence of time resolved PL spectroscopy show that the PL of *pm-$Si_{1-x}C_x$:H* is a remarkably stable, as summarized in figures 5.29-5.31. The results show that the effect of temperature on the PL of *pm-$Si_{1-x}C_x$:H* is several orders of magnitude lower compared to well-studied systems such as porous silicon [17, 18] and *nc-Si*/SiO_2 systems [21]. Such difference might be due to the modification of the surface states by the presence of carbon. Moreover, the stability of our films is also reflected by the evolution of the PL intensity with temperature as shown in Fig. 5.32. We can see that the PL intensity decreases but does not quench strongly. Note that it is possible to have different surface environment between our system and the others due to the different encapsulation process. The nanocrystals capping process and encapsulating material determine the surface passivation, which correlates to the surface states. Let us recall that in *pm-$Si_{1-x}C_x$:H*, the encapsulation of nanocrystals by the *a-$Si_{1-x}C_x$:H* matrix occurs in the plasma phase, which provides a more homogeneous passivation either by hydrogen or carbon terminations through plasma phase reactions. On the other hand, other systems, such as porous silicon and *nc-Si*/SiO_2, shall not be able to provide the same level of surface passivation and homogeneity compared to the plasma process. Moreover, the observed structure of deposited silicon nanocrystals as agglomerates might also contribute to this temperature behavior.

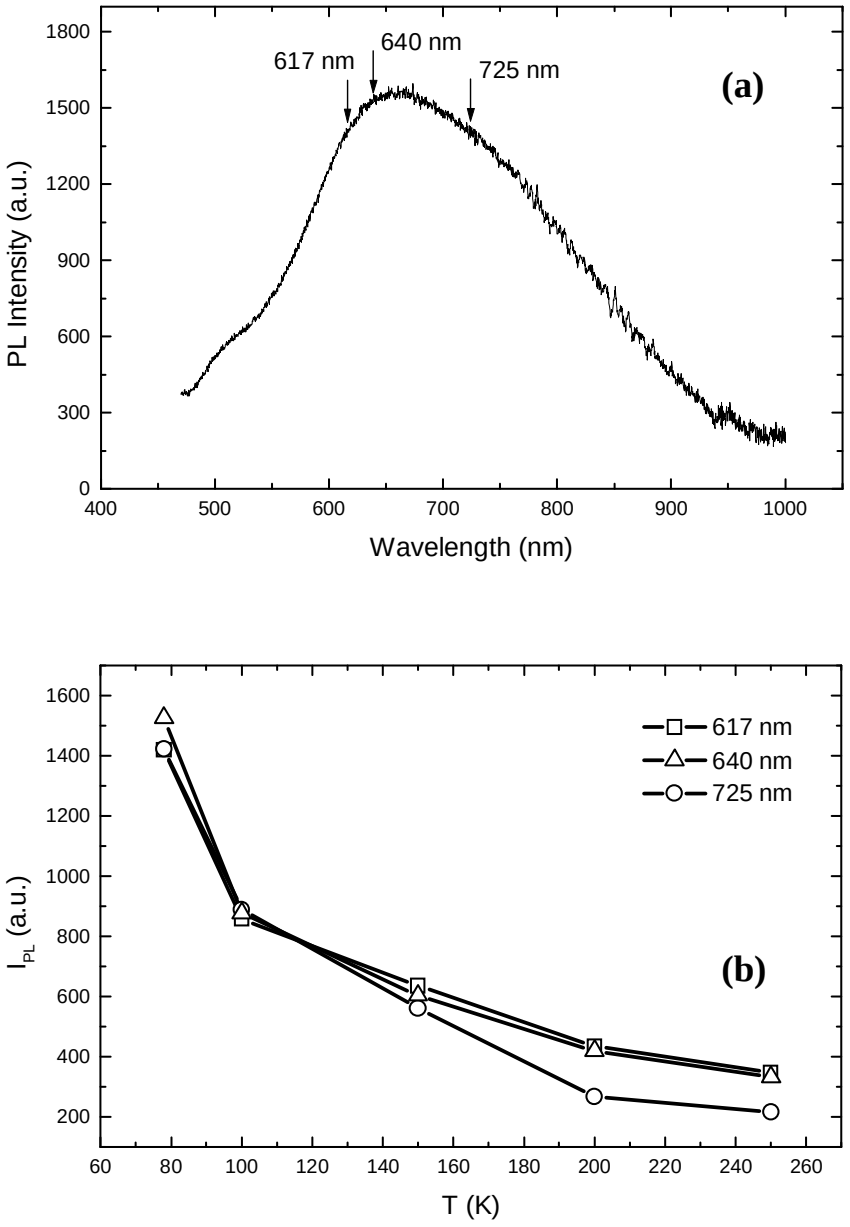

Fig. 5.32. The PL measurement results of the same sample as for time resolved measurements shown in Figs. 5.29-5.31: (a) the spectrum at 78 K (the arrows show the wave length at which we measured the PL temperature dependence) and (b) the effect of temperature on the PL intensity at various wavelengths.

PL spectra analysis based on the model of Islam-Kumar

In this section, we apply the PL spectra model for silicon nanocrystals developed by Islam and Kumar [15] to analyze our PL spectra. In our analysis, we chose the log-normal distribution for the nanocrystal size distribution (eq. A.18), due to a better agreement with the experimental data than the normal distribution (eq. A.17). As reported elsewhere, it is not uncommon to obtain the log-normal particle size distribution [15, 27, 28]. We fixed all parameters to the values of a hydrogen passivated silicon nanocrystal, which is close to our system and is consistent with the presence of silicon nanocrystal therein. These parameters and their values are: n = 1.39, C = 4.122 (for *c-Si* [29]); E_b = 0.07 (for L_0 ~ 2.5 – 5 nm); E_s = 0.05 (for hydrogen passivated surface); α = 3 (for spherical nanocrystals with L_0 > 2 nm) and E_g = 1.12 eV (for *c-Si* at room temperature) [15]. Thus, only three parameters were varied during fitting, which are the average size of nanocrystals L_0, the standard deviation σ in a normal distribution respectively, and a constant k representing the amplitude of the spectrum.

Fig. 5.33a gives an example of the fit of a PL spectrum from a *pm-*$Si_{1-x}C_x$*:H* sample deposited at 200 °C with 20 W of RF power, 3500 mTorr of total pressure and 25 sccm of CH_4 flow. The figure shows that the model can reproduce the experimental data with a good accuracy. By fitting the PL data, we can extract the average size of the nanocrystals and the standard deviation that represent their size distribution. In Fig. 5.33b-d, the average nanocrystals size is presented as a function of the experimental parameters, such as pressure, RF power and methane flow rate. In these figures, the standard deviations are presented by the error bars. A general view of the fitting is that the nanocrystals that give luminescence are spread in a wide size distribution, characterized by the important value of standard deviation, which is quite independent of deposition parameters as shown by the nearly uniform error bars in these three figures. The results of fitting are summarized in Table 5.5.

First, let us look at Fig. 5.33b, where the size of nanocrystals varies with deposition pressure. The nanocrystals average size (diameter) tends to decrease with pressure, in good agreement with the polymorphous deposition model. However, the decrease of nanocrystals size is not very significant and has a large size distribution with standard deviation around 15 %. Thus, the pressure is not a satisfactory parameter to control the size of nanocrystals, especially for device fabrication purposes.

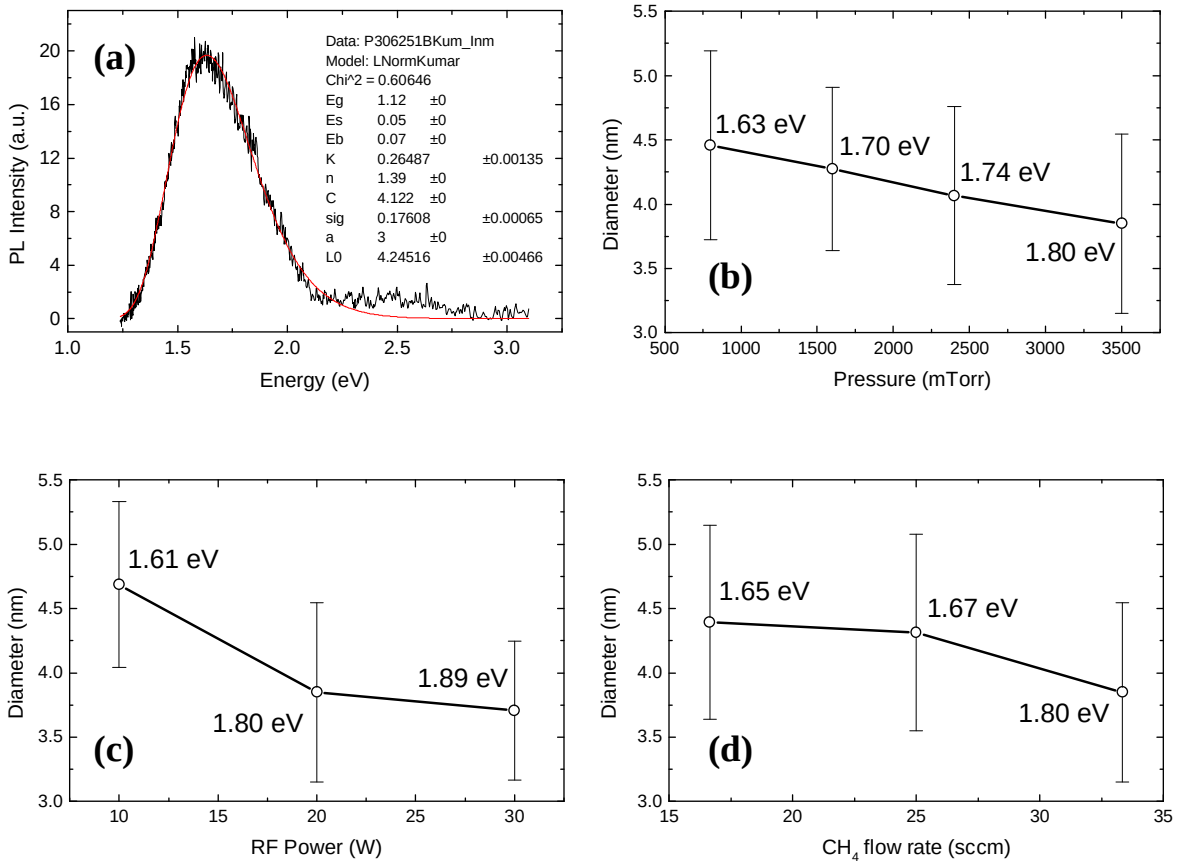

Fig. 5.33. (a) The fitting results of PL experimental data using Islam-Kumar model (see Appendix A) by applying the log-normal distribution for samples deposited at 3500 mTorr with substrate temperature of 200 °C, RF power of 20 W and 25 sccm of CH_4. The diameter of the nanocrystal obtained by fitting using this procedure is plotted as a function of various deposition parameters: (b) deposition pressure, (c) RF power, (d) CH_4 flow rate. The error bars represent the standard deviation from the fitting. E_{PL} value for each data point is also shown. Except for the varied parameter, the samples were deposited at 3500 mTorr with gas flow rate of 10, 33 and 90 sccm for SiH_4, CH_4 and H_2, a substrate temperature of 200 °C and an RF power of 20 W.

Fig. 5.33c shows the diameter of nanocrystals as a function of RF power. As the RF power increases, the size of nanocrystals decreases in the same manner as the the increase of the number of deposited agglomerates (see Fig. 5.24). Fig. 5.33d shows the size of nanocrystals as a function of methane flow rate. The increase of methane flow rate decreases slightly the size of deposited nanocrystals. Here, we can see that the effect of methane on the nanocrystals size is less significant than the other deposition parameters, but not on the PL intensity (see the value of proportionality coefficient *k* in Table 5.5). Thus, it tells that the introduction of methane (carbon) into the polymorphous system promotes the luminescent properties of deposited nanocrystals. It is signified by the nonlinear increase on PL intensity or *k* with methane flow rate, where it becomes more efficient at high flow rate. Further, the contribution of carbon on the energy level of surface state E_s and the oscillator strength α should be taken into account, where in this analysis is considered to be constant (see eq. A.22). All these results points towards the surface passivation as being the most important parameter controlling PL performance.

Table 5.5. Summary of crystalline size distribution deduced from fitting the experimental PL spectra for *pm-*$Si_{1-x}C_x$*:H* samples deposited at various deposition conditions using the Islam-Kumar spectral shape model as written in eq. A.22 (Appendix A).

*X**	μ (nm)[#]	SD[§] (nm)	*k* (a.u.)[&]
Pressure (mTorr)			
800	4.46	0.73	0.09
1600	4.28	0.64	0.30
2400	4.06	0.69	0.58
3500	3.85	0.70	1.00
RF power (Watt)			
10	4.69	0.65	0.12
20	3.85	0.70	1.00
30	3.70	0.54	2.69
CH_4 flow rate (sccm)			
16.65	4.39	0.76	0.13
25	4.31	0.76	0.26
33.35	3.85	0.70	1.00

*) deposition parameters: pressure, RF power, CH_4 flow rate
[#]) Average size of nanocrystals
[§]) Standard deviation
[&]) Proportionality coefficient for eq. A.22 representing the amplitude of the peak

5.4. Surface effects

Effect of immersing the sample into liquid nitrogen

Fig. 5.34 shows the PL spectra of the same sample, measured in two conditions: 1) at room temperature in open air and 2) immersed in a cryostat with liquid nitrogen. Here, we can observe an increase of PL intensity by more than three orders of magnitude. Moreover, the spectrum becomes narrower in liquid nitrogen. The high energy edge practically does not change, but the low energy part is shifted or disappears by immersing the sample in liquid nitrogen. If we compare effect of the temperature on the PL intensity with our previous experimental results, in which liquid nitrogen was not in contact with the sample surface, we can see a strong contrast (see Fig. 5.32b). In that case, the decrease of temperature from ambient to 78 K only yielded an increase of PL intensity by a factor of 5, much less than the factor of 1000 shown in Fig. 5.34.

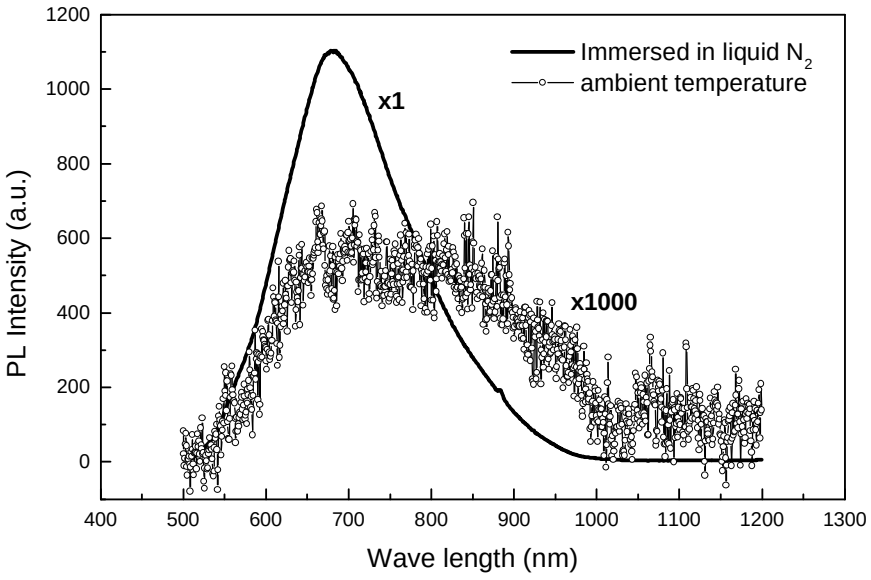

Fig. 5.34. PL spectra from the same *pm-$Si_{1-x}C_x$:H* sample measured at room temperature in open air (open circle) and immersed in liquid nitrogen (thick line). The sample was deposited under 3500 mTorr of total pressure, 20 W of RF power and 33.4 sccm of methane. The blue line of HeCd laser (441.6 nm) was used as an excitation source for both measurement conditions.

This surprising result suggests that the luminescent efficiency of polymorphous silicon carbon alloys can be increased only by changing their environment or microscopically by

modifying the surface condition. Here, we suggest that the surface states of luminescence centers might play an important role, i.e. that for the PL efficiency to increase significantly, the presence of nitrogen molecules in the surface vicinity plays a more important effect than the temperature. Note, that in PL measurements, we excited mostly the region close to the surface due to the shallow penetration depth of the blue or UV lasers used as excitation sources. Thus, the surface term here does not refer only to the surface of deposited films, but rather to the surface vicinity of films, which also includes the nanocrystals embedded or deposited in this region. In nanocrystals, the surface treatment shall alter the luminescent properties through the modification of their surface (matrix/nanocrystal interface), i.e. by chemical termination (passivation) or physical absorption, which changes the band structure (electronic states) [30-32] and/or the dielectric function of surrounding medium [15, 33].

It has been reported that some materials provide good passivation when they act as a matrix of nanoparticle system, such as SiO_2 in *nc-Si*/SiO_2 system [34] and SiC in Si nanowire [35]. However, the passivation by the matrix usually is not as effective as the direct interaction of the reactive centers with small molecules such as hydrogen [36-40] or nitrogen [41]. Here, the passivation can be achieved through annealing in certain atmosphere [37-39], low energy ion implantation [36] or plasma treatment (H_2/N_2 mixture) [41]. The target of the passivation process is the dangling bonds in the nanocrystals or on the nanocrystals/matrix interface, which act as the non-radiative centers that quench the luminescence [36-40, 42]. In the case of hydrogen, the passivation efficiency by atomic hydrogen was reported to be higher than the molecular one through the catalytic experiment using Al metal [39]. Recently, the hydrogen plasma treatments have been used to modify the surface properties of materials such as dielectrics [43] and improve the performance of the *p-i-n* thin film light emitting diodes by passivating the defects [44].

To study the effect of hydrogen plasma on PL of *pm-*$Si_{1-x}C_x$*:H*, we prepared several identical samples in the ARCAM reactor [45]. These samples were deposited under the following conditions: 3000 mTorr, 30 W, 200 °C, 200 sccm of hydrogen, 4 sccm of silane and 100 sccm of methane. This condition provides samples with a strong room temperature PL signal that might be sufficient for the accurate analysis of spectra before and after the treatments. Here, we varied the treatment duration, total pressure, RF power and substrate temperature to study the effect of hydrogen plasma on PL intensity.

Plasma treatments

a) Effect of treatment duration

Fig. 5.35a shows the effect of the treatment duration on the shape and intensity of PL spectra. The treatments were carried out under 3000 mTorr of pure hydrogen plasma with 10 W of RF power at 200 °C. The figure shows that after 15 minutes of treatment, the PL intensity increases slightly without any changes in shape. Longer treatment times increase the PL intensity until it reaches saturation after 60 minutes. The increase of PL intensity is accompanied by a slight blue shift in the PL spectra, which can be observed from the peak position. Longer treatment times do not increase the PL intensity, but only change the spectral shape by increasing slightly the intensity of the high energy part of the luminescence spectra. We attribute the increase of PL to the passivation of defect sites such as dangling or floating bonds on the nanocrystals/matrix interface. The increase of treatment duration being related to the increase of the diffusion length of hydrogen that increases the probability for atomic hydrogen to arrive and interact with defects. The saturation for treatment times above 60 minutes might be either due to the limitation by the penetration depth of hydrogen radicals when they diffuse into the film or rather to the penetration depth of the laser beam used to excite the samples (~20 nm).

The modification of the material by the hydrogen plasma can be observed through UV-Vis spectroscopic ellipsometry analysis as shown by the evolution of the imaginary part of pseudo-dielectric function in Fig. 5.35b. We can see that after 15 minutes of plasma exposure the amplitude of $<\varepsilon_2>$ at high energy drops significantly, while longer treatment times only reduce it slightly. The decrease of amplitude can be due to the decrease of the material density or to the increase of its surface roughness. Moreover, we observe that the interference fringes shift towards high energy with the treatment duration. This shift indicates the decrease of film thickness that might be due to the etching by hydrogen radicals. Fitting the experimental results on the basis of a three-layers model (roughness/modified layer/bulk layer) similar to the two-layers model described in Ch. 2, we confirmed that the thickness of the bulk layer decreases by 50 nm after 150 minutes of exposure time. Here, the formation of 20-30 nm thick porous modified layer (15-17 % of void) might be the reason for the decrease of the amplitude in the high energy part of spectrum and for the improvement of the PL.

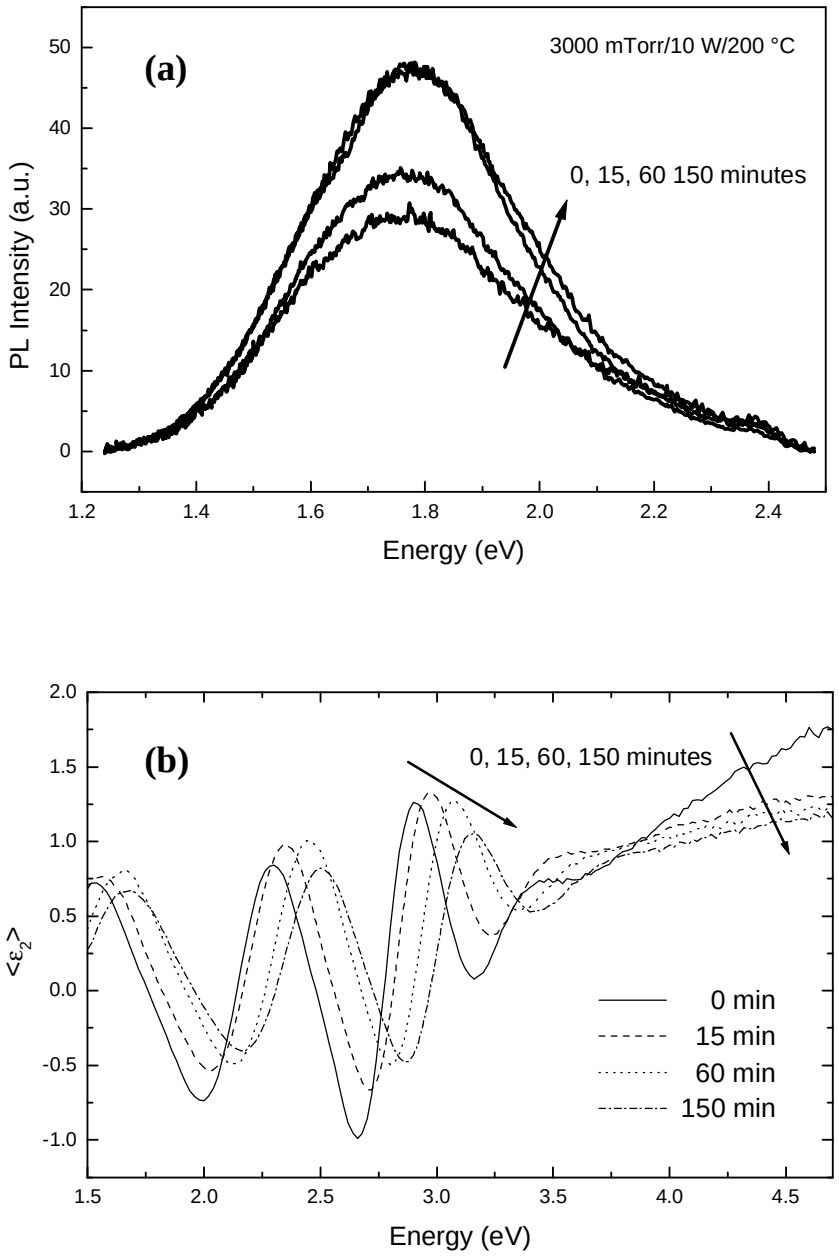

Fig. 5.35. (a) Room temperature PL spectra and (b) the imaginary part of the pseudo-dielectric function for samples treated with a hydrogen plasma at 200 °C under a pressure of 3000 mTorr and 10 W of RF power for various treatment times.

b) Effect of pressure

The effect of pressure during the hydrogen plasma treatment on the shape and intensity of PL spectra of *pm-$Si_{1-x}C_x$:H* samples is presented in Fig. 5.36. Plasma treatments were carried out at 200 °C for 60 min with 10 W of RF power. The figure shows that the efficiency of treatment increases with pressure. The treatment at 1000 mTorr slightly improves the PL performance of samples. At this pressure, mostly the high energy side of the spectrum, relative to as deposited sample is improved. On the other hand, the treatment at 3000 mTorr improves both sides of the PL spectrum with a slight blue shift of the maximum. Further increase of pressure up to 4000 mTorr produces further improvement of the PL intensity with a slight blue shift accompanied by the enhancement in high energy side of the peak. In general, the variation of pressure does not change the spectral shape significantly, which suggests that the hydrogen plasma treatment acts mostly to reduce the non-radiative recombination centers rather than the structure or size of nanocrystals.

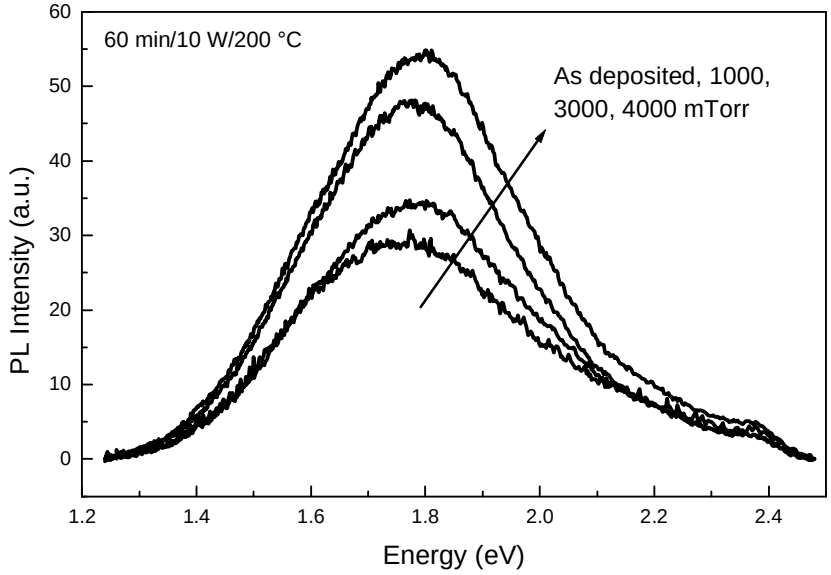

Fig. 5.36. Room temperature PL spectra for samples treated with hydrogen plasma at 200 °C for 60 minutes and 10 W of RF power and under various values of pressure.

c) Effect of RF power

The effect of RF power of the hydrogen plasma on the shape and intensity of PL spectra for *pm-$Si_{1-x}C_x$:H* samples is presented in Fig. 5.37. Here, the increase of RF power from 10 to 20 W gives no significant difference on the PL intensity for 60 minutes of exposure under 3000 mTorr of pure hydrogen plasma at 200 °C. Apparently, one hour of treatment only changes slightly the spectral shape by shifting the spectrum towards high energy. Here, we applied a lower RF power than for deposition to prevent the degradation of materials by the hydrogen plasma. A soft plasma with less ion bombardment but rich in hydrogen radicals should be preferable for the passivation process.

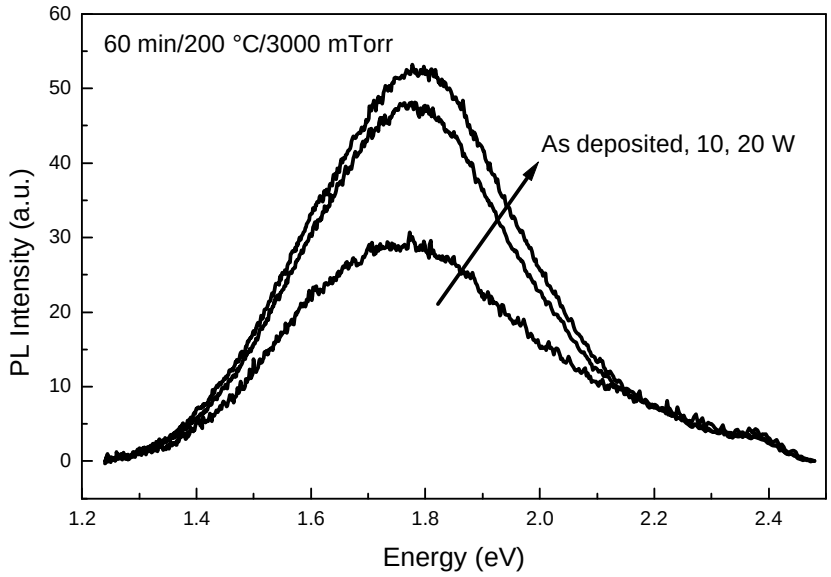

Fig. 5.37. The room temperature PL spectra for samples treated for 60 minutes with hydrogen plasma at 200 °C and 3000 mTorr for various values of RF power.

d) Effect of treatment temperature

In Fig 5.38, we show the effect of the temperature during the hydrogen plasma treatment on the shape and intensity of PL spectra for *pm-$Si_{1-x}C_x$:H* samples. Each sample was exposed to the hydrogen plasma for 60 minutes under a pressure of 3000 mTorr and 10 W of RF power. If the passivation process with hydrogen atoms is related to H diffusion, then we expect the passivation to be more efficient at high temperature as the diffusion coefficient of hydrogen increases exponentially with temperature [46]. The substrate temperature was varied between 200 and 300 °C. Fig. 5.38 shows that the increase of temperature from 200 to 250 °C does not improve the PL performance. It only increases slightly the high energy part of the PL peak, which is observed between 1.9 and 2.2 eV. However, further increase in temperature up to 300 °C gives an important increase in PL intensity, which is accompanied also with the blue shift of the PL peak maximum. As the samples were deposited at 200 °C, the effect of treatment is not only due to the hydrogen but it may also be induced by the annealing during the hydrogen plasma at temperature higher than the deposition one.

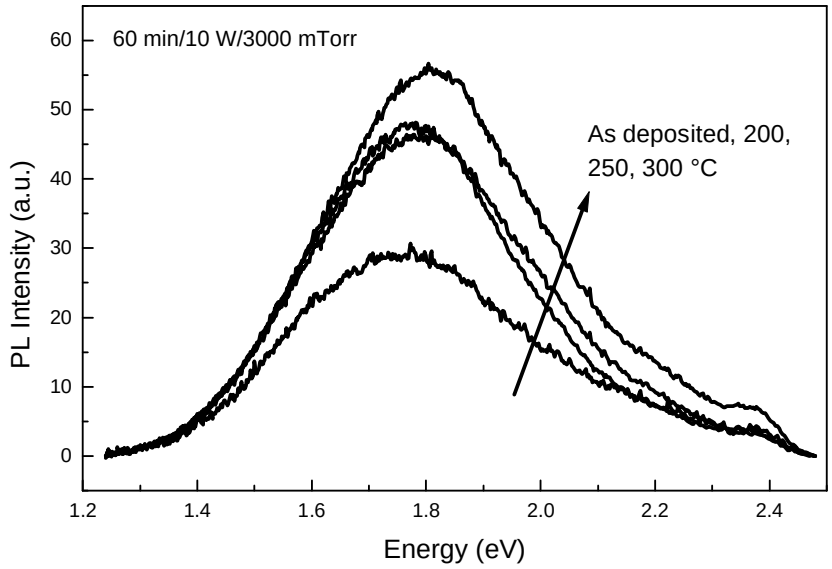

Fig. 5.38. Room temperature PL spectra for samples treated with hydrogen plasma under 3000 mTorr of pressure and 10 W of RF power for 60 minutes at various substrate temperatures.

Discussion on the surface treatment results

The effect of hydrogen plasma treatment suggests that the PL intensity increases due to the the interaction of atomic hydrogen with non-radiative recombination sites, such as dangling bonds. The treatment duration shows that the process is limited by the penetration depth of atomic hydrogen into the film. The ideal condition is to passivate all non-radiative sites in the entire film through the interaction with hydrogen radicals. In order to be able to interact, the hydrogen radicals have to diffuse into the film to reach the reactive sites. However, because atomic hydrogen is a reactive species, it may not be able to penetrate deep enough to reach defect sites inside the film. From the analysis of ellipsometry data, we obtain that the hydrogen can form a modified layer with thickness around 20-30 nm near the surface of the film, which is of the same order of magnitude as reported for amorphous silicon [46, 47]. The differences between two systems might be only on the etching rate, which is much lower in the case of *pm-$Si_{1-x}C_x$:H*. Furthermore, Kail et. al. observed that deuterium can diffuse in *p*-type *a-Si:H* film with penetration depth around 100 nm just after 5 minutes of exposure to the deuterium plasma [47].

If in *pm-$Si_{1-x}C_x$:H*, atomic hydrogen penetrates at approximately the same depth with respect to *a-Si:H*, then it would be enough to modify the whole film by applying a longer plasma exposure. However, we observed a saturation of PL intensity (Fig. 5.35). Thus, the increase of PL intensity is *à priori* either limited by the penetration depth of the atomic hydrogen in the film or by the penetration depth of excitation laser. In order to find which factor is responsible for the limitation of PL intensity, let us analyze the diffusion process of atomic hydrogen. If we consider that the penetration of hydrogen atomic into the film is only governed by a diffusion process, which is driven by the gradient of concentration of the diffusing species. In addition, we have to take into account the presence of C-H bonds in large amount but not involved in the diffusion nor in the transport of atomic hydrogen by hopping process. This is shown by the analysis of FTIR spectra, which shows a higher concentration of C-H with respect to Si-H (Fig 4.18). After the hydrogen plasma treatment, we suggest that the concentration of C-H bonds might increase as well. Then, we can have such a situation where the diffusion of hydrogen from plasma into bulk layer of the film is hindered by the modified layer which is rich in hydrogen but more rigid with respect to *a-Si:H*. From the modified layer to the depth of the films the diffusion is driven by the concentration gradient. However, the diffused hydrogen might not be able to move very far due to its reactivity. Thus, we suggest that the diffusion of hydrogen in *pm-$Si_{1-x}C_x$:H* is a slow process, which might be responsible

for the small increase of PL intensity. Another aspect such laser penetration depth might also limit the measurement but the effect should be much less than the hydrogen diffusion. Here, we can give a rough estimation by taking a continuous wave UV laser with low power of 2 mW at 325 nm (~3.3×10^{15} photons/s), which theoretically may show an strong effect of light penetration depth. We consider a 200 nm thick *pm-*$Si_{1-x}C_x$*:H* film with penetration depth at 325 nm (3.8 eV, $\alpha \sim 5 \times 10^5$ cm^{-1}) of around 20 nm, then we obtain the value of I/I_0 around 1.7×10^{-5}, which lets enough photons to excite deeper layer than 200 nm even for laser with weak lasing power such as 2 mW.

Among parameters studied, the gas pressure and the substrate temperature are the most efficient factors to affect PL intensity. As discussed above, the effect of the treatment duration is limited by the hydrogen penetration depth, while the RF power is excluded due to the probability to have a degrading effect on material properties by ion bombardment. Thus, only gas pressure and substrate temperature can be adjusted safely. In the case of substrate temperature, it still can be increased as long as it is lower than the degradation temperature of the material, related to the Si-H bonding energy. This information can be obtained from the exodiffusion measurements of samples. In principle, high substrate temperature will help the diffusion of atomic hydrogen inside the films by overcoming the activation energy to move through hopping between reactive sites. On the other hand, the increase of pressure improves the passivation process by reducing the energy of ions that arrive on the surface and increasing the partial pressure of diffusing components outside the film [48]. The increase of partial pressure of diffusing components will increase their chemical potential that acts as a driving force for the diffusion into the film.

Let us summarize the main idea of this study: to increase the PL performance by introducing other chemical elements (N, H, C, …) to passivate the defects near the luminescence center. In principle, the improvement of PL can only be realized when the radiative recombination process becomes dominant with respect to the non-radiative ones. This can be achieved through two different ways: first, the increase of PL efficiency can be achieved by decreasing the non-radiative recombination centers, i.e. the introduction of atoms or molecules can passivate the non-radiative recombination centers. The second way is by increasing the probability to have radiative recombination process, either by forming an energy fluctuation just like in the case of amorphous silicon [20, 49-51] or by creating an intermediate level such as the localized surface states in silicon nanocrystals [14, 16, 52, 53], which can confine the carriers with higher efficiency than the non-radiative centers. Later on, the confined carriers can recombine radiatively with higher probability. Here, the presence of

hydrogen is suggested to follow the former mechanism [40]. Let us recall, that in the case of semiconductors with indirect band gap, the presence of a right phonon is compulsory to conserve the momentum in band-to-band transitions, which has to be taken into account in the carrier recombination. Thus, in most cases they lose in competition with non-radiative processes which do not need a phonon. Our experiments show that the hydrogen plasma treatment improves the PL of *pm-$Si_{1-x}C_x$:H*. Hydrogen plasma treatments to passivate dangling bonds in silicon have been studied for long time [54], and one can expect that the same applies to amorphous silicon related material such as *pm-$Si_{1-x}C_x$:H*. The common proposed mechanism is the passivation of dangling bonds, which directly correlates with the PL improvement. Note that the presence of one dangling bond is enough to quench the luminescence in the entire nanocrystal [39, 52]. At high deposition pressure, the embedded nanocrystals do not exist as individual particles but in agglomerates, thus the probability of the dangling bond in a nanocrystal to affect others can be much higher than in the individual nanocrystal. However, the effect of hydrogen passivation is less than what we expected from the immersion in liquid nitrogen as shown in Fig. 5.38. Note that the effect of temperature alone increases the PL intensity by almost one order of magnitude, while the liquid nitrogen immersion yields more than three orders of magnitude. If hydrogen would act in the same way as liquid nitrogen, then we would expect an improvement by up to three order of magnitude. This difference leads us to suggest that either the presence of nitrogen improves the PL efficiently with the same mechanism as reported for passivation by nitridation [55, 56] or with another different mechanism. For the latter, we suggest that the presence of nitrogen molecules might not passivate the defects but only facilitate extra states on the surface of nanocrystals which open new routes for radiative recombination by analogy to the localized surface states [15].

5.5. Summary and conclusions

The studies of the optoelectronic properties of *pm-$Si_{1-x}C_x$:H* films have shown that there are many interesting characteristics in this material, which are different with respect to other related systems such as *a-$Si_{1-x}C_x$:H* and *nc-Si*. This fact is very encouraging for further studies and developments in this area. As previously described, the quantum confinement of carriers in the silicon nanocrystals is the main model proposed to explain the luminescence in our system.

In this chapter, we have shown and discussed about the optoelectronic properties of polymorphous silicon carbon alloys (*pm-$Si_{1-x}C_x$:H*) by focusing on their luminescent properties. We have shown that *pm-$Si_{1-x}C_x$:H* films give a strong luminescence, which can even be observed by naked eye at room temperature. The results of PL spectroscopy and time-resolved PL spectroscopy lead us to conclude that the origin of this strong luminescence is the silicon nanocrystals embedded in the matrix of silicon carbon alloys, as observed by TEM. We have shown that the PL peak energy and lifetime are in the same range as the luminescence from well-studied porous silicon (*p-Si*) or *nc-Si*/SiO_2 systems. Moreover, the shape of the luminescence peak also is well-fitted using the model proposed by Islam and Kumar with the minimum fitting parameters strictly fixed for hydrogen passivated silicon nanocrystals. The luminescent properties were observed to depend "strongly" on the deposition conditions, which allows us to improve the material properties by changing the deposition parameter such as pressure, RF power, gas flow rate and substrate temperature.

Based on UV-visible spectroscopic ellipsometry and PDS measurements, we found that *pm-$Si_{1-x}C_x$:H* films have a low defect density. The decrease of the absorption near the band edge is accompanied by the increase of the luminescence intensity, which makes this material suitable for luminescent device applications. Moreover, we found some discrepancies between our results with respect to *a-$Si_{1-x}C_x$:H* alloys, related to their optoelectronic properties:

1. The effect of the increase of RF power and methane flow rate on the defect density near band edge is contrary to their effect on *a-$Si_{1-x}C_x$:H* alloys.
2. The value of E_{04}-E_{PL} is spread in the range of 0.7-0.9 eV, which relative narrow even compared to "low power" *a-$Si_{1-x}C_x$:H* alloys for which E_{04}-E_{PL} ~ 0.6-1.2 eV.
3. The value of E_{04}-E_{PL} tends to decrease with the increase of methane flow rate, which indicates that the gap widening is less important than the blue shift of E_{PL}.

These discrepancies confirm that *pm-$Si_{1-x}C_x$:H* has a different structure compared to *a-$Si_{1-x}C_x$:H*. Moreover, the PL spectra characteristics of *pm-$Si_{1-x}C_x$:H*, such as a broad band emission (~0.4 eV) and slow decay (~60 μs) at room temperature, are similar to those of porous silicon, consistent with the presence of nanocrystals in *pm-$Si_{1-x}C_x$:H*. Therefore, we propose that the observed PL originates from those nanocrystals.

The temperature dependence of the PL intensity shows that *pm-$Si_{1-x}C_x$:H* is a remarkably stable material where the effect of temperature does not perturb much the radiative recombination probability. Indeed, the effect of temperature on the PL of *pm-$Si_{1-x}C_x$:H* is several orders of magnitude lower than for porous silicon or *nc-Si*/SiO_2 systems. This

leads us to suggest that the nanocrystals inside the *a-Si$_{1-x}$C$_x$:H* matrix are well passivated and encapsulated, thus facilitating a stable luminescence as a function of temperature. By comparing to those well-studied systems, we suggest that the stability comes either from the passivation of nanocrystal surfaces by carbon and hydrogen or by the agglomerate structure of nanocrystals.

The immersion of the samples in liquid nitrogen points out the importance of the surface passivation on the luminescence properties of *pm-Si$_{1-x}$C$_x$:H*. This fact opens the possibility to enhance the luminescent properties by surface treatments, which we have achieved through hydrogen plasma treatments. In principle, the hydrogen plasma treatment does not change the PL spectra but only increases their intensity. However, the efficiency of hydrogen plasma treatment is found to be less than the immersion in liquid nitrogen.

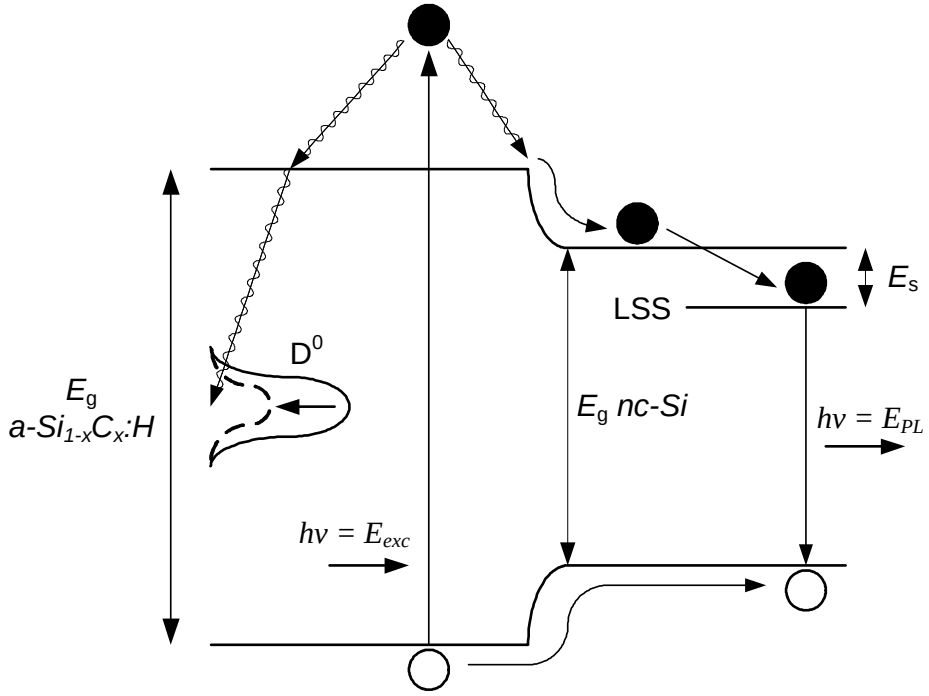

Fig. 5.39. Schematic diagram of the charge carriers recombination routes in *pm-Si$_{1-x}$C$_x$:H* involving the embedded nanocrystals, their localized states (LSS) and the defects as the dangling bonds (D^0) in the matrix.

Based on the description of a system consisting of nanocrystals having localized surface states (LSS) and a high band gap amorphous matrix with the presence of defects as dangling bonds, Fig. 5.39 summarizes the possible routes for charge carriers recombination in *pm-Si$_{1-x}$C$_x$:H*. As photo-excited electrons thermalize to the band edge, there are two competing routes for recombination. The first route is that electrons continue to thermalize through defects inside the gap of the *a-Si$_{1-x}$C$_x$:H* matrix and get trapped by dangling bonds (non-radiative). In

the second route, electrons thermalize towards the conduction band of the nanocrystals and recombine radiatively with holes through LSS. The effect of RF power on increasing the number of embedded nanocrystals demonstrates the increase of the probability for electron-hole pairs to find the nanocrystals. On the other hand, the hydrogen plasma treatment and the lowering of the silane flow rate are suggested as possible ways to decrease the concentration of dangling bonds and to improve the LSS that results the increase of PL intensity.

A further development that has to be made is the fabrication of luminescent devices based on this material. For this purpose, the enhancement of luminescent properties and the study on the transport properties of carriers in this materials are key aspects, which deserve further studies.

References

[1] W. Siebert, R. Carius, W. Fuhs, K. Jahn, *Phys. Stat. Sol.* (*b*) **140**, 311 (1987).

[2] C. Palsule, S. Gangopadhyay, D. Cronauer, B. Schröder, *Phys. Rev. B* **48**, 10804 (1993).

[3] D. Engemann, R. Fischer, J. Knecht, *Appl. Phys. Lett.* **32**, 567 (1978).

[4] S. V. Chernyshov, E. I. Terukov, V. A. Vassilyev, A. S. Volkov, *J. Non-Cryst. Solids* **134**, 218 (1991).

[5] I. Solomon, M. P. Schmidt, H. Tran-Quoc, Phys. Rev. B 38, 9895 (1988).

[6] V. A. Vasil'ev, A. S. Volkov, E. Musabekov, E. I. Terukov, V. E. Chelnokov, S. V. Chernyshov, Yu. M. Shernyakov, *Sov. Phys. Semicond.* **24**, 445 (1990).

[7] L. R. Tessler, I. Solomon, Phys. Rev. B 52, 10962 (1995).

[8] L. Boufendi, J. Gaudin, S. Huet, G. Viera, M. Dudemaine, *Appl. Phys. Lett.* **79**, 4301 (2001).

[9] J. Perrin, M. Shiratani, P. Kae-Nune, H. Videlo, J. Jolly, J. Guillon, *J. Vac. Sci. Technol. A* **16**, 278 (1998).

[10] G. E. Jellison, Jr., F. A. Modine, *Appl. Phys. Lett.* **69**, 371 (1996); G. E. Jellison, Jr., F. A. Modine, *Appl. Phys. Lett.* **69**, 2137 (1996).

[11] T. Stapinski, B. Swatowska, S. Kluska, E. Walasek, *Appl. Surf. Sci.* **238**, 367 (2004).

[12] Th. Nguyen-Tran, V. Suendo, P. Roca i Cabarrocas, *Appl. Phys. Lett.* **87**, 011903 (2005).

[13] G. Ambrosone, V. Ballarini, U. Coscia, S. Ferrero, F. Giorgis, P. Maddalena, A. Patelli. P. Rava, V. Rigato, *Thin Solid Films* **427**, 279 (2003).

[14] N. Chaâbane, A. V. Kharchenko, H. Vach, P. Roca i Cabarrocas, *New J. Phys.* **5**, 37.1 (2003).

[15] Md. N. Islam, S. Kumar, J. Appl. Phys. 93, 1753 (2003).

[16] C. Delerue, G. Allan, M. Lannoo, *Phys. Rev. B* **48**, 11024 (1993).

[17] L. Pavesi, M. Ceschini, *Phys. Rev. B* **48**, 17625 (1993).

[18] G. Mauckner, K Thonke, T. Baier, T. Walter, R. Sauer, *J. Appl. Phys.* **75**, 4167 (1994).

[19] T. Matsumoto, T. Futagi, H. Mimura, Y. Kanemitsu, *Phys. Rev. B* **47**, 13876 (1993).

[20] C. Tsang, R. A. Street, *Phys. Rev. B* **19**, 3027 (1979).

[21] M. Dovrat, Y. Goshen, J. Jedrzejewski, I. Balberg, A. Sa'ar, *Phys. Rev. B* **69**, 155311 (2004).

[22] P. D. J. Calcott, K. J. Nash, L. T. Canham, M. J. Kane, D. Brumhead, *J. Phys.: Condens. Matter* **5**, L91 (1993).

[23] M. L. Brongersma, P. G. Kik, A. Polman, K. S. Min, H. A. Atwater, *Appl. Phys. Lett.* **76**, 351 (2000).

[24] A. G. Cullis, L. T. Canham, P. D. Calcott, *J. Appl. Phys.* **82**, 909 (1997).

[25] J. Linnros, A. Galeckas, N. Lalic, V. Grivickas, *Thin Solid Films* **297**, 167 (1997).

[26] S. J. Xu, M. B. Yu, Rusli, S. F. Yoon, C. M. Che, *Appl. Phys. Lett.* **76**, 2550 (2000).

[27] H. Yorikawa, S. Muramatsu, *Appl. Phys. Lett.* **71**, 644 (1997).

[28] S. K. Ram, S. Kumar, D. Deva, R. Vanderhaghen , B. Drevillon, P. Roca i Cabarrocas, E-MRS proceeding 2005.

[29] J. P. Proot, C. Delerue, G. Allan, *Appl. Phys. Lett.* **61**, 1948 (1992).

[30] M. V. Wolkin, J. Jorne, P. M. Fauchet, G. Allan, C Delerue, *Phys. Rev. Lett.* **82**, 197 (1999).

[31] J.-B. Xia, K. W. Cheah, *Phys. Rev. B* **59**, 14876 (1999).

[32] I. Vasiliev, J. R. Chelikowsky, R. M. Martin, *Phys. Rev. B* **65**, 121302 (2002).

[33] P. G. Bolcatto and C. R. Proetto, *Phys. Rev. B* **59**, 12487 (1999).

[34] M. L. Brongersma, A. Polman, K. S. Min, E. Boer, T. Tambo, H. A. Atwater, *Appl. Phys. Lett.* **72**, 2577 (1998).

[35] X. T. Zhou, R. Q. Zhang, H. Y. Peng, N. G. Shang, N. Wang, I. Bello, C. S. Lee, S. T. Lee, *Chem. Phys. Lett.* **332**, 215 (2000).

[36] K. S. Min, K. V. Shcheglov, C. M. Yang, H. A. Atwater, *Appl. Phys. Lett.* **69**, 2033 (1996).

[37] S. Cheylan, R. G. Elliman, *Appl. Phys. Lett.* **78**, 1225 (2001).

[38] S. Cheylan, R. G. Elliman, *Appl. Phys. Lett.* **78**, 1912 (2001).

[39] A. R. Wilkinson, R. G. Elliman, *Appl. Phys. Lett.* **83**, 5512 (2003).

[40] A. R. Wilkinson, R. G. Elliman, *Phys. Rev. B* **68**, 155302 (2003).

[41] A. Daami, G. Bremond, L. Stalmans, J. Poortmans, *J. Lumin.* **80**, 169 (1999).

[42] A. Ekimov, *J. Lumin.* **70**, 1 (1996).

[43] M. Yamaguchi, H. Nagayoshi, M. Ikeda, Y. Yamamoto, K. Kamisako, Y. Tarui, *Jpn. J. Appl. Phys.* **34**, 791 (1995).

[44] J.-W. Lee, K. S. Lim, *Jpn. J. Appl. Phys.* **35**, L1111 (1996).

[45] P. Roca i Cabarrocas, J. B. Chévrier, J. Huc, A. Lloret, J. Y. Parey, J. P. M. Schmitt, *J. Vac. Sci. Technol.* **A9**, 2331 (1991).

[46] F. Kail, A. Fontcuberta i Morral, A. Hadjadj, P. Roca i Cabarrocas, A. Beorchia, *Philos. Mag.* **84**, 595 (2004).

[47] F. Kail, A. Hadjadj, P. Roca i Cabarrocas, *Thin Solid Films* **487**, 126 (2005).

[48] T. Novikova, B. Kalache, Kh. Hassouni, W. Morscheidt, P. Roca i Cabarrocas, *J. Appl. Phys.* **93**, 3198 (2003).

[49] F. Boulitrop, D. J. Dunstan, *Phys. Rev. B* **28**, 5923 (1983).

[50] D. J. Dunstan, F. Boulitrop, *Phys. Rev. B* **30**, 5945 (1984).

[51] R. A. Street in J. I. Pankove (Ed.), *Semiconductor and Semimetals* **Vol. 21** : *Hydrogenated Amorphous Silicon* **Part B**, Academic Press, Inc., Orlando, 1984, p197-244.

[52] M. Lannoo, C. Delerue, G. Allan, *J. Lumin.* **70**, 170 (1996).

[53] C. Delerue, G. Allan, M. Lannoo, *J. Lumin.* **80**, 65 (1999).

[54] K. L. Brower, *Phys. Rev. B* **38**, 9657 (1988).

[55] A. Daami, G. Bremond, L. Stalmans, J. Poortmans, *J. Lumin.* **80**, 169 (1999).

[56] L. Gubo, X. Hou, S. Yuan, H. Chen, F. Zhang, H. Fan, X. Wang, *J. Appl. Phys.* **80**, 5967 (1996).

Chapter 6
Conclusions and Perspectives

In this thesis we have extended the investigation of the production of silicon nanocrystals, originally developed at the PICM laboratory in the framework of polymorphous silicon thin films, to the case of polymorphous silicon carbon alloys. Indeed, while pm-Si:H thin films have been shown to be well-adapted for solar cells and thin film transistors, quantum size effects such as efficient emission from silicon nanocrystals had not yet been exploited. With this objective in mind we have moved from silane-hydrogen plasmas to silane-methane-hydrogen plasmas in order to produce *a-*$Si_{1-x}C_x$*:H* films with a wide optical gap, which can host silicon nanocrystals and provide i) confinement of the carriers within the nanocrystals and ii) negligible absorption of the emitted light. Therefore, before moving to the complex SiH_4-CH_4-H_2 system, we have studied the SiH_4-H_2 plasma with a particular emphasis on the conditions leading to nanocrystal synthesis in the plasma and their subsequent incorporation in the film.

The plasma diagnostics developed in parallel to these studies, including electrical and optical measurements, have then been applied to the optimization of the deposition conditions for *pm-*$Si_{1-x}C_x$*:H* films. As in the case of pm-Si:H, we found that the α–γ' transition can be observed from the evolution of the electrical properties of the plasma (V_{DC}, V_{PP}, and J_3) as well as by optical emission spectroscopy. In particular, we have demonstrated that the ratio of the $I_{H\alpha}/I_{Fulcher}$ lines, as well as the width of the H_α line, provide a clear signature of the transition from the nanocrystal growth regime to the agglomeration regime. While electrical measurements have so far been used to monitor the various phases of particle nucleation, agglomeration and growth in dusty plasmas, we have shown here that the presence of particles strongly modifies the OES spectra and that it can be equivalently used to precisely monitor the various phases of particle formation and growth.

The presence of silicon nanocrystals in the plasma and their contribution to deposition has been verified by TEM analysis of trapped particles on a cold substrate. Moreover, these studies have demonstrated that - in agreement with OES - the nanocrystals are deposited as individual particles before the α–γ' transition, and as agglomerates after the transition. Accordingly, the AFM analyses have shown a significant increase of the surface roughness at the α–γ' transition.

We have also shown a close correlation between the evolution of the plasma parameters with deposition conditions and the resulting film properties, i.e. their structure and optoelectronic properties. The PL studies have shown strikingly different behavior for *pm-$Si_{1-x}C_x$:H* films as compared to *a-$Si_{1-x}C_x$:H* alloys. Indeed, the PL lifetime and the shape of the spectra are consistent with PL from nanocrystals rather than from the *a-$Si_{1-x}C_x$:H* matrix. Along these lines, we have shown that the PL intensity is closely related to the number of nanocrystals in the film. Thus, we suggested that silicon nanocrystals are responsible for the luminescence in *pm-$Si_{1-x}C_x$:H*. Following this hypothesis, we improved the efficiency of the PL of *pm-$Si_{1-x}C_x$:H* using the following approaches:

i) by decreasing the non-radiative recombination probability, and

ii) by increasing the number of the radiative recombination centers (nanocrystals).

The first approach applied the use of a post-deposition treatment with a hydrogen plasma, which has been suggested to passivate dangling bonds in the vicinity of the nanocrystals. The second approach utilized the inhibition of the agglomeration process by reducing the silane flow rate.

Finally, we have observed that PL characteristics of *pm-$Si_{1-x}C_x$:H* alloys are relatively independent of temperature; a characteristic that may be useful for device applications. Indeed, we have observed that the PL intensity decreases only by a factor of 10 when the temperature is increased from room temperature up to 200 °C. Last but not least, we have produced test PIN diodes (Appendix B) with *p*- and *n*-type layers developed for solar cells. While these devices are not yet optimized, their room-temperature electroluminescence performance (visible with the naked eye, and stable up to 30 hours of continuous operation) is encouraging for the practical application of these materials. Of course, more research is required to achieve LEDs with higher efficiency which might challenge existing technologies.

The studies carried out here could also be extended to the development of a laser based on silicon nanocrystals. The realization of this device would permit the fabrication of a photonic processor bus, which would allow all electronic data transfer to be replaced by faster and non-“transmission-line-limited” optical transfer. The key point for the realization of these goals is a high performance material, such as optimized *pm-$Si_{1-x}C_x$:H* with high quantum efficiency and stability.

The next step that has to be carried out to achieve a higher luminescence efficiency in *pm-$Si_{1-x}C_x$:H* films is the implementation of an in-situ PL measurement setup. In principle, the measurement system would be the same as an ex-situ one except for the design of the probe, which has to be small enough to fit inside the reactor. Our results demonstrating the low

temperature-dependence of PL intensity in *pm-$Si_{1-x}C_x$:H* alloys indeed encourage performing in-situ PL measurements, which has many advantages such as:

i) the measurement of fresh samples before any exposure to air;

ii) providing a complement to UV-visible spectroscopic ellipsometry measurements, as in-situ PL increases the efficiency of the optimization process of luminescent materials. Within a few minutes after each deposition, one can obtain all the optoelectronic properties of deposited films (absorption coefficient, refractive index, complex dielectric function and emission spectrum, and even decay life time);

iii) simple optical alignment, as after calibration only minute adjustments are required for long operational periods. This feature allows the comparison of all measurements quantitatively, regardless of when the measurements were carried out;

iv) being a helpful tool to investigate the evolution of PL spectra due to thickness changes or during multi-layer depositions, and therefore to observe the cavity effect due to multiple reflections.

Besides in-situ measurements, experimental and theoretical studies should be carried out to achieve a better understanding of the mechanism of room temperature PL in polymorphous silicon carbon alloys. In particular, fast, time-resolved PL spectroscopy (down to picosecond timescales), a wide range of temperature-dependent PL spectroscopy (from liquid helium temperature up to the luminescence quenching temperature), resonance, and excitation PL spectroscopy should all be considered for future study.

Appendix A

Introduction to the silicon nanocrystal based photonics

Electron-hole pair formation and recombination

Almost all optoelectronic processes in semiconductor devices are based on the creation or annihilation of electron-hole pairs. Electron-hole pairs are formed by raising electrons in energy, from the valence band (VB) to the conduction band (CB), which creates holes in the valence band. In principle, any incident energetic particle on a semiconductor that can transfer a certain amount of energy, at least equal to the band gap energy, will create an electron-hole pair. The simplest way to create electron-hole pairs is by irradiating with photons of sufficient energy. The reverse process is called recombination, where the pair decays and gives up the excess energy through photon or phonon dissipations.

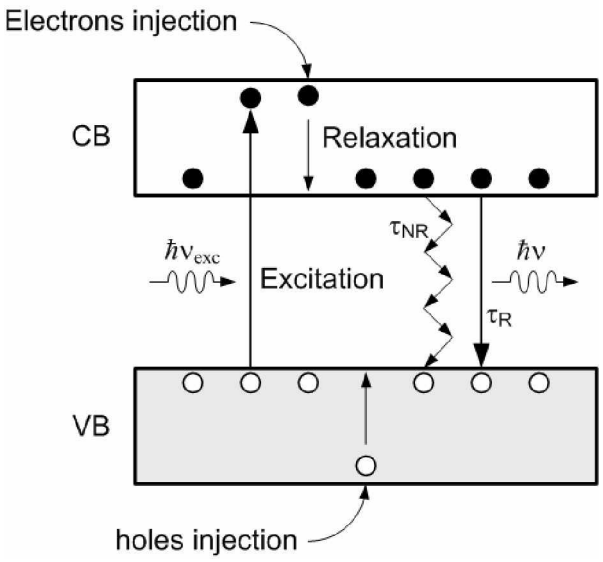

Fig. A.1. General scheme of luminescence in a solid. The e-h (electron-hole) pairs are obtained either by exciting electrons from VB to CB or by injecting them from contacts. The excited e-h pairs relax before recombining through both radiative and nonradiative recombination routes. The competition between these two types of recombination determines the luminescence efficiency [1].

Radiative and nonradiative recombination

In a system under continuous carrier generation, whether by optical excitation or charge injection, a steady-state or a quasi-equilibrium condition is achieved when the recombination rate is equal to the generation rate ($G = R$). The electrons and holes are created and annihilated in pairs. A steady-state excess carrier density $\Delta n = \Delta p$ is established in the system, which maintains the overall charge neutrality. In general, the excess carriers decay by radiative and/or nonradiative recombination processes as illustrated in Fig A.1, in which the excess energy is dissipated by photons and phonons. The decay of excess carriers usually follows an exponential law with respect to time ~exp(-t/τ), where τ is defined as the lifetime of excess carriers.

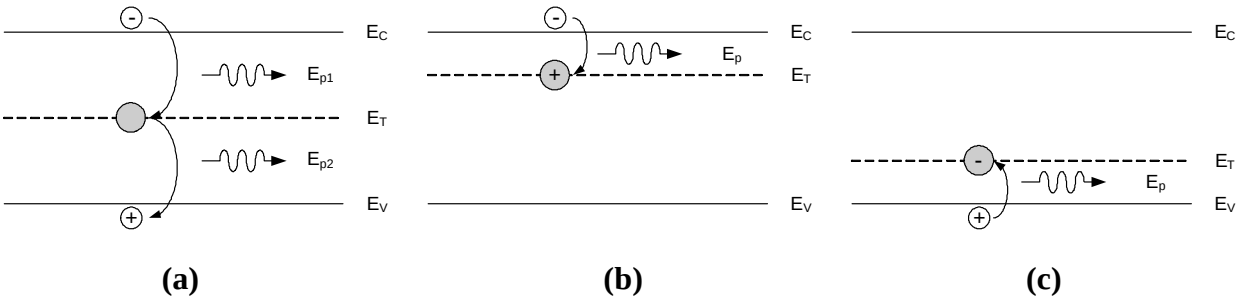

Fig. A.2. Nonradiative recombination processes by phonons dissipation at (a) recombination center, (b) electron trap, and (c) hole trap [2].

The radiative recombination is important for the realization of luminescent devices. In this process, the excess energy is dissipated by photons with energy usually equal to the band gap of the material ($\hbar\nu = E_g$). The process that involves the radiative recombination of electron-hole pairs created by injection of photons is called photoluminescence, while the process resulting from injection of carriers through a p-n junction or similar structure is called electroluminescence. Photoluminescence is also called fluorescence if the the emission happens less than about 1 μs after the excitation, and phosphorescence if it takes longer times, up to hours and days for the emission. In solids, we also can find nonradiative recombination processes which usually take place at surfaces or bulk defects and traps reducing the radiative efficiency of the materials (see Fig. A.2). Thus, the total lifetime of excess carriers τ can be written as:

$$\frac{1}{\tau} = \frac{1}{\tau_r} + \frac{1}{\tau_{nr}} \qquad \text{(A.1)}$$

where τ_r and τ_{nr} are the radiative and nonradiative lifetimes respectively. This can be expressed also as the total recombination rate R_{total} or spontaneous recombination rate R_{sp}, which is given by:

$$R_{total} = R_r + R_{nr} = R_{sp} \qquad \text{(A.2)}$$

where R_r and R_{nr} are the radiative and nonradiative recombination rates per unit volume, respetively. For luminescent device applications, the presence of nonradiative recombination centers as depicted in Fig A.2 is an undesired property. Thus, we want to produce a material with a low density of states (DOS) inside the gap.

Band-to-band recombination in a crystal

In crystalline semiconductors we can distinguish two types of materials based on their band structure, namely direct and indirect band gap semiconductors. This affects the generation and recombination processes of carriers across the band gap (Fig. A.3). In a direct band gap semiconductor (Fig. A.3a), the valence band maximum and the conduction band minimum have the same wave vector **k** at the center zone (**k** = 0), thus an upward or downward transition of electrons does not require any change in momentum or the involvement of a phonon. Therefore, in a direct band gap semiconductor such as GaAs, the excited electrons in the conduction band have only a very short dwelling or residence time, they recombine with holes and emit light of energy equal to the band gap. In this case, the probability of the radiative recombination process is very high. On the contrary, the processes are quite different in the case of indirect band gap semiconductors. As illustrated in Fig. A.3b and c, since the conduction band minimum is not located at **k** = 0, the upward or downward transition of carriers requires a change in momentum which only can be achieved by the help of a phonon. Thus an excited electron in the conduction band minimum at **k** $\neq$ 0 cannot recombine with a hole at **k** = 0 until a phonon with the right energy and momentum is available. In principle, the downward transition process can be assisted either by phonon emission or absorption. Fig. A.3c shows a radiative recombination process assisted by a phonon emission with $E_{ph} = E_g - E_p$, where E_{ph}, E_g and E_p are the energies of the emitted photon, the band gap and the emitted phonon, respectively. In order to have the right phonon collision to occur, the residence time of electrons in the conduction band has to increase. In a perfect crystal and a continuous carrier injection, it should not be a problem to have an efficient photon emission from indirect gap semiconductors. However, no crystal is perfect and there are always impurities and defects which manifest themselves as traps and

recombination centers for nonradiative processes. Thus, in reality, it is most likely that electrons and holes will recombine nonradiatively through such defects and dissipate their excess energy into the lattice as heat. The competition between these two processes reduces the probability of radiative recombination in indirect band gap materials such as Si, Ge, SiC or GaP. Therefore, in general, these materials are not suitable for the realization of light emitting devices.

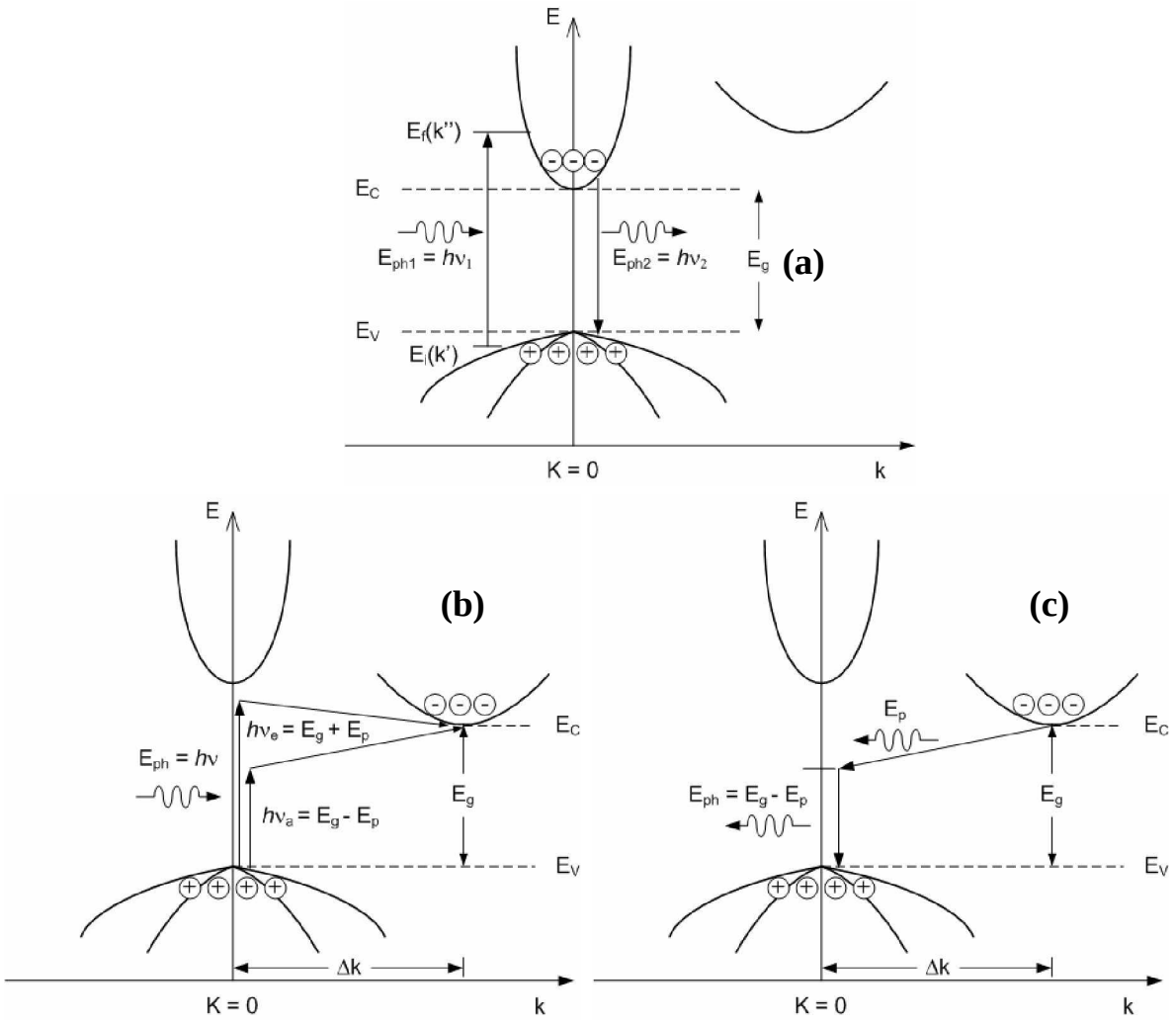

Fig. A.3. Schematic of band-to-band absorption and recombination processes in direct band gap (a) and indirect band gap semiconductors : (b) upward transition and (c) downward transition [2].

Lattice-mismatch problems in crystalline semiconductors

One of the most important problems in heterojuction technology for optoelectronics is the availability of lattice-matched substrates [2]. It is well-known that the careful growth of an epitaxial layer whose lattice constant is close but not equal to the lattice constant of the substrate can result in a coherent strain due to the lattice-mismatch. The lattice-mismatch or misfit is defined as:

$$\frac{\Delta a}{a} = \frac{a - a_0}{a} \qquad \text{(A.3)}$$

where a and a_0 are the lattice constant of the epitaxial overlayer and substrate, respectively. In the case of lattice-matched ($a = a_0$) epitaxial growth, the epitaxial film and the substrate join along a plane boundary in which a common two-dimensional cell structure is maintained (see Fig A.4a). On the other hand, in strained growth layers, the situation is different, either a biaxial tensile strain ($a < a_0$) or a biaxial compressive strain ($a > a_0$) occur, as illustrated in Fig A.4b and c, respectively.

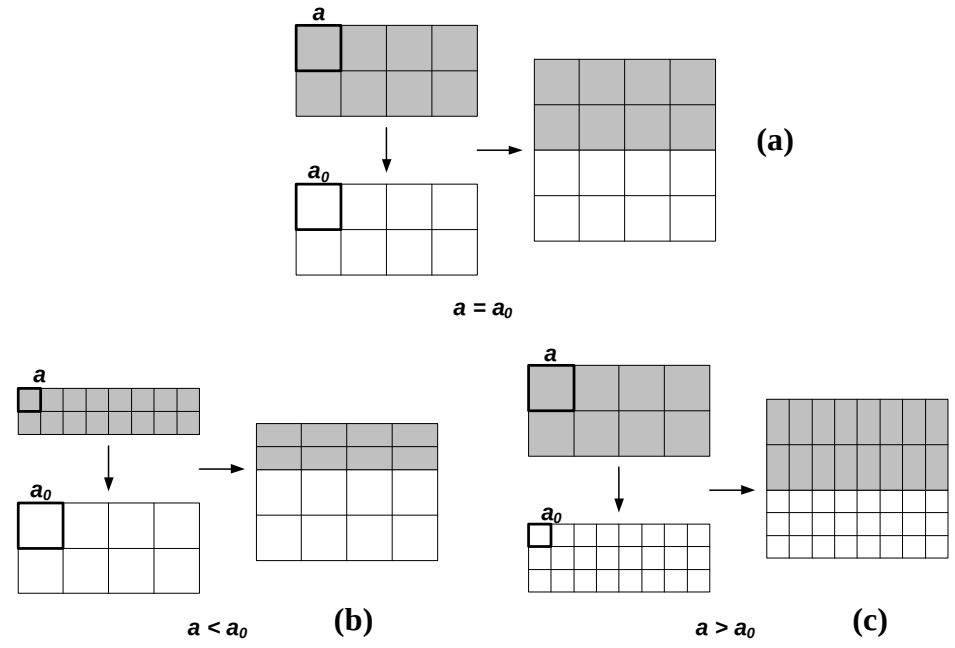

Fig. A.4. Schematic of epitaxial layer growth on a crystalline substrate for different cases : (a) lattice-matched growth, (b) biaxial tensile strain and (c) biaxial compressive strain [2].

Moreover, if we go further with the development of optoelectronic devices integrated on circuits, which must be on silicon, we will find several limitations as described above. They are either the low radiative recombination efficiency in the case of silicon as the active material, or lattice-mismatch if we use another type of semiconductor which has high

efficiency such as GaAs. For comparison to silicon, the lattice constant and band gap energy of several common semiconductors from group III-V are summarized in Table A.1. Therefore, many efforts have been done to increase the radiative recombination efficiency of silicon, such as the synthesis of nanocrystalline and porous silicon, and also their amorphous counterparts as summarized in Ch. 1.

Table A.1. Lattice constant and band gap energy of several semiconductors[2]

Material	Lattice constant, *a* ( ) at 25 °C	Band gap Energy, E_g (eV) at 25 °C
Si	5.4309	1.12
InAs	6.0584	0.36
GaAs	5.6532	1.43
AlAs	5.6611	2.16

Radiative recombination in amorphous semiconductors

In amorphous materials there is no exact direction as in crystals, thus the momentum conservation rules do not apply. Regardless the existence of defects, which are obviously much higher than in crystalline materials, the absence of crystal orientation in amorphous semiconductors increases their radiative recombination probability, which makes them to behave like a direct band gap semiconductor. Another advantage is that amorphous semiconductors can be deposited on any substrate without considering the lattice-mismatch problems.

Photoluminescence from silicon related materials has been largely studied. In the following, we summarize the main models which have been discussed in the literature.

Self-trapped holes model

According to Tsang and Street [3] *, the PL in a-Si:H is based on the following hypothesis*:

1. Holes are self-trapped in a shallow level with distortion energy from the band edge, W_p = 0.2 - 0.25 eV, while electrons are not strongly coupled to the lattice (see Fig A.5).
2. Fast recombination is due to electrons which are attracted by holes, and are not yet thermalized.
3. When the fast recombination ceases, the recombination is due to electrons trapped at band-edge localized states. If the electron is located near to the hole, the coulomb

attraction will lower the emitted energy. If it is far away at a distance *R*, tunneling is important in increasing the lifetime and it is expected to follow:

$$\tau = \tau_0 \exp\left(\frac{2R}{R_0}\right) \qquad \text{(A.4)}$$

where R_0 is the radius of the wave function of the carrier for which it is largest and $\tau_0 \sim 10^{-8}$ s. This fact explains why the PL lifetime distribution in *a-Si:H* is very wide (10^{-2} – 10^{4} μs).

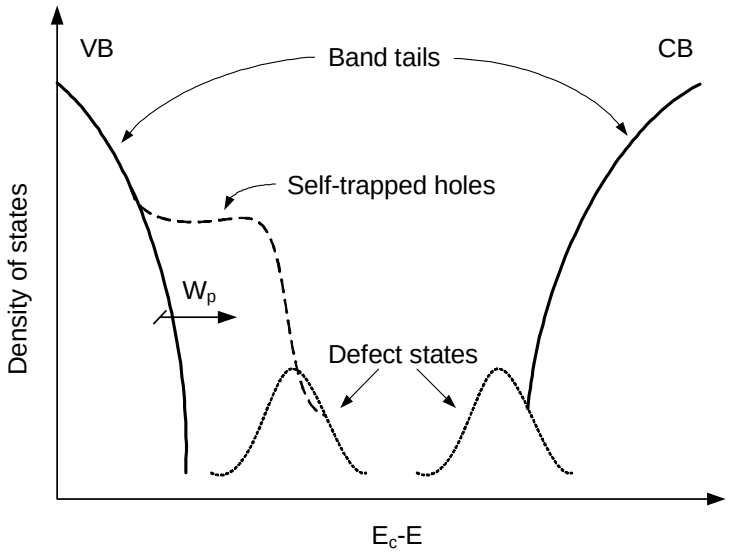

Fig. A.5. Schematic density of states according to the model of Tsang and Street [3]. It illustrates band tail states, self-trapped hole states which split off from the valence-band (VB) tail, and defect states inside the gap [3].

Band gap fluctuation model

This model has been propoesed by Dustan and Boulitrop for a-Si:H [4,5]. In this model, it is assumed that:

1. The band-edge states are dominated by long-range energy fluctuations, and thus the values of the band gap found locally are distributed in energy according to the following relation:

$$P(E_g) = P(E_0 - \varepsilon) \propto \exp(-\beta\varepsilon) \qquad \text{(A.5)}$$

where ε is the energy level below some suitably defined band gap E_0. Then the distribution of values of local minimum is given by

$$P_L(E_0 - \varepsilon) \propto \exp(-\beta_L\varepsilon)(1 - e^{-\beta_L\varepsilon})^N \qquad \text{(A.6)}$$

where typical *a-Si:H* PL spectra are fitted with β_L^{-1} ~100-150 meV and *N*~50.

2. Only the carriers at the minimum energy given by eq. 5.6, are considered to be responsible for PL.
3. Photoexcited carriers thermalize rapidly to the band edges and diffuse some distance apart, depending on the excitation energy. The distribution of energies lost in the thermalization transition is constant due to the exponential form of the tails.
4. The spatial position of a carrier, relative to the point where it was trapped for the first time, is determined by a random walk in which the steps have a distribution of values which shift to larger ones after each successive step. The radiative lifetime also has a distribution of values that depends on the density of carriers of the other sign.
5. The transition rate among tail states does not depend on the initial and final energy, except insofar as the initial energy is correlated with the distribution of distances to lower tail states.
6. The PL spectrum is given by the probabilities of occupation and of radiative recombination from a state as a function of its energy below the band edge, and convolved over the two bands.
7. The exact mechanism of nonradiative recombination is not clear, but assumed to be due to competitive tunneling to the defect states.
8. The Coulomb interaction between electrons and holes and its effect on the statistics of the thermalization transitions are considered. The interaction strength is given by:

$$E_C(r) = \frac{e^2}{4\pi\varepsilon\varepsilon_0 r} \qquad \text{(A.7)}$$

In brief, the luminescence transitions in hydrogenated amorphous silicon are summarized in Fig. A.6. The band-tail transition for 1.4 eV emission, the subsequent recombination proposed for 0.9 eV emission and nonradiative tunneling to the defects are shown. More detailed discussions and summaries of photoluminescence models of amorphous silicon and their related aspects have been reviewed elsewhere [6].

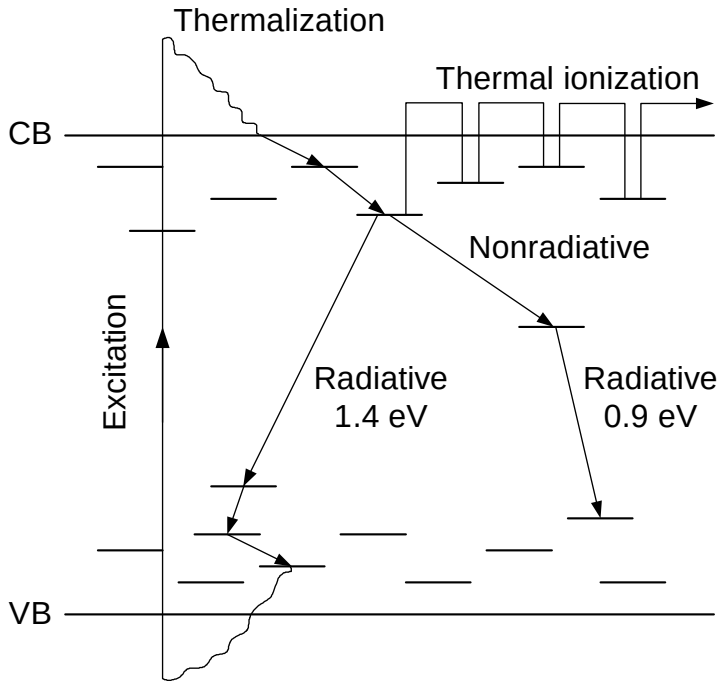

Fig. A.6. Schematic of the luminescence transitions in hydrogenated amorphous silicon [6].

a-$Si_{1-x}C_x$:H alloys case

The similar behavior of *a-$Si_{1-x}C_x$:H* alloys compared to *a-Si:H* shows that alloying does not drastically change the dominant recombination mechanism [7]. The most obvious result of alloying is the increase in band gap energy and band tails broadening [7-13]. Here, we summarize several important points as additional information for the models mentioned above in order to account for the PL behavior of *a-$Si_{1-x}C_x$:H* alloys:

1. The increase of carbon content broadens the band tails and thus the carriers will thermalize deeper into the gap and yield a broader energy distribution.
2. The incorporation of carbon into the amorphous network leads to enhanced structural disorder.
3. The radiative lifetime τ_r is drastically reduced by alloying with carbon, which is attributed to the reduction of e-h separation. Here, two possible mechanisms are proposed [7, 10]:
   a) The faster thermalization due to band tails broadening may reduce the influence of carrier diffusion.
   b) Stronger coulomb interaction between the recombining carriers enforces stronger localization.
4. The hydrogen content influences strongly the structural and optical properties of amorphous silicon carbon alloys (*a-$Si_{1-x}C_x$:H*), especially at low carbon concentration. It

has been suggested that hydrogen atoms do not solely act as bond terminators, but also reduce the distortion of the SiC network. Their concentration would determine the band gap energy for carbon content up to $x \approx 0.45$ [7].

5. The contribution of π orbitals of sp^2 hybridization should be taken into account in the case of carbon rich samples due to the presence of graphite nanograins ($x > 0.4$) [10, 12].
6. In the case of fast recombination processes (nanosecond time scale), the excitonic recombination is suggested to explain the PL mechanism [8].

Quantum-size effects (QSE) in nanostructured semiconductors

The discovery of luminescent properties from quantum well structures opened a new era in the photonics research [14]. As we know, the optical and electronic properties of solids usually do not depend on their size because in most cases we deal only with bulk materials. For example the conductivity and the refractive index of silicon wafers are always the same, regardless how big they are. In such cases, the electron mean free path or the de Broglie wavelength (~200-400 Å) is much smaller than the dimensions of the samples. However, when the dimensions are reduced and become comparable to the mean free path of carriers, quantum size effects (QSE) or quantum confinement effects (QCE) dominate the optoelectronic properties of the materials.

The basic principle of this effect is well-explained by the Heisenberg uncertainty principle, which tell us that if we confine a particle in a region along x-axis defined by Δx, then we will have an uncertainty in its momentum given by [1]:

$$\Delta p_x \sim \frac{\hbar}{\Delta x} \tag{A.8}$$

If the particle is otherwise free and has a mass m, we can express the confinement energy (E_{conf}) as an energy that acts against the kinetic energy with magnitude:

$$E_{conf} = \frac{(\Delta p_x)^2}{2m} \sim \frac{\hbar^2}{2m(\Delta x)^2} \tag{A.9}$$

The confinement effect will be significant when the value of E_{conf} overcomes or is comparable to the kinetic energy of the particle due to the thermal motion in the x direction. In other words, it should be:

$$E_{conf} \sim \frac{\hbar^2}{2m(\Delta x)^2} > \tfrac{1}{2} k_B T \tag{A.10}$$

which tell us that QSE will be important when

$$\Delta x \sim \sqrt{\frac{\hbar^2}{mk_B T}} \qquad \text{(A.11)}$$

Thus in order to have an important QSE, Δx must be of the same order of magnitude of the de Broglie wavelength for thermal motion ($\lambda_{deB} \equiv p_x/h$).

In general, QSE offer several advantages over the properties of the equivalent bulk materials for optical emission applications:

a) The shift of luminescence by the confinement energy allows the wavelength of light emitting devices to be tuned by varying the dimension of nanostructured active materials.
b) The increase overlap between the electron and hole wave functions in the quantum confined structures enhances the emission probability. It shortens the radiative lifetime, thus the radiative recombination wins over competing nonradiative recombination processes. In other words, it increases the radiative efficiency, and therefore the brightness of devices.
c) In the case of quantum well structures, their thickness is very small (~10 nm), which is below the critical thickness for dislocation formation in non-lattice-matched epitaxial layers. This allows to use non-lattice-matched combination of materials, which gives a larger flexibility on the choice of materials and emission wavelengths.

Quantum confinement structures are classified according to whether the electrons are confined in one, two or three dimensions, or based on their degree of freedom. These structures are called:

a) quantum wells for 1-D confinement (2 degrees of freedom)
b) quantum wires for 2-D confinement (1 degree of freedom)
c) quantum dots/box for 3-D confinement (0 degree of freedom)

Among theses structures, quantum dot structures are the most interesting and related to our work. A quantum dot structure maybe considered as a three dimensional quantum well, with zero degree of freedom, which confines the carriers for all directions of motion. If we have a rectangular dot with dimensions (d_x, d_y, d_z), the energy levels of the system will be given by:

$$E(n_x, n_y, n_z) = \frac{\pi^2 \hbar^2}{2m^*}\left(\frac{n_x^2}{d_x^2} + \frac{n_y^2}{d_y^2} + \frac{n_z^2}{d_z^2}\right) \qquad \text{(A.12)}$$

where m^* is the effective mass of electron and n_x, n_y, n_z are the quantum numbers that specify the quantized levels in each direction. In this work, we study nanostructured materials such as *pm-Si:H* and *pm-*$Si_{1-x}C_x$*:H*, which can be described as materials with quantum dots structure: silicon quantum dots embedded in a amorphous matrix of *a-Si:H* or *a-*$Si_{1-x}C_x$*:H* respectively.

Theoretical aspects of luminescence from nanostructured silicon

Another important quantum size effect, which can only be observed in indirect band gap semiconductors such as silicon, is the breakdown of ***k***-conservation rule [15-19]. As we know, in indirect band gap semiconductors, the optical transitions are allowed only by the assistance of phonons to conserve the crystal momentum, which refers to a second-order process [16]. In this type of process, for each transition to occur, it has to wait for a right phonon to collide, which means that the excited electron has to have a long lifetime before it recombines. As a consequence, it increases as well the probability for the nonradiative processes to occur, which normally is a few orders of magnitude higher than the radiative one [20, 21]. Therefore, the luminescence from bulk crystalline silicon is weak due to competition with the more efficient nonradiative recombination processes. The decrease of crystal size down to nanometer scale results in a spatial confinement of electron-hole pairs in real space inside a nanocrystal, which leads to a spread of the wave functions in the reciprocal space. This increases the uncertainty of their crystal momentum, which allows optical transitions in which phonons are not involved. As a consequence, the radiative recombination is a first order process, which can be defined from the Fermi golden rule [16]:

$$\frac{1}{\tau_r} = \frac{16\pi^2}{3} n \frac{e^2}{h^2 m^2 c^3} E_0 \left| \left\langle i_{CB} \left| p \right| f_{VB} \right\rangle \right|^2 \qquad \text{(A.13)}$$

where $|\, i_{CB}\rangle$ is the initial state of the electron in the conduction band and $|\, f_{VB}\rangle$ is the final state in the valence band. E_0 is the energy of the transition and n is the refractive index. The approximation of exciton wave function by the product of $|\, i_{CB}\rangle |\, f_{VB}\rangle$ is valid as the crystalline radius is smaller than the silicon free-exciton Bohr radius (~ 43 Å).

However, we remark here that the transition between indirect and direct band gap condition in the case of quantum dot structures such as silicon nanocrystals or other isolated nanostructures is different compared to the superlattice structures. In superlattices, a direct band gap material results from the size reduction of the Brillouin zone, and the folding of the conduction band bottom to the Γ-point [22]. This effect cannot be observed in isolated nanostructures due to the absence of periodicity, thus the picture of zone folding cannot be applied. Silicon nanostructures can be considered as an intermediate between direct and indirect band gap materials with a certain proportion depending on their size. The indirect nature of the silicon band gap will reduce the radiative recombination, which is important for large crystallites (E_g < 2 eV) [16, 17].

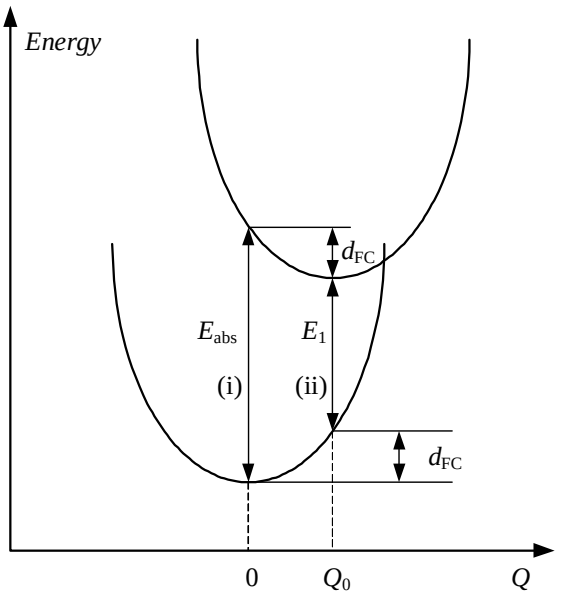

Fig. A.7. Schematic of configuration coordinate representing the variation of the transition energy and the lattice-displacement coordinate Q, which explains the Stokes shift process. The lower curve represents the ground state of the system, while the upper curve represents its excitonic state.

In silicon nanostructures, as in most localized systems, a difference in transition energy is observed between absorption and emission, which refers to the Stokes shift. A common origin is the electron-phonon interaction which leads to the lattice reorganization or relaxation in the excited state as illustrated in Fig A.7 [17, 23]. It shows that under excitation, the maximum absorption occurs for the vertical transition (i) at $Q = 0$, which then relaxes to the minimum configuration in the excited state, centered at $Q = Q_0$. Finally, the radiative recombination occurs with maximum probability at the vertical transition (ii) at $Q = Q_0$. In this simplified representation, we can express the relation between the luminescence energy (E_1) and the absorption energy (E_{abs}) as given by [17]:

$$E_{abs} = E_1 + 2d_{FC} \tag{A.14}$$

where d_{FC} is the Franck-Condon shift, which equals to the energy lost due to the lattice relaxation after capture.

Moreover, the involvement of surface states as deep luminescent centers has to be considered as well to understand the mechanism of luminescence in silicon nanostructures [17, 24, 25]. This has to be taken into account due to the fact that a Stokes shift larger than the predicted one, and practically independent of the size [16, 17, 25], has been observed in small

crystallites. These states were proposed to exist in the form of "self-trapped excitons" as illustrated in Fig. A.8 [17, 26].

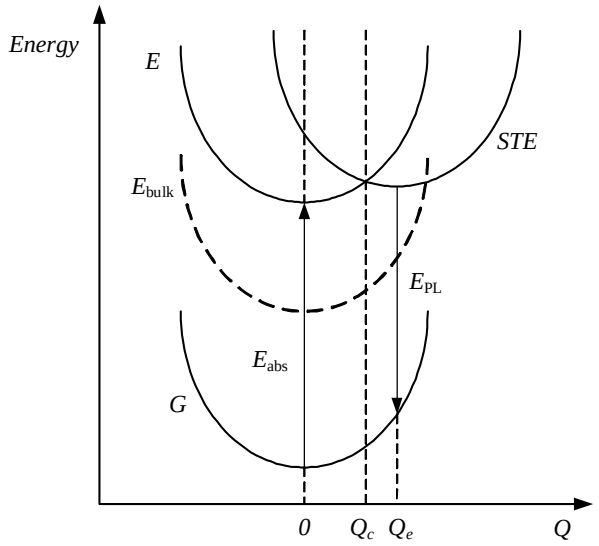

Fig. A.8. Schematic configuration of coordinate system that shows the energy of the ground state (*G*), the normal excitonic state (*E*) and the self-trapped exciton state (STE). The dash curve (E_{bulk}) corresponds to a very large crystallite or bulk crystal with no blue shift, it shows that the STE might not exist in this system.

Let us consider a system consisting of an isolated single covalent bond, which is characterized by a σ bonding state filled with two electrons and an empty σ* antibonding state. In this case, the binding energy is defined as the energy gained from having the two electrons in the lower bonding state. Thus, the excited case, e.g. by photon absorption, can be correlated to a non binding situation, where the repulsive force between atoms dominates and the molecule eventually dissociates. However, if we put this molecule in an elastic medium which retains the molecule from dissociation but allows to have a large distance between its constituent atoms, this will reduce the separation between the σ and σ* states. Therefore, the resulting luminescence energy is much smaller than the optical absorption energy, which corresponds to a Stokes shift of the order of the binding energy (~1eV) [17, 26]. Fig. A.8 shows the configuration coordinate diagram that corresponds to the stretching of a covalent bond. For a small *Q*, the ground and the first excited states are delocalized over the crystallite and show a normal parabolic behavior. However, when *Q* becomes larger and overcomes a critical value Q_c, the system localizes the electron-hole pair on a particular single bond, leading to a larger bond length Q_e and smaller luminescence energy. It refers to self-trapped state or self-trapped exciton state, which can exist as a stable or metastable state. This type of

self-trapped exciton may exist only in small enough crystallites and it is likely favored at surfaces where the elastic response of the environment is weaker than in the bulk.

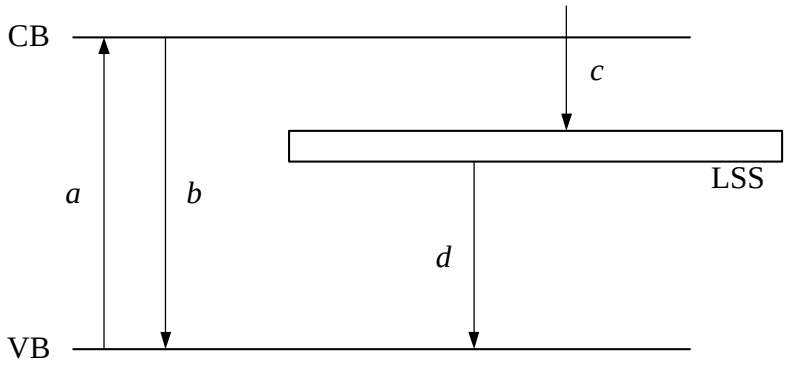

Fig. A.9. Schematic diagram of the possible excitonic recombination paths : a) excitation from ground states (VB) to excited states (CB), b) band-to-band radiative recombination, c) relaxation from CB to localized surface states (LSS), d) radiative recombination from LSS to ground states [27].

A model for a system consisting of a size distribution of nanocrystals having localized surface states (LSS) has been proposed to analyze the PL spectra for both porous silicon and nc-Si embedded in silica, as described in Fig. A.9 [27]. The energy of the emitted photon from the a crystallite will then be given as:

$$E_{PL} = E_g + \Delta E - E_s - E_b \qquad \text{(A.15)}$$

where E_g is band gap of the bulk crystalline material, ΔE is the amount energy that shifts up the gap due to quantum confinement effect (QCE) or QSE, E_s is the localization energy of the surface states and E_b is the exciton binding energy. In principle, ΔE, E_s and E_b are functions of the crystallite size. In a general simple model, the energy upshift due to the QCE (ΔE) can be expressed as [16, 27, 28]:

$$\Delta E = \frac{C}{L^n} \qquad \text{(A.16)}$$

where C and n are constants due to the QCE, which depends strongly on the band gap upshift calculation method being employed. In this model, two types of distribution function of crystal size were taken into account [27]:

a) Normal distribution function:

$$\varphi(L) = \frac{1}{\sigma\sqrt{2\pi}} \exp\left[-\frac{(L - L_0)^2}{2\sigma^2}\right] \qquad \text{(A.17)}$$

where L_0 and σ represent the mean crystallite size and the standard deviation respectively.

b) Log-normal distribution function

$$\varphi(L) = \frac{1}{\sigma\sqrt{2\pi}\,L}\exp\left[-\frac{\{\ln(L)-\ln(L_0)\}^2}{2\sigma^2}\right] \tag{A.18}$$

$$\mu = L_0 \exp\left(\frac{\sigma^2}{2}\right) \tag{A.19}$$

$$SD = \mu\left\{\exp(\sigma^2)-1\right\}^{\frac{1}{2}} \tag{A.20}$$

where μ and SD represent the mean crystallite size and the standard deviation for the log-normal distribution respectively.

Thus, by a standard procedure [27-29], we can obtain PL spectra expressions for each type of crystal size distribution:

a) Normal distribution

$$I(\Delta E) \propto \frac{(C/\Delta E)^{(6-\alpha+n)/n}}{nC\sigma}\exp\left[-\frac{\left\{(C/\Delta E)^{1/n}-L_0\right\}^2}{2\sigma^2}\right] \tag{A.21}$$

b) Log-normal distribution

$$I(\Delta E) \propto \frac{(C/\Delta E)^{(5-\alpha+n)/n}}{nC\sigma}\exp\left[-\frac{\left\{\ln(C/\Delta E)^{1/n}-\ln(L_0)\right\}^2}{2\sigma^2}\right] \tag{A.22}$$

where α is the exponential constant related to oscillator strength, which depends on the material properties and the surrounding environment.

References

[1] M. Fox, *Oxford Master Series in Condensed Matter Physics: Optical Properties of Solids*, Oxford University Press, Oxford, 2001.

[2] P. Bhattacharya, *Semiconductor Optoelectronic Devices*, Prentice-Hall, Inc., New Jersey, 1994.

[3] C. Tsang, R. A. Street, *Phys. Rev. B* **19**, 3027 (1979).

[4] F. Boulitrop, D. J. Dunstan, *Phys. Rev. B* **28**, 5923 (1983).

[5] D. J. Dunstan, F. Boulitrop, *Phys. Rev. B* **30**, 5945 (1984).

[6] R. A. Street in J. I. Pankove (Ed.), *Semiconductor and Semimetals* **Vol. 21** : *Hydrogenated Amorphous Silicon* **Part B**, Academic Press, Inc., Orlando, 1984, p197-244.

[7] W. Siebert, R. Carius, W. Fuhs, K. Jahn, *Phys. Stat. Sol.* (*b*) **140**, 311 (1987).

[8] C. Palsule, S. Gangopadhyay, D. Cronauer, B. Schröder, *Phys. Rev. B* **48**, 10804 (1993).

[9] D. Engemann, R. Fischer, J. Knecht, *Appl. Phys. Lett.* **32**, 567 (1978).

[10] S. V. Chernyshov, E. I. Terukov, V. A. Vassilyev, A. S. Volkov, *J. Non-Cryst. Solids* **134**, 218 (1991).

[11] I. Solomon, M. P. Schmidt, H. Tran-Quoc, Phys. Rev. B 38, 9895 (1988).

[12] V. A. Vasil'ev, A. S. Volkov, E. Musabekov, E. I. Terukov, V. E. Chelnokov, S. V. Chernyshov, Yu. M. Shernyakov, *Sov. Phys. Semicond.* **24**, 445 (1990).

[13] L. R. Tessler, I. Solomon, Phys. Rev. B 52, 10962 (1995).

[14] L. Esaki, R. Tsu, *IBM Journal of Research and Development* **14**, 61 (1970).

[15] D. Kovalev, H. Heckler, M.Ben-Chorin, G. Polisski, M. Schwartzkopff, F. Koch, *Phys. Rev. Lett.* **81**, 2803 (1998).

[16] C. Delerue, G. Allan, M. Lannoo, *Phys. Rev. B* **48**, 11024 (1993).

[17] M. Lannoo, C. Delerue, G. Allan, *J. Lumin.* **70**, 170 (1996).

[18] C. Delerue, G. Allan, M. Lannoo, *J. Lumin.* **80**, 65 (1999).

[19] S. Horiguchi, *Superlattices and Microstructures* **23**, 355 (1998).

[20] J. I. Pankove, *Optical Processes in Semiconductors*, Dover Publications, Inc., New York, 1971.

[21] A. Hangleiter, *Phys. Rev. B* **35**, 9149 (1987).

[22] T. Takagahara, K. Takeda, *Phys. Rev. B* **46**, 15578 (1992).

[23] A. Puzder, A. J. Williamson, J. C. Grossman, G. Galli, *J. Am. Chem. Soc.* **125**, 2786 (2003).

[24] Y. Kanemitsu, T. Ogawa, K. Shiraishi, K. Takeda, *Phys. Rev. B* **48**, 4883 (1993).

[25] Y. Kanemitsu, *Phys. Rev. B* **49**, 16845 (1994).

[26] G. Allan, C. Delerue, M. Lannoo, Phys. Rev. Lett. 76, 2961 (1996).

[27] Md. N. Islam, S. Kumar, J. Appl. Phys. 93, 1753 (2003).

[28] V. Ranjan, V. A. Singh, G. C. John, Phys. Rev. B 58, 1158 (1998).

[29] G. C. John, V. A. Singh, Phys. Rev. B 50, 5329 (1994).

Appendix B

From material to devices

Based on the results shown in chapter 5, the low EL intensity observed here is an inevitable problem concerning the deposition at low RF power that leads to the low concentration of nanocrystals in the films (see Fig 5.31). This is a dilemma, in one hand we need nanocrystals as the luminescence source but it needs high power, while on the other hand high RF power can deteriorate the doped layer during deposition. The damage in doped layer during deposition of *i*-layer means the decrease of device performance. The most important step here is to realize a working device before we can go further, thus we have chosen to reduce RF power from standard condition of 20 W down to 10 W.

In this section, we briefly show the characteristics of our first *p-i-n* light emitting diodes (LED), using *pm-*$Si_{1-x}C_x$*:H* as *i*-layer with a thickness of ~200 nm. The structure of the cell is depicted in Fig. 2.20b. Here, we used boron doped *a-*$Si_{1-x}C_x$*:H* as *p*-layer and a phosphorous doped *a-Si:H* as *n*-layer, both deposited at low power in the ARCAM reactor [1]. The thickness of the doped layers are typically 15 nm. In this structure, the glass/ITO/n-layer acts as the optical window for the LED. For this reason, the n-layer should be deposited thin enough to reduce the absorption of emitted light. The surface of the diodes (typically 0.12 cm^2) was defined by 100 nm thick Aluminum dots thermally evaporated through a shadow mask. The emitted power was measured using a silicon photodiode, while the electroluminescent (EL) spectrum was measured using a spectrometer equipped with a liquid nitrogen cooled CCD detector through an optical fiber.

Fig. B.1a shows the dark *I-V* characteristics of a *pm-*$Si_{1-x}C_x$*:H* diode, with a rectification ratio of 5 orders of magnitude at 5 V. The EL diode under forward bias at room temperature emits visible light which can be observed with a naked eye. The threshold voltage for EL is about 6 V, which is shown by the emission power as function of applied voltage in Fig. B.1b. The figure shows that for applied voltages below 6 V there is practically no light emitted from the diode. Figure B.2a shows the EL spectrum of the diode operated at room temperature compared with the room temperature PL spectrum of the same material. This diode was operated in forward bias at 9.3 V with a current of 80 mA. It shows that the intensity of EL is more intense than the PL one, which is due to the different optical system in measurement. The difference in shape between PL and EL spectra could be due to interference effect by

multi-reflection, which does no exist in PL. Note that the measured samples for PL were deposited on Corning glass with a refractive index close to that of the film, while EL diodes have a multilayer structure with different refractive index, including a reflective layer of Aluminum contact. However, the large blue shift shown in Fig B.2a cannot be explained by the presence of the multilayer structure only. Moreover, this behavior is opposite with respect to that observed in $a\text{-}Si_{1-x}C_x{:}H$ EL diodes, where a red shift of EL with respect to PL is usually observed [2, 3]. Another reason for the blue shift could be the different carrier injection range or efficiency, where the p-n junction might open a higher possibility to inject the carriers to the nanocrystals in the whole thickness of films, while in PL case is limited only in surface vicinity and depends on the size.

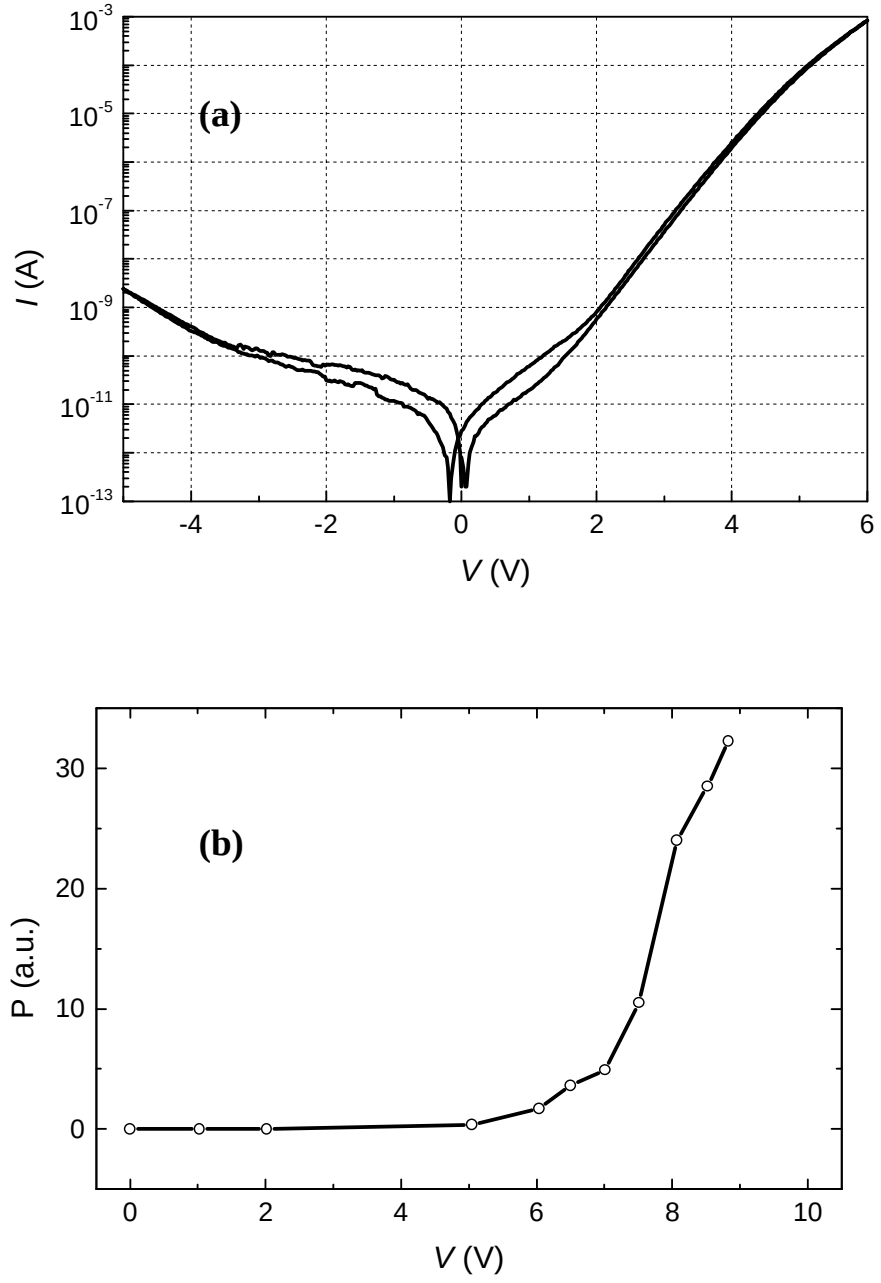

Fig. B.1. (a) The I-V characteristics of *pm-*$Si_{1-x}C_x$*:H* EL *p-i-n* diode for samples with structure as mentioned in Fig. 2.16b. (b) The emitted power as function the applied voltage for the same electroluminescent diode.

Finally, the most remarkable property of our diodes is that they are stable under continuous operation. This confirms that the nanocrystals are well encapsulated by the matrix of *pm-$Si_{1-x}C_x$:H*. Moreover, we observed that the EL intensity tends to increase slightly with the operation time as shown in Fig. B.2b. The increase in intensity here is suggested to be due to the interface between film and metal contact. Note that the measured sample in Fig. B.2 is a virgin sample, measured just after deposition. Thus, after few minutes of operation, there may be an improvement in film/metal contact interface, which allows better injection as shown by the increase of EL intensity. For longer operation times the increase in intensity becomes less important and reaches a saturation.

In EL devices, the basic improvement of performance must be correlated with the competition between the radiative and non-radiative recombination processes. Here, the passivation of non-radiative recombination defects, such as dangling bonds is considered as an important factor. In this case, the plasma hydrogen treatment is reported to be efficient to improve the device performance signified by the increase of brightness and the decrease of threshold voltage [4]. In the case of *pm-$Si_{1-x}C_x$:H*, this treatment has been shown to decrease the non-recombination probability indicated by the increase of the PL intensity (see Ch. 5). Another important device related issue is the injection of carriers, especially for *pm-$Si_{1-x}C_x$:H* films where their luminescence centers (silicon nanocrystals) are embedded in a high electric resistive matrix with a wide band gap. Thus, to find an efficient way to bring the carriers from the electric contacts (electrodes) to the nanocrystals is another task that has to be improved to enhance the efficiency of LEDs.

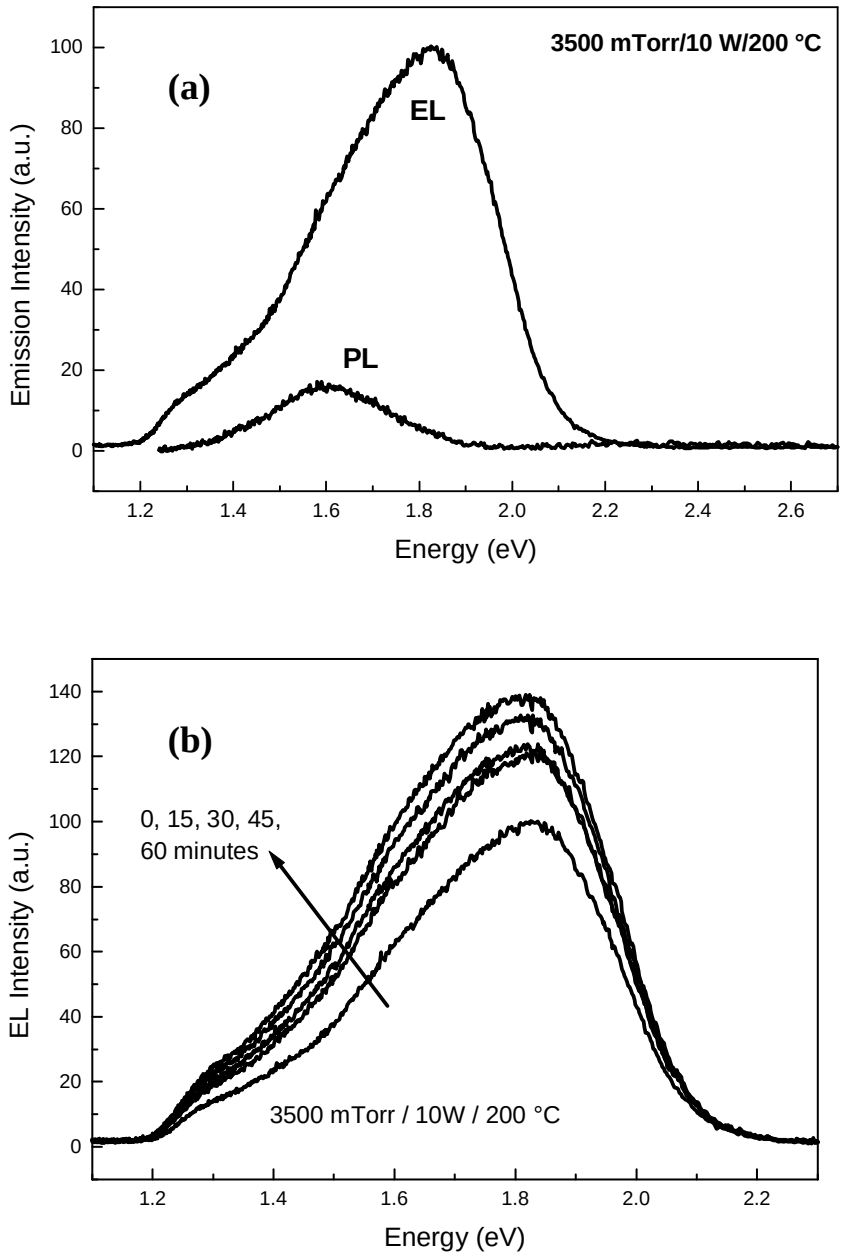

Fig. B.2. (a) The typical spectrum of *pm-*$Si_{1-x}C_x$*:H* EL *p-i-n* diode compared to PL spectrum of the same material as *i*-layer (3500 mTorr, 10 W, 200 °C and 33.35 sccm of CH_4). (b) The evolution of EL spectra with time for continuous operation in the direct current mode, which is operated with injected current of 80 mA and applied voltage of 9.3 V.

References

[1] P. Roca i Cabarrocas, J. B. Chévrier, J. Huc, A. Lloret, J. Y. Parey, J. P. M. Schmitt, *J. Vac. Sci. Technol.* **A9**, 2331 (1991).

[2] H. Munekata, H. Kukimoto, *Appl. Phys. Lett.* **42**, 432 (1983).

[3] D. Kruangam, M. Deguchi, T. Toyama, H. Okamoto, Y. Hamakawa, *IEEE Trans. Electron Devices* **35**, 957 (1988).

[4] J.-W. Lee, K. S. Lim, *Jpn. J. Appl. Phys.* **35**, L1111 (1996).

Appendix C

List of publications

C.1. Journals and proceedings on polymorphous silicon related subjects:

1. A. V. Kharchenko, V. Suendo, P. Roca i Cabarrocas, *Plasma studies under polymorphous silicon deposition conditions, Thin Solid Films* **427** (2003) 236.
2. V. Suendo, A. V. Kharchenko, P. Roca i Cabarrocas, *The effects of RF plasma excitation frequency and doping gas on the deposition of polymorphous silicon thin films, Thin Solid Films* **451-452** (2004) 259.
3. A. V. Kharchenko, V. Suendo, D. Daineka, P. Roca i Cabarrocas, *Effect of dopants on the dynamics of powder formation and the properties of polymorphous silicon thin films, Materials Science Forum* **455-456** (2004) 536.
4. S. Tchakarov, D. Das, O. Saadane, A. V. Kharchenko, V. Suendo, F. Kail, P. Roca i Cabarrocas, *Helium versus hydrogen dilution in the optimization of polymorphous silicon solar cells, J. Non-Cryst. Solids* **338-340** (2004) 668.
5. O. Saadane, S. Lebib, A. V. Kharchenko, V. Suendo, C. Longeaud, P. Roca i Cabarrocas, *Helium versus hydrogen dilution of silane in the deposition of polymorphous silicon films: Effects on the structure and the transport properties, Mat. Res. Soc. Symp. Proc.* **762** (2003) A5.1.
6. V. Tripathi, Y. N. Mohapatra, Md. N. Islam, V. Suendo, P. Roca i Cabarrocas, *Size distribution of embedded nano-crystallites in polymorphous silicon studied by Raman spectroscopy and photoluminescence, Mat. Res. Soc. Symp. Proc.* **762** (2003) A19.7.
7. D. Daineka, V. Suendo, P. Roca i Cabarrocas, *Temperature dependence of the optical functions of amorphous silicon-based materials: application to in situ temperature measurements by spectroscopic ellipsometry, Thin Solid Films* **468** (2004) 298.
8. V. Suendo, P. Roca i Cabarrocas, G. Patriarche, *Luminescence of polymorphous silicon carbon alloys, Optical Materials* **27**, 953 (2005).
9. Th. Nguyen-Tran, V. Suendo, P. Roca i Cabarrocas, *Optical study of disorder and defects in hydrogenated amorphous silicon carbon alloys, Applied Physics Letter* **87**, 011903 (2005).

10. V. Suendo, G. Patriarche, P. Roca i Cabarrocas, *Influence of deposition parameters and post-deposition plasma treatments on the photoluminescence of polymorphous silicon carbon alloys, J. Non-Cryst. Solids* (2005), submitted.
11. V. Suendo, P. Roca i Cabarrocas, *Plasma diagnostics in silane-methane-hydrogen plasmas under pm-$Si_{1-x}C_x$:H deposition conditions, J. Non-Cryst. Solids* (2005), submitted.

C.2. Conferences and workshops on polymorphous silicon related subjects:

1. 1st aSi-Net Workshop jointly held with 8th Euroregional Workshop on "Thin Silicon Device" Materials, characterization, new applications; Salerno, Italy, 6-8 March 2002.
2. 29th European Physical Society Conference on Plasma Physics and Controlled Fusion, Montreux, Switzerland, 17-21 June 2002.
3. International Center of Advanced Materials and Electron Microscopy, Autumn School 2002: "Progress in Materials Science through Electron Microscopy", Berlin, Germany, September 28th - October 3rd 2002.
4. Journée thématique du MRCT (Mission des Ressources et Compétences Technologies du CNRS), Nucléation, croissance et transport de nano-micro particules dans les plasmas, Gif-sur-Yvette, France, 7-8 January 2003.
5. 2st aSi-Net Workshop jointly held with 9th Euroregional Workshop on Thin Silicon Devices, Lisbon, Portugal, 19-21 February 2003.
6. The Board of European Students of Technology (BEST) spring course: "Nanotechnologies: a revolution in progress", Ecole Polytechnique, Paris, France, 24-29 March 2003.
7. E-MRS 2003 Spring Meeting 20th Anniversary, Strasbourg, France, 10-13 June 2003.
8. Réseau Nanominiaturisation CNRS/STIC: "Deuxième reunion de l'Equipe-Projet Plasmas Froids pour l'Elaboration de Micro et Nanostructure", Col de Porte, Isère, France, 4-6 February 2004.
9. E-MRS 2004 Spring Meeting, Strasbourg, France, 24-28 May 2004.
10. Colloque-atelier sur le thème : «Bandes Interdites Photoniques et Emission Pour Systèmes Intégrés de Communication », 20 septembre 2004, Amphi Blandin, bât 510, Université Paris XI, Orsay.

11. 4th International Conference on the Physics of Dusty Plasmas, Orléans, France, 13-17 June 2005.
12. 21st International Conference on Amorphous and Nanocrystalline Semiconductors, Calouste Gulbenkian Foundation, Lisbon, Portugal, 4-9 September 2005.

C.3. Other publications:

1. V. Suendo, R. Eto, T. Osaki, M. Higa, A.Tanioka, *Ionic environmental effect on the time-dependent characteristics of membrane potential in a bipolar membrane, J. Colloid Interface Sci.* **240** (2001) 162.
2. V. Suendo, M. Minagawa, A.Tanioka, *Membrane potential of a bipolar membrane: the effect of concentration perturbation of the intermediate phase around a certain value, J. Electroanal. Chem.* **520** (2002) 29.
3. V. Suendo, R. Eto, A. Tanioka, Ionic rectification properties of a bipolar interface consisting of a cationic surfactant and cation-exchange membrane, *J. Colloid Interface Sci.* **250** (2002) 507.
4. V. Suendo, M. Minagawa, A.Tanioka, *Bipolar interface formation of cationic surfactant on the surface of a cation-exchange membrane: current-voltage characteristics in aqueous electrolyte solution, Langmuir* **18** (2002) 6266.